Acetylene: Dispersed Fluorescence Spectroscopy and Intramolecular Dynamics

by

Jonathan Paul O'Brien

B.S. Chemistry (1991)

Hope College

Submitted to the Department of Chemistry in Partial Fulfillment of the Requirements for the Degree of

DOCTOR OF PHILOSOPHY

at the

MASSACHUSETTS INSTITUTE OF TECHNOLOGY

September 1997

© 1997 Massachusetts Institute of Technology.
All rights reserved

Signature of Author _____
Department of Chemistry
June 27, 1997

Certified by _____
Robert W. Field
Professor of Chemistry
Thesis Supervisor

Accepted by _____
Dietmar Seyferth
Chairman, Department Committee on Graduate Students

MASSACHUSETTS INSTITUTE OF TECHNOLOGY

SEP 17 1997

LIBRARIES

This doctoral thesis has been examined by a Committee of the Department of Chemistry as follows:

Professor Moungi G. Bawendi _____
Chairperson

Professor Robert W. Field _____
Thesis Supervisor

Professor Sylvia T. Ceyer _____

for my best friend and wife, Amelia

Acetylene: Dispersed Fluorescence Spectroscopy and Intramolecular Dynamics

by

Jonathan Paul O'Brien

Submitted to the Department of Chemistry on June 27, 1997 in
Partial Fulfillment of the Requirements for the Degree of Doctor
of Philosophy in Chemistry

ABSTRACT

In this thesis a study of the Intramolecular Vibrational Redistribution (IVR) on the ground ($\tilde{X}^1\Sigma_g^+$) state of acetylene is presented. For this purpose, several dispersed fluorescence (DF) spectra were recorded. The transitions originate from different vibronic levels on the first excited singlet $\tilde{A}^1A_u$ state but terminate on the same vibrational levels of the $\tilde{X}^1\Sigma_g^+$ state.

Each of the DF spectra are composed of several overlapping progressions of the same $\tilde{A}^1A_u \rightarrow \tilde{X}^1\Sigma_g^+$ initially excited states, the Franck-Condon allowed zero-order bright states (ZOBS). These are the CC stretching (v_2'') and *trans*-bending (v_4'') vibrational modes. Each ZOBS is associated with a distinct fractionation pattern caused by anharmonic coupling with surrounding Franck-Condon dark states ($v_1'' = 0, v'' = 0_3, v_5'' = 0$) on the $\tilde{X}^1\Sigma_g^+$ state. Identification of the distinct ZOBS fractionation patterns is accomplished by simultaneously comparing the relative intensities of the DF spectra. A manual pattern identification procedure is presented first.

Significant changes to the technique of traditional DF spectroscopy are described. These enable high quality frequency ($\pm$ 4.0 cm^{-1}) and intensity ($\pm$ 20%) calibration for spectra recorded over a 20,000 cm^{-1} energy range. DF spectra recorded in this way are used in a new statistical pattern recognition technique.

From the disentangled fractionation patterns, $\tilde{A}^1A_u \rightarrow \tilde{X}^1\Sigma_g^+$ Franck-Condon factors and deperturbed energies for progressions of the ZOBS (nv_2,mv_4) are be obtained. These results are useful in defining an effective Hamiltonian model which describes the ZOBS fractionation patterns. Qualitative IVR trends along each ZOBS progression are also investigated. The results presented here indicate that initial excitation in the CC stretch and *trans*-bend vibrations is redistributed by strong Bend-Bend interactions prior to weaker Stretch-Bend or Stretch-Stretch interactions.

Several previously undocumented features were observed in the DF spectra and the process of identifying them is described.

Thesis Supervisor: Robert W. Field
Title: Professor of Chemistry

Acknowledgments:

Looking back over the past six years, reminiscing about my experience at MIT, I am immediately drawn to one of the most difficult times; this past year. A little over a year ago, I under went an experimental eye surgery to repair a laser injury that occurred in one of our laboratories. As I recovered, lying face down for almost two months, I honestly wondered if I would ever be able to finish my degree. While I have recovered quite nicely, I would *never* have made it back without the loving support of my wife, my research group, my research supervisor, and the other physical chemistry graduate students at MIT. For all of their help, I am extremely grateful and will always remember their enormous amount of kindness and generosity.

I am truly grateful to Bob Field. He has been an incredible supervisor over the last six years. He is packed full of enthusiasm and ingenious ideas about spectroscopy and dynamics. He never ceased to amazed me with his ability to derive back-of-the-envelope calculations that *always* seemed to point in the favor of *his* argument. Bob is an unique manager! He lets his students have considerable intellectual freedom but is careful to add the necessary prodding to keep a student on track. I appreciate the freedom he gave me in reorganizing the spectroscopy laboratory and in running the acetylene DF experiments.

I spent a large portion of my first few semesters in the Undergraduate Chemistry Office. Launa Calendar and Melinda Cerny always made me smile. I am thankful for my interactions with Melinda both as a teacher, professional advisor, and friend. I wish her the best.

During my six years, I have interacted with many undergraduates both as a teaching assistant and through the undergraduate research program. I was very fortunate to meet a very special person, Jennifer Sokol. Beyond her natural gifts, she is one of the most motivated and hard working undergraduates that I have ever encountered. She was incredibly helpful in the laboratory and made *substantial* contributions to my research. I wish her the best as she starts a new phase in her life. I know that she will succeed at anything she decides to do.

I was fortunate to have worked with many talented Field graduate students during my early years at MIT. Dave Jonas, Jim Lundberg, Bhavani Rajaram, Mike McCarthy, Jonathan Bloch, Nicole Harris, George Adamson, and Chris Gittins were extremely helpful. I also was able to work with many graduate students from other labs. Jody Klassen and I spent a month one summer recording energy transfer data on acetylene. One semester late at night, Manoj Nirmal and I tried desperately to record gain measurements of their CdSe quantum dots. Ken Kuno and I tried to revive the same project a couple of years later. It was always pleasant to interact with David Norris and his wife Beth.

I helped to setup a Resonance Raman experiment with Brian Gilbert. Brian talked me through some difficult times. We also drank and brewed a lot of beer. Steve Drucker and I collaborated on the acetylene triplet work described in Chapter 8 of this thesis. I enjoyed the numerous conversations we had about life, science, and acetylene.

The current Field group members are incredible! I have enjoyed my interactions with Richard Duan, James Janni, Leah Ruslen, Michelle Silva, Ilia Dubinsky, David Moss, and Sergey Panov. Jason Clevenger was extremely helpful this past year with computer questions and in reorganizing the superlab disaster. I don't think that anyone could have done the job he's had to do for the past 10 months. (I know that I would not have!) I enjoyed our

occasional trip to the real world for dinner. Kevin Cunningham has always been willing to lend an ear to my rantings. His presence has kept me from the edge and in good spirits. It has been fun living with Fred Mikulec for the past year.

After ten years and nearly a million people hours, the acetylene isomerization problem may finally be solved! There are two unique individuals that I have had the pleasure of working with on the dynamics of acetylene:

Stephani Solina was an inspiration that drew me towards the world of dynamics and acetylene. Over the years, her friendship, constant excitement, and encouragement helped me to better formulate who I am. Her ambitious style started numerous theoretical and experimental collaborations that have become an essential part of the acetylene project at MIT. I wish her the best in her new career and look forward to her continued friendship.

Matt Jacobson and I have developed a strong collaboration on acetylene which I hope continues beyond my years at MIT. The beautiful results presented in this thesis would never have been possible without Matt's hard work and input. I enjoyed our conversations about acetylene, dynamics, and the future of physical chemistry. During the writing phase of this thesis, Matt and Judy surprised me with a dinner and musical. That evening out really helped me to relax.

Steve Empedocles and I frequented the Muddy Charles to share some spirits and conversation. We also have spent some time in the gym playing basketball. Even though we are both atrocious, it was fun! The meals and slide shows courtesy of Steve and Marianne gave me an opportunity to relax and enjoy life a bit.

I had many great times with my good friend Bashir and his wife Rasha. Now that they have returned to Saudia Arabia, I will miss their home cooked meals, movies, and adventurous drives to where ever Bashir wanted to eat. I wish them both the best of luck with their new move and newest addition to their family, Dana.

My family has been a source of great inspiration to me. For their constant support and understanding I am extremely grateful. My wife, Amelia, continues to be my best friend. I would not have made it without her by my side. She was always understanding when it came to late nights in the lab, the occasional science banter at MIT functions, and the mood swings accompanying my apparent successes and failures.

Table of Contents

Chapter 1: Understanding the IVR Processes in Acetylene: Dispersed Fluorescence Spectra, Theoretical Models, and Pattern Recognition

Motivation

The following summary describes the research conducted for this dissertation and serves as a general introduction to the main body of the thesis. This chapter is organized into five major sections: Introduction, Background on Acetylene, Current Work, Future Work, and Notation.

1.1 Introduction

Chemists have always sought to understand the nature of chemical reactions. All chemical reactions require the "breaking and making" of single and sometimes multiple chemical bonds. These chemical processes involve complex motion of atoms contained in a molecular species. Over the last one hundred years, physical chemists have studied a multitude of molecular species using quantum mechanical, kinetic and thermodynamic theory. The advent of lasers in the 1960's provided revolutionary ways for physical chemists' to study chemical reactivity.[1-5] Scientists believed that lasers could eventually be used to *control* chemical reactivity. Initial experiments hoped to control reactivity by using laser light to excite very specific high vibrational levels of a molecule. In principle, this excitation process could activate chemical reactivity by increasing the probability that a selected bond will be broken or would become more susceptible to reactive attack. However, results from those experiments revealed that the excitation did not remain localized in a specific bond. The initial vibrational energy was redistributed throughout the rest of the molecular framework before the molecule could undergo chemical reaction.[1,6-8] These redistribution processes have made most laser control strategies designed to

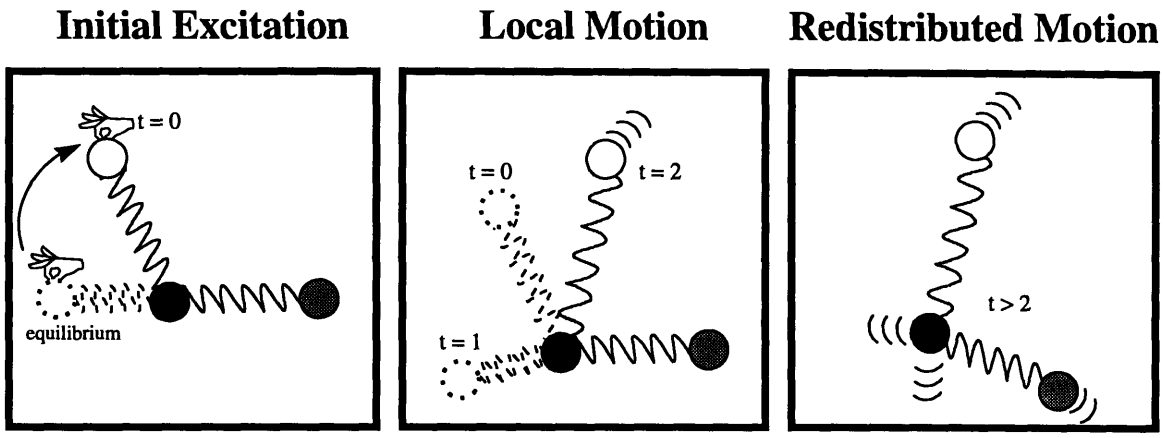

Figure 1.1: Schematic representation utilizing balls and springs of the redistribution of localized vibrational motion. At early times the initial vibrational motion stays localized. However, the localized motion is soon distributed through out the molecular framework.

activate chemical reactivity within a single chemical bond mostly ineffective. (Recently, Crim and co-workers have demonstrated how lasers can be used to control the chemical selectivity of dissociation processes.[1]) This energy randomization can be thought of in terms of a set of coupled balls and springs. We know that if we displace one of the balls and release it at t=0, the excitation of the specific plucked ball and spring will remain localized for some time, but energy eventually will leak to the other balls and springs and they will start to move as well, see Figure 1.1. Physical chemists involved in the study of molecular dynamics have been striving to understand exactly how, when and where does the redistribution of energy take place for real molecules. A comprehensive understanding of these processes may lead to possible *control* mechanisms for many molecules.

For molecules near their equilibrium, with low internal energy, we have very good descriptions, harmonic oscillator and rigid rotor, of the vibrational and rotational motions. However, chemical reactions seldom occur near equilibrium. Therefore, we have chosen to focus on highly excited molecular species which contain significant amounts of internal energy.

To develop an effective laser control strategy, we begin by asking where the molecule redistributes vibrational energy. Does the rate and primary path for redistribution of vibrational motion differ for initial excitation in a pure stretching vibration, a pure bending vibration, or a combination of stretch and bend? Molecular interactions with the environment, such as with solvents, can make it difficult, due to the high density of states and the loss of frequency domain resolution, to interpret the results of experiments designed to answer questions of this nature. Our group's research avoids these problems by conducting low pressure gas phase experiments which are directed at the characterization of the vibrational redistribution processes of an isolated molecule. The characterization of the important molecular reaction pathways of vibrational redistribution necessitates a strong knowledge of the intramolecular vibrational redistribution (IVR). IVR processes for many molecular species have been the subjects of intense study, leading to a general and fundamental understanding of the IVR of many molecular systems.[9,10] The complexity of the IVR changes as the molecular species is altered, i.e. as the size, functional groups, and isotopes are changed. However, we do not know quantitatively how or why IVR changes from molecule to molecule or within a molecule at different vibrational energies. To develop a global standard or model for IVR of a particular molecule, we need to learn about individual IVR processes for a range of initially excited molecular vibrations and to try to understand how the IVR mechanism changes for different initial excitation conditions. The multi-dimensional potential energy surface of a polyatomic molecule, $V \equiv \left(\frac{1}{2} \sum_{i=1}^{3N-6} Q_i^2 \right)$, controls the IVR coupling. In practice, we are limited by the types of initial molecular excitations that we can create in the laboratory, probing only a small region of the full potential energy surface. We hope that this localized view of the molecular dynamics gives us enough insight so that we will

be able to extrapolate the dynamics over a range of different initial excitation conditions. This knowledge will help to develop laser control strategies which utilize IVR and laser excitation as useful ways to control chemical reactivity.

We chose to determine the IVR structure of a molecular species by conducting a series of high- and low- resolution frequency-domain laser experiments. The complementarity of frequency and time-domain is well established, see References 11 and 12 for examples. Information extracted from a frequency domain spectrum will give the same insight into the molecular dynamics as a time domain experiment. For either a high resolution (long time) or low resolution (short time) frequency domain experiment, one samples the eigenstates of a system. Confusion usually arises when one starts to think about interpreting an eigenstate spectrum in terms of yielding information about dynamics or energy flow. Eigenstates describe stationary probability distributions. They cannot move. A frequency domain experiment measures the molecular eigenstate spectrum, a distribution of energies and intensities, which arises from the coupling of an initial bright state, $|\Phi_B\rangle$, to a series of dark levels, $\sum_i |\Phi_D\rangle_i$, through high-order (cubic and quartic) potential energy coupling, V_{BD}, see Figure 1.2. Any eigenstate of a system may be expanded by using a linear superposition of an orthonormal set of basis states,

$$|\Psi_j\rangle = \sum_i c_i |\Phi\rangle_i . \qquad (1.1)$$

For our work we expand the vibrational eigenstates using a zero-order basis of harmonic normal mode vibrational "states", $\sum_i |\Phi_D\rangle_i$ (dark) and $|\Phi_B\rangle$ (bright).

$$|\Psi_j\rangle = a_{jB}|\Phi_B\rangle + \sum_i c_{jD}|\Phi_D\rangle_i \qquad (1.2)$$

The observed spectral intensities are proportional to the fractional bright state character in the j^{th} eigenstate.

$$I \propto |a_{jB}|^2 \tag{1.3}$$

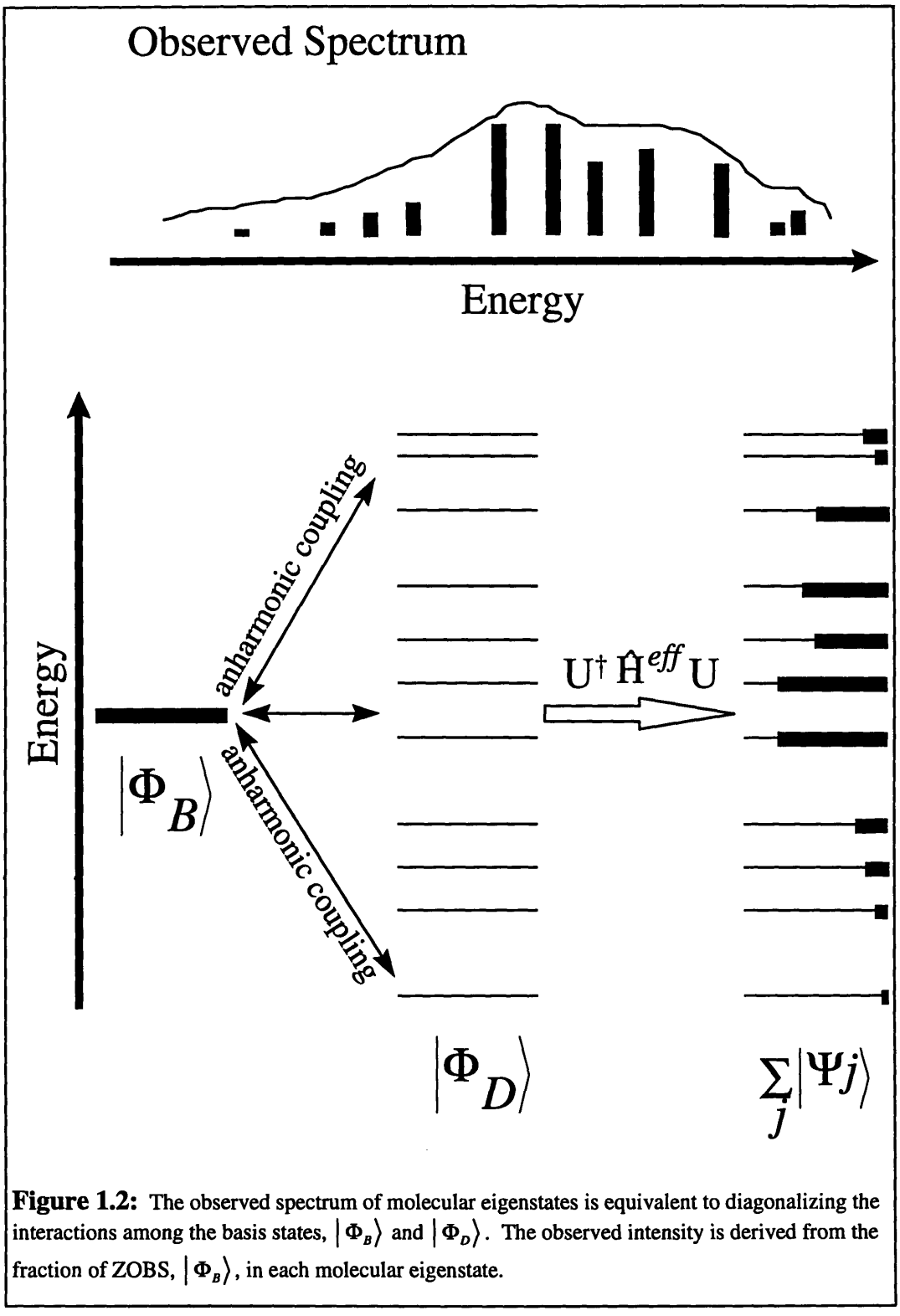

Figure 1.2: The observed spectrum of molecular eigenstates is equivalent to diagonalizing the interactions among the basis states, $|\Phi_B\rangle$ and $|\Phi_D\rangle$. The observed intensity is derived from the fraction of ZOBS, $|\Phi_B\rangle$, in each molecular eigenstate.

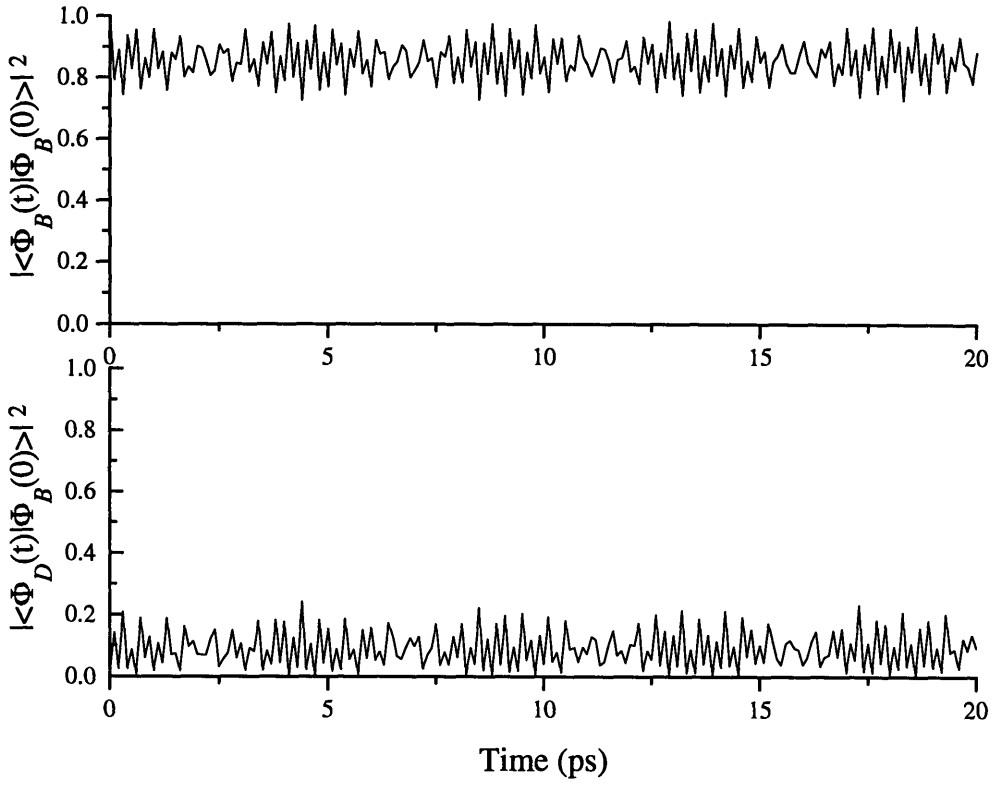

Figure 1.3: The top panel displays a schematic time dependent probability of the ZOBS, $|\Phi_B(t)\rangle$. The lower panel displays the time dependent probability of the ith zero-order dark state, $|\Phi_D(t)\rangle_i$.

We can also express the zero order bright state (ZOBS), at t=0, in terms of the molecular eigenstates.

$$|\Phi_B(0)\rangle = \sum_j c_j |\Psi_j\rangle \tag{1.4}$$

where

$$c_j = \langle\Psi_j|\Phi_B\rangle. \tag{1.5}$$

The ZOBS, which is not an eigenstate of the system, will evolve in time according to

$$|\Phi_B(t)\rangle = \sum_j c_j |\Psi_j\rangle e^{-i(E_j t/\hbar)}. \tag{1.6}$$

This state will have a time dependent probability distribution

$$P(t) = \left|\left\langle \Phi_B^*(0) \,\middle|\, \Phi_B(t) \right\rangle\right|^2 = \sum_J |c_J|^4 \left|\left\langle \Psi_J \,\middle|\, \Psi_J \right\rangle\right|^2 + \sum_{i>J} c_i^2 c_J^{*2} \left|\left\langle \Psi_i \,\middle|\, \Psi_J^* \right\rangle\right|^2 e^{-i(E_J - E_i)t/\hbar} + c.c \quad (1.7)$$

Figure 1.3 displays a schematic survival probability of an initial ZOBS and the time dependent probability of the i-th dark state. The energy splittings and intensity information extracted from the high-resolution, frequency-domain spectrum reveals the nature of the IVR ("dynamics") for an initial zero-order bright state. Realize that we are not discussing the "dynamics" of individual eigenstates, which are by definition stationary. The frequency distribution of the molecular eigenstates (and the intensity distribution of transitions terminating on them) provides us with a "picture" of the IVR dynamics for an initially localized (and perfectly known) excitation! High resolution frequency domain experiments provide information about long time because the static eigenstate picture contains information pertaining to the long time evolution dynamics, which is exquisitely sensitive to an enormous number of weak interactions of the initially localized excitation and the dark states. In contrast, a low resolution frequency domain experiment contains only the short or early time dynamics, a few strong interactions between the initially localized excitation and the dark states.

1.2 Background for the study of acetylene IVR

The study of C_2H_2 is ideal for five reasons. First, the small size--four atoms--and lack of complicated molecular structure, two carbons and two hydrogens, simplify the IVR processes. More specifically, a tetratomic species with only two heavy atoms lowers the density of states that can participate in the IVR processes at a given energy. Second, in the $\tilde{X}^1\Sigma_g^+$ state, S_0, C_2H_2 exists only as two chemical geometric isomers, acetylene and vinylidene. The C_2H_2 geometrical isomers are located on the ground state potential energy surface (S_0) see Figure 1.4. Either

isomer can react via an unimolecular isomerization, the simplest chemical reaction, to produce the other isomer. The transition state to this chemical reaction is predicted by high level quantum chemical calculations to lie near $E_{vib} \approx 16{,}000\ cm^{-1}$ above the linear acetylene zero-point level of the ground state. [13] Third, the study of small unsaturated hydrocarbons such as C_2H_2 is important for a wide range of applications, such as in combustion processes, atmospheric chemistry, astrophysics, and synthetic chemistry.

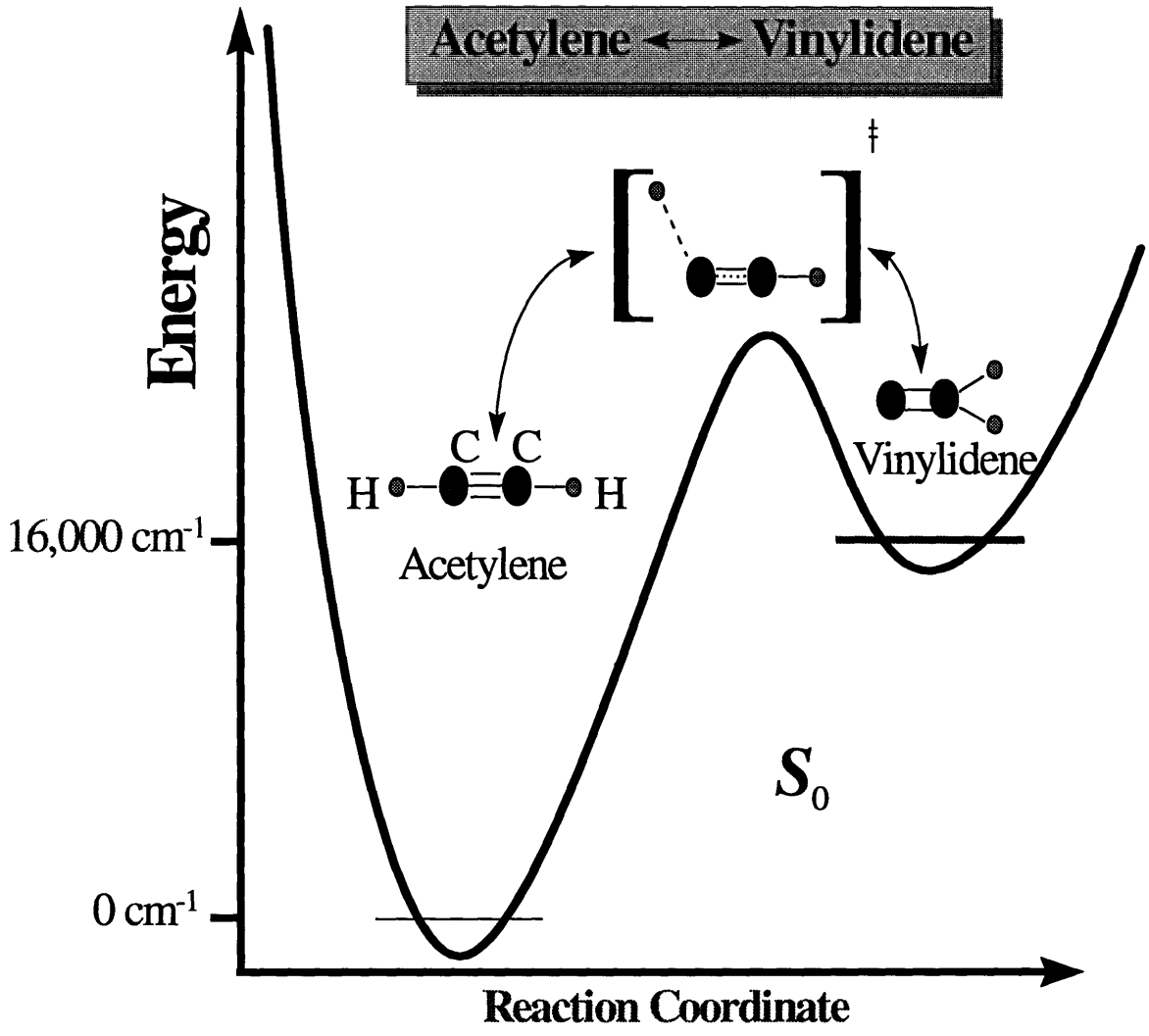

Figure 1.4: The ground electronic $\tilde{X}^1\Sigma_g^+$ state (S_0) of C_2H_2. The vinylidene (C_{2v}) isomer has a minimum which lies approximately 16,000 cm^{-1} above the acetylene ($D_{\infty h}$) zero-point level.

Fourth, vinylidene is of special interest to scientists because it is a highly reactive species, a carbene, which survives for only a few picoseconds before isomerizing to form acetylene.[14] Synthetic chemists have posited that carbenes are important as intermediates in many chemical reactions. Ultimately, we hope to learn more about the properties of vinylidene through the study of the acetylene $\leftrightarrow$ vinylidene isomerization. Fifth, acetylene, a permanent gas, is inexpensive and easy to purify and use.

My research has focused on the study of the IVR processes that are expected to be important in the acetylene isomerization to vinylidene. With this knowledge, we may be able to control the production of vinylidene such that we may learn more about its physical properties. We have started to obtain this knowledge by employing laser spectroscopic and theoretical methods. The focus of my research has been to understand the IVR structure that occurs in the acetylene S_0 spectrum at low vibrational energies. After modeling the low vibrational energy IVR we can begin to extrapolate our model to vibrational energies at and above the energy of the isomerization barrier.

Infrared absorption and Raman experiments of the $\tilde{X}^1\Sigma_g^+$ state are plentiful and have been used to determine the fundamental vibrational parameters, $\left(\sum_{i=1}^{5} \omega_i^0, \sum_{i=1}^{5} x_{ii}, \sum_{i \neq j}^{5} x_{ij} \right)$.[15-19] The study of highly vibrationally excited eigenstates by absorption methods is made difficult by increasingly weak transitions. As a rule of thumb, the successive overtone transitions for the CH stretches will have intensities which scale as [20,21]

$$I \propto 10^{-\Delta V} \qquad (1.8)$$

where

$$\Delta V \equiv \sum_{i=1}^{3N-5} |\Delta v_i|. \qquad (1.9)$$

At high internal energies, the only eigenstates with significant transition moments in an absorption experiment are the X-H stretching modes. Therefore, the intensity scaling limitations have forced many of the absorption studies to focus on the IVR of X-H stretches, where X=C, N, or O. We are interested in probing the high lying vibrational states of acetylene which will have favorable interaction with vinylidene states. Figure 1.5 displays the normal modes and fundamental frequencies for linear ($D_{\infty h}$), *trans*-bent (C_{2h}) and vinylidene (C_{2v}) C_2H_2. While, the 5th overtone of the acetylene CH stretch will occur in the 16,000 cm^{-1} energy region, a pure stretching vibrational motion does not contain the large amplitude local CC-H bending needed to facilitate an acetylene $\leftrightarrow$vinylidene interaction, see Figure 1.4. To reach $E_{vib} \approx 16{,}000$ cm^{-1} via pure overtone and combination bands of the CC-H bends, the CC-H bending frequencies, $\omega_4^0 =$ 620 cm^{-1} and $\omega_5^0 = 720\,\text{cm}^{-1}$, would necessitate the spectroscopy of the 20th bending overtone. These transitions are extremely weak.

By utilizing the first excited singlet ($\tilde{A}\,^1A_u$) state as an intermediate in a double resonance experiment, $\tilde{X}^1\Sigma_g^+$ state spectra can be recorded which contain long progressions in highly excited Franck-Condon active vibrational modes, *trans*-bending and moderately excited CC stretching. The Franck-Condon activity of these modes arises from the specific geometrical differences between the first excited singlet state ($\tilde{A}\,^1A_u$) of acetylene, which has a *trans*-bent geometry and nominal double bond, and the $\tilde{X}^1\Sigma_g^+$ state with linear geometry and a triple bond.[45]

The $\tilde{A}^1A_u\ (\pi^* \leftrightarrow \pi)\ \tilde{X}^1\Sigma_g^+$ transitions will have favorable Franck-Condon intensity for the *trans*-bending, $\Delta\theta_{CCH} = 60^0$, and CC stretching, $\Delta r = 0.18$ Å vibrations.

There are two basic types of double resonance experiments conducted in our laboratory for recording spectra of the highly excited bending vibrational levels in the $\tilde{X}^1\Sigma_g^+$ state. One of these, stimulated emission pumping (SEP) spectroscopy, was invented by our group and has been extensively documented.[22-25] Briefly, SEP spectroscopy excites a single rovibrational level in the first excited state, $\tilde{A}\ ^1A_u$, of acetylene with a nanosecond laser, called the **PUMP**. Molecules in the $\tilde{A}\ ^1A_u$ state *spontaneously* fluoresce to $\tilde{X}^1\Sigma_g^+$. A second nanosecond laser, called the **DUMP**, ***stimulates*** allowed $\tilde{A}\ ^1A_u \rightarrow \tilde{X}^1\Sigma_g^+$ transitions. This causes a depletion of the total *spontaneous* emission. The SEP signal is observed by detecting the difference between the total amount of spontaneous emission in the presence and absence of the **DUMP** laser. The other technique, dispersed fluorescence (DF) spectroscopy, utilizes only one laser, which is used to populate a single rovibrational level within the $\tilde{A}\ ^1A_u$ state. This serves the same purpose as the **PUMP** laser used in the SEP scheme. The total spontaneous emission from molecules in the $\tilde{A}\ ^1A_u$ state is collected and imaged into a monochromator, dispersed by a grating, and the $\tilde{A}\ ^1A_u \rightarrow \tilde{X}^1\Sigma_g^+$ spectrum is recorded as a function of emission frequency.

1.3 Previous Work

In the late 1980's, SEP experiments conducted by our research group recorded acetylene $\tilde{X}^1\Sigma_g^+$ spectra which sampled vibrational energies slightly below and above the isomerization barrier.[26,27] The complexity and incomplete understanding of the IVR

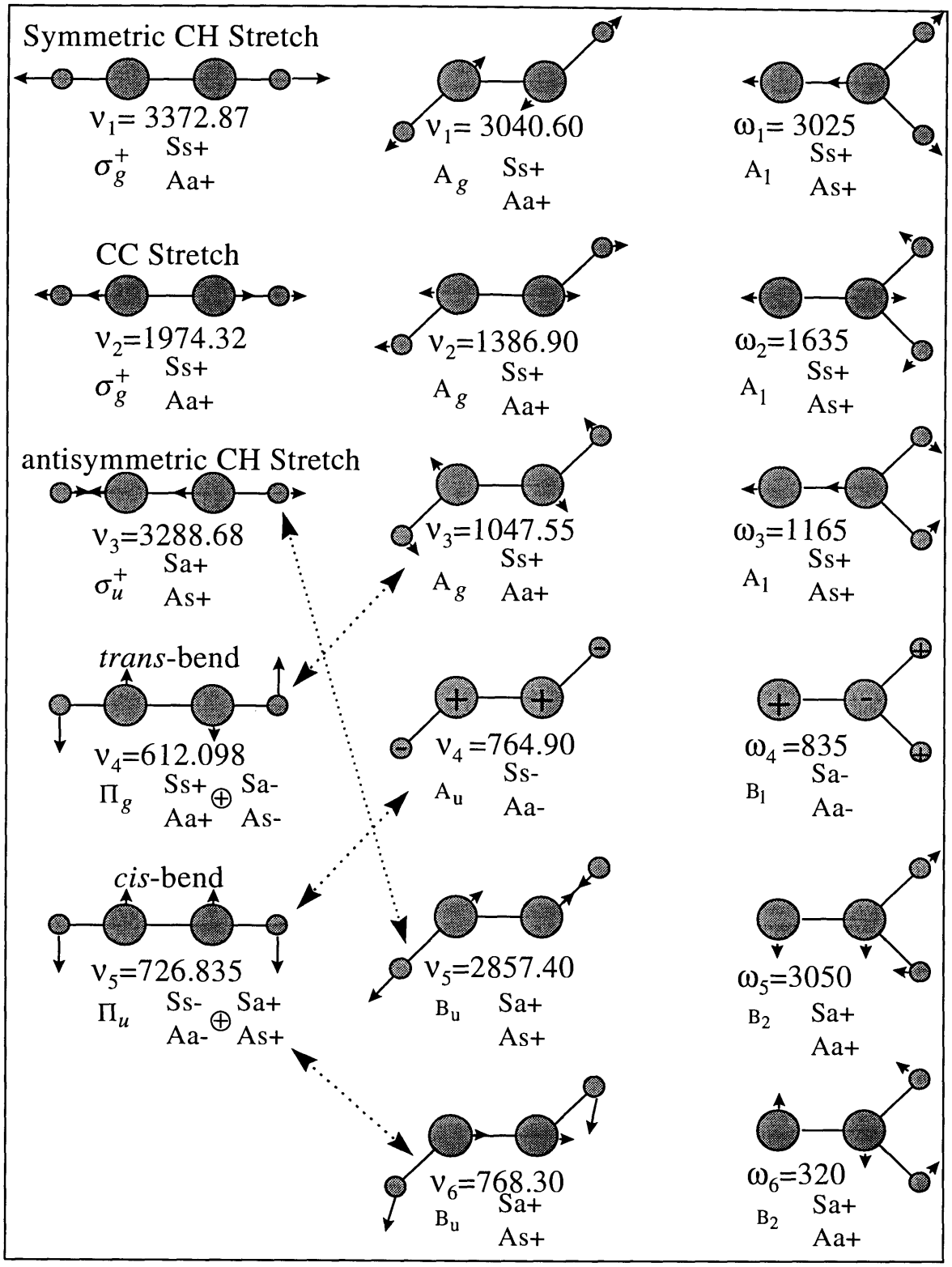

Figure 1.5: The normal modes for linear ($D_{\infty h}$), *trans*-bent (C_{2h}), and vinylidene (C_{2v}) structures of C_2H_2. Note that the frequencies are expressed in terms of $\nu_i = \omega_i^0 + x_{ii}$ for linear and *trans*-bent C_2H_2 while the vinylidene frequencies are expressed in terms of ω_i^0's. The double headed dashed arrows indicate the correlation of the different vibrational motion between linear and *trans*-bent C_2H_2.

processes made these spectra of acetylene appear to be intrinsically unassignable. Many plausible explanations for the discrepancies observed in the early SEP spectra were made, but none fully accounted for the complexity of the IVR at such high vibrational energies. Since that time, SEP experiments conducted by Jonas *et. al.* in the 7,000 cm^{-1} energy region have provided the most useful information in developing an initial picture of IVR at low vibrational energy.[7,28] Analysis of these experiments revealed that on the shortest time scales, vibrational excitation initially localized in the *trans*-bend and CC stretch, is redistributed into *cis*-bending and CH stretching vibrations. These results have prompted our group to design a series of experiments which would extend our knowledge of IVR to highly excited vibrational energies.

1.4 Current Work

Development of a new laser strategy to probe the acetylene $\leftrightarrow$vinylidene interactions relies on achieving two research objectives. First, we need to develop a *complete* understanding of the acetylene spectrum and IVR at E_{vib} below the barrier to isomerization. This approach necessitates a complementary use of both experiment and theory. We begin by recording high quality dispersed fluorescence (DF) spectra of the low energy region, E_{vib}< 16,000 cm^{-1}, of the acetylene $\tilde{X}^1\Sigma_g^+$ state. The method for recording such high quality DF spectra will be discussed at length in Chapter 3. By extracting energy positions and intensity distributions from the DF spectra, we can create an effective Hamiltonian model (H^{eff}) that models quantitatively the IVR processes that occur at low vibrational energy. Second, once we are confident about the dynamics at low E_{vib}, we can extrapolate our effective Hamiltonian model to higher energy regions and look for deviations in the recorded DF spectra from the scaled predictions of the IVR structure.

1.4.1 Effective Hamiltonian

The successful theoretical modeling of spectra at E_{vib} below the barrier to isomerization creates a strong foundation that is useful in predicting and interpreting spectra recorded at higher energies. A theoretical model, an effective Hamiltonian, currently being developed to describe the IVR of acetylene, is based upon a *normal mode harmonic oscillator* basis set.[28-30, 32,33] This choice of basis set allows us to conveniently express the resonances which are responsible for coupling vibrational energy from one normal mode into another. The theoretical model is a matrix where all of the diagonal terms contain the oscillator zero-order energies and anharmonicities.[31]

$$T_{vr}=G_v + F_r \qquad (1.10)$$

where

$$G_v=G_v(v_1, v_2, v_3, v_4^{l_4}, v_5^{l_5}; J_l) =$$

$$\sum_{i=1}^{5}\omega_t^0 v_i + \sum_{i=1}^{5}\sum_{j=i}^{5} x_{i,j}^0 v_i v_j + \sum_{t=4}^{5}\sum_{t'=t}^{5} g_{tt'}^0 l_t l_{t'} + \sum_{t=4}^{5}\sum_{t'=tt''=t'}^{5}\sum^{5} y_{tt't''} v_t v_{t'} v_{t''} + \sum_{i=1}^{5}\sum_{t=4}^{5}\sum_{t'=t}^{5} y_i^{tt'} v_i l_t l_{t'} + \ldots - B_v l^2$$

$$F_r = F_r(v_1, v_2, v_3, v_4^{\ell_4}, v_5^{\ell_5}; J_\ell) = B_v J(J+1) + \ldots$$

and

$$\mathbf{B}_v = \mathbf{B_0} - \sum_{i=1}^{5}\alpha_t^0 v_t + \sum_{t=4}^{5}\sum_{t'=t}^{5}(\gamma_{tt'} v_t v_{t'} + \gamma_\ell^{tt'} \ell_t \ell_{t'}) + \ldots$$

The off-diagonal matrix elements are expressed in terms of the potential energy, $V \equiv \left(\frac{1}{2}\sum_{i=1}^{3N-6} Q_i^2\right)$, anharmonic oscillator coupling terms, such as $kQ_iQ_jQ_kQ_l$.[34-36] All of the matrix elements are easily generated and extrapolated by simple harmonic oscillator scaling

rules. Therefore, knowledge of the low energy DF (and/or absorption) spectrum can be used to determine the basic coupling strengths, $K_{i,j,k}$ and $K_{i,j,k,l}$. The low E_{vib} coupling is extrapolated to higher E_{vib} by the harmonic oscillator scaling rule,

$$\left\langle \sum_{i=1}^{3N+5} v_i \left| \sum_{i=1}^{M} k_M \hat{Q}_M^n \right| \sum_{i=1}^{3N+5} \Delta v_i \right\rangle \alpha \sqrt{\prod_{i=1}^{M} V^n} \,. \tag{1.11}$$

The structure of this matrix is *not universal* for all chemical species, but is dictated by the unique set of states and state-specific coupling of each molecule. In the case of acetylene, the effective Hamiltonian matrix can be block diagonalized, see Figure 1.6. All of the states within a particular block interact *via* off-diagonal anharmonic couplings with each other, but **do not** interact with oscillators belonging to different blocks. Each block of oscillators is called a polyad. Each polyad is associated with a set of approximate polyad quantum numbers $[N_s, N_{res}, l]$; where N_s is the total number of quanta of stretching vibrational motion, N_{res} reflects the vibrational frequency ratios ($5\omega_1$: $3\omega_2$: $5\omega_3$: ω_4: ω_5), and l is the total vibrational angular momentum.[37,38] Depending upon which states have optical activity, the coupling scaling and selection rules from the H^{eff} model indicate that each polyad will be represented by a unique intensity and frequency pattern within the acetylene spectrum. These patterns are dependent upon the identity of the initially excited state(s) within the polyad block. In the case of acetylene, the optically bright initial states are called the zero-order bright states (ZOBS). Both the strength of the resonances and the specific set of zero-order energies and anharmonicities control each spectral pattern, which may be as simple as a three line pattern spread over 30 cm^{-1}, or as complex as a 200 line pattern spread over 550 cm^{-1}. (Some anharmonic resonances cause stronger mixing than others, and any given zero-order state is assumed to interact only with a certain subset of other zero-order states.)

The effective Hamiltonian model predicts that acetylene spectra of the $\tilde{X}^1\Sigma_g^+$ state will be composed of many partially overlapping polyad patterns. The onset of the acetylene↔vinylidene isomerization will introduce new resonances, causing interactions **between** polyads to turn on abruptly. This will likely cause the polyad patterns to be destroyed or degraded in the energy region of the acetylene ↔ vinylidene interaction. A complete picture of the complex IVR involved in the acetylene isomerization could in principle be generated by observing the onset of the polyad pattern breakdown. Developing a clearer understanding of the role that IVR plays in these processes can only occur once the breakdown has been observed. We can begin to look for polyad breakdown once we have recorded and completely understood the low E_{vib} DF spectra.

1.4.2 Dispersed Fluorescence Spectra

The $\tilde{A}\,^1A_u \rightarrow \tilde{X}^1\Sigma_g^+$ dispersed fluorescence (DF) spectrum will contain progressions of the Franck-Condon active modes, (these are the zero-order bright states, ZOBS)

$$\left(v_1,\, v_1,\, v_1,\, v_4^{l_4},\, v_5^{l_5}\right)^{l_{Total}=l_4+l_5} \equiv \quad (0,\, n,0,\, m,0)^{l_{Total}=m,m-2,m-4,\ldots,-m} \qquad (1.12)$$

where the values of m and l_{Total}, the total vibrational angular momentum, are determined by the intermediate vibrational level chosen in the $\tilde{A}\,^1A_u$ state. The $\tilde{A}\,^1A_u \leftrightarrow \tilde{X}^1\Sigma_g^+$ transition follows c-type selection rules (the transition moment lies along the symmetry c-axis) $\Delta J=0,\pm1$, $\Delta K \equiv \Delta l = \pm 1$. ($K = K_a'$ is the vibrational angular momentum of the near prolate top $\tilde{A}\,^1A_u$ state projected onto the symmetry a axis), g↔u, and parity $e \leftrightarrow f$ for $\Delta J=0$, and $f \leftrightarrow f$ or $e \leftrightarrow e$ for $\Delta J=\pm1$.[45] Because the *cis*-bending vibration is Franck-Condon inactive, the value of l_{Total} is equal to l_4.

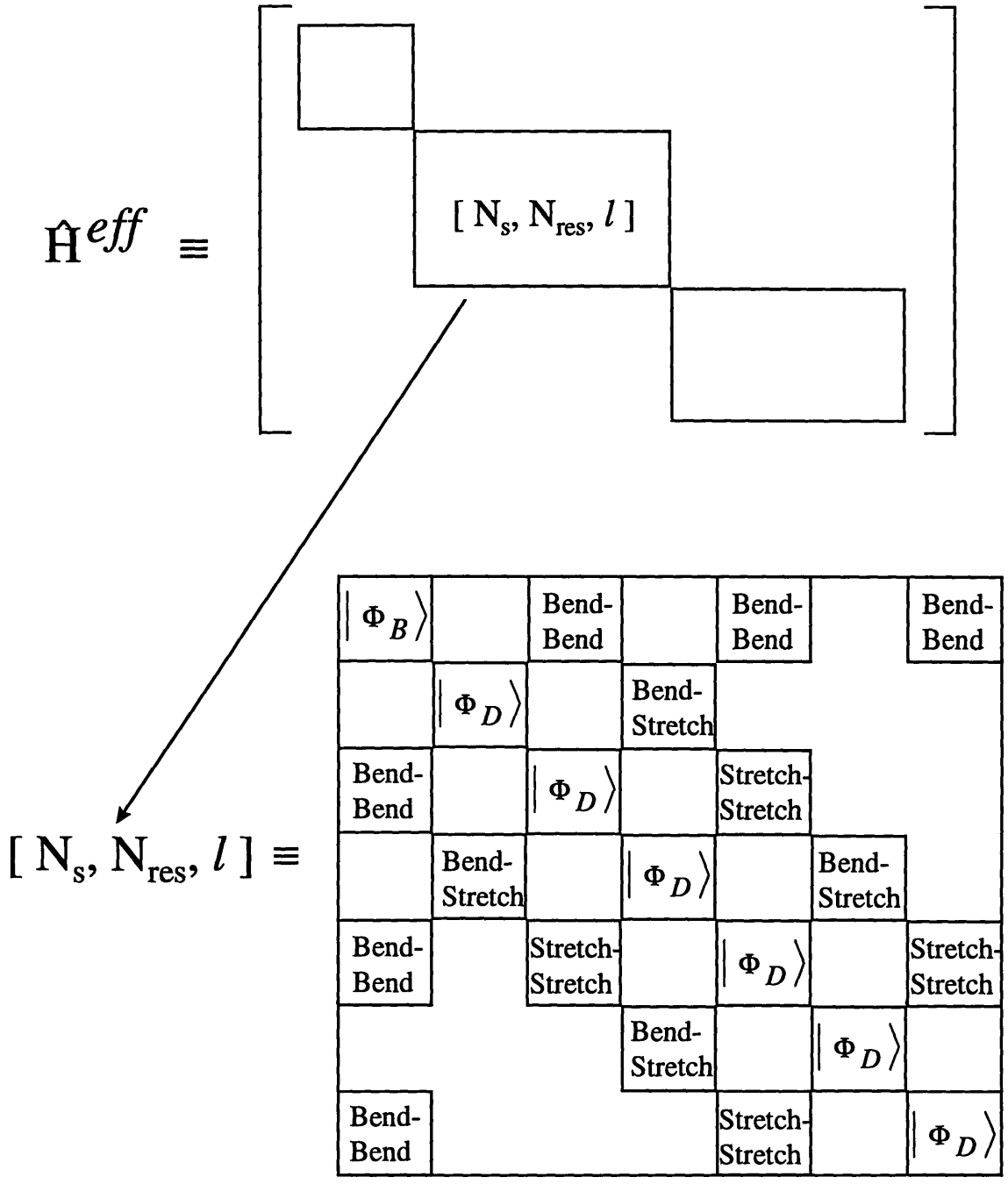

Figure 1.6: The effective Hamiltonian model is a block diagonal matrix. Each block is described by a set of unique polyad quantum numbers, $[N_s,N_{res},l]$, and contains the zero order energies of the bright and dark states on the diagonal and with anharmonic couplings off the main diagonal.

The projection of the quanta in the *trans*-bending vibration, quantized in units of $\hbar$, can only have values of l_4=v_4, v_4-2, v_4-4, ...-v_4 ($v_4 \geq |l_4|$).[39] Any intermediate state with K_a' = odd will

terminate on l_{Total}= even and vice versa. This forces the number of quanta of ν_4 to be either even $\left(K'_a = \text{odd}\right)$ or odd $\left(K'_a = \text{even}\right)$. Due to both the structure of the effective Hamiltonian and the $\tilde{A}\,^1A_u \leftrightarrow \tilde{X}^1\Sigma_g^+$ acetylene electric dipole transition selection rules, there is only one ZOBS per polyad, see Chapter 2.

In order to observe individual polyad patterns and their breakdown, high quality spectra recorded over several thousand cm^{-1}, at and below the energy of isomerization, with excellent frequency and intensity calibration, are necessary. This is accomplished by our optimized implementation of dispersed fluorescence spectroscopy, see Chapter 3. At low vibrational energies, E_{vib}< 7,000 cm^{-1}, the polyad patterns are clear and are easily extracted from the DF spectra. However, the polyad patterns at higher E_{vib} are difficult to identify for two reasons. First, there is an increasing number of ZOBSs in a given energy region. Second, some of the polyads become highly fractionated due to stronger IVR interactions.

Regardless of the spectrum quality, the overlap of adjacent polyad patterns would often appear to corrupt polyad pattern recognition. Within the regions probed by dispersed fluorescence, there are more than 100 overlapping polyad patterns. Unlike the relative intensity distribution **within** a polyad, the relative intensity distribution **between** polyad patterns is dependent upon the specific intermediate level used in the $\tilde{A}^1A_u$ state. By recording and comparing the intensity patterns from *several* dispersed fluorescence spectra which utilize different intermediate rovibronic states in S_1, the overlapping polyad patterns can in principle be extracted. In practice, however, once the spectra are recorded, it is difficult to accurately recognize complex overlapping polyad patterns by eye. The lack of a clear criterion for

recognizing patterns causes ambiguities in assigning spectral line positions and intensities, see Chapter 2. This in turn damages our ability to create a reliable understanding of IVR processes.

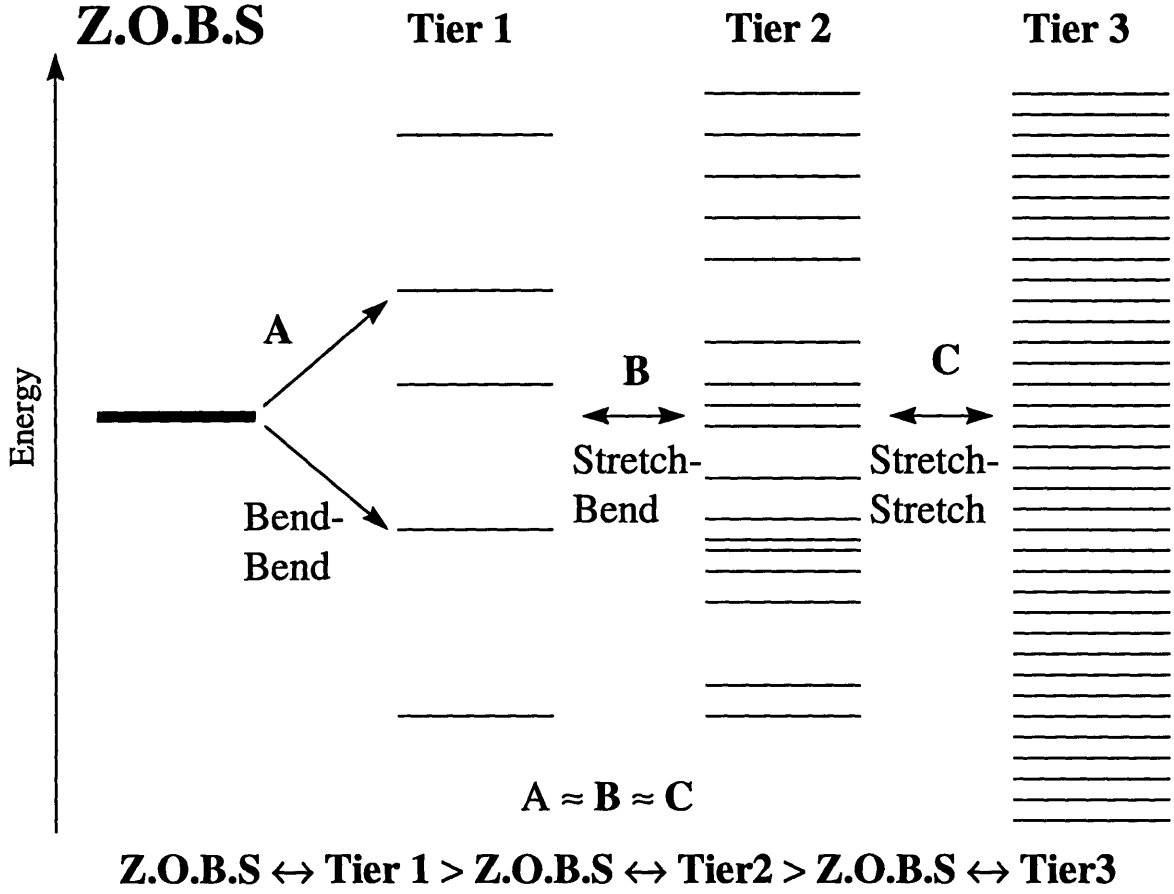

Figure 1.7: The IVR in acetylene is organized into tiers of interacting states: bend-bend, stretch-bend, and stretch-stretch. The hierarchical structure of the IVR is due to the strengths of the different anharmonic couplings, see Chapter 2 for more details.

We have successfully developed a rigorous and unbiased statistical method (Extended Cross Correlation) for recognizing spectral polyad patterns, see Chapter 4.[40,41]

Several dispersed fluorescence spectra have been recorded and calibrated. Recently, the XCC statistical method has successfully identified all polyad patterns with significant Franck-Condon factors up to 15,000 cm^{-1}, just below the isomerization barrier. This offers strong evidence that our simple model of coupled harmonic oscillators is valid in predicting the IVR.

Next, the nature of the IVR can be characterized by examining the intensity and frequency distributions within each polyad. From this type of analysis, the importance of the resonances can be ordered in terms of the strongest to weakest interactions, see Chapter 2. In our experiments, the order from strongest to weakest is as follows: bend-bend interaction (between trans and cis bending vibrations), stretch-bend interactions, and stretch-stretch interactions, see Figure 1.7.[32,33] These are the controlling features of the IVR processes in acetylene.

1.5 Future Work

This thesis represents our nearly complete understanding of the IVR processes in acetylene at E_{vib} below the isomerization barrier. We must extrapolate our understanding of the IVR processes to energy regions near the isomerization barrier where we will begin to look for a breakdown of the polyad patterns. The greater understanding of IVR and the role it plays in the acetylene $\leftrightarrow$ vinylidene isomerization will be essential for devising an optimal laser control strategy. There are several recommendations in this thesis for future DF experiments. In the acetylene $\leftrightarrow$ vinylidene isomerization region, there may be a specific breakdown of the polyad structure for polyads with moderate CC stretch and high bending vibrational motion. Polyads with only bending or stretching motions may be less susceptible to isomerization. In any event, we are extremely close to generating a complete understanding of the early-time molecular dynamics of acetylene up to 16,000 cm^{-1}.

1.6 Notation

Figure 1.5 displays the normal mode numbering and symmetry, following the format of Herzberg.[31] Notice, that due to the reduced symmetry of the $\tilde{A}^1A_u$ state (C_{2h} point group)

compared that of the $\tilde{X}^1\Sigma_g^+$ state ($D_{\infty h}$ point group) the vibrational mode number of the *trans*-bending vibration changes from ν_4 in the ground state to ν_3 in S_1. Therefore, the $\tilde{A}^1A_u \leftarrow \tilde{X}^1\Sigma_g^+$ transitions involving the *trans*-bending mode will be denoted by $V^{\nu_3'}_{\nu_4''}$. The subscript and superscript describe the initial and final number of quanta of bending, respectively. In the case of $\tilde{A}^1A_u \leftarrow \tilde{X}^1\Sigma_g^+$ transitions involving CC stretch, the vibrational mode numbering is the same in the S_0 and S_1 states and will be denoted by $2^{S_1}_{S_0}$.

We use Hougen and Watson's isomorphic Hamiltonian to express the linear acetylene rotational wavefunctions in a prolate top basis with the constraint that $K \equiv l$.[42] (K is the vibrational angular momentum in the S_1 state). The $\tilde{A}^1A_u$ state is a near prolate top (the moments of inertia have the following characteristics: $A >> B \approx C$) and $K=K_a$. l is the vibrational angular momentum in the $\tilde{X}^1\Sigma_g^+$ state, as discussed in 1.4.2. Throughout this thesis the compact vibronic notation, $V^{S_1}_{S_0}\ K_l^{K_a}$, introduced by Watson, will be used to describe the $\tilde{A}^1A_u \leftarrow \tilde{X}^1\Sigma_g^+$ transitions.[43]

The rotational prolate top wavefunctions are described in a signed-*k* basis set, where *k* represents either signed-K_a or *l*. This basis is extremely useful in writing matrix elements. However, photons and the molecule have a definite parity (inversion of the space fixed axis system), the signed-*k* basis set is not an eigen-representation of the parity basis. Therefore we use the Condon and Shortley phase convention as adopted by Hougen and Watson[44]

$$\Pi_\nu |J,+k\rangle = (-1)^{J-K} |J,-k\rangle \qquad (1.13)$$

to produce a rotational parity basis, described by linear combinations of the signed-*k* basis states.

Value of k	Linear Combination	Rotational Parity
$\|k\| = 0$	$\|J, k = 0\rangle$	$(-1)^J$
$\|k\| \geq 0$	$1/\sqrt{2}\left(\|J,+k\rangle + \|J,-k\rangle\right)$	$(-1)^{J-k}$
$\|k\| \geq 0$	$1/\sqrt{2}\left(\|J,+k\rangle - \|J,-k\rangle\right)$	$(-1)^{J-k+1}$

The total parity alternates with J. Therefore we employ *e* and *f* parity labels, where *e* parity is defined as even total parity with even J and odd total parity with odd J, and the *f* parity label is defined as even total parity with odd J and odd total parity with even J. Note that the total parity is determined by the parity of the rotational, vibrational, and electronic wavefunctions. (A simplified way of describing *e* and *f* parity is $(-1)^J$ and $-(-1)^J$, respectively.)

In this thesis, the most common $\tilde{A}^1A_u \leftarrow \tilde{X}^1\Sigma_g^+$ transition will be via the Q(1) rotational transition, where a Q branch implies $\Delta J=0$ and $e \leftrightarrow f$. The (1) refers to the initial value of J in the $\tilde{X}^1\Sigma_g^+$ state. This excitation process is denoted by ${}^{\Delta K}\Delta J_K(J)$. For example, the transition $\left|1_{1,f}\right\rangle \leftarrow \left|1_{0,e}\right\rangle$, $\left|J_{K,ef}\right\rangle \leftarrow \left|J_{l,ef}\right\rangle$, is denoted as ${}^rQ_0(1)$.

1.7 References

1. G.J. Scherer, K.K. Lehmann, and W. Klemperer. *J. Chem. Phys.* **78**, 2817 (1983).

2. F.F. Crim, *Ann. Rev. Phys. Chem.* **35**, 675 (1984) *and references cited therein.*

3. T.R. Rizzo, C.C. Hayden, and F.F. Crim, *J. Chem. Phys.* **81**, 4501 (1984).

4. D.S. King, *Adv. Chem. Phys.* **50**, 105 (1982).

5. J.J. Scherer, A.L. Cooksey, R. Sheeks, J. Heath, and R.J. Saykally, *Chem. Phys. Lett.* **172**, 4 (1990).

6. S.L. Coy, R. Hernandez, and K.K. Lehmann, *Phys. Rev. A*, **40**, 10 (1989).

7. K. Yamanouchi, N. Ikeda, S. Tsuchiya, D.M. Jonas, J.K. Lundberg, G.W. Adamson, and R.W. Field, *J. Chem. Phys.* **95**, 6330 (1991).

8. Y. Chen, D.M. Jonas, C.E. Hamilton, P.G. Green, J.L. Kinsey, and R.W. Field, *Ber. Bunsenges. Phys. Chem.* **92**, 329 (1988).

9. Crim, F.F. *J. Phys. Chem.* **100**, 12725 (1996) *and references cited therein.*

10. Nesbitt, D.J.; Field, R.W. *J. Phys. Chem.* **100**, 12735 (1996) *and references cited therein.*

11. E.J. Heller, *J. Chem. Phys.* **68**, 3891 (1978).

12. K. Kulander and E.J. Heller, *J. Chem. Phys.* **69**, 2439 (1978).

13. M.M. Gallo, T.P. Hamilton, H.F. Schaefer III., *J. Am. Chem. Soc.* **112**, 3714 (1990) *and references cited therein.*

14. K.M. Ervin, J. Ho, and W.C. Lineberger, *J. Chem. Phys.* **91**, 5974 (1989).

15. B.C. Smith and J.S. Winn, *J. Chem. Phys.* **89**, 4638 (1988).

16. B.C. Smith and J.S. Winn, *ibid.* **94**, 4120 (1991).

17. J. Pliva, *J. Mol. Spectrosc.* **44**, 165 (1972).

18. W.J. Lafferty and A.S. Pine, *ibid.* **141**, 223 (1990).

19. H. Finsterholzl, H.W. Schrotter, and G. Strey, *J. Raman Spectrosc.* **11**, 375 (1981).

20. R.G. Bray and M.J. Berry, *J. Chem. Phys.* **71**, 4909 (1979).

21. K.K. Lehmann and A.M. Smith, *J. Chem. Phys.* **93**, 6140 (1990).

22. C. Hamilton, J.L. Kinsey, and R.W. Field, *Ann. Rev. Phys. Chem.* **37**, 493 (1986).

23. C. Kittrell, E. Abramson, J.L. Kinsey, S.A. McDonald, D.E. Reisner, and R.W. Field, *J. Chem. Phys.* **75**, 2056 (1981).

24. D.E. Reisner, R.W. Field, J.L. Kinsey, and H.L. Dai, *J. Chem. Phys.* **80**, 5968 (1984).

25. C. Kittrell, *Stimulated Emission Pumping by Fluorescence Dip: Experimental Methods*, Molecular Dynamics and Spectroscopy by Stimulated Emission Pumping, World Scientific, New Jersey (1995).

26. E. Abramson, R.W. Field, D. Imre, K.K. Innes, and J.L. Kinsey, *J. Chem. Phys.* **83**, 453 (1985).

27. Y. Chen, D.M. Jonas, J.L. Kinsey, R.W. Field, *J. Chem. Phys.* **91**, 3976 (1989).

28. Jonas, D.M.; Solina, S.A.B.; Rajaram, B.; Silbey, R.J.; Field, R.W.; Yamanouchi, K; Tsuchiya, S.J. *J. Chem. Phys.* **1993,** *99*, 7350.

29. M.A. Abbouti-Temsamani and M. Herman, *J. Chem. Phys.* **102**, 6371 (1995).

30. M.A. Abbouti-Temsamani, M. Herman, S.A.B. Solina, J.P. O'Brien, R.W. Field, *J. Chem. Phys.* **105**, 11357 (1996).

31. G. Herzberg, *Molecular Spectra and Molecular Structure, Vol. II Infrared and Raman Spectroscopy of Polyatomic Molecules*, Kreiger, Malabar (1991).

32. Solina, S.A.B.; O'Brien, J.P.; Field, R.W. *J. Phys. Chem.* **100**, 7797 (1996).

33. Solina, S.A.B.; O'Brien, J.P.; Field, R.W. *Ber. Bunsen-Ges. Phys. Chem.* **99**, 555 (1995).

34. W. H. Shaffer and A.H. Nielson, *J. Chem. Phys.*, **9**, 847 (1941).

35. G. Strey and I.M. Mills, *J. Mol. Spectrosc.*, **59**, 103 (1976).

36. E.B. Wilson, J.C. Decius and P.C. Cross, *Molecular Vibrations*, McGraw-Hill, New York (1955).

37. M.E. Kellman, *J. Chem. Phys.* **93**, 6630 (1990).

38. M.E. Kellman and G. Chen, *ibid.* **95**, 8671 (1991).

39. C.H. Townes and A.L. Schallow, *Microwave Spectroscopy*, Dover Publications, Inc., New York, NY (1975).

40. M. Jacobson, S.L. Coy and R.W. Field, *J. Chem. Phys.*, *accepted.*

41. S.L. Coy, M. Jacobson and R.W. Field, *J. Chem. Phys.*, *submitted.*

42. P.R. Bunker, *Molecular Symmetry and Spectroscopy*, pp. 330-332, Academic Press, New York (1979).

43. J.K.G. Watson, M. Herman, J.C. van Craen, and R. Colin, *J. Mol. Spectrosc.* **95**, 101 (1982).

44. J.T. Hougan, J.K.G. Watson. *Can. J. Phys.* **43**, 298 (February 1965).

45. C.K. Ingold, and G.W. King, J. Chem. Soc. **00**, 2702 (1953).

Chapter 2: Preliminary Dispersed Fluorescence Spectra

This chapter represents a three year collaboration with Stephani Solina. At the end of this chapter, results from a recent collaboration with Professor M. Herman are presented. Parts of this chapter have been published in the *Ber. Bunsenges. Phys. Chem.*, the *Journal of Physical Chemistry* and the *Journal of Chemical Physics.*[16,38,39]

2.1 Introduction

Describing a system in a zero-order basis (uncoupled harmonic oscillator product states) that accurately depicts the initial state prepared by the laser enables elucidation of the dominant intramolecular vibrational redistribution (IVR) pathways. These pathways are equivalent to the anharmonic resonances described by matrix elements evaluated in the anharmonic oscillator product zero-order basis. Although high-resolution, frequency-domain spectroscopy is often naively considered to determine only "static" information, such as equilibrium molecular structure, spectroscopy can also generate a complete, compact, and intuitive description of complex dynamical processes, such as IVR, by the elucidation of the subset of resonances most important to the dynamics. This compact, intuitive description is an effective Hamiltonian model.

This chapter will focus on the preliminary analysis of the states at E_{vib}< 10,000 cm^{-1} in a new high resolution $\tilde{A} \leftrightarrow \tilde{X}$ $V_0^0K_0^1$ dispersed fluorescence (DF) spectrum of acetylene, Figure 2.1. The improved frequency resolution, when compared to previous DF spectra, and meaningful relative intensities, compared to those in stimulated emission pumping (SEP) spectra, allow this new $V_0^0K_0^1$ DF spectrum to be of great use in the initial stages of developing an effective Hamiltonian model and in elucidating the initial energy-flow pathways responsible for IVR.

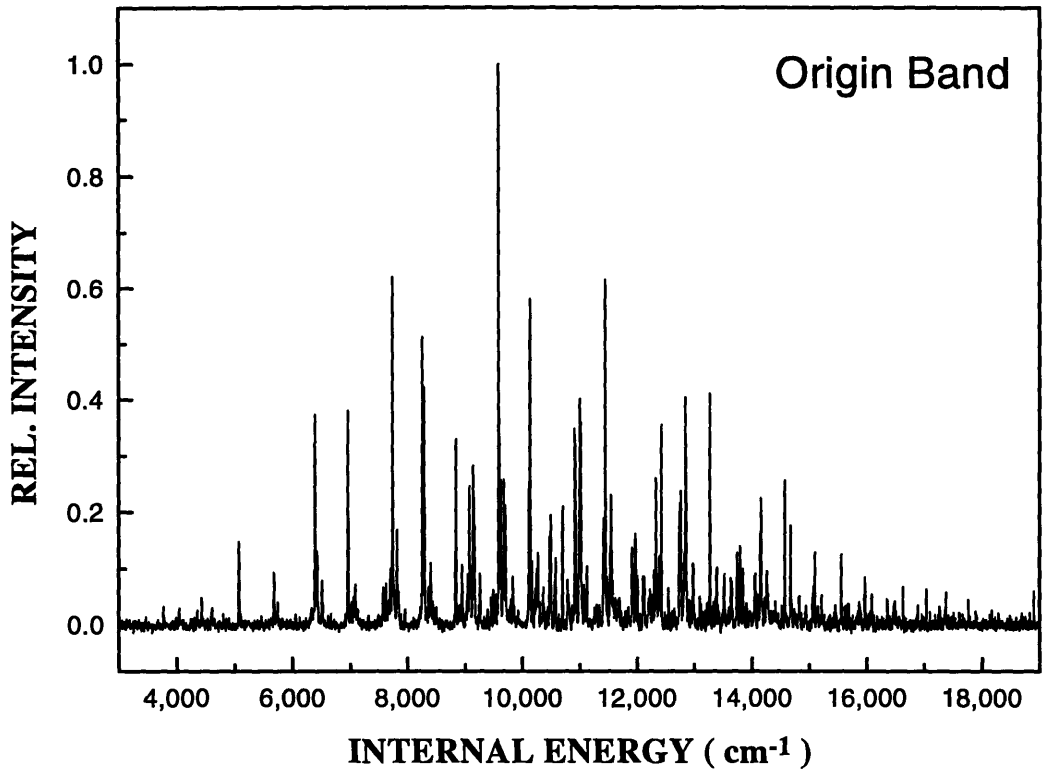

Figure 2.1: High-resolution $\tilde{A}^1A_u \rightarrow \tilde{X}^1\Sigma_g^+$ dispersed fluorescence (DF) spectrum, of the ground state, $\tilde{X}$ state, of acetylene-h_2 recorded from the zero-point level (Origin band) of the $\tilde{A}$ state.

2.2 Experimental Setup

The high resolution DF spectra that sample the electronic ground state of acetylene-h_2, $\tilde{X}\,^1\Sigma_g^+$, were recorded originating from the zero-point level, $V_0^0K_0^1$, of the first excited singlet electronic state, $\tilde{A}\,^1A_u$. The third harmonic of a Lumonics HY~1200 Nd:YAG laser pumped a Lumonics HyperDYE-300 dye laser. The Coumarin 480 output of the dye laser was doubled in a β-BBO crystal to produce ~3mJ of tunable 240 nm radiation which was used to populate the $V_0^0K_0^1\ J'_{Ka,Kc} = 1'_{Ka,Kc}$ rovibronic level.[1] Matheson Gas Products purified acetylene (99.6% min.),

used without further purification at a backing pressure of 1.5 atm, was expanded into vacuum through a 0.8mm diameter General Valve Series 9 pulsed nozzle at 90^0 to the excitation laser beam, producing an effective pressure of acetylene in the beam of 350mTorr. The relative rotational line intensities obtained from a fluorescence excitation (FE) scan were consistent with a rotational temperature of 30K.

The fluorescence was collected in a direction perpendicular to both the laser excitation beam and the jet and focused into a ¾ meter monochromator (Spex 1700). The monochromator was operated in first and second orders, utilizing a 1200gr/mm grating blazed at 500nm, and the dispersed fluorescence was imaged onto a Princeton Instruments intensified CCD (ICCD) Model 576LDG/RB. Roughly, 6000 laser shots were averaged for each segment. The advantages of using an ICCD are twofold. First, 576 spectral elements are recorded in parallel; *i.e.* a large segment of the spectrum is recorded simultaneously. At each monochromator setting the ICCD covers a spectral width of ~200 Å in first order. Second, and most importantly, frequency and intensity calibration can be carried out directly following each DF scan *without moving the grating*. This arrangement avoids corruption of the wavelength calibration by the stick/slip problems associated with many scanning monochromators.

A complete description of the calibration routine is forthcoming, see Chapter 3. Briefly, we used thorium, neon and mercury atomic transitions for calibration, and by comparing successive slightly overlapping scans along a series, systematic errors could be compensated for, allowing overall high accuracy and precision. The precision was found to be 1.5cm^{-1} $2\bar{\sigma}$ at 7.0 cm^{-1} resolution by comparing peak centers in spectra recorded on separate days. The accuracy was found to be 1-2 cm^{-1} at 7 cm^{-1} resolution by comparing a DF spectrum to higher resolution

stimulated emission pumping (SEP) spectra recorded previously with absolute experimental errors of $2\overline{\sigma}$ =0.020 cm^{-1}.[3]

Since the fluorescence intensity was the limiting factor in sensitivity, a series of spectra was recorded with entrance slit widths corresponding to resolutions of 10, 12 and 30 cm^{-1} at 355 nm in first order and 7 cm^{-1} for 355 nm photons in second order (grating position at 710 nm). Features with very low intensity in the higher resolution spectra were easily discernible in the spectra recorded at larger slit widths.

2.2.1 Spectral Purity of the PUMP Transition

Since the PUMP transition in this experiment was the Q(1) rotational line ($J'_{Ka,Kc} = 1'_{1,1} \leftarrow J''_{\ell,parity} = 1''_{0,e}$) of the origin band, the intermediate level cannot be affected by B-type Coriolis[4] interactions ($\Delta K_a = \pm 1$, $\Delta K_c = \pm 1$), and there are also no $\Delta K_a = \pm 2$ asymmetric top interactions for this level. Since the closest C-type Coriolis perturber would be the $\nu_3' \cong 1048$ cm^{-1} level with a matrix element on the order of $C_v\sqrt{J(J+1)} \cong 1$ cm^{-1}, an estimate of the maximum contribution of $K'_a = 0$ character would be $\cong 0.0001\%$. The contribution of $K'_a = 0$ character in the intermediate level, which arises from the axis-switching mechanism at J'=1, is on the order of 0.001%.[5] Therefore, with its exceedingly pure $K'_a = 1$ character, the only allowed rovibronic transitions from the selected single rovibronic intermediate level terminate on $\tilde{X}$-state rotational levels with $J_{l,parity} = 1_{0,e}$ or $2_{2,f}$.

Since we use a normal mode product basis set, the $\tilde{X}$-state Coriolis coupling is minimized. In a worst case, the proportion of admixed l=1 fractional character would be roughly $\sim \nu_{Stretch}\nu_{Bend} \times 10^{-5}$.[6] The DF spectrum of acetylene has a smaller sensitivity range (100:1) than the SEP spectrum of acetylene (1000:1).[7] Indeed, the fluorescence intensity from the particular

intermediate state we have selected here was at least three orders of magnitude weaker than that from the more Franck-Condon allowed $2\nu_3$ or $3\nu_3$ intermediate levels excited under comparable conditions. Therefore, we do not anticipate significant contributions in the $V_0^0K_0^1$ DF spectrum from levels with l=1.

Furthermore, the only rotational structure in our DF spectra will be collapsed into a single feature even at higher resolution. This can be seen from the modified Dunham expression,[3]

$$T_{vr}=G_v + F_r \qquad (2.1)$$

where

$$G_v=G_v(\nu_1, \nu_2, \nu_3, \nu_4^{l4}, \nu_5^{l5}; J_{l,\text{parity}}) =$$

$$\sum_{i=1}^{5}\omega_t^0\nu_i + \sum_{i=1}^{5}\sum_{j=i}^{5}x_{i,j}^0\nu_i\nu_j + \sum_{t=4t'=t}^{5}\sum^{5}g_{tt'}^0 l_t l_{t'} + \sum_{t=4t'=tt''=t'}^{5}\sum^{5}\sum^{5}y_{tt't''}\nu_t\nu_{t'}\nu_{t''} + \sum_{i=1}^{5}\sum_{t=4t'=t}^{5}\sum^{5}y_i^{tt'}\nu_i l_t l_{t'} + \ldots - B_v l^2$$

$$\mathbf{F_r} = \mathbf{F_r}(\nu_1,\nu_2,\nu_3,\nu_4^{\ell_4},\nu_5^{\ell_5};\mathbf{J}_{\ell,\text{Parity}}) = \mathbf{B}_v\mathbf{J}(\mathbf{J}+1)+\ldots$$

and

$$\mathbf{B}_v = \mathbf{B_0} - \sum_{i=1}^{5}\alpha_t^0\nu_t + \sum_{t=4t'=t}^{5}\sum^{5}(\gamma_{tt'}\nu_t\nu_{t'} + \gamma_\ell^{tt'}\ell_t\ell_{t'})+\ldots$$

For the $1_{0,e}$ and $2_{2,f}$ pairs of rotational levels with the same $\mathbf{V} = (\nu_1,\nu_2,\nu_3,\nu_4,\nu_5)$ and l_4=0 or l_5=0, $T_{vr}(V;1_{0,e}) \cong T_{vr}(V;2_{2,f})$ since

$$F_r(V;1_{0,e}) - F_r(V;2_{2,f}) = B_v(1)(2) - B_v(2)(3)+\ldots \approx -4B_v \qquad (2.2)$$

and

$$G_v(V;1_{0,e}) - G_v(V;2_{2,f}) = \ldots -B_v(0)^2 + B_v(2)^2 \approx 4B_v \qquad (2.3)$$

This rotational simplicity, combined with the accurate frequency calibration and meaningful relative intensity information, should make this data set of substantial interest to theoreticians. Although SEP has a much higher resolution and allows simplified rotational

assignments (since it is a double resonance technique), SEP's relative intensities are inaccurate due to saturation effects.[7] Hence, theoretical analysis requiring moderate resolution and accurate intensities benefits from the use of high resolution DF spectra.

2.3 The Effective Hamiltonian and Separation of Polyads

Our effective Hamiltonian, $\hat{H}_{eff}^{R}$, is expressed in terms of a normal mode product basis set, where the zero-order states, see Table 2.1, are coupled by harmonic oscillator matrix elements associated with the set of all resonances[10], $R_{C_2H_2}$, which have been identified in the previous IR, Raman and CH- overtone spectra, as well as the SEP study, see Table 2.2. Each resonance is characterized by a selection rule (which defines a group of strongly coupled zero-order levels) and a scalable harmonic oscillator matrix element. The resonances may be summarized as follows:

$$R_{C_2H_2}=B_{C_2H_2} \cup X_{C_2H_2} \cup S_{C_2H_2} \tag{2.4}$$

where

Bend-Bend Resonances:

$$B_{C_2H_2}=\{\text{DD Bend I, DD Bend II,vib-}l\text{-res}\} \tag{2.5}$$

Bend-Stretch Resonances:

$$X_{C_2H_2}=\{\text{“3,245”, “1,244”, “1,255”, “14,35”}\} \tag{2.6}$$

Stretch-Bend Resonances:

$$S_{C_2H_2}=\{\text{DD Stretch}\}. \tag{2.7}$$

By inspection of the set of all known[10] resonances, $R_{C_2H_2}$, listed in Table 2.2, or by simple linear algebra [3,11-13], it can be shown that out of the *seven* zero-order vibrational quantum numbers, there remains a set, $N_{C_2H_2}$, of *three* conserved quantities or polyad numbers,

$$N_{C_2H_2} \equiv [N_S , N_{Res} , l], \quad (2.8)$$

where

$$N_S = \nu_1 + \nu_2 + \nu_3 \quad (2.9)$$

$$N_{res} = 5\nu_1 + 3\nu_2 + 5\nu_3 + \nu_4 + \nu_5 \quad (2.10)$$

$$l = l_4 + l_5 \quad (2.11)$$

N_S is the total stretch quantum number, l is the total vibrational angular momentum quantum number, and N_{res} is a "resonance" quantum number arising from the frequency ratios of the normal modes, see Reference 3. The conserved polyad numbers mean that the effective Hamiltonian anharmonic oscillator product basis set for acetylene is effectively block diagonalized into groups of zero-order states, each labeled by $[N_S , N_{Res} , l]$. Each group of strongly coupled states is called a "polyad". The set of known resonances, Table 2.2, connects the zero-order states *within* each polyad but never *between* polyads. These dynamically conserved polyad numbers (conserved on the timescale, *ie* resolution, of the experiment) can be used to label the eigenstates in addition to the rigorously conserved symmetries of acetylene that correlate to J, g/u point group inversion, and +/- parity labels. The three polyad numbers plus the J, g/u, and +/- parity labels provide a unique name for each polyad as well as a recipe for automatically setting up individual polyad blocks in an effective Hamiltonian matrix.

In contrast to the linear and CC triple-bonded ground state geometry, acetylene's first excited singlet electronic state, $\tilde{A}\ ^1A_u$, has an equilibrium geometry that is *trans*-bent and has a nominal CC double bond. This results in Franck-Condon (FC) activity in very high excitation of the *trans*-bend, ν_4, and moderate excitation in the CC stretch, ν_2, for spectroscopic schemes that probe the ground state using the $\tilde{A}$-state as an intermediate such as DF and SEP.

Table 2.1: Molecular Constants (in cm^{-1}) for Acetylene-h_2

ω_1^0	3398.74[a]	x_{34}^0	-6.96[a]	y_{444}	0.0062[b]
ω_2^0	1981.71[a]	x_{35}^0	-8.69[a]	y_{445}	-0.0379[b]
ω_3^0	3316.09[a]	x_{44}^0	3.082[b]	y_{455}	0.1576[b]
ω_4^0	609.016[a]	x_{45}^0	-2.406[b]	y_{555}	0.0141[b]
ω_5^0	729.170[a]	x_{55}^0	-2.335[b]		
		g_{44}^0	0.759[b]	B_0	1.176608[c]
x_{11}^0	-26.57[a]	g_{45}^0	6.541[b]	α_1^0	0.00686[c]
x_{12}^0	-12.62[a]	g_{55}^0	3.490[b]	α_2^0	0.00621[c]
x_{13}^0	-105.09[a]			α_3^0	0.00560[c]
x_{14}^0	-15.58[a]	y_4^{44}	0.0083[b]	α_4^0	-0.00129[c]
x_{15}^0	-10.85[a]	y_4^{45}	0.0114[b]	α_5^0	-0.00215[c]
x_{22}^0	-7.39[a]	y_4^{55}	-0.0632[b]	γ_{44}	0.0000010[b]
x_{23}^0	-6.10[a]	y_5^{44}	0.0639[b]	γ_{45}	-0.0000236[b]
x_{24}^0	-12.48[a]	y_5^{45}	0.0518[b]	γ_{55}	0.0000167[b]
x_{25}^0	-1.57[a]	y_5^{55}	-0.0070[b]	γ_l^{44}	-0.0000710[b]
x_{33}^0	-27.41[a]			γ_l^{45}	-0.0002255[b]
				γ_l^{55}	-0.0001125[b]

a See Ref (3) b See Ref(18) c See Ref(34)

Note: the effective Hamiltonian constants listed here somewhat out dated, see Chapter 5.

These two particular FC-active modes, ν_2 and ν_4, in combination with the particular set of active resonances, $R_{C_2H_2}$, lead to a fortuitous coincidence such that there will be *only one FC bright state per polyad.* This can be explained as follows. To a good approximation, the symmetric CH stretch (ν_1), the anti-symmetric-CH stretch (ν_3) and the *cis*-bend(ν_5) are FC-inactive, whereas the CC stretch(ν_2) and the *trans*-bend(ν_4) are FC-active. This defines a set of zero-order bright states, or "chromostates", for SEP or DF spectra as the set of (ν_1,V_2 , ν_3, V_4, ν_5)'s where ν_1, ν_3, and ν_5 are held constant and V_2 and V_4 are variable.[14] By inspection of the definitions of [N_S , N_{Res} , l], it is impossible to find more than one (V_2,V_4) pair with the same

Table 2: For the Standard Coupled Normal Mode Hamiltonian, the Complete Set of Scalable Resonances, $R_{C_2H_2}$.

$R_{C_2H_2}$: anharmonic resonances[a] in $\hat{H}^R_{eff}$	H_{ij} = $\langle v_i^{l_i}\lvert\hat{H}^R_{eff}\rvert(v_i+\Delta v_i)^{(l_i+\Delta l_i)}\rangle$	Scaling Matrix Element, H_{ij} In the signed-l-basis
	$B_{C_2H_2}$: Bend-Only Interactions	
DD Bend Resonance I	$\Delta v_5 = -\Delta v_4 = 2$	$\left(\frac{1}{4}\right) S_{45}\sqrt{(v_4 - l_4)^2(v_5 - l_5 + 2)^2}$
DD Bend Resonance II	$\Delta v_5 = -\Delta v_4 = 2$ $\Delta l_4 = -\Delta l_5 = 2$	$\left(\frac{1}{16}\right) d_{45}^{eff}\sqrt{(v_4 \pm l_4 - 2)(v_4 \pm l_4)(v_5 \pm l_5 + 2)(v_5 \pm l_5 + 4)}$
vibrational-l-resonance	$\Delta v_5 = -\Delta v_4 = 2$ $\Delta l_4 = -\Delta l_5 = \mp 2$	$\left(\frac{1}{4}\right) r_{45}^{eff}\sqrt{(v_4 \pm l_4)(v_4 \mp l_4 + 2)(v_5 \mp l_5)(v_5 \pm l_5 + 2)}$
	$X_{C_2H_2}$: Stretch-Bend Interactions	
"3,245" Resonance	$\Delta v_3 = -\Delta v_2 = -\Delta v_4 = -\Delta v_5 = 1$ $\Delta l_4 = -\Delta l_5 = \pm 1$	$-\left(\frac{1}{8}\right) K_{3,245}\sqrt{(v_2)(v_3 + 1)(v_4 \pm l_4)(v_5 \mp l_5)}$
"1,244" Resonance	$\Delta v_1 = -\Delta v_2 = -\frac{1}{2}\Delta v_4 = 1$	$-\left(\frac{1}{4}\right) K_{1,244}\sqrt{(v_1 + 1)(v_2)(v_4^2 - l_4^2)}$
"1,255" Resonance	$\Delta v_1 = -\Delta v_2 = -\frac{1}{2}\Delta v_5 = 1$	$-\left(\frac{1}{4}\right) K_{1,255}\sqrt{(v_1 + 1)(v_2)(v_5^2 - l_5^2)}$
"14,35" Resoance	$\Delta v_1 = -\Delta v_3 = \Delta v_4 = -\Delta v_5 = 1$ $\Delta l_4 = -\Delta l_5 = \pm 1$	$-\left(\frac{1}{8}\right) K_{14,35}\sqrt{(v_1 + 1)(v_3)(v_4 \pm l_4 + 2)(v_5 \pm l_5)}$
	$S_{C_2H_2}$: Stretch-Only Interactions	
DD Stretch Resonance	$\Delta v_1 = -\Delta v_3 = 2$	$\left(\frac{1}{4}\right) K_{11,33}\sqrt{(v_1 + 1)(v_1 + 2)(v_3)(v_3 - 1)}$

Reduced Coupling Constants (in cm^{-1}) for Acetylene-h_2		
$S_{45}^0 \cong -11.0^e$	$\lvert K_{3,245}\rvert = 18.28^d$	$d_{45}^{eff} = r_{45}^{eff} + 2g_{45}^{eff}$
$r_{45}^0 = -6.238^e$	$\lvert K_{1,244}\rvert = 6.379^f$	$r_{45}^{eff} = r_{45}^0 + \sum_{t=4}^{5} r_{t45}(v_t - 1)$
$r_{445} = 0.2125^e$	$\lvert K_{1,255}\rvert = 6.379^f$	$g_{45}^{eff} = g_{45}^0 + \sum_{i=4}^{5} y_i^{45} v_i$
$r_{545} = -0.1063^e$	$\lvert K_{14,35}\rvert = 29.044^f$	
	$\lvert K_{11,33}\rvert = 105.83^d$	

(v_1, v_3, v_5) for a given $[N_S, N_{Res}, l]$. Therefore, there is only one bright state per polyad in the $V_0^0 K_0^1$ DF spectrum *as long as the polyad numbers remain good.* The polyad numbers will be

conserved as long as any previously undetected resonance only connects states within and not between polyads.

2.3.1 The $\hat{H}_{eff}^{R'}$: The Original Effective Hamiltonian

The $\hat{H}_{eff}^{R'}$ Hamiltonian is the Hamiltonian used to describe the peaks observed in the SEP experiments carried out in the 7,000 cm^{-1} region.[3] This Hamiltonian contains the resonances known in the SEP, IR, Raman, and overtone[10] acetylene-h_2 data at that time. Since then, Temsamani and Herman[17,39] have fit the 122 known experimental vibrational energy levels of acetylene-h_2 up to 12,000 cm^{-1}. These levels are predominantly characterized by high quanta in the CH stretches and only minimal quanta in the bends. The comparison of the Reference 17 Hamiltonian, $\hat{H}_{eff}^{H}$, to ours will be discussed in Section 2.6. Temsamani and Herman found it necessary to include additional stretch/bend resonances, $R''_{C_2H_2}$, to the set of resonances traditionally used for acetylene-h_2, $R'_{C_2H_2}$, to accurately describe the levels included in their global fit. The effect of these extra resonances was examined by comparing the old $\hat{H}_{eff}^{R'}$ to the new $\hat{H}_{eff}^{R} = \hat{H}_{eff}^{R'}$ +new resonances. The sets of resonances may be summarized as follows:

$$R'_{C_2H_2} = B_{C_2H_2} \cup S_{C_2H_2} \cup \{\text{“3,245”}\} \qquad (2.12)$$

$$R''_{C_2H_2} = \{\text{“1,244”}, \text{“1,255”}, \text{“14,35”}\} \qquad (2.13)$$

$$R_{C_2H_2} = R'_{C_2H_2} \cup R''_{C_2H_2} \qquad (2.14)$$

It is interesting to note that $R_{C_2H_2}$ is linearly dependent on $R'_{C_2H_2}$. In other words, $R''_{C_2H_2}$ does not destroy any polyad numbers, and the new resonances only connected states within the same

polyad as the $R'_{C_2H_2}$ Hamiltonian. Also since the pure bend polyads, N_S=0, have no states with any stretch quanta, $\hat{H}^{R}_{eff} = \hat{H}^{R'}_{eff} = \hat{H}^{B'}_{eff}$ (Bend-only resonances) for [0,N_{Res}] polyads.

2.3.2 Utilizing the Appropriate Data Set

Previous acetylene $\tilde{A} \rightarrow \tilde{X}$ DF[8] and SEP[3] experiments have led to a description of the earliest time dynamics that results when energy is initially localized in very high excitation of the *trans*-bend and moderate excitation in the CC stretch (the Franck-Condon active modes). Our new higher resolution $V_0^0 K_0^1$ DF spectrum recorded from the zero-point level of the $\tilde{A}$-state, see Figure 2.2, allows us to elaborate a more complete picture of the energy flow pathways on the acetylene $\tilde{X}$-state potential surface. The new DF spectrum has a Franck-Condon (FC) envelope, $5{,}000 \leq E_{vib} \leq 20{,}000$ cm^{-1}, that extends to lower $\tilde{X}$-state energy than the previous $2\nu'_3$ and $3\nu'_3$ DF spectra, see Figure 2.2, allowing a comparison of the DF data to an effective Hamiltonian model that was initially developed for the high resolution SEP studies in the E_{vib}=7,000 cm^{-1} region.[3]

Also, since the intermediate level used to record this new DF spectrum is the zero-point level of the $\tilde{A}$ state, there are *no nodes* in the $\tilde{A}$-state vibrational wavefunction, in contrast to the previous $2\nu'_3$ and $3\nu'_3$ DF spectra. Therefore features that were absent in the previous studies, especially at lower energy in the $\tilde{X}$-state have been recovered, see Figure 2.3, such as the [0,12] and [1,15] polyads in the $2\nu'_3$ DF spectrum (due to a node in the $\tilde{A}$-state that corresponds to 12 quanta in the *trans*-bend). The most important advantage of this new DF spectrum is that the increase in resolution is sufficient to discern fractionation[9] at lower $\tilde{X}$-state energies, see Figure 2.4, where the initial IVR should be describable by our effective Hamiltonian model.

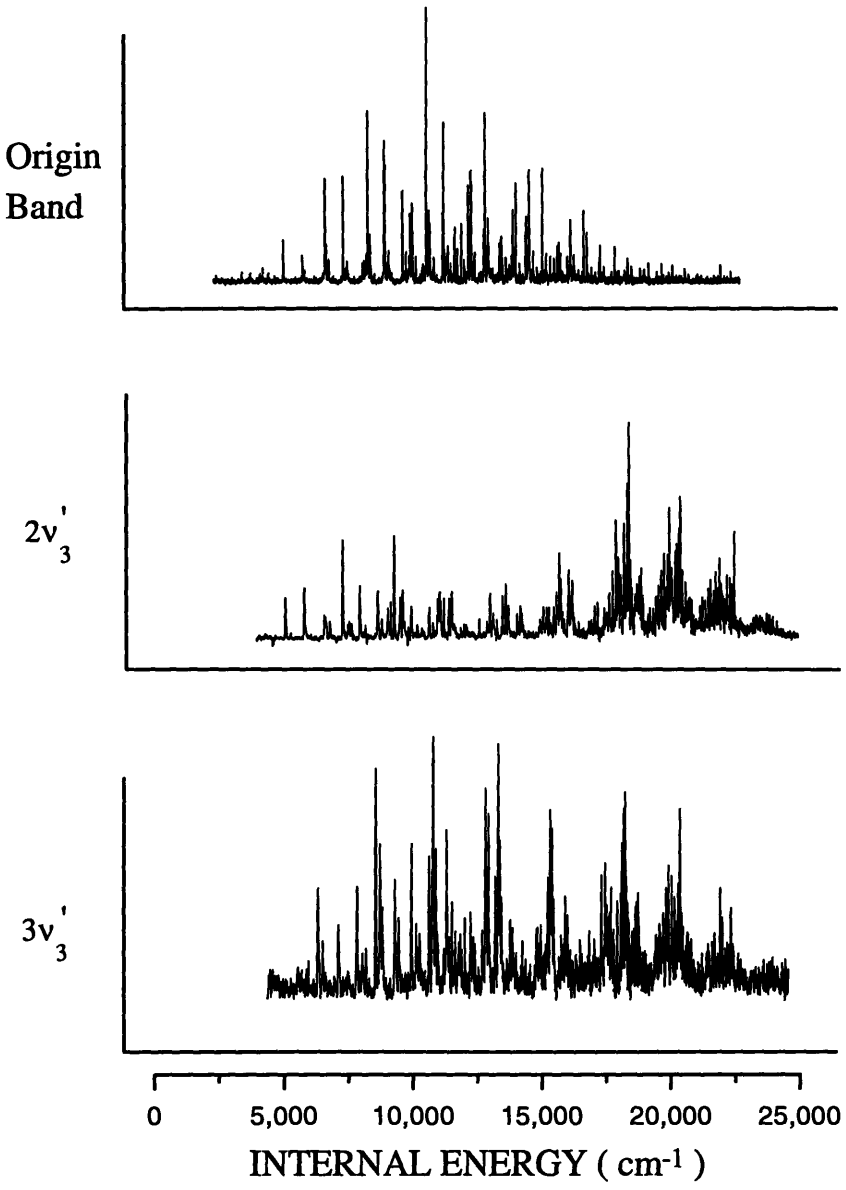

Figure 2.2: Franck-Condon (FC) envelope of the Origin, $V_0^0K_0^1$, band DF spectrum extending to lower $\tilde{X}$-state energies than the previously recorded $2\nu_3'$ and $3\nu_3'$

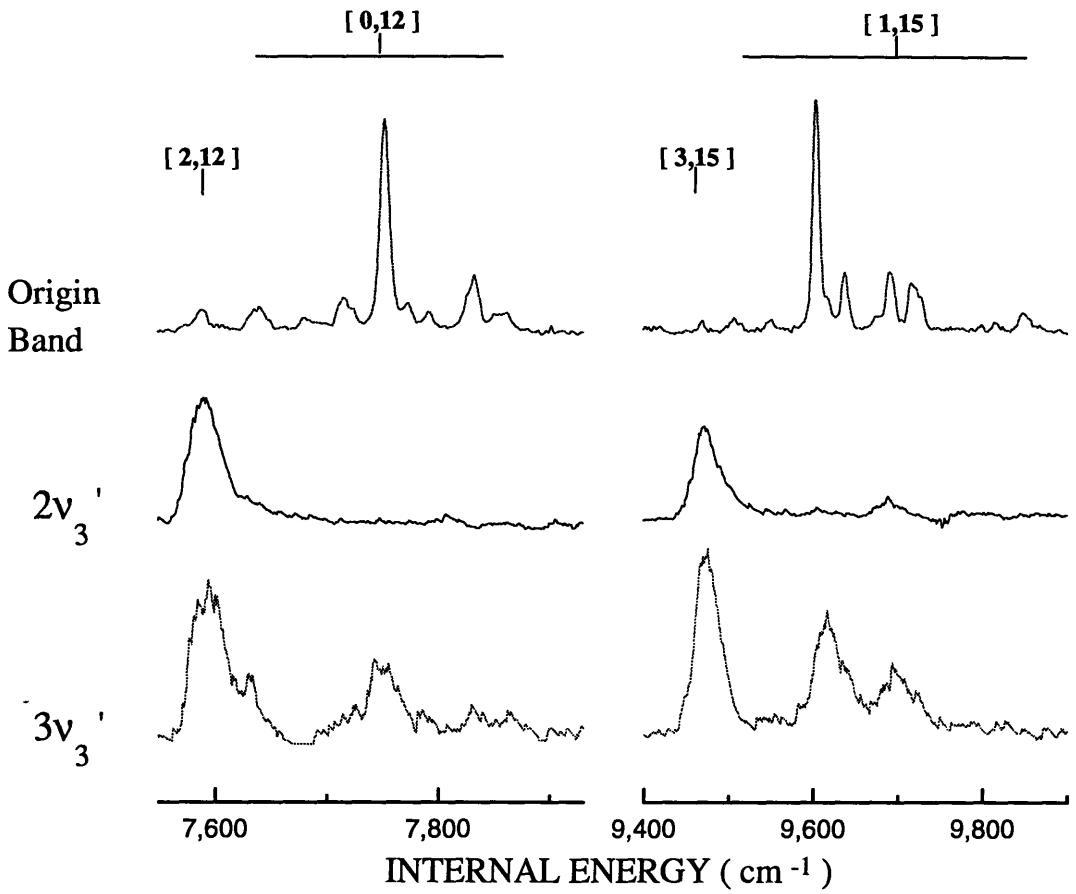

Figure 2.3: Comparison of the new origin, $V_0^0K_0^1$, band DF spectrum to the previous $2\nu_3'$ and $3\nu_3'$ DF spectra[8] showing that features such as the [0,12] and [1,15] polyads which were missing in the $2\nu_3'$ DF spectum are recovered in the origin, $V_0^0K_0^1$, band spectrum.

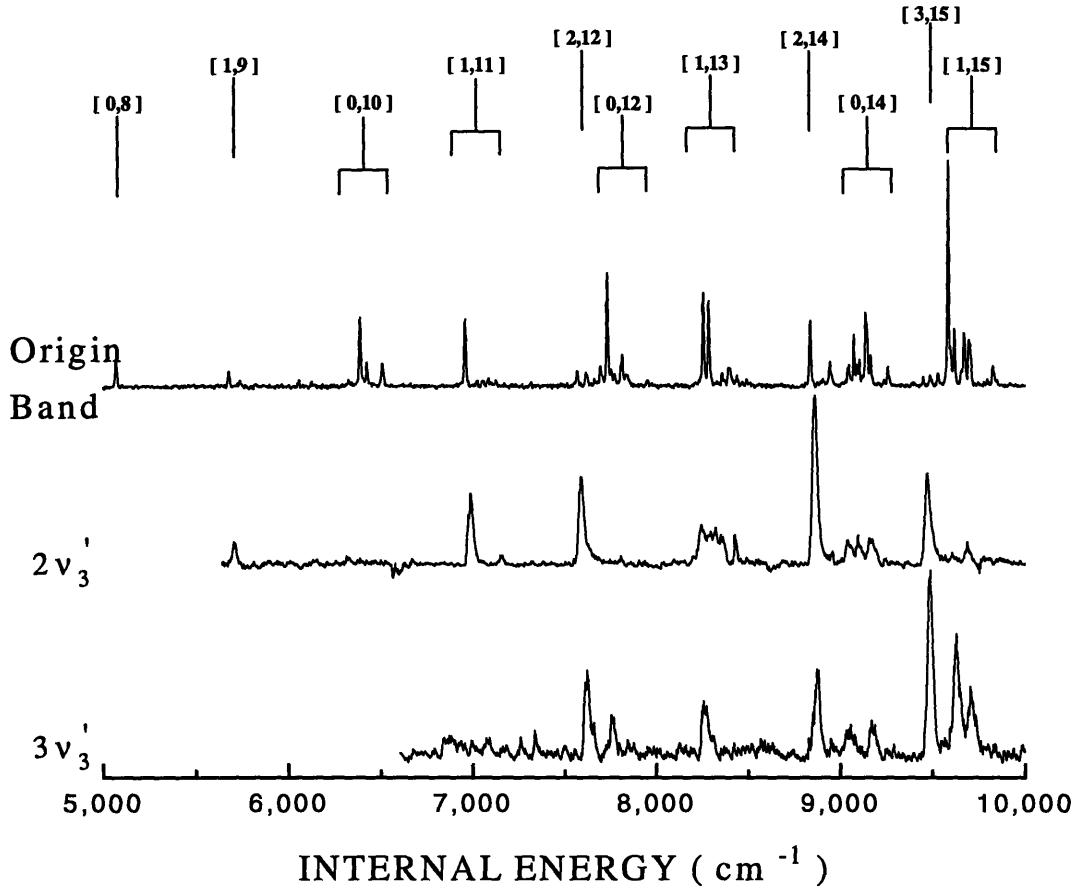

Figure 2.4: New Origin band DF spectrum recorded at sufficiently increased resolution relative to the previous $2\nu_3'$ and $3\nu_3'$ DF spectra that fractionation can be discerned at lower $\tilde{X}$ state energies.

2.4 Polyad Pattern Recognition

The pattern formed in the DF spectrum for each polyad is the distribution of the intensity of the zero-order bright state, or chromostate, among the ground state molecular eigenstates. Therefore, the intensity pattern within each polyad is solely a function of the ground state resonances, or dynamics, and the particular choice of chromostate. By comparing two or more DF spectra originating from different intermediate states that prepare the same set of chromostates, but in which the relative intensities of the different chromostates vary from one

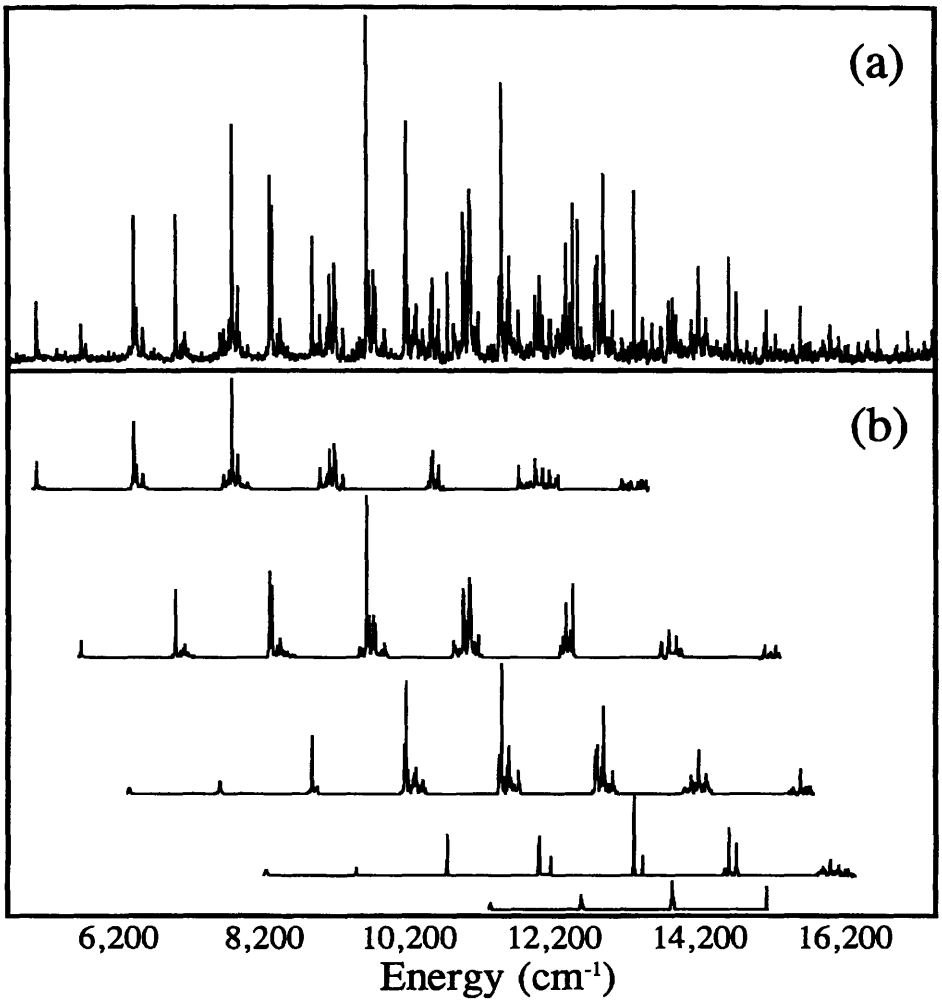

Figure 2.5: (a) Full Origin, $V_0^0K_0^1$, band DF spectrum. The complicated spectrum is composed of overlapping polyad progressions. (b) The polyad progressions from the Origin, $V_0^0K_0^1$, band DF spectrum. Once the polyad patterns have been pulled apart insight into the acetylene molecular dynamics is greatly enhanced.

intermediate state DF spectrum to another, we see that the intensity pattern *within* each polyad is the same in each spectrum but the relative intensity of each entire polyad pattern varies from one DF spectrum to the next. By taking advantage of this intrapolyad intensity invariance, the polyads may be separated from each other; *i.e.*, each DF spectrum may be pulled apart into its component polyads, see Figure 2.5.

The fact that the DF spectrum can be pulled apart into polyad patterns also serves as a verification that the polyad numbers remain good. That is, the destruction of the polyad quantum numbers will result in a breakdown our ability to pull apart polyad patterns. By comparing our $2\nu_3'$ and $V_0^0K_0^1$ DF spectra[38] and Yamanouchi's $2\nu_3'$ DF spectrum[8], these DF spectra, which prepare zero-order bright states with very high excitation in the *trans*-bend (up to ν_4=20) and moderate excitation of CC stretch (up to ν_2=4), can be used in a manual polyad pattern recognition technique. We can compare, by *eye*, the relative intensities between the DF spectra and pull apart different polyad patterns. While this manual procedure may seem archaic and sloppy, it is sufficient to recognize the gross intensity patterns for polyads up to *at least* 16,000 cm^{-1}, see Figure 2.5. It may be obvious to the reader that we do not have any means to quantify how well the polyad patterns were recognized. Questions about the validity of such a procedure may resemble the following: What about spectral features which are overlapped? Can these be pulled apart by eye? What about spectral features which have small intensities? In fact, these types of questions are the main motivation for the later chapters of this thesis where we utilize a rigorous pattern recognition technique to pull apart polyad progressions. It is important at this stage to appreciate the gross structure of the polyads and realize that at some degree of certainty the manual polyad recognition procedure is a viable means of extracting highly pronounced

polyad patterns. We conclude that to a good approximation that the three polyad numbers remain good, for initial excitation very high in *trans*-bend and moderate CC stretch, at least up to 16,000 cm^{-1}. Stronger evidence for this will be presented in Chapters 4 and 5.

This is interesting because one would expect to lose some conserved vibrational quantities when acetylene isomerizes to vinylidene. A normal mode basis set meant to describe a linear tetratomic molecule should be ill-suited to describing the energy levels of vinylidene or the transition state. Locating the E_{vib} (and its dependence on the nature of the intermediate state) at which one loses the ability to pull apart the DF spectrum could provide a way of characterizing the adiabatic barrier to vinylidene. One could compare the current series of DF spectra to a series with one added quantum in the antisymmetric CH stretch or symmetric CH stretch and thereby systematically map regions of the potential energy surface.

2.5 Analysis of States Below 10,000 cm^{-1}

All of the peaks found in the $\tilde{A} \rightarrow \tilde{X}$ $V_0^0K_0^1$ DF spectrum below 16,000 cm^{-1} are summarized in Table 2.3. It should be no surprise that a traditional spectroscopic polynomial expansion cannot describe all of the features in the $V_0^0K_0^1$ DF spectrum, since the higher resolution $V_0^0K_0^1$ DF spectrum shows more fractionation, compared to the previous $2\nu_3'$ and $3\nu_3'$ DF spectra, even for $E_{vib} \leq$ 10,000 cm^{-1} levels, see Figure 2.4. For the analysis presented here, polyad quantum numbers are assigned to groups of $E_{vib} \leq$ 10,000 cm^{-1} features, see Table 2.4, and polyad spectral intensity patterns are compared to the predictions of the $\hat{H}_{eff}^{R}$ and $\hat{H}_{eff}^{R'}$ models.

Table 2.3: Observed Term Values (cm^{-1}), $2\overline{\sigma}$ = 2.0 cm^{-1}, and Intensities (au), $2\overline{\sigma}$ = 3.0% for the Origin Band DF Spectrum for levels E_{Vib} < 16,000 cm^{-1}.

Term Value (cm^{-1})	Rel. Int.	Term Value (cm^{-1})	Rel. Int.	Term Value (cm^{-1})	Rel. Int.	Term Value (cm^{-1})	Rel. Int.	Term Value (cm^{-1})	Rel. Int.
5072.1	0.115	9106.1	0.113	10786.1	0.071	12157.7	0.013	13003.7	0.020
5678.9	0.067	9119.8	0.059	10806.3	0.046	12195.0	0.050	13015.1	0.017
6331.1	0.026	9127.0	0.044	10828.2	0.017	12220.6	0.051	13051.7	0.009
6369.4	0.019	9140.0	0.314	10862.9	0.030	12238.7	0.053	13091.8	0.034
6389.9	0.309	9147.6	0.269	10881.1	0.019	12256.6	0.041	13139.3	0.028
6407.0	0.038	9154.5	0.072	10913.8	0.324	12267.6	0.029	13182.8	0.026
6427.0	0.104	9165.9	0.136	10919.8	0.293	12275.9	0.032	13218.8	0.039
6445.5	0.021	9177.0	0.038	10924.8	0.241	12290.9	0.086	13239.7	0.029
6461.3	0.013	9209.4	0.017	10935.6	0.195	12307.3	0.106	13251.5	0.040
6512.3	0.091	9240.1	0.029	10951.8	0.025	12322.8	0.119	13268.0	0.379
6961.3	0.301	9260.2	0.082	10965.4	0.012	12328.8	0.274	13303.9	0.019
7025.1	0.026	9268.6	0.044	10974.3	0.047	12343.7	0.095	13316.5	0.048
7128.7	0.023	9452.0	0.041	10985.8	0.185	12362.2	0.060	13327.7	0.031
7572.0	0.065	9492.0	0.049	11000.4	0.426	12369.5	0.034	13342.7	0.013
7621.6	0.059	9532.8	0.054	11016.9	0.374	12383.0	0.109	13366.9	0.034
7645.4	0.012	9587.3	0.962	11030.8	0.055	12395.7	0.092	13385.2	0.093
7666.7	0.030	9600.1	0.165	11048.5	0.048	12401.2	0.087	13411.6	0.050
7699.8	0.086	9620.9	0.251	11068.7	0.060	12425.0	0.321	13431.8	0.022
7735.3	0.504	9658.2	0.066	11077.0	0.057	12464.6	0.014	13464.7	0.008
7755.9	0.071	9675.5	0.233	11099.3	0.026	12484.2	0.022	13475.3	0.014
7774.4	0.055	9699.8	0.201	11119.0	0.071	12496.1	0.013	13489.7	0.021
7815.7	0.139	9707.2	0.196	11128.0	0.116	12512.0	0.018	13515.2	0.068
7840.6	0.050	9799.7	0.042	11297.3	0.032	12541.9	0.066	13537.6	0.022
7954.6	0.025	9833.4	0.089	11347.6	0.029	12548.7	0.038	13558.4	0.014
8217.6	0.029	9851.3	0.027	11411.4	0.163	12554.1	0.048	13572.6	0.023
8257.5	0.417	10113.4	0.248	11422.0	0.167	12616.6	0.020	13583.8	0.031
8287.0	0.382	10134.1	0.537	11447.7	0.626	12645.2	0.032	13595.9	0.025
8302.2	0.045	10144.1	0.116	11480.1	0.064	12653.8	0.016	13627.7	0.036
8329.4	0.018	10152.0	0.025	11525.9	0.180	12669.1	0.019	13644.6	0.063
8360.1	0.059	10168.8	0.097	11546.6	0.233	12693.8	0.008	13662.0	0.025
8373.9	0.028	10204.8	0.028	11556.4	0.124	12729.7	0.176	13692.3	0.007
8400.4	0.085	10218.2	0.021	11575.4	0.071	12741.3	0.201	13717.6	0.024
8439.5	0.044	10247.8	0.082	11679.3	0.061	12757.1	0.148	13726.6	0.032
8469.7	0.021	10273.4	0.122	11692.4	0.042	12763.5	0.238	13740.4	0.138
8498.3	0.029	10285.4	0.048	11812.4	0.022	12791.9	0.043	13751.0	0.067
8798.0	0.007	10311.9	0.020	11834.0	0.030	12800.5	0.032	13759.1	0.027
8816.0	0.016	10359.9	0.067	11873.3	0.024	12818.7	0.113	13782.3	0.036
8839.4	0.299	10438.3	0.028	11904.9	0.156	12825.0	0.126	13789.6	0.071
8856.0	0.025	10457.1	0.034	11917.4	0.076	12845.0	0.422	13795.8	0.138
8879.1	0.021	10475.4	0.126	11931.4	0.043	12853.9	0.247	13805.4	0.034
8896.7	0.029	10494.2	0.178	11962.1	0.153	12865.5	0.070	13813.9	0.029
8910.3	0.036	10505.4	0.062	11973.4	0.183	12884.2	0.014	13824.8	0.017
8936.3	0.034	10524.4	0.013	12003.2	0.081	12894.4	0.039	13843.7	0.104
8946.4	0.103	10536.8	0.014	12011.5	0.088	12903.2	0.045	13851.7	0.045
8954.9	0.054	10550.7	0.038	12034.7	0.010	12916.4	0.027	13868.9	0.008
9012.7	0.017	10564.6	0.083	12056.8	0.019	12925.6	0.058	13906.1	0.034
9047.3	0.088	10579.0	0.128	12091.7	0.020	12944.5	0.022	13916.3	0.031
9061.5	0.034	10617.2	0.009	12101.8	0.084	12961.1	0.045	13935.7	0.004
9076.0	0.221	10635.2	0.016	12111.1	0.049	12974.3	0.088	13947.8	0.020
9093.2	0.093	10699.6	0.194	12125.0	0.074	12993.5	0.029	13971.8	0.028

Table 1. (cont.): Observed Term Values (cm^{-1}), $2\overline{\sigma}$ = 2.0 cm^{-1}, and Intensities (au), $2\overline{\sigma}$ = 3.0% for the Origin Band DF Spectrum for levels E_{Vib} < 16,000 cm^{-1}.

Term Value (cm^{-1})	Rel. Int.	Term Value (cm^{-1})	Rel. Int.	Term Value (cm^{-1})	Rel. Int.	Term Value (cm^{-1})	Rel. Int.	Term Value (cm^{-1})	Rel. Int.
13995.2	0.015	14292.8	0.028	14672.5	0.180	15143.0	0.016	15480.1	0.014
14010.8	0.011	14314.1	0.010	14686.1	0.027	15151.5	0.038	15499.7	0.013
14021.6	0.019	14333.8	0.025	14693.7	0.046	15157.5	0.027	15516.9	0.005
14052.7	0.086	14370.2	0.026	14736.8	0.030	15173.3	0.015	15530.7	0.032
14058.5	0.077	14391.8	0.018	14743.4	0.030	15181.9	0.009	15546.8	0.030
14068.1	0.046	14398.8	0.022	14750.2	0.031	15193.1	0.011	15555.0	0.115
14096.4	0.024	14406.3	0.037	14768.3	0.022	15204.0	0.023	15564.8	0.038
14103.2	0.051	14422.5	0.019	14783.3	0.014	15209.5	0.032	15581.3	0.016
14120.2	0.015	14432.1	0.015	14795.5	0.017	15215.6	0.050	15597.8	0.015
14132.2	0.031	14448.7	0.009	14805.8	0.019	15223.3	0.022	15609.0	0.034
14141.0	0.046	14459.1	0.017	14821.9	0.036	15259.7	0.019	15621.4	0.033
14148.4	0.145	14466.5	0.005	14834.9	0.020	15284.5	0.013	15630.7	0.030
14159.2	0.198	14479.3	0.006	14860.0	0.018	15302.8	0.008	15647.1	0.014
14171.0	0.055	14502.8	0.012	14919.3	0.019	15309.2	0.005	15668.6	0.031
14176.8	0.033	14519.5	0.023	14940.5	0.032	15320.2	0.015	15679.3	0.013
14187.3	0.035	14529.8	0.039	14949.5	0.012	15328.2	0.010	15687.6	0.033
14213.0	0.031	14537.6	0.023	14964.8	0.006	15338.7	0.020	15692.8	0.030
14222.6	0.041	14549.9	0.003	15026.3	0.011	15347.9	0.009	15704.2	0.003
14228.7	0.032	14572.5	0.306	15047.5	0.033	15354.9	0.029	15715.4	0.012
14237.3	0.017	14586.1	0.026	15055.2	0.030	15386.3	0.009	15733.4	0.003
14244.3	0.045	14594.8	0.021	15065.4	0.065	15396.8	0.012	15745.8	0.009
14255.1	0.115	14604.9	0.020	15093.0	0.110	15429.5	0.014	15755.4	0.012
14261.2	0.100	14614.5	0.018	15107.6	0.005	15446.1	0.007		
14266.8	0.075	14641.8	0.004	15120.2	0.021	15451.5	0.043		
14280.6	0.051	14655.2	0.016	15128.4	0.015	15467.6	0.019		

2.5.1 Pure Bending Polyads (N_s=0)

As a consequence of the FC selectivity, the $V_0^0K_0^1$ DF spectrum contains (among others) polyads illuminated by **pure bending overtone states**. By inspection of $R_{C_2H_2}$ (or equivalently the definition of N_0), it is evident that a pure bend overtone state can ONLY couple to other pure bend states. A bright state with nonzero excitation in the CC stretch would be mandatory for further IVR, such as occurs via stretch-bend, $B_{C_2H_2}$, or stretch-only, $S_{C_2H_2}$, interactions. Consequently, pure bend polyads offer an *ultra-restrictive* test of the extent to which $R_{C_2H_2}$ describes the dynamics of acetylene.

2.5.2 Polyads with CC Stretch ($N_s>0$)

The intermediate states used in our DF spectra result in FC activity in very high quanta of the *trans*-bend, ν_4, and moderate quanta in the CC stretch, ν_2. Thus $(0,V_2,0,V_4,0)$ is the set of zero-order bright states, or chromostates, prepared in our DF spectrum. The polyads that contain these states have low values of N_S and high values of N_{res} because

$$N_S=\nu_1+\nu_2+\nu_3=V_2 \qquad (2.15)$$

and

$$N_{res}= 5\,\nu_1 + 3\nu_2 + 5\nu_3 + \nu_4 + \nu_5 = 3V_2+V_4. \qquad (2.16)$$

Although the $\hat{H}^R_{eff}$ qualitatively describes the spectral pattern observed in the $V_0^0K_0^1$ DF spectrum for the pure bend polyads ($N_s=0$) up to $V_4=12$, the polyads in the DF spectrum with even minimal stretch character ($N_s=1$) do not agree with predictions of the $\hat{H}^R_{eff}$ for $V_4>8$. Possible reasons for the disagreement can be understood by inspection of the structure of the $\hat{H}^R_{eff}$: the typical matrix elements, H_{ij}, and zero-order energy denominators, ΔE.

2.5.3 Internal Structure of the Polyads

As described at the beginning of this chapter, the $\hat{H}^R_{eff}$ was constructed from a normal mode basis set and includes diagonal anharmonicities and off-diagonal couplings.[23,24] The quantum number dependence of the scalable off-diagonal matrix elements and the values of the fitted constants are given in Table 2.1 and 2.2.

Intramolecular vibrational redistribution (IVR) is manifested in spectra by the degree of fractionation of the zero-order state among the molecular eigenstates. Once the polyad progressions are recognized, two trends in IVR become apparent. For the particular chromostates selected in these experiments, IVR increases with increasing excitation in the

trans-bend, ν_4, and, surprisingly, IVR decreases with increasing excitation in the CC stretch,

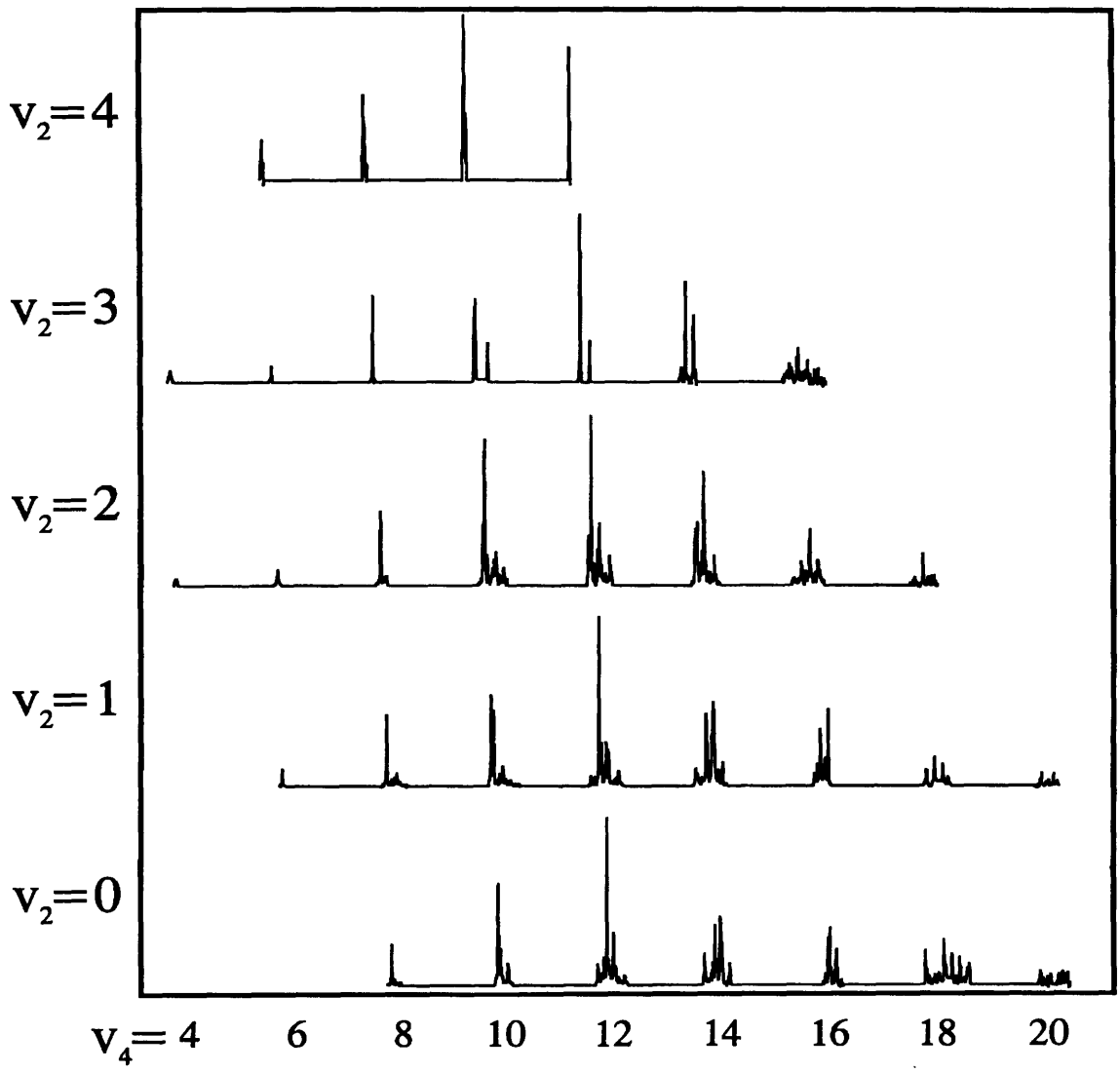

Figure 2.6: Polyad patterns from the Origin, $V_0^0K_0^1$, Band DF spectrum arranged in progressions of ν_4 such that each row has constant ν_2 and each column has constant ν_4. Note that the IVR, or fractionation, increases with increasing ν_4 and decreasing ν_2. See text for explanation.

ν_2. This can be seen by inspection of Figure 2.6 which displays the polyads arranged as progressions in ν_4, where the rows are constant ν_2 and columns constant ν_4. The extent of IVR, or fractionation, increases across a row, increasing ν_4, but the fractionation decreases up a column, increasing ν_2. For each row, constant ν_2, ν_4 increases to the right, and for each column, constant ν_4, ν_2 increases up a column; therefore, energy increases to the right and up a column. Since the number of states per polyad and the density of states per polyad both increase with increasing ν_2 and ν_4, one would expect for statistical reasons to observe an increase in IVR with increasing ν_4, consistent with the spectrum, and increasing ν_2, contrary to the spectrum. As opposed to statistical expectations, *both* IVR trends turn out to be local effects. The extent of IVR, for the initial states prepared in these experiments, is controlled by the strength of the off diagonal matrix elements, H_{ij}, and the zero-order energy differences, ΔE, of the first few initial resonance steps, or tiers, and is independent of the number or density of states of the statistical bath many tiers away.[37]

In the [*low* N_s , *high* N_{Res}] polyads, the zero-order bright state $(0,V_2,0,V_4,0)$ lies at the low energy extreme of its polyad, see Figure 2.7a, as can be seen from the location of the strongest peak in the theoretical spectrum for $\hat{H}^R_{eff}$ in Figure 2.9 for the polyads [0,8], [0,10], [1,11] and [1,13], which correspond to chromostates (0,0,0,8,0), (0,0,0,10,0), (0,1,0,8,0) and (0,1,0,10,0). As can be seen in Figure 2.7b, the nearest neighbor intrapolyad zero-order state to $(0,V_2,0,V_4,0)$ is $(0,V_2,0,V_4\text{-}2,2)$, which also happens to be a state to which the bright state can couple most strongly via a Darling-Dennison (DD) bend resonance with a typical matrix element and zero-order energy denominator, $H_{ij}/\Delta E \approx 55/75$ cm^{-1} at V_4=10. Entering the next tier of coupled levels, by again applying the DD bend resonance, the $(0,V_2,0,V_4\text{-}2,2)$ state is

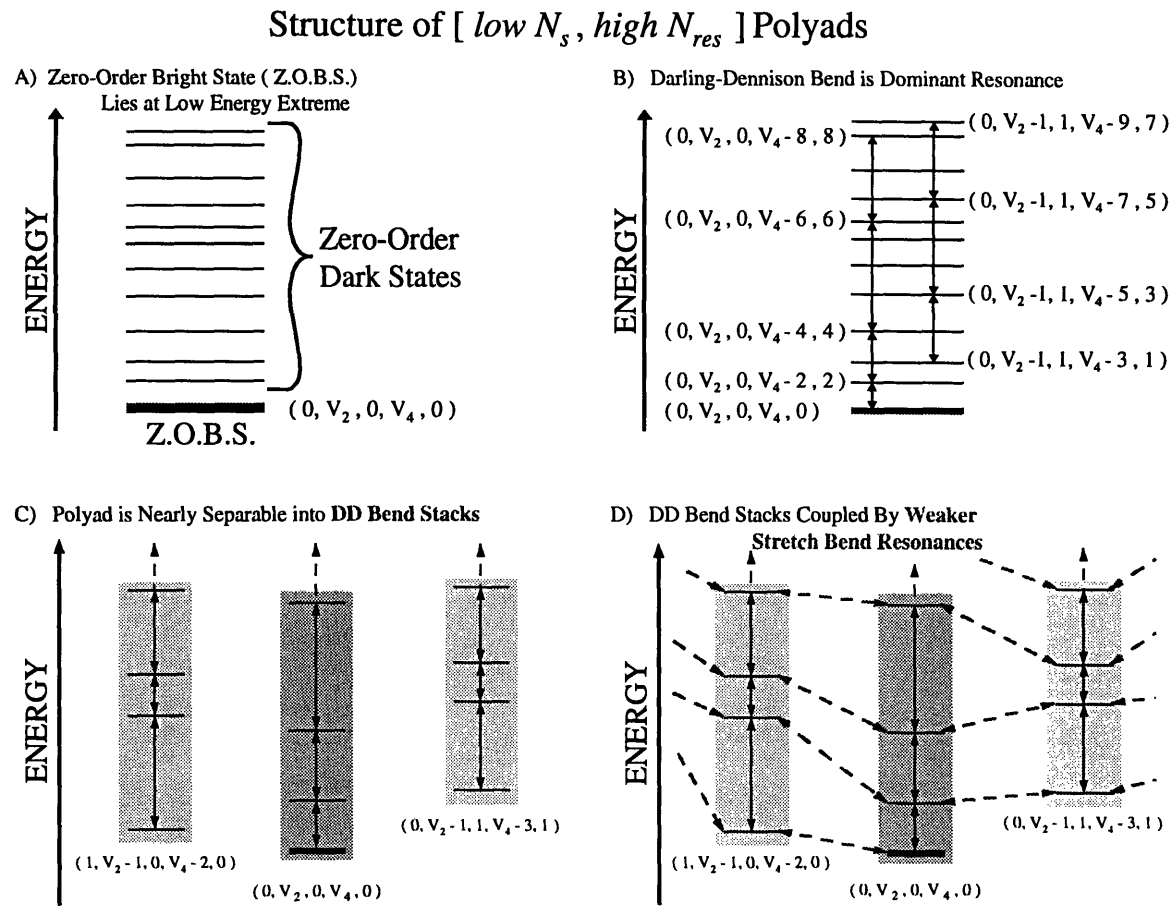

Figure 2.7: Structure of the low-energy extreme of the [*low* N_S, *high* N_{Res}] polyads. See text for details.

coupled to (0,V_2,0,V_4-4,4), with $H_{ij}/\Delta E \approx 88/80$ cm^{-1}, and so on, forming a "DD Bend stack", see Figure 2.8. In the low energy region of the [*low* N_s , *high* N_{Res}] polyads, the strongest resonances, in terms of $H_{ij}/\Delta E$, are generally the bend-only resonances, $B_{C_2H_2}$. This partitions the low energy end of the polyad into DD Bend Stacks, see Figure 2.7c, one for each unique (ν_1, ν_2, ν_3) combination.[16,38,39] These DD Bend stacks, {(0,V_2,0,V_4,0),(0,V_2,0,V_4-2,2), ...} and {(1,V_2-1,0,V_4-2,0),(1,V_2-1,0,V_4-4,2),...}, *etc.* , see Figure 2.7d, are interconnected by a web of weaker resonances, stretch-bend ($X_{C_2H_2}$) and stretch-only ($S_{C_2H_2}$), typically with $H_{ij}/\Delta E \approx 9/30$ cm^{-1}.

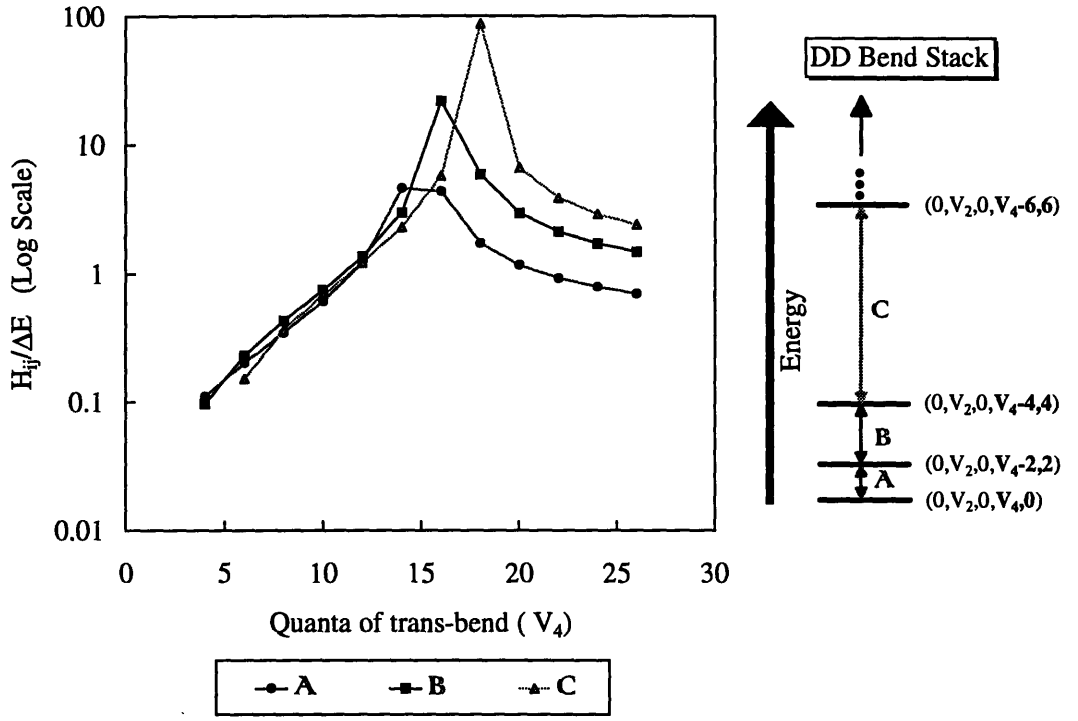

Figure 2.9: Within a DD bend stack, the coupling matrix elements, H_{ij}, increase and ΔE decreases with increasing ν_4 until the crossing of the zero-order energies, E^0, as a function of $\left(\omega_4^0, x_{44}^0\right)$ and $\left(\omega_5^0, x_{55}^0\right)$ around ν_4 = 16-18.

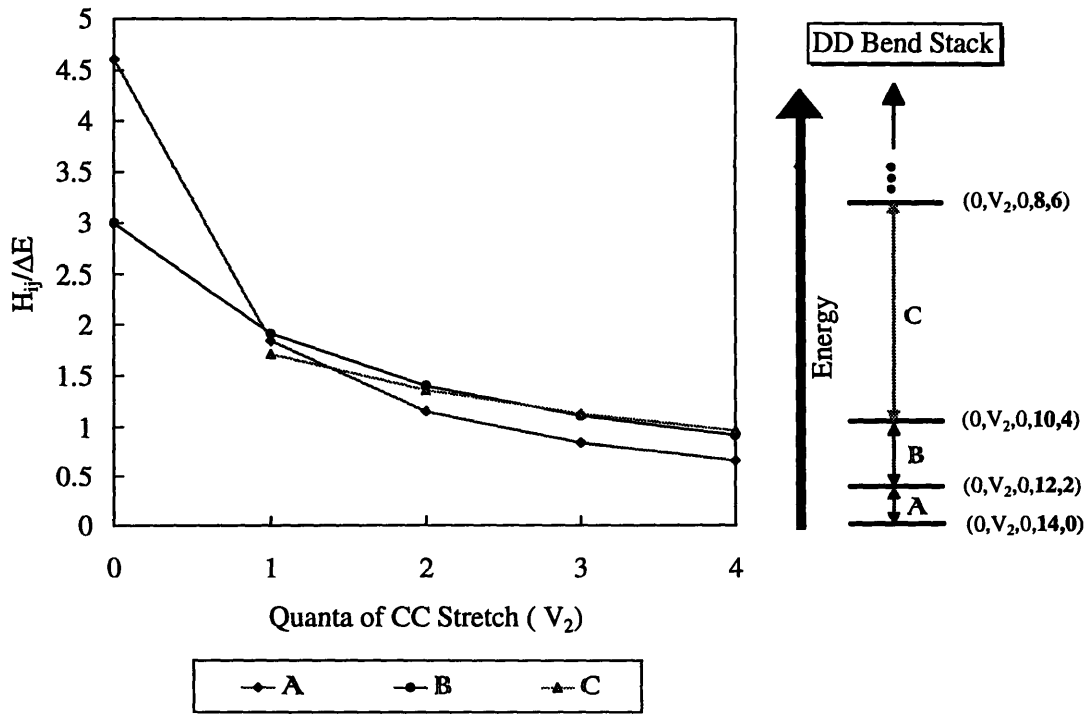

Figure 2.8: Within a DD stack, the coupling matrix elements, H_{ij}, increase but ΔE increases faster resulting in a reduction of the ratio of H_{ij} and ΔE.

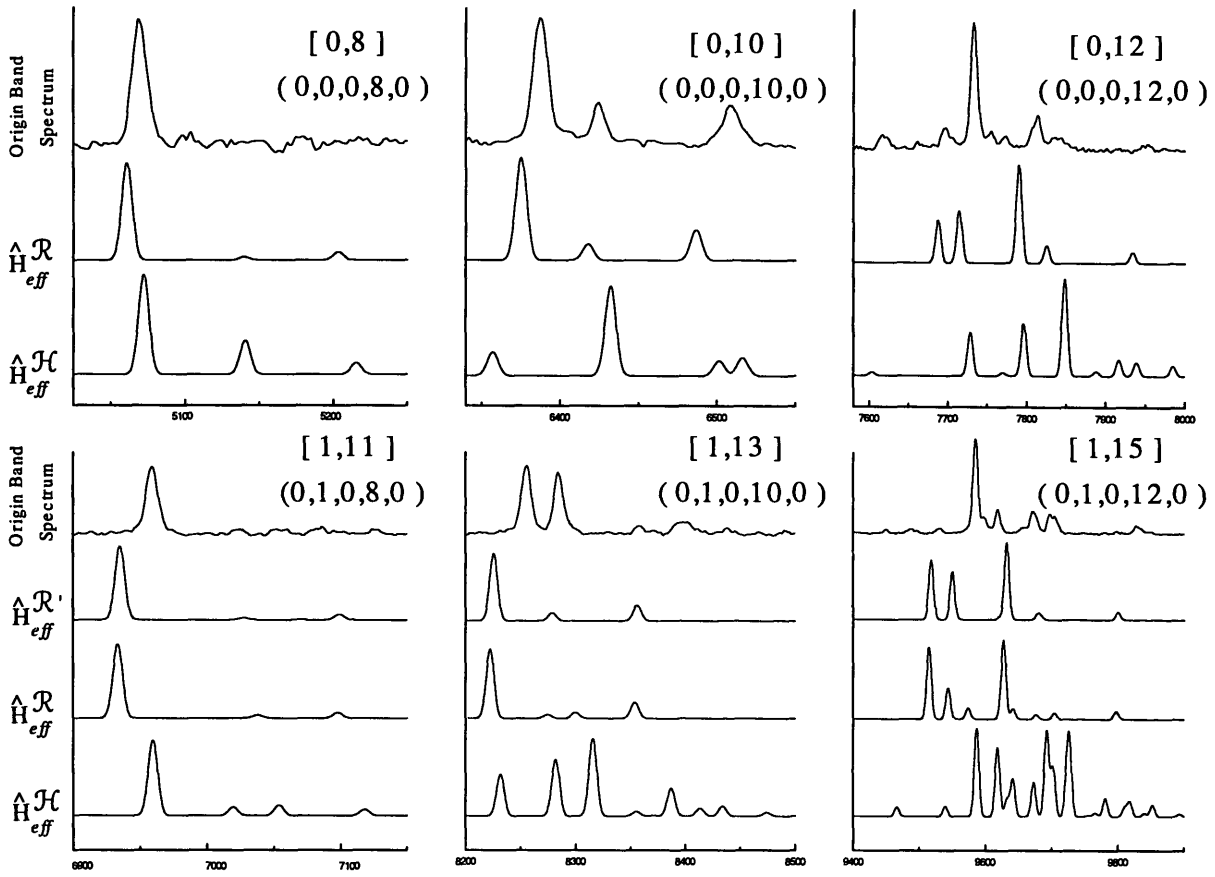

Figure 2.10: Comparison of the observed and theoretical spectra for the pure bend polyad series and the N_s=1 polyad series ([0,8], [0,10], [0,12] and [1,11], [1,13], [1,15]. See text for description of the different effective Hamiltonian models.

2.5.4 Intramolecular Vibrational Redistribution

Polyad fractionation, and hence the extent of IVR, increases with increasing V_4, and therefore N_{Res}, see Table 2.2. First, since the DD Bend matrix element is roughly proportional to ~ $v_4(v_5+2)$, see Table 2.2, increasing v_4 increases H_{ij}. Second, since ω_4^0 (609 cm^{-1}) is less than ω_5^0 (729 cm^{-1}) but x_{44}^0 is positive(+3.1 cm^{-1}) and x_{55}^0 is negative(-2.3 cm^{-1})[3], the ΔE 's between successive members of the DD Bend stacks decrease as V_4 increases; thus, the DD Bend stacks compress, see Figure 2.8. The increase in polyad fractionation with increasing V_4 (hence N_{Res}), due to the increase in H_{ij} combined with the stack compression (decrease in ΔE) is evident

in the evolution of the polyad fractionation pattern for the polyads [0,8] to [0,10] to [0,12] from (one peak) to (one strong peak/two weak peaks on the high energy side) to (one strong/many weak peaks) in both the $V_0^0K_0^1$ DF spectrum and the theoretical spectrum for $\hat{H}_{eff}^{R}$, see Figure 10. Since each polyad in the [0, N_{Res}] polyad series has only one DD Bend Stack, the preceding evolution of the polyad fractionation pattern (increasing fractionation with increasing N_{Res}) reflects increasing IVR further into the DD Bend Stack.

For a given value of V_4, the decrease of the IVR as a function of V_2 can be explained by a similar argument. Since x_{24}^0 = -13 cm^{-1} and x_{25}^0 = -2 cm^{-1}, as V_2 increases the DD bend matrix element does not change, but the ΔE's change rapidly. For example, the first DD bend resonance, connecting the bright state, $(0,V_2,0,V_4,0)$ to $(0,V_2,0,V_4\text{-}2,2)$, has $H_{ij}/\Delta E \approx 70/10$ cm^{-1} at V_2=0, but $H_{ij}/\Delta E \approx 70/80$ at V_2=4. The next DD bend resonance connecting $(0,V_2,0,V_4\text{-}2,2)$ to $(0,V_2,0,V_4\text{-}4,4)$ has $H_{ij}/\Delta E \approx 120/30$ cm^{-1}at V_2, but $H_{ij}/\Delta E \approx 120/160$ at V_4, and so on, see Figure 2.9. As the zero order energy positions of the ZOBS and dark states are changing the ZOBS, which is already at the low energy end of the polyad, is decreasing faster in energy than the rest of the dark states in the DD stack. This effectively "turns off" the IVR. There is also a subtle effect which occurs between the DD stacks. First, the entire DD bend stack containing the ZOBS drops faster in energy than the other DD bend stacks, because the ZOBS contains the most quanta of V_4 and V_2. Second, although the H_{ij}'s between the DD bend stacks increase proportional to $\sqrt{v_2}$, see Table 2.2, the H_{ij}'s do not increase enough to compensate for the increase in ΔE, see Figure 2.11. The IVR effects for V_2 and V_4 also explain why the [N_S, N_{Res}] polyads with (n_2V, mV_4) where $n \geq m$ have the same spectral pattern as polyads with (0, mV_4), see Figure 2.10. By understanding how the IVR changes with respect to the scalable H_{ij}'s and

ΔE's one can predict energy regions where normally weak resonances will become significantly strong. This is a powerful tool which will play an important role in our efforts to understand the polyad structure at $E_{vib} > 10{,}000\ cm^{-1}$.

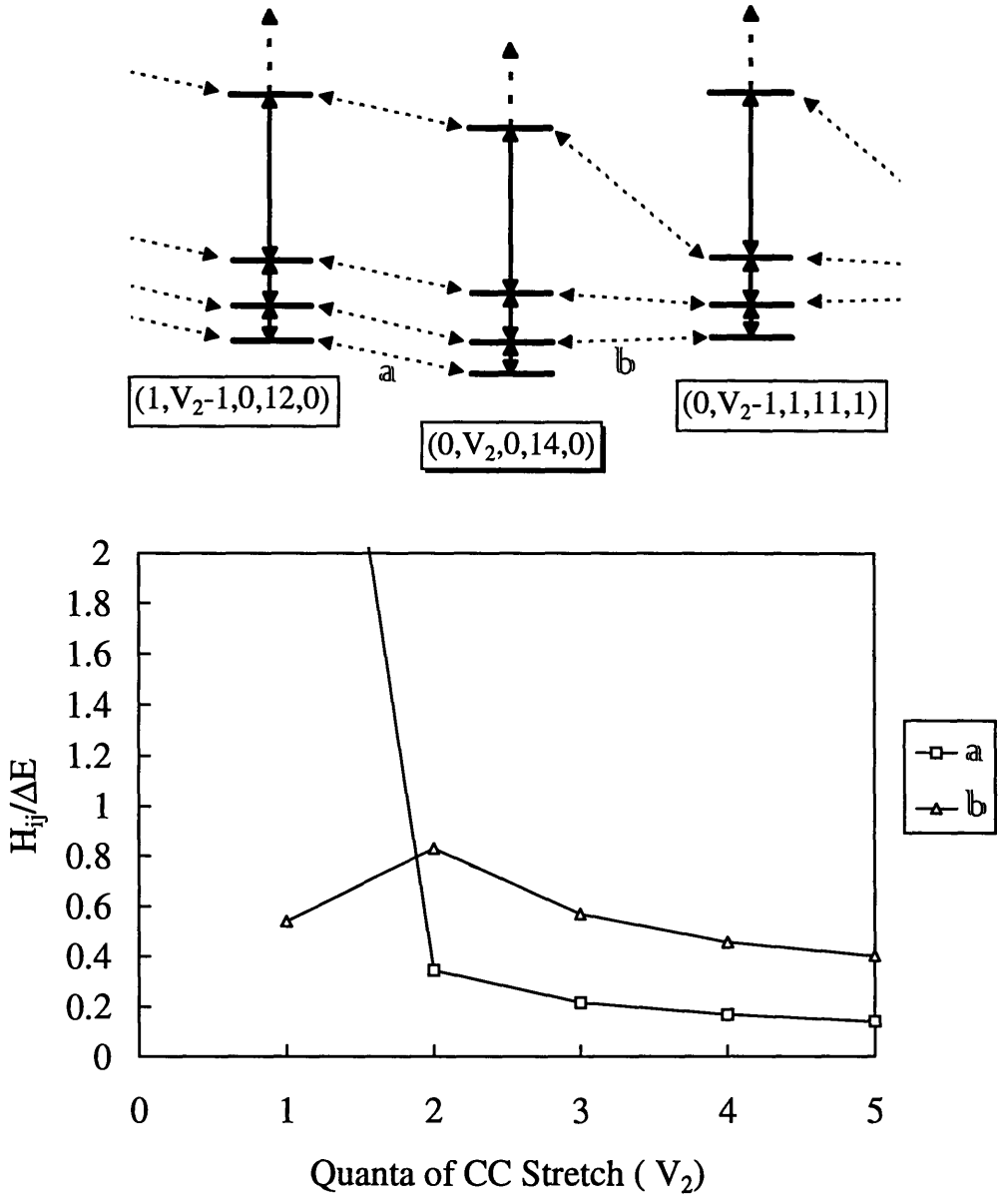

Figure 2.11: The entire DD bend stack containing the ZOBS as a whole pulls away from the other DD bend stacks (ΔE increases) as ν_2 increases, because the DD stack with the chromostate contains the most quanta of both bend and CC stretch. Although the stretch bend coupling, H_{ij}, between stacks increases with increasing ν_2, H_{ij} does not increase rapidly enough to overcome the increase in ΔE.

2.5.5 Acetylene Polyad Franck-Condon Factors

Since only one bright state per polyad exists, this system provides a nice opportunity to examine FC intensity trends, once a DF spectrum has been pulled apart into polyad progressions. Each of these polyads can be associated with a unique chromostate having (nV_2, mV_4) character. In Figure 2.12a the polyads from the $V_0^0K_0^1$ DF spectrum are arranged as progressions in V_4 such that each row has constant V_2 and each column has constant V_4. By inspection of Figure 2.12a or the plot of integrated intensity per polyad, Figure 2.12b, each progression in V_4 has the same smooth Gaussian-like intensity profile for each value of V_2. The same is also true if the polyads are plotted as progressions in V_2. As expected, there are no nodes in either the CC stretch or *trans*-bend unzipped progressions, since the intermediate for the $V_0^0K_0^1$ DF spectrum, the zero-point level, should have no nodes in its $\tilde{A}$ state vibrational wavefunctions. On the contrary, the same plots for the DF spectrum recorded from $2\nu'_3$ in the $\tilde{A}$ state, Figures 2.13a-b, show two distinct nodes in the *trans*-bend progression at V_4=12 and V_4=18, and no nodes in the V_2 (CC stretch) progression, as is expected for an intermediate that has two nodes in its *trans*-bend wavefunction. As can be seen, polyad pattern recognition in the DF spectrum facilitates the arrangement of the polyads the polyad intensities into progressions. These types of progressions are useful for theoretical studies of acetylene molecular dynamics and polyatomic Franck-Condon factors (FCF). Uncertainties with manual pattern recognition and lack of intensity calibration would possibly distort quantitative information about the FCF from these DF spectra. Nevertheless, the general FCF show that the ZOBS do follow, qualitatively, the predicted FC

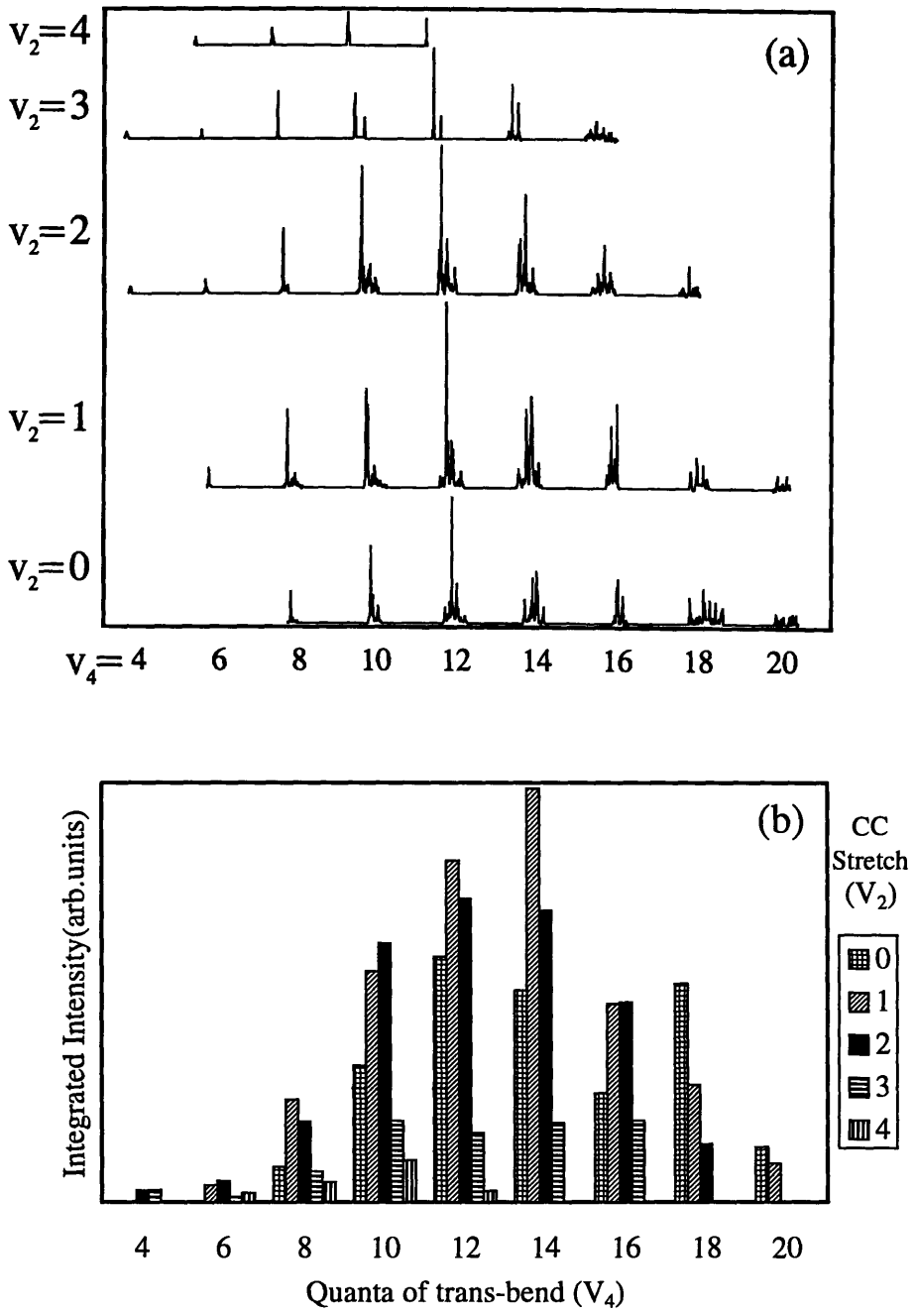

Figure 2.12: (a) polyad progressions from the Origin, $V_0^0K_0^1$, band DF spectrum arranged along ZOBS progressions in terms of (ν_2, ν_4) such that each row has constant ν_2 and each column has constant ν_4. (b) Integrated intensity for each polyad, [N_S, N_{Res}], from the $V_0^0K_0^1$ DF spectrum.

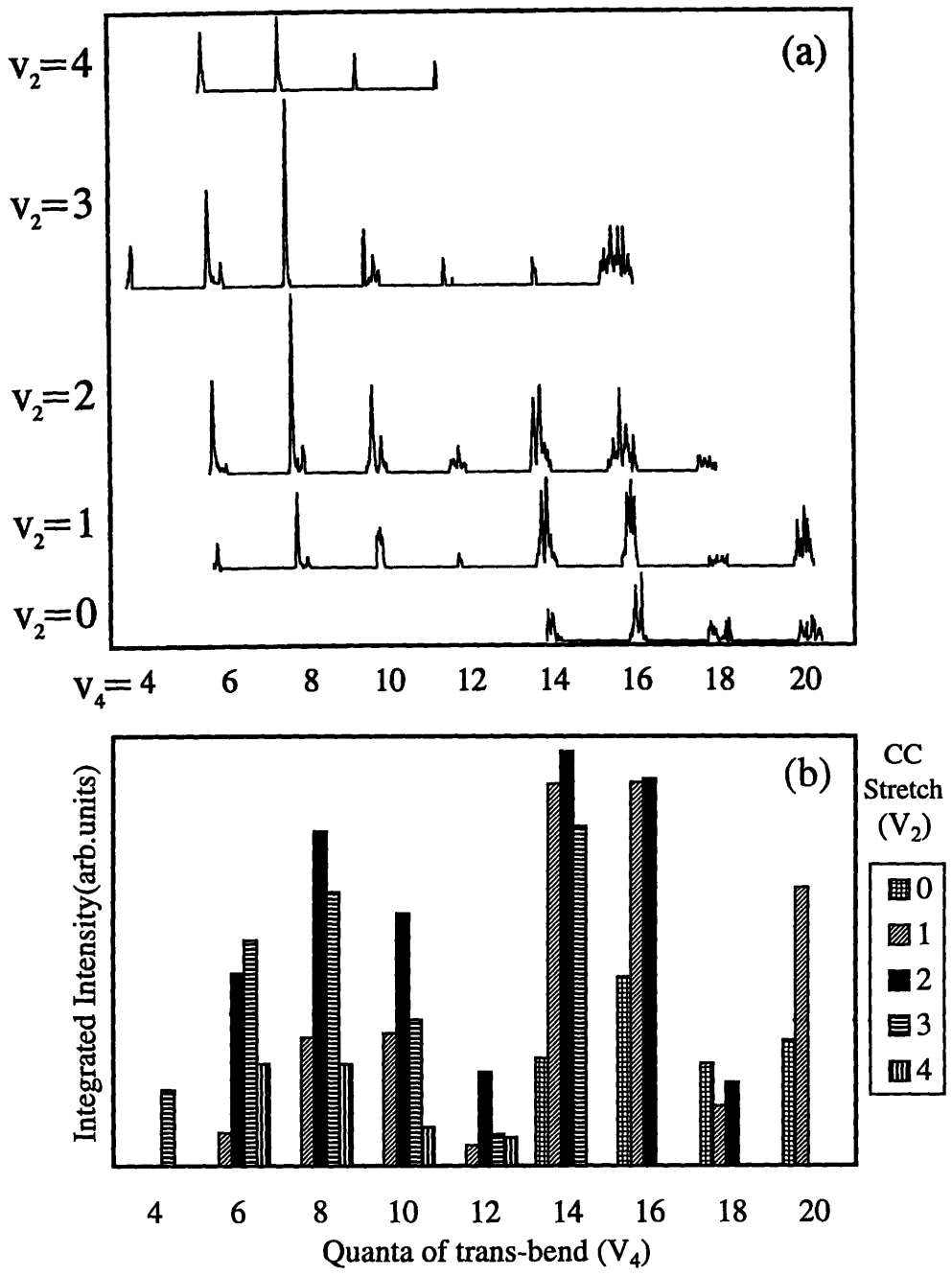

Figure 2.13: (a) Polyad progressions from the $V_0^2K_0^1$ DF spectrum arranged along ZOBS progressions in terms of (v_2, v_4) such that each row has constant v_2 and each column has constant v_4. (b) Integrated intensity for each polyad, [N_S, N_{Res}], from the $V_0^2K_0^1$ DF spectrum.

trends. Issues surrounding pattern recognition and reported FCF are addressed in Chapters 3 and 4.

2.6 Comparison of the N_s=0 Polyads to the N_s=1 Polyads

The polyad fractionation patterns for the theoretical spectra of the $\hat{H}_{eff}^{R}$ for the [0,8], [0,10], [0,12] polyad series are very similar to the polyad fractionation patterns for theoretical spectra of the $\hat{H}_{eff}^{R}$ and $\hat{H}_{eff}^{R'}$ for the [1,11], [1,13], [1,15] polyad series (the respective polyads only differ by one quantum of CC stretch, V_2), see Figure 2.10. The fractionation patterns for polyads [0,8] and [1,11] that have V_4=8 show one strong peak with two extremely weak peaks on the high energy side, while the fractionation patterns for polyads [0,10] and [1,13] that have V_4=10 show one strong peak with two weak peaks on the high energy side, and the fractionation patterns for polyads [0,12] and [1,15] that have V_4=12 show a strongest middle peak surrounded by several peaks, the weaker of which lie on the high energy side of the main peak. This similarity in appearance of the polyads with the same V_4 shows that, in the $\hat{H}_{eff}^{R}$ for the low energy extreme of the [*low* N_S, *high* N_{Res}] polyads, the main IVR pathway is still upward along the initial DD Bend Stack rather than outward to nearby stacks, since the spectral patterns for the polyads which contain only one stack, N_S=0, match the spectral patterns for the polyads with three stacks, N_S=1, for the same quanta of V_4. This is also borne out by the similarity of the spectral patterns for $\hat{H}_{eff}^{R}$ and $\hat{H}_{eff}^{R'}$.

The similarity of the spectral patterns for the [1,11], [1,13], [1,15] polyad series for both the $\hat{H}_{eff}^{R}$ and $\hat{H}_{eff}^{R'}$ shows that, even with additional stretch/bend resonances, the main IVR pathway is through the DD Bend Stack, rather than out to near by stacks. Unfortunately, the experimental $V_0^0K_0^1$ DF spectrum does not even qualitatively match the theoretical spectrum for

the [1,13] and [1,15] polyads, in marked contrast to the reasonable match for the [0,8], [0,10], [0,12] series. It seems that the $\hat{H}_{eff}^{R}$ does not describe the dynamics for $V_4>8$ when $V_2=1$. Either a new resonance has become important, or the values of the fitted diagonal and off-diagonal molecular constants are too far off to reproduce the polyads with even minimal stretch character.

The Hamiltonian of Temsamani and Herman[17], $\hat{H}_{eff}^{H}$, included fitted values only up to the x_{ij}'s for the diagonal terms. Since the original fit to the bend-only states located at low E_{vib} included higher order diagonal terms for the bends and the DD Bend II resonance (which was not included in Reference 17), it is not surprising that the $\hat{H}_{eff}^{R}$ qualitatively matches the $V_0^0K_0^1$ DF spectrum better than the $\hat{H}_{eff}^{H}$, see Figure 2.10. Since the $\hat{H}_{eff}^{H}$ theoretical polyad spectral patterns, especially the [1,13] and [1,15] polyads, show much more fractionation than the $V_0^0K_0^1$ DF spectrum, it is plausible that the off-diagonal couplings in the $\hat{H}_{eff}^{H}$ are too strong. Qualitatively speaking, a reduction in the magnitudes of the off-diagonal coupling constants and inclusion of higher-order terms on the diagonal might produce an effective Hamiltonian model that would match all of the known acetylene levels! This seems logical since, $\hat{H}_{eff}^{R}$ is a subset of $\hat{H}_{eff}^{H}$.

2.7 Refined Hamiltonian

The work reported above lead to a fruitful discussion and collaboration between the R.W. Field and M. Herman research groups.[39] The pure bend polyad progressions extracted from the $V_0^0K_0^1$ DF spectrum were utilized in a refined fit of the Herman and Temsamani Hamiltonian model, $\hat{H}_{eff}^{H}$. Briefly, starting with the parameters from the original Herman and Temsamani fit, a total of 41 pure bending levels were used to refine the effective Hamiltonian. This resulted in a Hamiltonian model which effectively reproduced the energies and fractionation patterns

(splittings and relative intensities) of the polyad patterns for [N_s,N_{Res},l,g] polyads where [N_s=0, $N_{Res}\leq$ 14, l=0 and 2, g] and [N_s=1, $N_{Res}\leq$15, l=0 and 2, g].[39] It is remarkable that the original parameters which were determined by class of chromostates, with moderate quanta of CH stretch and low quanta of *cis*-bend, could be successful in reproducing the DF chromostates with moderate quanta of CC stretch and high quanta of *trans*-bend! This result strongly supports the universality of the effective hamiltonian model in predicting the dynamics for a range of chromostates.

The 14 bend parameters are listed in Table 2.5. Using these values, the [0,8,0/2,g], [0,10,0/2,g], [0,12,0/2,g], [0,14,0/2,g] polyads can be calculated. The simulated stick spectra (where the intensities are derived from the fractional character of the ZOBS in each eigenvector) are convoluted with a Gaussian to reproduce the 7 cm^{-1} FWHM of the DF spectra. Figures 2.14a-b, displays the observed and calculated spectra for the N_s=0 polyads. The semi-quantitative agreement is remarkable! Note that there are several discrepancies in the N_s= 12 and 14 energy regions. These features were misassigned as belonging to the N_s= 0 polyads. It is possible that these features belong to the [2,12,0/2,g] and [4,12,0/2,g] polyads respectively. Discrepancies between the observed and calculated polyad patterns will be addressed in Chapter 4. Figure 2.15, contains the calculated and observed [1,15,0/2,g] polyad. The model does a sufficient job of reproducing the qualitative nature of the observed polyad pattern. Several of the features at low energy in the observed [1,15,0/2,g] polyad spectra are possibly due to different polyads, such as [3,15,0/2,g], and were misassigned. Discussion of the extra features will be presented in Chapter 4.

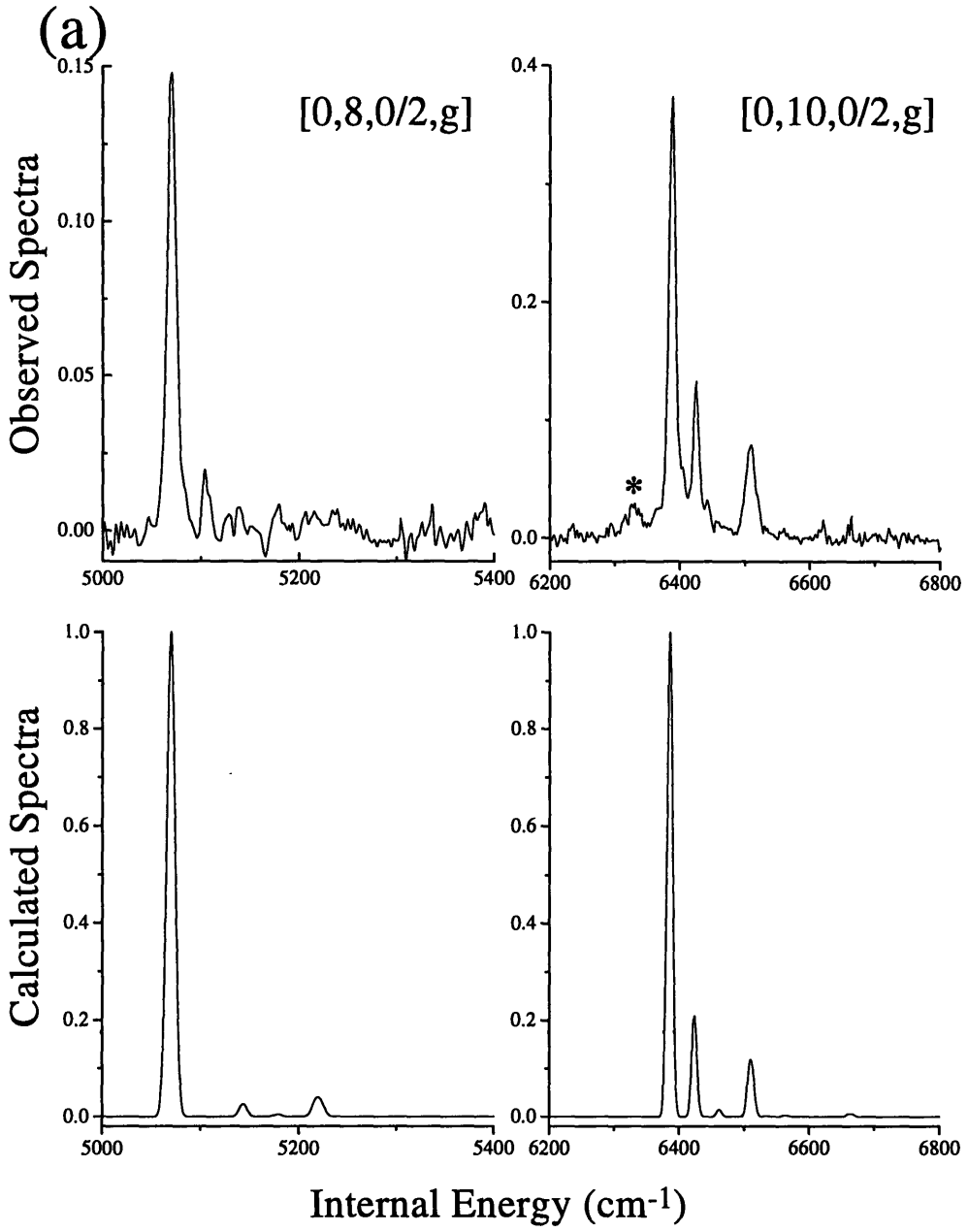

Figure 2.14a: The first row contains the [0,8,0/2,g] and [0,10,0/2,g] polyad patterns extracted via a manual pattern recognition technique, from the $V_0^0K_0^1$ DF spectrum. The second row contains polyad patterns calculated by the refined $\hat{H}_{eff}^{H}$. Notice the good agreement between the line positions and relative intensities of the observed and calculated polyad patterns. The asterisk denotes a feature which occurs in the observed spectrum but not in the calculated spectrum (see text for details).

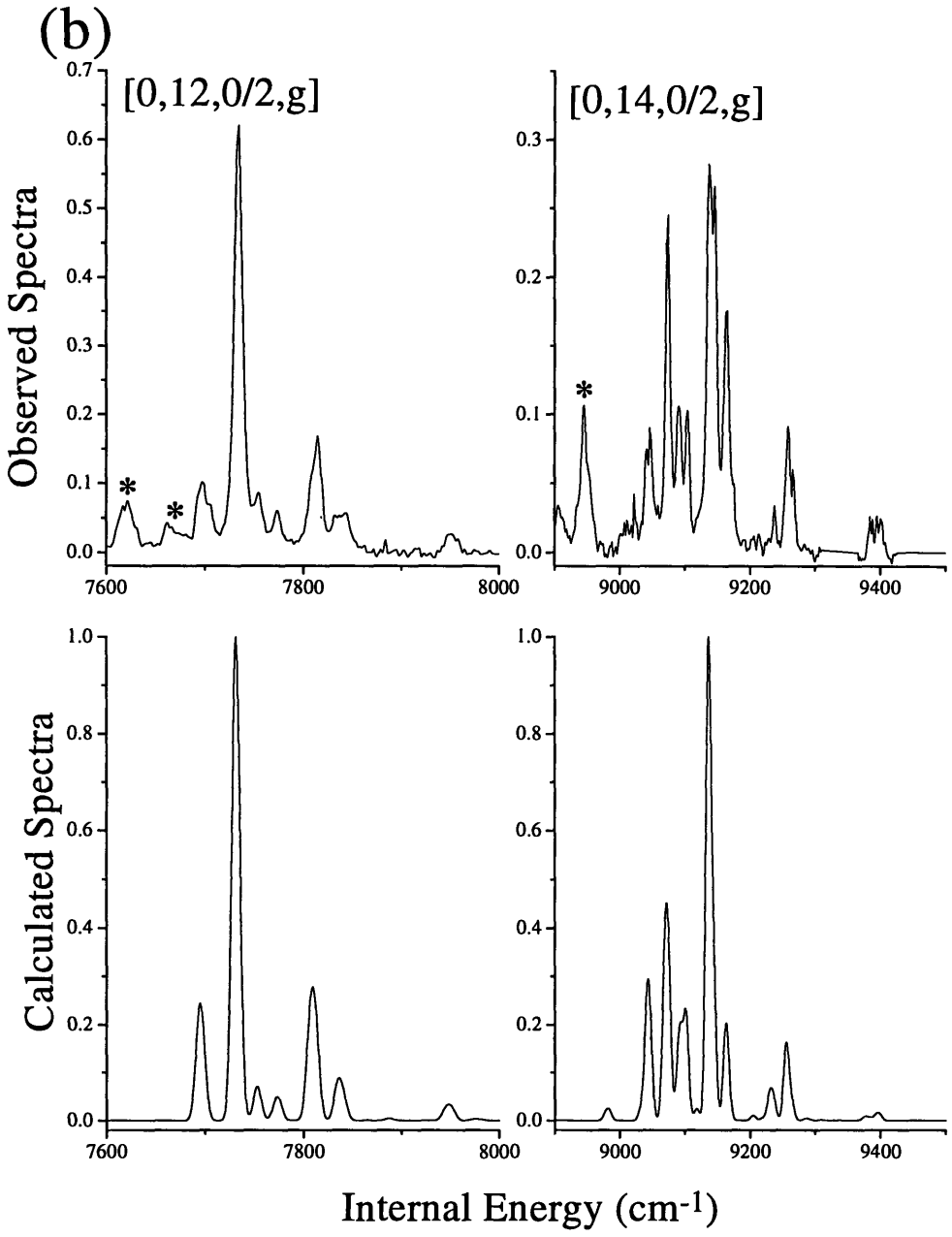

Figure 2.14b: The first row contains the [0,12,0/2,g] and [0,14,0/2,g] polyad patterns extracted via a manual pattern recognition technique, from the $V_0^0K_0^1$ DF spectrum. The second row contains polyad patterns calculated by the refined $\hat{H}_{eff}^{H}$. Notice the good agreement between the line positions and relative intensities of the observed and calculated polyad patterns. The asterisks denote features which occur in the observed spectra but not in the calculated spectra (see text for details).

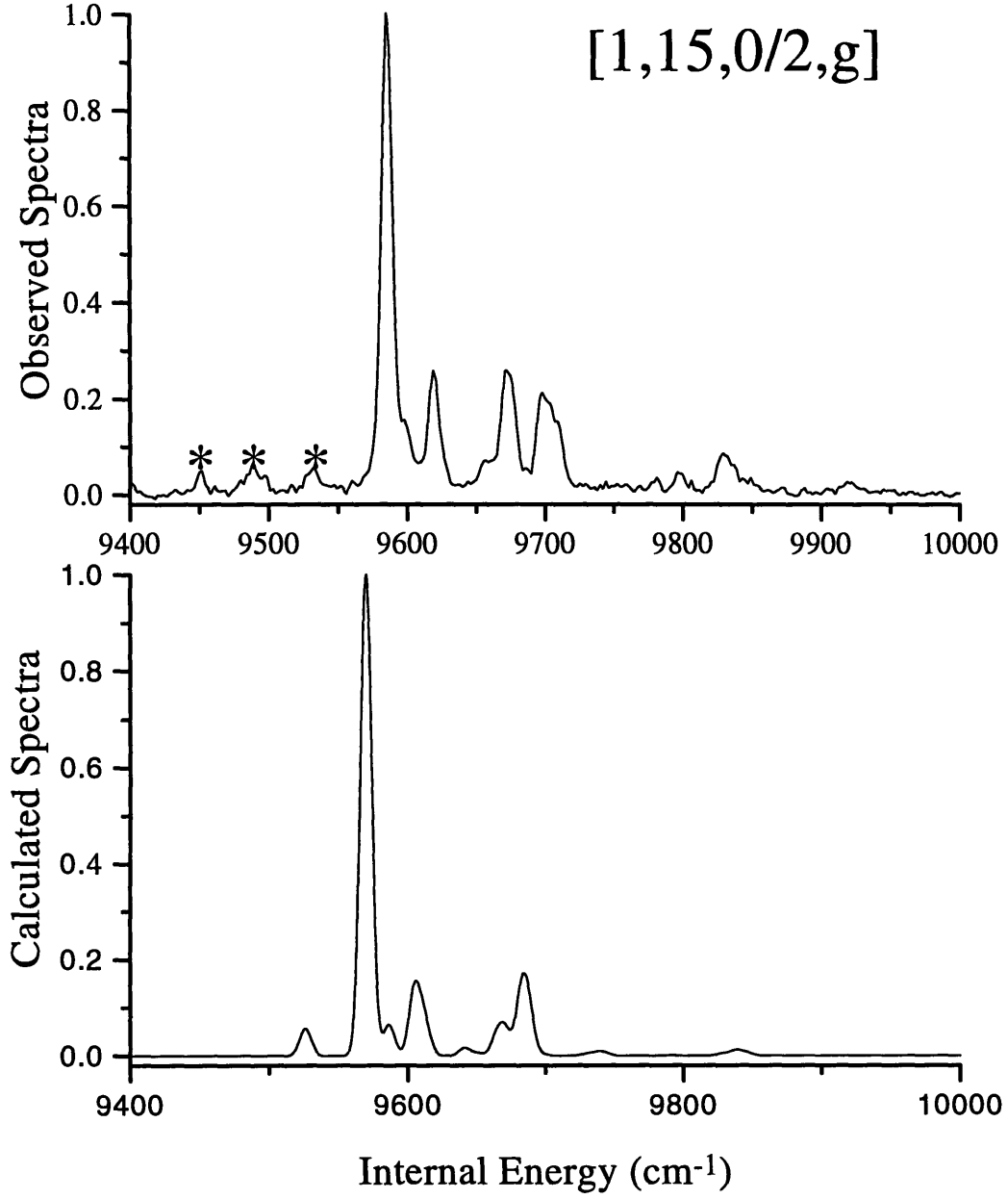

Figure 2.15: The upper plot contains the [1,15,0/2,g] polyad pattern extracted via a manual pattern recognition technique, from the $V_0^0K_0^1$ DF spectrum. The lower plot contains the polyad pattern calculated by the refined $\hat{H}_{eff}^{H}$. Notice that the agreement between the line positions and relative intensities of the observed and calculated polyad patterns starts to deviate. The asterisks denote features which occur in the observed spectra but not in the calculated spectra (see text for details).

Table 2.5: Refined Bend parameters for $^{12}C_2H_2$

Parameters[a]	Fit Values (cm^{-1})[b]
ω_4^0	608.36(13)
ω_5^0	729.25(18)
x_{44}^0	3.600(36)
x_{55}^0	−2.403(51)
x_{45}^0	−2.304(67)
g_{44}^0	0.582(37)
g_{45}^0	6.723(61)
g_{55}^0	3.534(38)
y_{444}	−0.0347(28)
y_{445}	0.0[c]
y_{455}	0.093(16)
y_{555}	0.0[c]
S_{45}^0	−8.37(12)
r_{45}^0	−5.942(62)
r_{445}	0.033(12)
r_{545}	−0.167(31

a Defined by Ref. 18
b The number in parentheses correscponds to the 1σ uncertainty in the last quoted digit.
c Held fixed in the fitting routine.

2.8 Conclusion

A new higher resolution dispersed fluorescence (DF) spectrum has been recorded from the zero point level $V_0^0K_0^1$ of the Ã-state, which allows us to elaborate a more complete picture of the energy flow pathways on the acetylene $\tilde{X}$-state potential surface than previous spectra have permitted. The new DF spectrum has a Franck-Condon (FC) envelope that extends to lower $\tilde{X}$-state energy than the previous DF spectra. There are *no nodes* in the Ã-state zero-point vibrational wavefunction, and this allows features that were absent in the previous studies to be recovered. The increase in resolution is sufficient to discern fractionation at lower $\tilde{X}$-state energies, where the initial IVR can be described by our $\hat{H}_{eff}^{R}$ model. In this chapter, analyses of the DF spectra are presented for levels with $E_{vib} \leq 10{,}000\ cm^{-1}$. Results from the manual pattern

recognition procedure were instrumental in refining a multi-resonant, block diagonal effective Hamiltonian model, $\hat{H}_{eff}^{H}$. This powerful tool will play a central role in our ability to understand and unravel the complexities in the acetylene spectrum and molecular dynamics.

2.9 References

1. J.K.G. Watson, M. Herman, J.C. Van Craen, R. Colin, *J. Mol. Spectrosc.* **95,** 101 (1982).

2. R.J. Bouwens, J.A. Hammerschmidt, M.M. Grzeskowiak, T.A. Stegink, P.M. Yorba, W.F. Polik, Pure Vibrational Spectroscopy of S_0 Formaldehyde by Dispersed Fluorescence Spectroscopy, *J. Chem. Phys.*, in press.

3. D.M. Jonas, S.A.B. Solina, B. Rajaram, R.J. Silbey, R.W. Field, K. Yamanouchi, S.J. Tsuchiya, *J. Chem. Phys.* **99**, 7350 (1993).

4. H.L. Dai, C.L. Korpa, J.L. Kinsey, R.W. Field, *J. Chem. Phys.* **82**, 1688 (1985).

5. J.T. Hougan and J.K.G. Watson, *Can. J. Phys.* **43**, 298 (1965).

6. D.M. Jonas, Spectroscopy of Vibrationally Hot Molecules: Hydrogen Cyanide and Acetylene. Ph.D. Thesis, Massachusetts Institute of Technology, 1992.

7. D.M. Jonas, S.A.B. Solina, B. Rajaram, R.J. Silbey, R.W. Field, K. Yamanouchi, S.J. Tsuchiya, *J. Chem. Phys.* **97**, 2813 (1992).

8. K. Yamanouchi, N. Ikeda, S.J. Tsuchiya, D.M. Jonas, J.K. Lundberg, G.W. Adamson, R.W. Field, *J. Chem. Phys.* **95**, 6330 (1991).

9. "*Fractionation*, or *fragmentation*, is defined to mean the complicated spectrum resulting from IVR, as opposed to *congestion*, a spectrum that looks complicated but NOT resulting from IVR." J. Hougen, Talk MH01, The Ohio State University International Symposium on Molecular Spectroscopy, June 14, 1993.

10. A single sixth order resonance, $K_{33,1244}$, has been reported by Smith and Winn.[33] This is probably an "accidental" resonance in the sense that the two levels in question are very close in energy, and therefore a higher order (small anharmonic resonance) term could efficiently transfer spectral intensity, zero-order character, as opposed to a "dynamical" resonance that is strong and active throughout the spectrum. Also, the effective Hamiltonian fit by Abbouti-Temsamani and Herman[17] showed that the intensity borrowing could also be by the extended net of fourth-order resonances listed in Table 2.

11. M.E. Kellamn, *J. Chem. Phys.* **93**, 6630 (1990).

12. M.E. Kellman, G.J. Chen, *J. Chem. Phys.* **95**, 8671 (1991).

13. L.E. Fried, G.S. Ezra, *J. Chem. Phys.* **86**, 6270 (1987).

14. l is determined by the choice of K_a in the intermediate state (l=K_a±1). See ref. 1 or 1.7.

15. J.P. O'Brien, M. Jacobson, J.J. Sokol, R.W. Field, Statistical Pattern Recognition and Acetylene Dispersed Fluorescence Spectra, In preparation. J.P. O'Brien, M. Jacobson, J.J. Sokol, R.W. Field, Dispersed Fluorescence Polyad Patterns: Deperturbed Zero-order energies and Franck-Condon Factors, In Preparation. M. Jacobson, J.P. O'Brien, J.J. Sokol, R.W. Field, Dispersed Fluorescence Polyad Patterns and Effective Hamiltonians, In preparation.

16. S.A.B. Solina, J.P. O'Brien, R.W. Field, W.F. Polik, *Ber. Bunsen-Ges. Phys. Chem.* **99**, 555 (1995).

17. M.A. Abbouti-Temsamani, M. Herman, *J. Chem. Phys.* **102**, 6371 (1995).

18. J. Plíva, *J. Mol. Spectrosc.* **44**, 165 (1972).

19. Although undetermined directly, s_{45}, is not independent of $x_{tt'}$, $g_{tt'}$, r_{45}, and α_t (t=4,5; t'=4,5). See refs 3, 18.

20. T.R. Huet, M. Herman, C. J.W. Johns, *J. Chem. Phys.* **94**, 3407 (1991).

21. M.J. Bramley, S. Carter, N.C. Handy, I.M. Mills, *J. Mol. Spectrosc.* **157**, 301 (1993).

22. A.B. McCoy, E.L. Sibert III., *J. Chem. Phys.* **95**, 3476 (1991).

23. G. Amat, H.H. Nielson, G. Tarrago, *Rotation-Vibration of Polyatomic Molecules*; Marcel Dekker: New York, 1971.

24. D. Papousek, M.R. Aliev, *Molecular Vibrational-Rotational Spectra*; Elsevier Scientific: Amsterdam, 1982.

25. E.L. Sibert III., R.C. Mayhofer, *J. Chem. Phys.* **99**, 937 (1993).

26. J.A. Bentley, R.E. Wyatt, M. Menou, C. Leforestier, *J. Chem. Phys.* **97**, 4255 (1992).

27. The number of Darling-Dennison stacks is determined by the value of N_s.

28. E.H. Abramson, R.W. Field, D. Imre, K.K. Innes, J.L. Kinsey, *J. Chem. Phys.* **83**, 453 (1985).

29. E.H. Abramson, Molecular Acetylene in States of Extreme Vibrational Excitation. Ph.D. Thesis, Massachusetts Institute of Technology, 1985.

30. Due to slightly higher J, better sensitivity, and higher resolution (therefore, coupling over longer time scales is resolvable), weak SEP transitions may derive their intensity from axis-switching[7], Coriolis, or interpolyad dynamics.

31. If a transition terminating in the $4_{2,f}$ rotational level was strong enough to detect, then the transition into the $6_{2,f}$ rotational level of the same vibrational state would also be easily detected.

32. Y. Chen, S. Halle, D.M. Jonas, J.L. Kinsey, R.W. Field, *J. Opt. Soc. Am.* **7**, 1805 (1990).

33. B.C. Smith, J. S. Winn, *J. Chem. Phys.* **89**, 4638 (1988).

34. G. Strey, I.M. Mills, *J. Mol. Spectrosc.* **59**, 103 (1976).

35. B.C. Smith, J.S. Winn, *J. Chem. Phys.* **94**, 4120 (1991).

36. G. Di Lonardo, P. Ferracuti, L. Fusina, E. Venuti, *J. Mol. Spectrosc.* **164**, 219 (1994).

37. A.A. Stuchebrukhov, R.A. Marcus, *J. Chem. Phys.* **98**, 6044 (1993).

38. S.A.B. Solina, J.P. O'Brien, R.W. Field, W.F. Polik, *J. Phys. Chem.* **100**, 7797 (1996).

39. M. Abbouti-Temsamani, M. Herman, S.A.B. Solina, J.P. O'Brien, R.W. Field, *J. Chem. Phys.* **105**, 11357 (1996).

Chapter 3: Dispersed Fluorescence Spectroscopy Methodology

3.1 Introduction:

As was evident from the preceding chapters, future experiments will be designed to gain better insight about the most important intramolecular vibrational redistribution pathways in C_2H_2. This will be done by recording spectra of the $\tilde{X}^1\Sigma_g^+$ state at high levels of vibrational excitation. Future experiments must accomplish three main goals.

1. The $\tilde{X}$-state vibrational spectrum must be recorded over a large energy range. This extensive sampling of the ground state potential will allow meaningful refinement of the anharmonic and Coriolis coupling constants, zero-order frequencies, and diagonal anharmonicities, which control the early time intramolecular redistribution in acetylene. For example, the $\tilde{A} \rightarrow \tilde{X}$ emission spectrum of acetylene has Franck-Condon factors which favor progressions in the CC stretch (ω_e=1,200cm^{-1}) and *trans*-bend (ω_e=620cm^{-1}) vibrations. Refinement of the energy positions of the zero-order bright states (nV_2 , mV_4) (where n=0,1,2,3,4 and m=4,6,8,10....22) of the [N_s,N_{res}] polyads extends from 2,000 cm^{-1} to at least 17,000 cm^{-1}. It might seem appealing to use high resolution double-resonance techniques, such as stimulated emission pumping, which has a typical resolution of 0.1-0.06 cm^{-1}. These methods would certainly yield spectra that contained a wealth of information about the eigenstate energies. In particular, these spectra would be sensitive to the long time dynamics of acetylene. As was stated in previous chapters, we are primarily interested in understanding the early time dynamics of acetylene as sampled through low resolution DF spectra. We want to learn about the strong *local* coupling forces of the potential which influence the initial redistribution of vibrational motion.

High resolution spectra which sample the long time dynamics are extremely sensitive to the weak coupling forces of the potential, as well. Still, one could argue that it would be possible to record the high resolution spectra and degrade the resolution to yield pertinent information about the short time dynamics. Unfortunately, high resolution techniques are only capable of probing localized energy regions on the ground state surface (200-300 cm^{-1}) and this requires several weeks of scanning. The major limitation is that one needs to scan the dump laser. However, this is not an insurmountable obstacle. Beyond requiring months to record a high resolution spectrum over a 17,000 cm^{-1} region, the use of stimulated emission pumping is known to have non-linear intensity effects. The relative intensities within a typical SEP scan of 30 cm^{-1} often do not indicate true transition strengths. The intensities of some of the weakly allowed transitions can be increased by a factor of five by saturation effects.[1] This flaw would severely inhibit the achievement of our goal.

2. The procedure to refine our molecular Hamiltonian depends intrinsically upon both the eigenstate energy positions and transition intensity distributions. Spectra should have the best possible frequency and intensity calibrations. Recording a meaningful relative intensity distribution within one polyad, with an energy width of 200 cm^{-1} at 10,000 cm^{-1}, is feasible for many experiments (absorption or optical double resonance techniques). However, we are interested in knowing the relative intensities within polyads and between polyads. What is the intensity ratio between the [0,4,0] polyad at E_{vib}≈2,400 cm^{-1} and the [0,24,0] polyad E_{vib}≈16,000 cm^{-1}? The relative intensities must be accurate over 13,000 cm^{-1}. The global intensity information in the spectrum can be used to extract experimental Franck-Condon factors. The experimentally determined Franck-Condon factors are

valuable to compare with current polyatomic Franck-Condon calculation results, particularly those of the acetylene $\tilde{A} \leftrightarrow \tilde{X}$ band, with a change in the molecular symmetry group and change in the number of vibrational degrees of freedom. More importantly, the experimental Franck-Condon factors help in refining our molecular Hamiltonian.

3. Multiple spectra -originating from several intermediate states- which probe the same $\tilde{X}$ -state energies, are necessary in order to successfully perform pattern recognition routines, either manually or statistically. Each of the polyad patterns observed in a DF spectrum has specific classes of intensity information which is derived either from the intermediate state or from the dynamics of the specific bright state evolving on the $\tilde{X}$ -state surface. Each of the intermediate states will illuminate a series of zero-order bright states which have a unique intensity (Franck-Condon factor) distribution. No two intermediate states will possess the same intensity distribution of transitions into zero-order bright states. The Franck-Condon intensity controls how much of a particular pattern is visible in a given spectrum. Having more spectra which sample the same $\tilde{X}$ -state patterns with differing amounts of oscillator strength will allow the statistical pattern recognition routines to disentangle complicated and overlapping spectral patterns. These patterns are often overlooked or incorrectly assigned when one tries to disentangle spectral patterns by eye. Lost or incorrectly assigned patterns hamper efforts to understand the short time dynamics of acetylene and ultimately, our ability to refine the acetylene molecular Hamiltonian.

Dispersed Fluorescence (DF) spectroscopy has been an extremely valuable technique for recording low resolution emission spectra of many molecular species. Modifications on this basic technique have been made by our research group to produce an experimental setup

that is capable of fulfilling the three requirements listed above. The basic DF technique typically has many less than desirable and seldom understood (not well characterized) experimental artifacts that have hindered previous efforts to obtain spectra of the quality discussed above. The main method of recording a DF spectrum has involved scanning a dispersive element, usually a grating, to obtain the frequency spectrum. As a dispersive element is scanned, the drive mechanism often sticks and jumps stochastically. The sticking and slipping of scanning mechanism introduces many uncorrectable frequency errors into the DF spectra. The initial DF experiments conducted in this lab on acetylene in the late 1980's had many frequency and intensity calibration defects. These errors may have been as large as 30-50 cm^{-1} and were found to be nonsystematic; the frequency errors in the spectrum cannot be corrected by a constant shift! Locally, over region containing a few hundred cm^{-1}, many DF spectra can be recorded with a 0.1nm precision and accuracy. Our experimental needs are unique. The initial attempt to learn more about the intramolecular vibrational redistribution (IVR) through the spectral patterns in the DF spectra was severely compromised by the absence of reliable frequency and intensity calibration. At that time, it was not possible to apply intensity corrections to the DF spectra. Therefore, DF spectra with nonlinear and uncorrectable frequency calibration and without intensity calibration cannot be rigorously or optimally used in a pattern recognition technique. Our scheme for recording artifact free DF spectra is presented below.

3.2 Experimental Setup

As with any spectroscopic experiment, there are three main factors that critically affect the probability of success: light, molecules and detection. Detailed information about these factors is presented below.

3.2.1 Production of Light

A xenon chloride excimer laser, Lambda Physik LPX210 icc, can produce 250-350 mJ of 308 nm light. Typically 125mJ of the excimer output is used to pump an FL2002 Lambda Physik dye laser with intracavity etalon. This dye laser can accommodate a range of laser dyes. The accessible range of wavelengths depends upon the exact configuration of the dye laser. Typically, the available wavelength range is from 550-400 nm for the fundamental output. This range is limited on both the blue and red edges by the wavelength of the pump laser. In particular, it may seem odd that the 308 nm pump can only pump laser dyes with fundamental emission at wavelengths shorter than 550 nm. The limitation arises from the photodegradation of redder dyes by the intense short wavelength pump laser. This process, while degrading the dye efficiency, also results in the formation of particulates which can damage the dye cuvette walls. There have been some attempts to use a mixture of red and blues dyes to extend the available fundamental wavelengths further to the red. This can be accomplished by experimenting with the relative concentrations of the two dyes.

The dye laser output intensity depends on the efficiencies of the various laser dyes. Most of the Coumarin laser dyes have 10-15% efficiencies (R6G is rated at 25-27% efficiency).[2] Our experiments on acetylene, in the 430-490 nm region typically utilize dyes at the blue end of the Coumarin series. The fundamental wavelength output by the dye laser is scanned either by rotating the grating in the oscillator cavity or by pressure scanning. Pressure scanning is described in detail elsewhere.[3] Briefly, the oscillator cavity is contained in an airtight box which can be evacuated and filled with different gases. The wavelength is changed by varying the amount of gas in the box. As the gas pressure is added or removed, the change in the index of refraction inside the pressure box influences the wavelength that

can resonate in the oscillator cavity. We use N_2 and SF_6 as pressure scanning gases. Typically, introduction of an atmosphere of gas corresponds to a 20 or 35 cm^{-1} scan. Since we typically lock the dye laser frequency to single rovibrational level in the $\tilde{A}^1A_u$ state for the duration of our DF experiments (6-8 hours), we use nitrogen as the pressure gas to avoid large frequency changes introduced by atmosphere leaking into the pressure box. The acetylene $\tilde{A}^1A_u \leftrightarrow \tilde{X}^1\Sigma_g^+$ transitions for our experiments occur in the 240 nm to 220 nm region. By passing the fundamental output of the dye laser, of wavelength λ, through a β Barium Borate crystal (BBO doubling crystal) we can produce ultra-violet radiation of wavelength $\lambda/2$. In order to maximize the amount of UV radiation produced for our dispersed fluorescence (DF) experiments the FL-2002 dye laser has been modified as follows. After the oscillator and preamplifier stages of excitation, the fundamental laser beam passes through a telescope used to collimate the dye laser output. This telescope has been adjusted so as to increase the typical beam diameter by a factor of two. This adjustment necessitates the following amplifier stage adjustment. The excimer laser pump beam input to the amplifier cuvette must be slightly defocused to allow for good spatial overlap with the larger diameter oscillator beam. These modifications are done to maximize the production of ultra-violet radiation. In normal operation, the FL-2002 dye laser has a beam diameter of 2-3mm. A 10 mJ beam of 450 nm light with this diameter will at least burn and possibly drill holes through our β–BBO doubling crystal. Most experiments conducted in our laboratory use only a few hundred μJ of ultraviolet radiation produced from 1 mJ of fundamental radiation, so typically, there is no need to make any adjustments in the dye amplifier. For the laser dye Coumarin 450 (C450), with a quoted 15% efficiency[2], the dye laser fundamental output can easily reach 10-15 mJ

with a 125 mJ pump laser. This fundamental output, now with a larger beam diameter, can be passed through our doubling crystal to yield ~1mJ of 225 nm light. The importance of increasing the amount of ultra-violet light available for our experiment is that it allows for a increase in the total amount of total spontaneous fluorescence.

After passing through the β–BBO doubling crystal, the fundamental and frequency doubled beams are spatially separated by a series of 60^0 prisms, see Figure 3.1. The ultraviolet beam is passed through a series of adjustable irises (typically set at 6-10 mm diameter) and passed through a static gas fluorescence cell. The residual fundamental beam is split. One beam is passed through a frequency calibration cell consisting of a quartz cell containing either I_2 or $^{130}Te_2$ and heated in a tube furnace.[4,5] For a 450 nm laser beam, we use a $^{130}Te_2$ calibration cell heated to 783 K.[6] The calibration beam impinges on a photodiode. An absorption spectrum of either I_2 or $^{130}T_2$ is recorded as the fundamental wavelength is tuned. These species have well characterized high resolution (0.003 cm^{-1}) spectra, and are often used as absolute frequency calibration standards. Our experiments typically rely on $^{130}Te_2$ for calibration of the C440, C450, C460, C470, and C480 laser dye fundamental outputs. A very extensive collection of calibration atlases for these two molecules has been assembled, bound, and is located in the laboratory and the main office. The other beam is passed through a bi-concave lens, focal length -5 cm, followed by a monitor etalon, low finesse (~10) with a free spectral range of ~30 GHz. The visible etalon interference ring pattern is an essential diagnostic tool for evaluating the dye laser performance. The typical frequency FWHM of the fundamental output, with the intracavity etalon, is 0.02 cm^{-1}. See Figure 3.1 for a schematic layout.

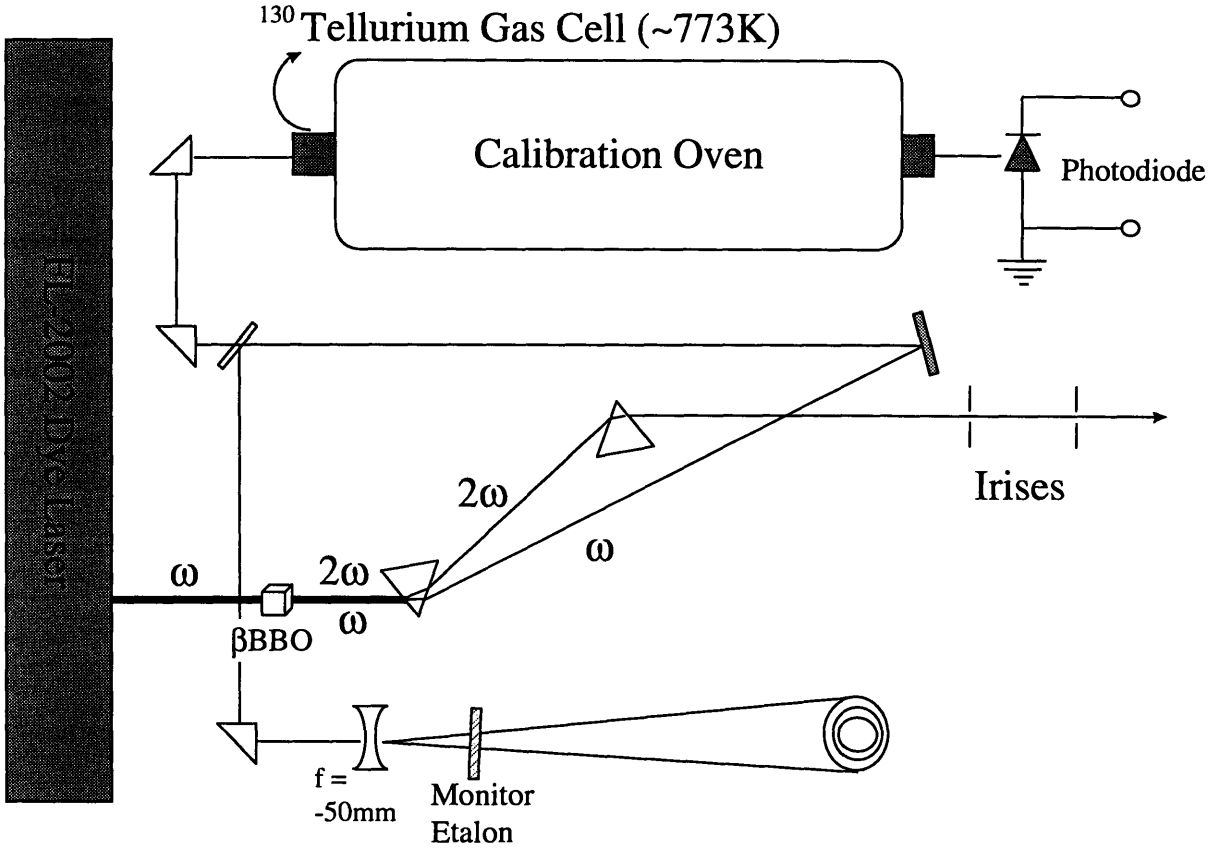

Figure 3.1: Schematic representation of fundamental and doubled light separation and dye laser calibration apparatus.

3.2.2 Molecules

The traditional static gas cell used in this group for fluorescence excitation and stimulated emission pumping experiments has been modified slightly. Instead of using two linear cells that have been connected in the middle (the cell resembles an H configuration). We use a standard six way cross (MDC) as a static gas cell; see Figure 3.2. Three of the six arms on the cross are typically equipped with small (1 inch diameter, 1/16 inch thick) quartz window flanges. Located in the same plane, these windows are used as the entrance and exit ports, for the excitation laser beam, and to collect the total ultraviolet fluorescence. The

entrance and exit ports are located directly across from each other. Two of the other arms, located directly across from each other and lying in a plane perpendicular to the entrance, exit, and total fluorescence ports, are equipped with larger (1.75 inch) quartz window flanges. The final arm is equipped with a 1 inch valve flange. This is used to evacuate and fill the cell. This flange lies across from the total fluorescence collection port. Figure 3.2 is a schematic representation of the static gas cell.

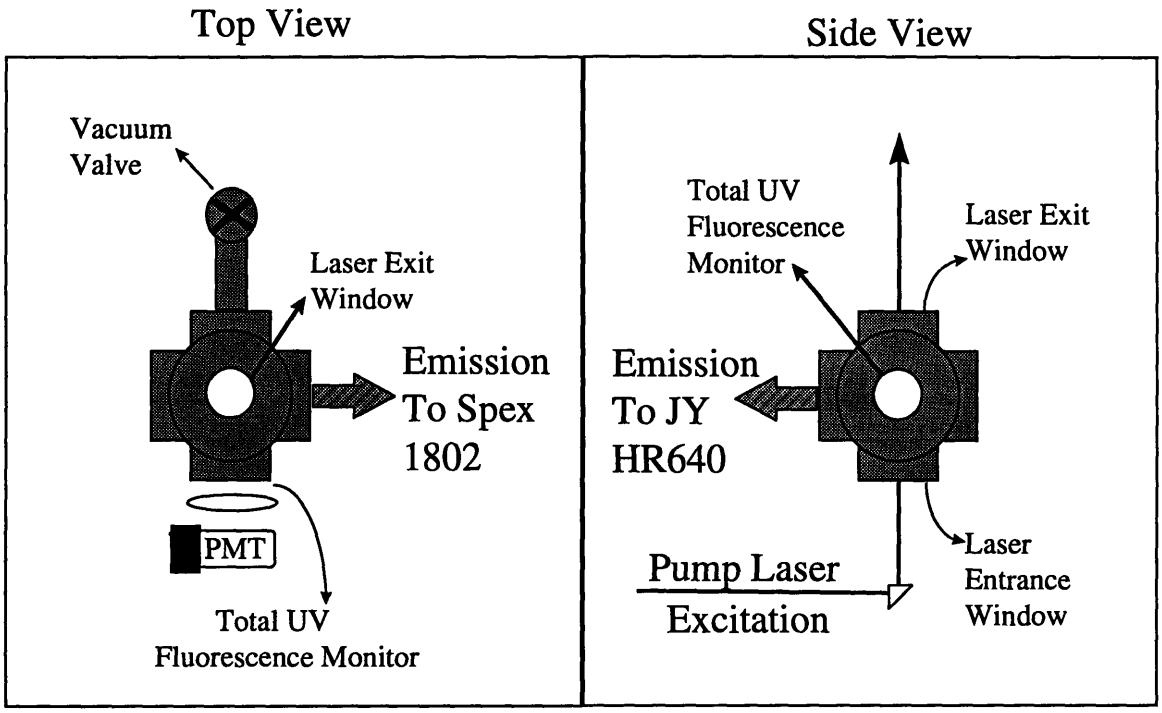

Figure 3.2: Schematic representation of the Dispersed Fluorescence static gas cell.

The cell has been designed without a permanent vacuum line attached to the cell. (The cell is mobile.) The mobility of the cell maximizes the versatility of the DF setup. The cell can be filled from any gas manifold with any of several molecular species. For example, once

placed on a vacuum line, with ultimate pressure of 3 x 10^{-6} Torr, the cell can be evacuated and then filled with an appropriate quantity of acetylene. Various pressures of acetylene gas are used in the dispersed fluorescence experiments (5 Torr is typically used). The cell can be isolated from the vacuum station and removed. The cell is placed into a large mount (Oriel) with x,y, and z translation capabilities. The cell is oriented such that the laser beam entrance and exit windows are facing down and up respectively. During the course of the experiment it is necessary to remove the cell from the mount either to clean the windows or to record the frequency standards used in the frequency calibration of the DF spectra.

A two lens system collects and images the spontaneous emission from acetylene into either of two separate monochromators, either a 640 mm HR640 Jobin-Yvon (HR640 JY) or a 1000 mm 1802 Spex. Each lens system is comprised of two plano convex lenses, for collection and imaging. For imaging the acetylene fluorescence into the HR640, we use two fused silica plano-convex lenses (Esco), with a 1.0 inch diameter and 3.0 inch focal length. For imaging the acetylene fluorescence into the Spex 1802, we use two fused silica plano-convex lenses(Esco), with a 1.0 inch diameter and 5 inch focal length. The *f* number is the ratio of the effective focal length and the image height. (Our detector is 0.5 inches in height.) Each of the collection lens assemblies was selected to best match the *f* number of its respective monochromator. The Spex 1802 is *f*/10 and the HR640 is *f*/5.8. The lens collection optics are mounted on translation stages such that the flat side of each optic is directed towards either the monochromator entrance slits or the DF static gas cell. (See Figure 3.3) The alignment of the lenses relative to the optical axis of the two monochromators is accomplished by first establishing the optical axis of the monochromator with a Helium Neon

laser and then inserting and adjusting the lens system so each optic is centered and the flat surface is normal to the He-Ne laser. This procedure has been modified slightly. The details will be specified below.

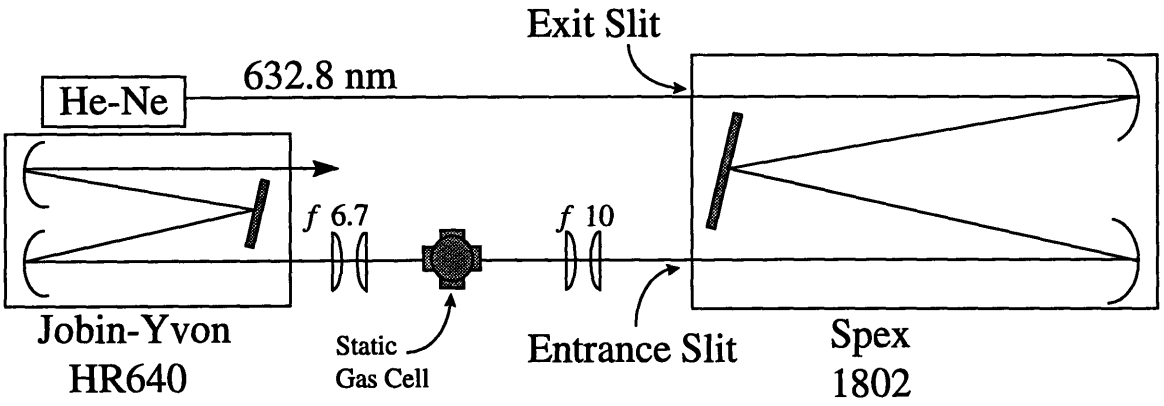

Figure 3.3: Schematic representation of experimental DF setup. Both monochromators are positioned such that each shares the same optical axis. This axis is defined by a He-Ne laser (632.8nm). The spontaneous fluorescence is collected by a lens assembly composed of two fused silica plano-convex lenses. The HR640 imaging optics have a 1.0 inch diameter and a 3.0 inch focal length. The Spex 1802 imaging optics have a 1.0 inch diameter and a 5.0 inch focal length.

Each of the monochromators is equipped with a classically grooved grating, 1200 grooves per mm, blazed at 500 nm. The HR640 JY is used to record low resolution DF spectra (15-20 cm^{-1} at 350 nm with a ~100 μm slit width). The 1802 Spex can record high resolution DF spectra. (4-10 cm^{-1} at 350 nm with a ~25-100 μm slit width) Recently, a 750 mm Spex monochromator was purchased with several new gratings. This system could be used to record higher resolution DF spectra. The new gratings are compatible with the old style grating mounts located in the 1802 Spex. The configuration of our experimental setup combines both of these monochromators into an optical arrangement that easily facilitates

recording of spectra by both of the monochrometers either individually or simultaneously. Currently only one detector, a Princeton Instruments intensified charge coupled device (ICCD) (1024-M059413), is available; a second detector would be needed to record simultaneous DF spectra on both monochromators. As seen in Figure 3.3, the entrance slits for the HR640 JY and the 1802 Spex are facing each other and share the same optical axis. Spontaneous emission is simultaneously collected and imaged by each *f* number matched lens system. The alignment of the optical axes is accomplished by directing the He-Ne laser through the exit slits of the 1802 Spex. When the 1802 Spex and HR640 JY share the same optical axis, a 632.8 nm He-Ne beam exits the 1802 entrance slit and proceeds into the HR640 entrance slit. The task of aligning the He-Ne, 1802 Spex, HR640, AND the collection lenses (4 optics) is NOT TRIVIAL (the initial setup and alignment took a couple weeks). The optical axis has been carefully defined over a 5 meter pathlength. Any slight displacement (X > 2mm) of the He-Ne, 1802 Spex, or imaging lenses can cause the optical axis to be off center for the HR640. Similarly, the 1802 Spex is susceptible to misalignment. In practice, the optical axis remains relatively well defined over a period of a few weeks. Inevitably, there is some drift of the He-Ne and optical mounts, and routine alignments must be performed. The He-Ne beam also serves as a spatial guide when positioning the pump laser beam through the static gas cell. The removability of the static gas cell tremendously simplifies the pump beam positioning process.

3.2.3 Detection

The fluorescence dispersed by the grating is imaged onto and detected by a Princeton Instruments Intensified Charge Coupled Device (ICCD), model number 1024M-059413. This

two dimensional array is 256 pixels in height and 1024 pixels in length. Each pixel is 25 microns by 25 microns. The intensifier, which is glued onto the surface of the array, is only 18 mm in diameter (covering only 70% of the length of the array). The intensifier and array are thermoelectrically cooled to -40^0C. The ICCD can be run in either of two modes, gated or continuous. The gated feature allows the intensifier to be cycled on and off with variable repetition and gate width. We typically have a gate width of 1.5 μs, centered in time on the 300 ns fluorescence decay of acetylene. The entire experiment is usually performed at 65 Hz. The intensifier gating allows for discrimination against background noise, scatter and undesirable emission (such as that produced from photofragments of a photolysis experiment). For our experiments, we record dispersed emission from acetylene in consecutive spectral segments ranging from 230 nm to 470 nm. When spectra are recorded using the HR640 JY monochrometer, the consecutive sections are obtained at 20 nm intervals; *i.e.*, consecutive segments are centered at wavelengths differing by 20nm. For spectra recorded on the 1802 Spex monochromator, the sections are recorded every 10 nm. The spectral segments have approximately a 2.0-5.0 nm overlap with adjacent segments.

3.3 Recording Dispersed Spontaneous Fluorescence

A flow chart of the steps necessary to record, calibrate, and concatenate each DF spectrum is given below. Descriptions of each of the steps are presented after the flow charts.

Recording Dispersed Fluorescence Spectra

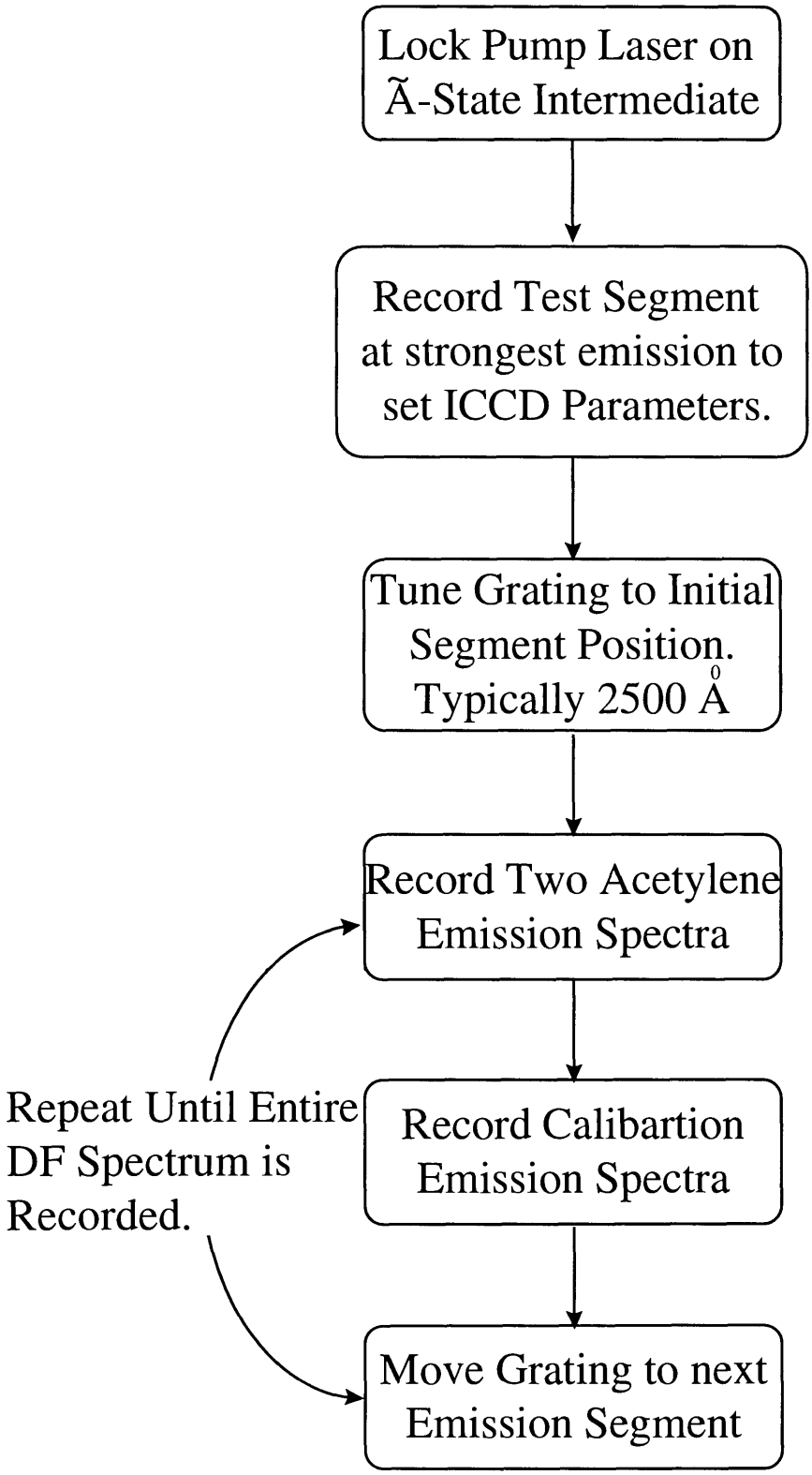

Calibrating Dispersed Fluorescence Spectra

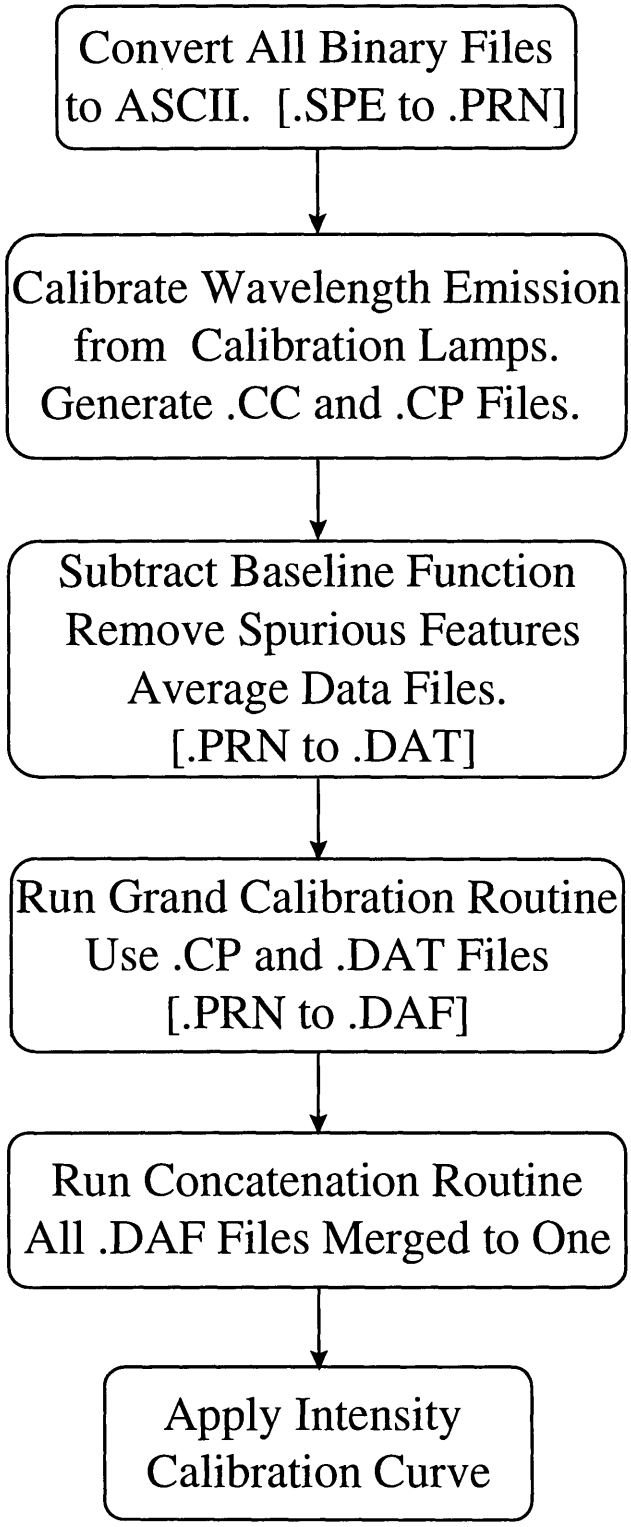

All of our DF spectra originate from single $\tilde{A}$ -state rovibrational eigenstates whose energies are precisely known.[7,8] We use our pump laser to record an initial fluorescence excitation spectrum, see Figure 3.4.

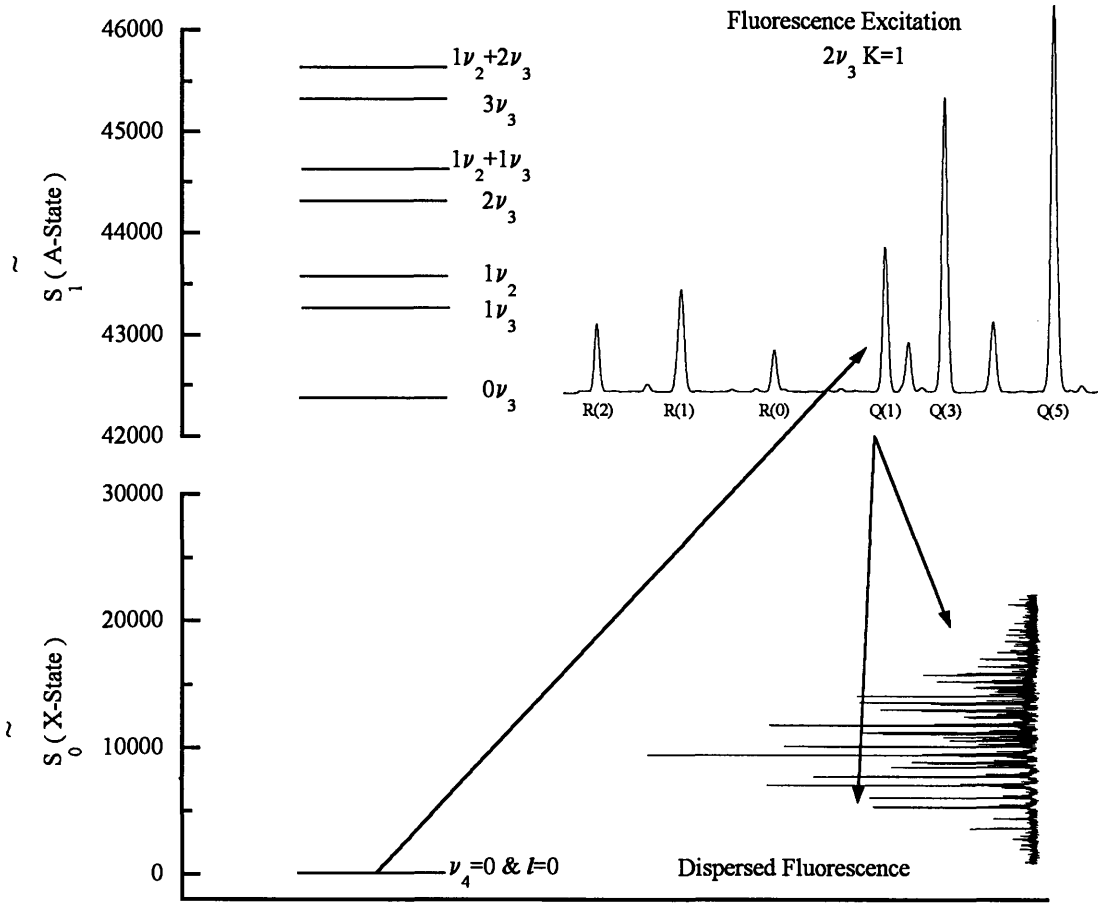

Figure 3.4: The laser wavelength is scanned to record a fluorescence excitation spectrum of the vibrational band used to excite the intermediate level used in dispersed fluorescence. The excitation laser is locked onto a single rotational feature. The spontaneous emission spectrum is dispersed and recorded.

Well resolved Q and R branches are evident in the fluorescence excitation spectrum (The P branch is not pictured). The linewidth of the recorded spectrum is dominated by the intrinsic linewidth of the pump laser (0.03 cm^{-1}). The frequency of the pump laser is tuned to excite a single rotational transition within a specific $\tilde{A}^1A_u \leftarrow \tilde{X}^1\Sigma_g^+$ vibrational band. Most of our experiments have utilized Q(1), Q(3), and Q(9) rotational transitions.

Once the pump laser frequency has been locked onto the transition of the correct intermediate state, the total spontaneous fluorescence is imaged by a *f*/1.7 lens assembly, two fused silica plano-convex lenses (Esco), through a colored glass filter (either a Schott BG3 or UG11) onto a photomultipler tube (PMT) (Hamamatsu 166 UH). The output signal is averaged on a Le Croy 6903 oscilloscope for a period equal to and coincident with the recording of each dispersed fluorescence segment. (This averaged signal is extremely important for normalization of the DF spectra.)

The DF spectrum is recorded in the following manner. The monochromator is scanned to an initial wavelength. This wavelength is typically 250 nm. However, one of the main goals of our experiment is to collect spectra which sample the ground state at low energies as low as 2,000 cm^{-1} above v=0 of the $\tilde{X}^1\Sigma_g^+$ state. DF spectra originating from different $\tilde{A}$ -state vibrational levels but which terminate on the same ground state levels will be recorded on slightly different monochromator positions. These differences in monochromator settings correspond to the differences in the term values for the intermediate rovibronic transitions. For example the vibrationless level ($V_0^0K_0^1$), excited via the $\tilde{A} \leftarrow \tilde{X}$ ${}^rQ_0(1)$ transition, has a term value of 42,209.3 cm^{-1}. Emission to the $\tilde{X}$ -state vibrational

levels at 2,000 cm^{-1} will be recorded at 250 nm. Whereas, the emission excited via ${}^{r}Q_0(1)$ of the $2_0^1 V_0^2 K_0^1$ level, with a term value of 45678.5 cm^{-1}, will be recorded at 230 nm. This difference in monochromator positions makes it difficult to compare directly two DF spectra which access the same $\tilde{X}$ -state energy. Each individual segment must have precise wavelength calibration, **relative** to the other segemnts. The paucity of meaningful relative (spanning 250-500 nm) wavelength calibrations, ±0.05 nm at 250nm is the source of a majority of the frequency errors associated with previous dispersed fluorescence experiments. In order to compare directly the DF spectra orginating from five to six different intermediate levels, these frequency errors must be minimized. The current experiment allows for better frequency and intensity calibration than was achieved previously. The procedures to accomplish this are explained in detail in the following sections.

At each monochromator position, two types of spectra are recorded. The dispersed fluorescence, which is detected on the ICCD, is recorded twice. A series of fluorescence spectra from the following frequency calibration lamps: neon, iron, thorium, uranium, argon, krypton, xenon, and mercury, are recorded.[9] The argon, krypton, xenon and mercury are termed frequency "pen" lamps and were purchased from Oriel. These lamps are powered by a variable Oriel DC power supply. Each lamp is operated at a particular current specified by Oriel. The fluorescence from neon, iron, and thorium is produced from hollow cathode lamps (HCL) purchased from Starna Cells. The neon fluorescence is produced from the HCL lamps containing a neon buffer gas. The HCL lamps are powered from a variable DC power supply set at approximately 100 volts. The series of frequency calibration spectra are used to

calibrate the acetylene dispersed fluorescence spectra. A calibration book has been assembled for all of the lamps listed above and is located in the main Field Group office.

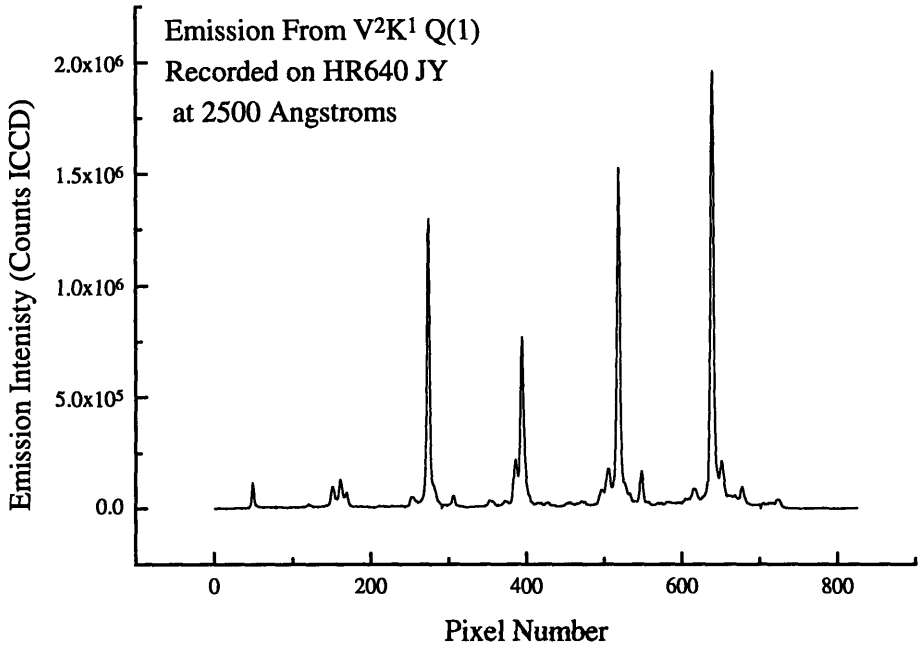

Figure 3.5a: The dispersed fluorescence from $2\nu_3$ K=1 Q(1). Recorded at 250 nm on the HR640 JY monochromator. The resolution in this segment is approximately 18 cm^{-1}. The corresponding $\tilde{X}$ -state energy is approximately 4,000 cm^{-1}.

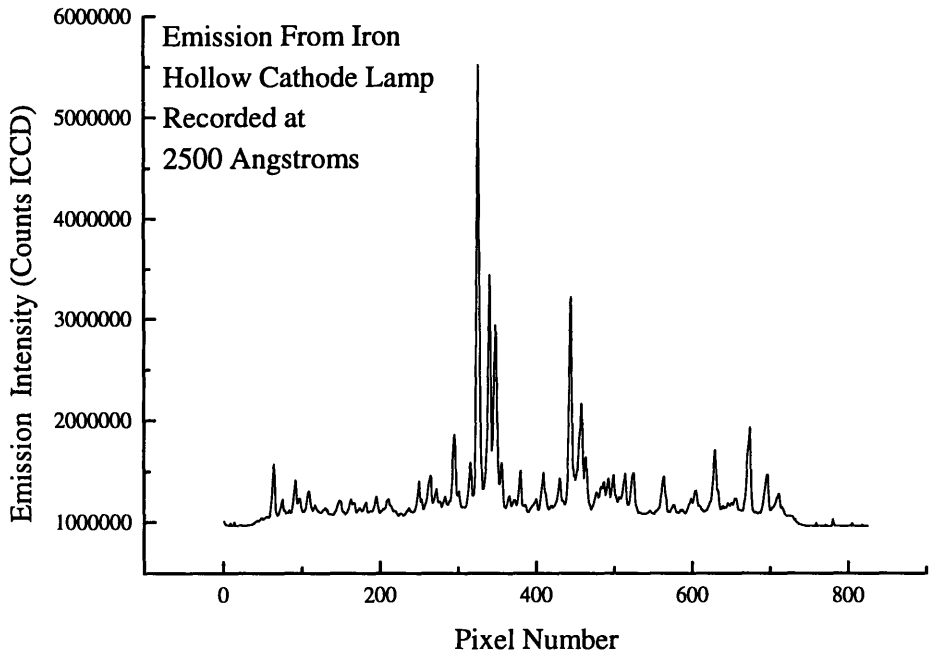

Figure 3.5b: The emission spectrum of Iron. Recorded at the same monochrometer position as in Figure 5a. The emission is produced from a iron hollow cathode lamp from Starna Cells. The DC lamp voltage was 100 V.

The following experimental parameters are typical for intermediate states with strong transition strengths. (The strong transitions have been classified as such from the absorption work by Watson.)[7] The intensifier of the ICCD is gated in our experiments. Typically, the intensifier is turned on for 1.5μs. The gate delay is adjusted to locate the fluorescence decay of acetylene, 200ns, in the center of the 1.5μs gate. The repetition rate of the excimer laser is typically 65 Hz. For an ICCD exposure time of 5 seconds a total of 3250 1.5μs exposures (65pulses/second * 5 seconds) are integrated. This process is repeated 30 times (called the accumulation number). After each of the 3250 1.5μs exposures, the integrated signal as a function of pixel position is added to the previously accumulated data. The choice of 3250

exposure is controlled by the repetition rate of the pump laser and the exposure time set by the software. The later parameter, exposure time, is frequently changed to optimize/increase the amount of integrated signal from the weaker emitting bands ($V_0^1K_0^1, 2_0^1K_0^1$). The maximum signal that the array can accumulate without saturation is 65,000 counts. Of course this signal is read and then discharged after each accumulation. Initial setup of the DF experiment includes initial DF scans at the wavelengths of maximum acetylene fluorescence. These scans are used to set the laser repetition rate, exposure, and accumulation times. The wavelength of maximum fluorescence intensity depends slightly upon intermediate state but generally is found at monochromator settings of 290-310 nm.

The reason for recording two spectra at each monochromator position (beyond being able to average the two spectra, becomes apparent only after observing the actual recorded data) is that the ICCD array is extremely sensitive to cosmic rays and scattered light. Often strong spurious peaks (only a pixel or two in width) can either mask small emission features from acetylene or masquerade as a normal feature of the DF spectrum. By comparing two spectra recorded separately, these spurious features can be identified and removed.

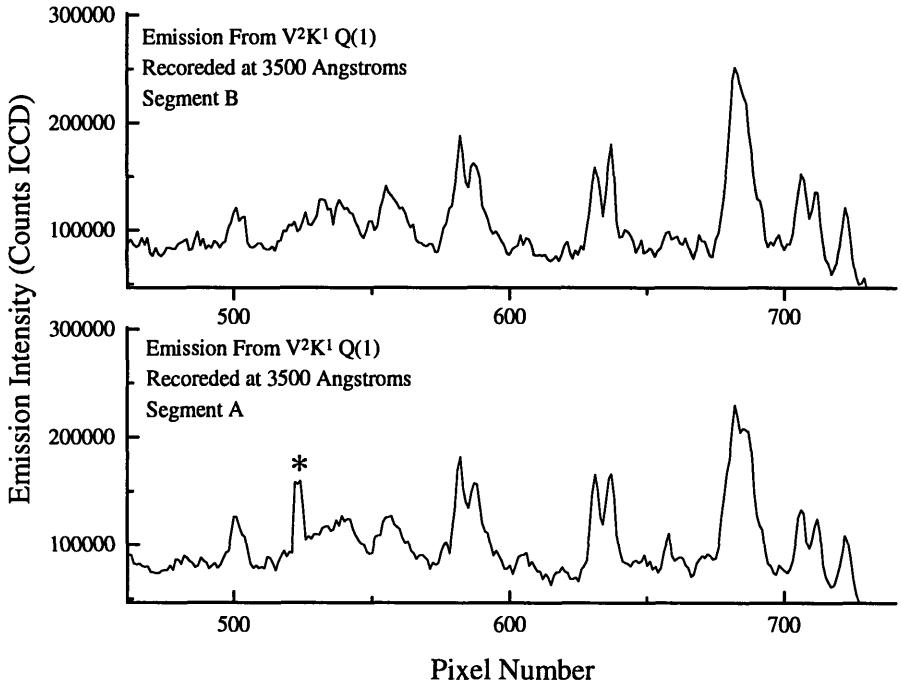

Figure 3.6: By comparing two emission spectra recorded at the same monochromator position, spurious features, indicated in Segment A by an asterisk, can be eliminated.

All of the data files recorded on the array are stored in binary under FILENAME.SPE. A binary to ASCII conversion program, SPE2PRN.EXE, has been written. The command line should read as follows:

SPE2PRN FILENAME.SPE

The program will write an ASCII file, FILENAME.PRN. These ASCII files are used in the initial calibration routines.

3.4 Frequency Calibration

3.4.1 Individual Segment Calibration

The frequency calibration spectra are recorded at the exact (the grating has not been rotated) monochromator position as the DF spectrum segment. This allows a calibration curve, wavelength as a function of pixel position, to be transposed onto the fluorescence spectrum. The frequency calibration curves are generated by a program named Calcurve. This program allows the user to load in a frequency calibration file, fit each emission feature in the displayed (intensity versus pixel position) spectrum to a Lorentzian lineshape, and enter a standard wavelength corresponding to the fit center position. This procedure is repeated until all of the identifiable features have been fit and a center wavelength has been entered for each. At this stage a plot of the center wavelengths versus center pixel positions can be generated and fit to an n^{th}-order polynomial function. For our experimental data we utilize a least-squares fitting routine to generate the parameters for a 1^{st} order polynomial function, see Figure 3.10.

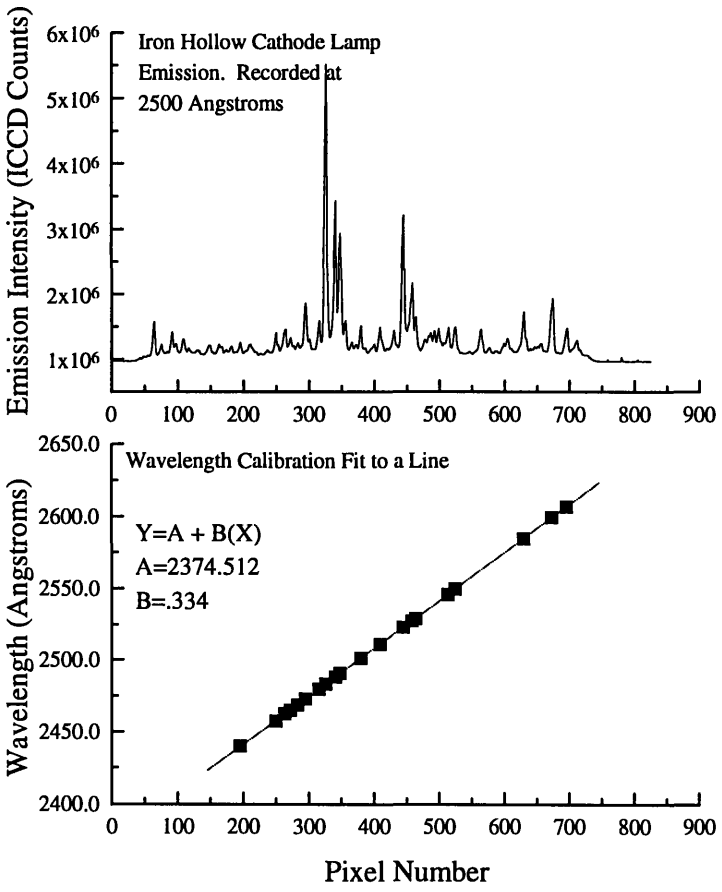

Figure 3.10: The top panel is an emission spectrum of an Iron Hollow Cathode Lamp. Emission peaks are fit and assigned a calibration center wavelength. The lower panel contains a plot of the center wavelengths versus their corresponding pixel position. These points are fit to a straight line. The parameters from this fit define the dispersion across this segment.

The dispersion (wavelength/pixel) is **nearly** linear across the (700X25 um) 175mm length of the array. The fundamental grating equation is given by[10]

$$\sin(\alpha) + \sin(\beta) = 10^{-6} * K * g * \lambda \qquad (3.1)$$

where α is the angle of incidence in degrees, β is the angle of diffraction in degrees, K is the diffraction order, the groove density (grooves/mm) is g, and λ is the wavelength of interest in nm. Linear dispersion, nm/mm, varies directly with cos(β).

$$d\lambda/dx = (10^6 \cos(\beta))/ (K*n*L_B) \qquad (3.2)$$

where the linear dispersion is the inverse product of the angular dispersion and the effective focal length, L_B, of the monochromator.[10] The HR640 JY has a 1.3nm/mm dispersion at 300 nm. The 700 active pixels in the array will cover approximately

$$700\text{Pixels}*.025\text{mm/pixel}=17.5\text{ mm} \qquad (3.3)$$

$$17.5\text{mm}*1.3\text{nm/mm} = 22.75\text{ nm} \qquad (3.4)$$

22.75 nm. It should be noted that the above calculation assumes that the dispersion is linear across the array. In fact, this is only approximately true. The linear dispersion for a wavelength that is not at the center of the ICCD array will modified by the cosine function of the following form:[10]

$$d\lambda_n/dx = (10^6 *\cos(\beta) *\cos^2(D))/K*g*L_B \qquad (3.5)$$

where D is the difference in angle of dispersion for the two wavelengths relative to a plane normal to the grating surface, see Figure 3.11.

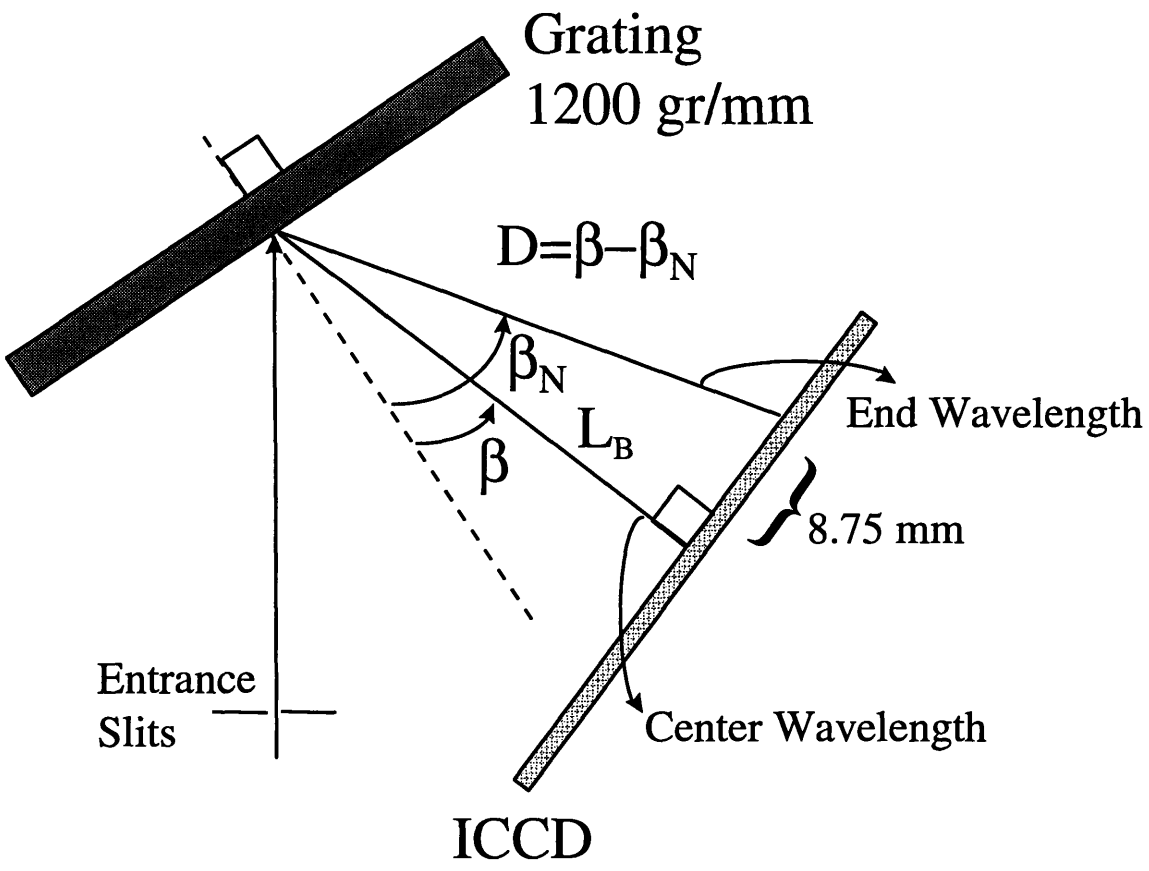

Figure 3.11: Schematic representation of the dispersion characteristic for wavelengths other than the center wavelength.

We can estimate the importance of the nonlinearity of the dispersion in the following manner.

The difference in the center position and the end of the active area of the array is 350 pixels.

$$350 \text{ Pixels} * 0.025 \text{ mm/Pixel} = 8.75 \text{ mm} \qquad (3.6)$$

$$D = \sin^{-1}(8.75\text{mm}/1000\text{mm}) = 5.02^0 \qquad (3.7)$$

$$\cos^2(5.02) = 0.99985 \qquad (3.8)$$

In reference to the center wavelength, where $\cos^2(D)=1$, the relative difference in dispersion at the ends of the array is only +/- 0.015%. Therefore, fitting each recorded DF segment to a straight line dispersion function produces calibration errors of only a few ten thousandths of an Å. Future calibration fitting routines could be improved by including the explicit cosine dispersion function for each individual segment.

The Calcurve program generates two ASCII files. One file contains the fit parameters needed to generate the calibration curve, Filename.CC. The other file, Filename.CP, contains a listing of all of the calibration wavelengths and the center pixel position (these are the x,y data used in the fitter). Each segment has an .CC and an .CP file. The .CP files are used in the calibration procedures used later to calibrate all of the segments together. The above procedure of fitting wavelength calibration features and generating calibration curves and positions is done at each monochromator position (for each recorded segment). The entire spectrum will consist of at least 10 monochromator positions. On average we use five different wavelength lamps at each setting, which has two major advantages. First, many of the lamps have features that are well resolved and isolated. This eliminates problems with fitting spectral calibration features which are actually several blended lines. Blended lines, shoulders, and general broadening can nonreproducibly distort the peak center position. Second, single calibration sources, such as an iron hollow cathode lamp, may not have appreciable emission in each of the spectral segments being recorded. Often one calibration lamp may have a dense and overlapped emission spectrum at a given wavelength while the majority of the others do not. The combination of the spectral lamps listed above gives approximately 12-20 well resolved spectral calibration features per 200 Å.

3.4.2 Baseline Functions

Each of the acetylene spectral fluorescence segments have an intrinsic DC baseline function due to the read out noise characteristics of the ICCD array.[11] This function must be subtracted from each segment. This baseline function is unique to each series of experiments. It is dependent upon exposure time, accumulation time, and cooling temperature. Typically, 4-10 blank scans are recorded for each set of experimental conditions. These can be averaged to form a baseline function.

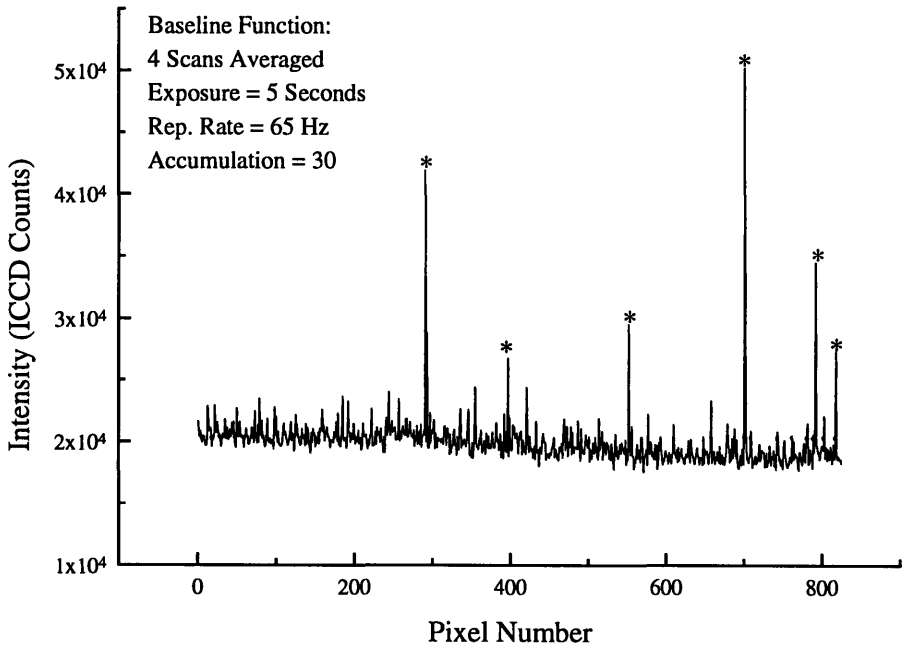

Figure 3.12: Four averaged baseline scans. The experimental parameters used are indicated. Many strong but artificial features are indicated by asterisk.

A closer view of the baseline function reveals several strong features across the array that have distinct patterns which appear in every baseline scan. However, most of the baseline

structure is not constant (i.e. intrinsic). Qualitative inspection of the baseline function reveals that the baselines are neither constant nor linear. There is a slight slope and curvature which occurs across the array. The general shape of the baseline is useful in correcting the individual data segments, see Figure 3.12. Removal of the baseline function eliminates small, >1%, localized (they occur only over 700 pixels), systematic (they occur in each segment) intensity errors. The baseline function is subtracted from each of the original data files, FILENAME.PRN, and the two .PRN files (we record at least two independent emission spectra at each monochromator setting) are averaged and saved as FILENAME.DAT. Note that this procedure eliminates only the baseline function which is due to the read-out-noise of the array. In addition, there appears to be an additional molecular intrinsic baseline function that occurs on each DF segment. This baseline is not constant and appears to have some structure. This will be addressed in Chapter 6.

3.4.3 Grand Calibration

All of the individual calibrated wavelength files generated by Calcurve are used to refine the wavelength calibration for all of the emission segments and to transpose the wavelength calibration onto the acetylene emission data. Using a program called Winnie, all of the calibration files containing the wavelength and pixel positions and the raw emission data are loaded for the final stage of wavelength calibration. The execution line for Winnie is as follows:

WINNIE Filename.TXT TermValue N <RET>

where n is the order of the grating (usually 1st or 2nd). The term value is for the intermediate used for that particular set of DF segments. Filename.TXT is an input text file with the following format:

Filename1.CP Filename1.DAT 1 1

Filename2.CP Filename2.DAT 1 1

Etc.....

where the Filename.CP is the calibration file generated from Calcurve. This file corresponds to the same monochromator position as the data, Filename.DAT. The last two columns are used to include or exclude a particular file from the grand calculation. The last column indicates whether the calibrated data file will be written, step four of Winnie. (See the text in the following paragraphs for an explanation of the different calibration steps.) The second-to-last column indicates whether the .CP file should be used in the grand dispersion fit, step two of Winnie. This feature becomes very valuable if a given DF segment has very poor wavelength calibration; the .CP can be excluded from the fit, but still receive the grand calibration function. That is, a segment at wavelength x that is not used in the grand calibration fit can still utilize the information about the dispersion at wavelength x generated from all of the other segments with different wavelengths. A segment can be corrupted when only one or two calibration points are available for that segment. By itself, the linear calibration of such a segment would be atrocious. But the purpose of the grand calibration procedure is to refine the calibration of each segment based on the calibration of *all of the segments*. In the collective, the calibration of such a segment becomes quite acceptable.

The first stage, of Winnie, is designed to correct for the overall dispersion characteristics of the monochromator. The program loads all of the .CP files (pixel number, wavelength) and fits the x,y data to a straight line. Using the parameters, slope and y-intercept, from the initial linear fit, the program calculates the middle pixel position in terms of wavelength. This value is called the middle segment position.

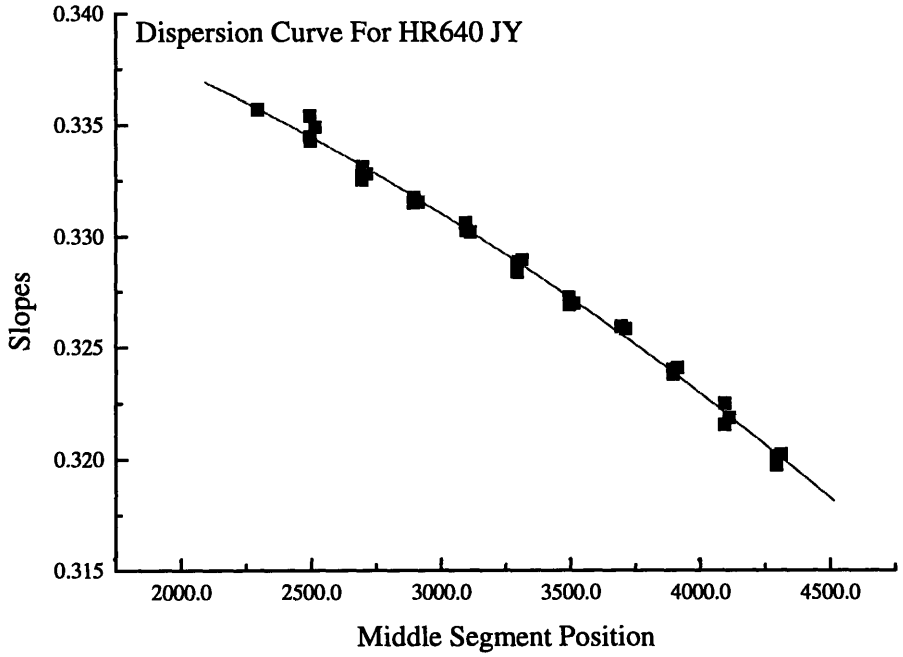

Figure 3.13: A plot of the slopes obtained from Calcurve versus the middle segment positions. The dispersion function is fit to a 2nd order polynomial function.

In stage two, the dispersion curve for the monochromator is obtained by plotting the slopes obtained from the linear fit versus the middle segment position, see Figure 3.13. The

linear dispersion of the central wavelengths will vary directly with a cosine function, see Equation 2. A power series expansion of the cosine function is $1-\frac{x^2}{2!}+\frac{x^4}{4!}-\frac{x^6}{6!}+\cdots$. Currently, the grand calibration fitting routine can only refine an n^{th} order polynomial. This is limited by the fitting program currently used. A 2^{nd} order polynomial fit is used to calculate a complete dispersion function. This function is used to refine the slope values at each middle segment position.

In stage three, the new slope values are used to refit the y-intercepts obtained from step one. At each stage of the calibration routine, graphics display the differences between the observed and calculated values. Winnie also writes several output files which contain all of the observed minus calculated values for every calibration point at each stage of the fitting process. The graphics and the output files are useful as diagnostic tools to monitor each stage of the calibration routine. As stated above, certain calibration files can be designated so that they will not be included in the fitting process of stage two, yet will receive wavelength calibration in the final stage. It becomes evident which files should and should not be included in the dispersion curve fitting by running an initial calibration routine with all files included in the fitting. Through a careful inspection of the output files, a series of outlier calibration points can be eliminated. These points lie more than 2σ away from the calculated curve, see Figure 3.14.

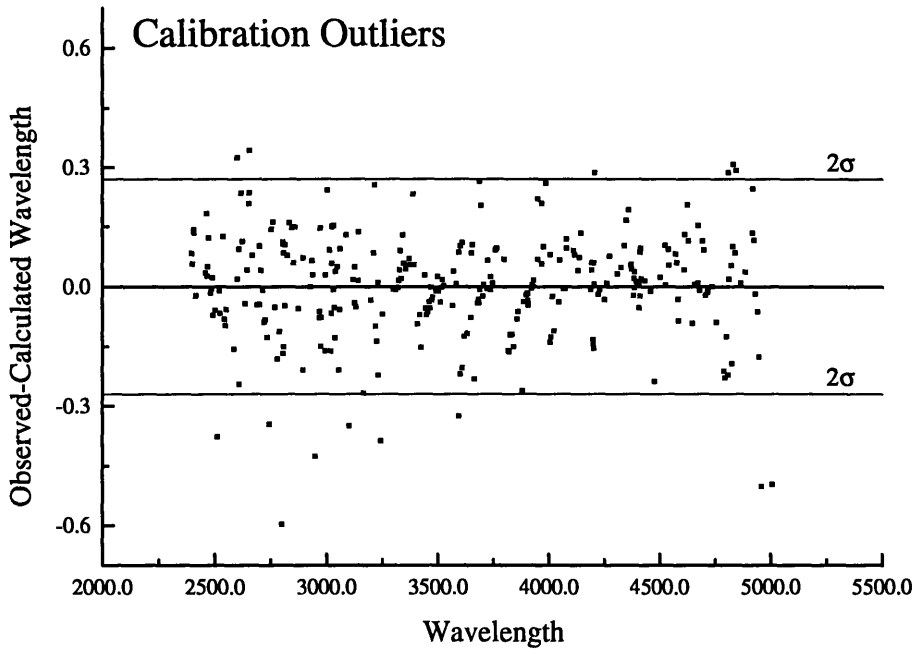

Figure 3.14: Plot of the difference in observed and calculated wavelengths for each segment. Calibration points outside of 2σ will be targeted for review and possible removal from the grand fitting procedure.

In stage four, an ICCD function is built. The ICCD function is necessary to correct for two effects. First, the dispersion for each segment although nearly linear, is a slightly non-linear function. Second, the ICCD array is an imperfect device. Each pixel is not exactly 25 μm X 25 μm. Some pixels are lager and others are smaller. The ICCD function is determined by plotting the calculated differences in the pixel positions of the observed wavelength standards minus the calculated wavelength standards versus pixel position, see Figure 3.15.

$$\text{ICCD}(\Delta\text{pixel, pixel position}) = \sum_{i=1}^{N} observed\lambda_{N}(pixel_{N}) - calculated\lambda_{N}(pixel) \quad (3.9)$$

For example, a wavelength standard of 2537.13 Å was observed at pixel number 350. The refined fit parameters, slope and y-intercept, calculate 2537.69 Å to be at pixel number 350. Using the refined fit parameters, the calculated pixel position for 2537.13 is now 349.33. The difference at pixel 350 is 0.67 pixels. This procedure is completed for each calibration point

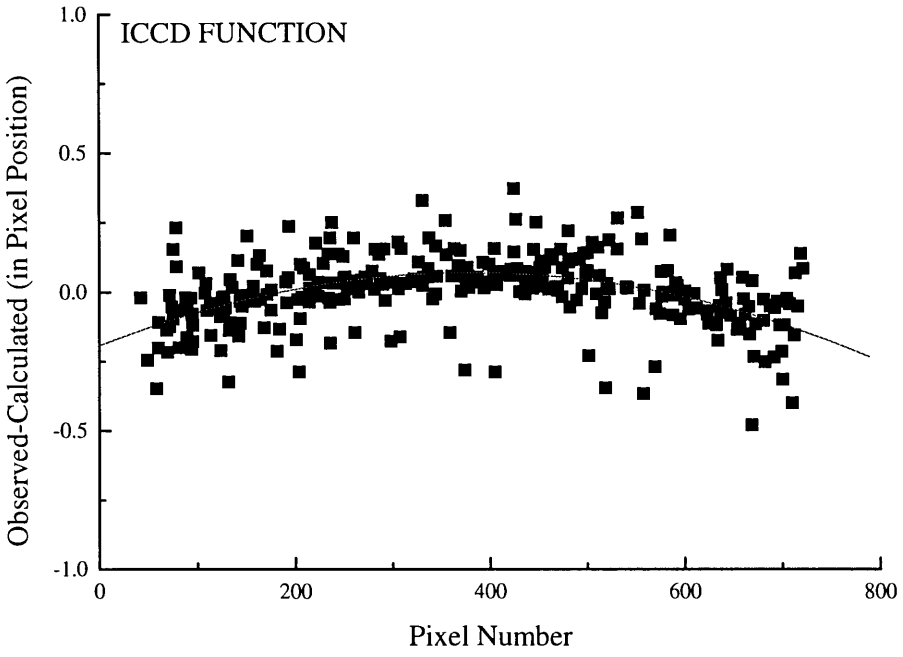

Figure 3.15: A plot of the ICCD function. This function is for the DF spectra recorded on the HR640 JY. There is very little pixel error in the center of the array. The largest error is approximately 0.25 pixels. This corresponds to ~1 cm^{-1} error.

for each segment. This process will reveal all of the systematic errors in the pixels. A spline fitter is used to generate a smooth ICCD function using all of the calibration points from all segments. Note, that a large error in the ICCD function, which could have resulted from using a linear fit instead of cosine function would have created wavelength dependent errors on the

order of 0.015%. The main reason for the observed distribution about the smooth ICCD function is due to misasigned peaks and/or the limititations of fitting the peak centers in Calcurve.

The final stage of the program is designed to transfer (transpose) the calibration functions onto the acetylene fluorescence spectra. For each pixel position a wavelength is calculated using the parameters and ICCD correction functions obtained from steps one through three. Each of the wavelength standards are reported in units of wavelength in air. The original numbers **do not** contain the air to vacuum correction. (All frequencies are reported in terms of cm^{-1} in vacuum) All of the wavelengths need to be corrected to reflect the correct vacuum cm^{-1} values. An iterative method is used to calculate the conversion from air to vacuum cm^{-1} uses Edlén's formula[12,13]

$$\sigma_{vac} = \left(\frac{1}{n\lambda_{air}} \right) \tag{3.10}$$

where n is the index of refraction given by

$$n = 1 + 6432.8 \times 10^{-8} + \frac{2{,}949{,}810}{146 \times 10^{8} - \sigma_{vac}^{2}} + \frac{25{,}540}{41 \times 10^{8} - \sigma_{vac}^{2}} \tag{3.11}$$

After wavelength-to-frequency conversion, the acetylene fluorescence spectrum is referenced to the term value for that specific intermediate state (term value-fluorescence frequency = $\tilde{X}$-state internal energy). The $\tilde{X}$ state energies, $T(\tilde{X})$, are calculated by

$$T(\tilde{X}) = T(\tilde{A}) - 10^{-7}/\lambda_{Vac}, \tag{3.12}$$

where $T(\tilde{A})$ is the $\tilde{A}$-state term value and λ_{vac} is the corrected wavelength in vacuum. Finally, the program outputs calibrated ASCII data files for each fluorescence segment, Filename4.DAF.

3.5 Concatenation

As stated above, each segment covers approximately 25.0 nm. The individual segments, recorded at 20.0 nm intervals will have a 2.5 nm overlap with the two adjacent segments. For example, the 250.0 nm segment will overlap the 270.0 nm segment by 2.5 nm. One of the last stages involved in the calibration of the data is to concatenate all of the individual segments into one complete spectrum. All of the .DAF files output by Winnie are loaded into a program called BALOO. The command to run BALOO is :

BALOO Concatenatedfilename.DAF List.DIR <RET>

The concatenatedfilename.daf will contain the final concatenated spectrum. LIST.DIR is a text file with the following format:

Segment1Filename.daf 1

Segment2Filename.daf 1

Etc.....

The first column contains the segment filenames to be loaded. The second column is used for intensity normalization of each segment. As mentioned above, the total ultraviolet emission is integrated while each segment was recorded. This information is used to normalize the relative intensities for all of the segments. The normalization factors are loaded as the second column of the LIST.DIR file (indicated by 1's).

Once loaded there are four sections to the concatenation routine. Currently, there is no way to exit temporarily the program until all four sections are completed. This process can take most of a day. The first stage of the concatenation program is designed for additional baseline manipulation. The program allows the user either to load a baseline file or to define a baseline function at each segment. If a baseline function is created for a given segment, the baseline function is saved as SegmentFilename.PIX. After completion of a baseline at one segment, the next segment emission spectrum is loaded. The user can subtract the baseline created for the previous section, load a different function, or define a new baseline. Previously, we had subtracted a baseline function which was created by recording baseline experiments on the ICCD and we no longer use this part of the concatenation program. It is conceivable that the recorded fluorescence spectrum may have additional molecular emission features, such as a broad continuum, that the previous baseline subtraction could not account for. For this reason, additional baseline subtraction is available at this point in the concatenation program. Obviously, the user must be very confident that the broad emission is not due to the molecule being investigated before subtracting an additional baseline function from each spectral segment. The additional baseline subtraction may become more important in DF experiments which use photolysis, ablation, or other methods of generating a transient species. In those types of DF experiments there is a greater probability of simultaneously recording the emission from the intended species as well as those of several other molecular species.

The second stage allows the user to translate or delete points in each segment spectrum. When creating the .DAT files, we were able to delete spurious spectral features by

comparing multiple spectra recorded at the same monochromator position. In this stage we can extract sharp features which appear in all of the spectra recorded at the same monochromator position. For example, scattered light from the laser fundamental and frequency doubled laser beams can be removed.

The third stage allows the user to scale the relative intensities of individual segments. This is extremely useful when no power normalization data is available. More importantly, the entire spectrum can be viewed as a whole, all 20,000 cm^{-1}, and fine adjustments to the ultraviolet power normalization, from LIST.DIR, can be conducted. These adjustments are only on the order of 1-2 % of the total intensity of each segment.

The last stage of the program allows the user to correlate all of the segments of the spectrum. All of the segments are put on the same x grid by using a "Numerical Recipes" interpolation routine.[14] The user can define the exact grid size and spacing. Prior to concatenating the segments, the user must remove the data that is distorted by the edges of the intensified region. All of the data recorded on the extremes of the array must be removed because there is no intensifier in this region. In addition to those pixels, several pixels in the intensified region must also be removed because of edge effects. The first few pixels at both edges of the intensifier always exhibit a lower intensity response than the rest of the intensified pixels. For our current array, we have turned off the first and last 100 pixels (there is no intensifier in this region). We only record 825 pixels. (This helps to speed up the read/write process on the array.) Of these central 825 pixels, pixels 1-64 and 706-825 must be removed owing to lack of intensifier and/or edge effects. This leaves each useable segment with 641 pixels. After eliminating the ends of each segment, there is an approximately 1.5 nm

overlap with the adjacent segments recorded on the JYHR640, see Figure 3.16. The overlap segments will be averaged and correlated with the remaining segments. This final stage completes the concatenation of one DF spectrum.

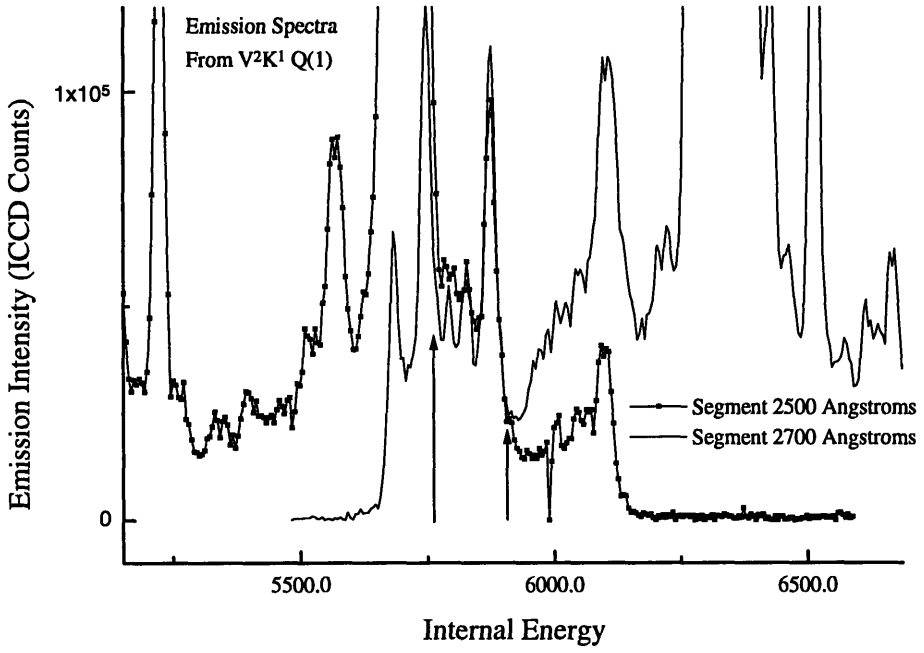

Figure 3.16: Two overlapping emission segments. The concatenation program will average the sections located between the two arrows. The end of the 250.0 nm data file and the beginning of the 270.0 nm data file are removed because of edge effects.

3.6 Relative Intensity Corrections

After frequency calibration and concatenation, the DF spectrum can be corrected for intensity. An intensity response curve for each monochromator has been recorded and calibrated in a manner that is similar to that described above. We use a standard of spectral irradiance from Optronic Labroratories, 200 Watt quartz tungsten (OL220M M-877). Figure 3.17 displays the observed intensity response curve for the JY HR640 monochromator,

collection optics, and ICCD array. Figure 3.18a displays the calculated intensity emission from the standard irradiance lamp. The relative intensity response function for the instrument, collection optics and detector, is obtained from the ratio of the observed and calculated intensity response, see Figure 3.18b. Notice that at 250 nm in Figure 3.18b, there is a slight increase in the instrument response. Initially this seemed abnormal because the grating response efficiency, see Figure 3.19, was known to be small and exponentially decreasing with decreasing wavelength. However, the ICCD array has an intensifier which is enhanced for short wavelength response. Figure 3.18c displays the plots of radiant sensitivity and quantum efficiency for the ICCD array. The intensity enhancement at 250 nm is real and due to the ICCD array. It is important that these curves are used to normalize the relative intensity changes that occur over the 20,000 cm^{-1} of each recorded DF spectrum. For emission to 16,000 cm^{-1} in the $\tilde{X}$ state of acetylene, the differences in $\tilde{A}$-state term values could cause intensity errors as large as a factor of 2-3 for DF spectra which are not intensity normalized.

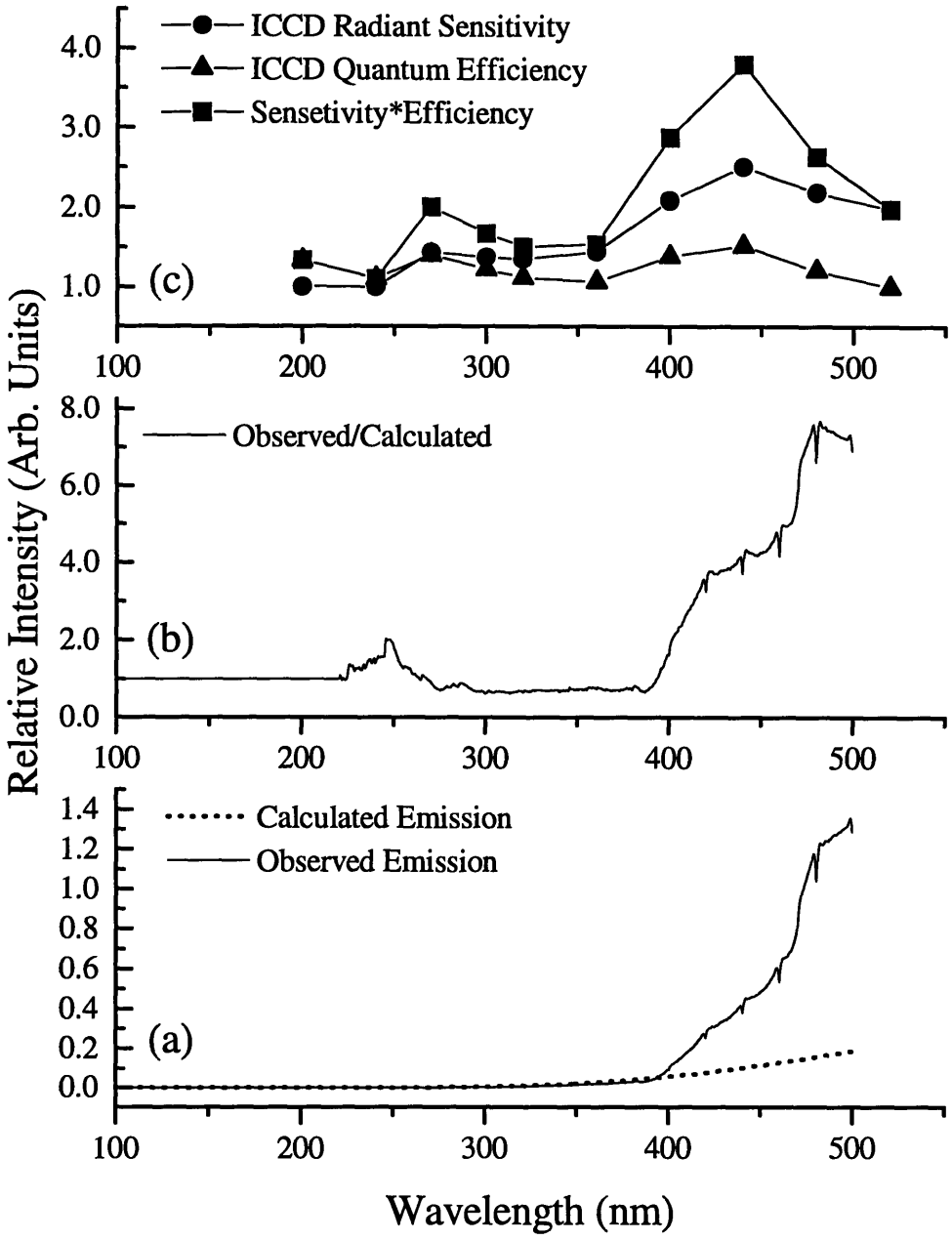

Figure 3.18: Plot (a) displays the observed and calculated irradiance spectrum from a 200 Watt Quartz tungsten lamp. Plot (b) display instrument function as determined from the ratio of the observed and calculated irradiance spectra. Plot (c) display the sensitivity and quantum efficiency response from the ICCD array.

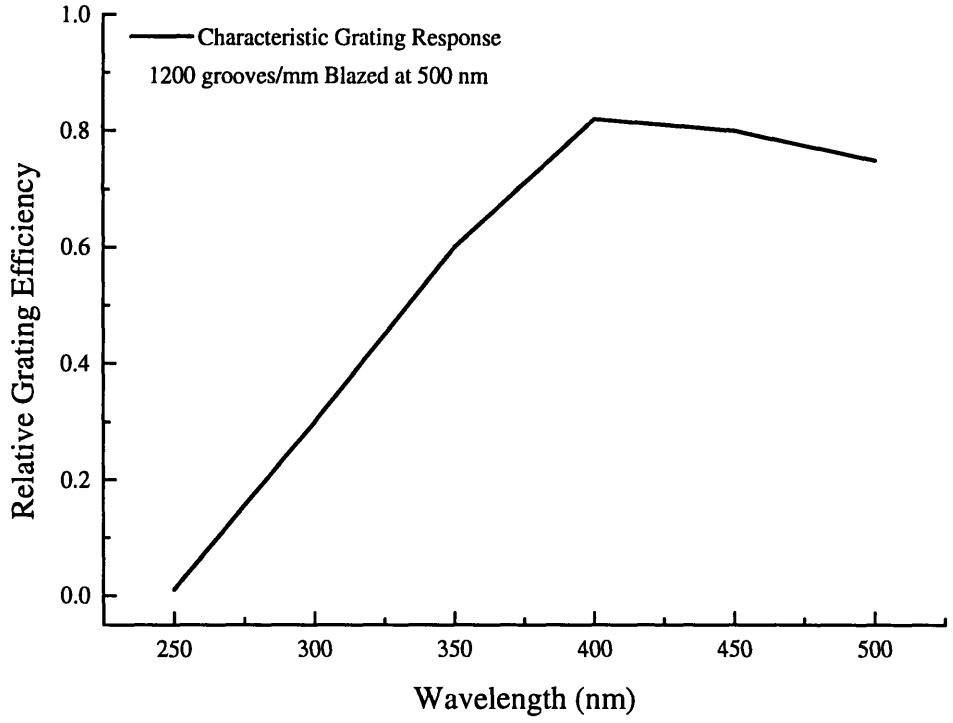

Figure 3.19: Schematic representation of the efficiency response of a classically ruled grating, 1200 grooves/mm blazed at 500 nm.

3.7 Conclusion

We have designed a dispersed fluorescence experiment to record high quality spectra of the $\tilde{A}^1A_u \rightarrow \tilde{X}^1\Sigma_g^+$ acetylene transition. Use of an intensified charge coupled device enables us to quickly record and calibrate DF spectral segments over a 20,000 cm^{-1} energy region. We have documented how frequency and intensity calibration should be applied to each DF spectral segment and have provided the essential details describing the concatenation of the spectral segments. The DF method described here will prove to be extremely instrumental in developing a better understanding of the molecular dynamics of acetylene.

The following are suggestions for future improvements in recording DF spectra. First, the spectral segments should be recorded every 10 nm on the Jobin-Yvon monochromator and every 5 nm on the Spex monochromator. This creates a better segment overlap region. Second, a cosine fitting function could be used to calibrate the individual segments and the whole DF spectrum.

3.10 References

1. D.M. Jonas, Ph.D. Thesis, Massachusetts Institute of Technology, 1991.

2. Lambda Physik Laser Dye catalog, (1995).

3. Lambda Physik FL2002 or 3002 Dye Laser Manual, (1988).

4. J. Cariou, P. Luc. *Atlas du Spectre d'Absorption de la Molecule de Tellure.* Editions du C.N.R.S., Orsay (1979).

5. S. Gerstenkorn, P. Luc. *Atlas du Spectre de la Moleculair de l'iode.* Editions du C.N.R.S., Orsay (1979).

6. The exact temperature setting of the tube furnace is dependent upon the fundamental wavelength, λ.

7. J.K.G. Watson, M. Herman, J.C. van Craen, and R. Colin, *J. Mol. Spectrosc.* **95**, 101 (1982).

8. M. Herman, *Acetylene:* $\tilde{A} \leftarrow \tilde{X}$ *Transition Frequencies*, Private Communication.

9. Emission wavelengths can be obtained from the Massachusetts Institute of Techology Wavelength Tables.

10. ISA Jobin-Yvon and Spex, *Guide to Spectroscopy*, New Jersey (1996).

11. Princeton Instruments Inc., *ICCD Users Manual*, PI, New Jersey (1994).

12. B. Elden, *J. Opt. Soc. Am.*, **43**, 339 (1953).

13. NBS Monograph III, *Table of Wavenumbers*, US Government, Washington D.C. (1960).

14. W.H. Press, B.P. Flannery, S.A. Teukolsky, W.T. Vetterling, *Numerical Recipes: The Art of Scientific Computing*. Cambridge University Press, New York, NY (1991).

Chapter 4: Numerical Pattern Recognition: Polyad Zero-Order Energies and Franck-Condon Factors for $^{12}C_2H_2$ $\tilde{A}\ ^1A_u \rightarrow \tilde{X}\ ^1\Sigma_g^+$ Emission

4.1 Introduction

A slightly modified form of this chapter will be submitted for publication in the *Journal of Chemical Physics*. Experimental and theoretical work continues with the goal of developing a compact, scalable, and transferable understanding of molecular dynamics at high vibrational excitation.[1,2] Experimental results have demonstrated that the short-time molecular dynamics in acetylene are controlled by a set of eight anharmonic resonances.[3-8] All of the known anharmonic resonances can be assembled into an effective Hamiltonian model. The block diagonalized H^{eff}, in which each block possesses a unique set of values of the conserved quantum numbers, $[N_s,N_{res},l,g/u]$, has been discussed in recent work.[3-8] Recently, a refined fit of the pure bend anharmonic coupling constants, included the pure bending polyads [N_s=0, N_{res}< 14, l=0 and 2,g] obtained from experimental dispersed fluorescence (DF) spectra and infrared absorption data. The refined H^{eff} model has been shown to be quite successful in reproducing the observed pure bend polyads at E_{vib} < 10,000 cm^{-1}.[8] This strongly supports the usefulness of the [N_s, N_{res}, l,g/u] polyad model in describing the molecular dynamics on the $\tilde{X}$ state of acetylene for different classes of zero-order bright states. Our goal is to combine the predictive powers of the H^{eff} model and our ability to extract polyad spectral patterns to help elucidate the dynamics at higher vibrational energies, E_{vib}>10,000 cm^{-1}.

The ability of our H^{eff} model to specify the vibrational eigenstate character at high bending excitation provides an important insight into the chemical dynamics known as

intramolecular vibrational redistribution (IVR). The dominant vibrational character assignments are simplified by the structure of the H^{eff} and the zero-order states accessed in our DF spectra. By comparing several DF spectra, preliminary vibrational assignments have been made up to $E_{vib}\approx12{,}000\ cm^{-1}$. The nature of the acetylene $\tilde{A}\,^1A_u \rightarrow \tilde{X}\,^1\Sigma_g^+$ transition, with optical selection rules, $\Delta J=0, \pm1$ and $\Delta K= | K'-l| = \pm1$,[9] and the primary allowed Franck-Condon activity in CC stretch, ν_2, and *trans*-bend, ν_4, when combined with the definitions of the polyad quantum numbers, leads to a simplification of the polyad structure. This results, to a good approximation, in a single primary zero-order bright state (chromostate) per polyad! Therefore, the acetylene polyads, $[N_s,N_{res},l,g]$ are born from a distinct set of chromostates, all of which are composed of $(n\nu_2,m\nu_4)$, where, for any given n (n=0,1,2,3...), m can have values of 0,2,4,6.....etc. This simplification presents a unique opportunity to gain insights into the molecular dynamics of acetylene. By organizing the information from the polyad patterns into specific progressions in the two Franck-Condon (FC) active modes, the dynamics can be systematically surveyed and the H^{eff} model refined. The power of this technique is evident in the insight gained from the pure bending progressions, $(0, m\nu_4)$, and their use in honing our understanding of the low energy molecular dynamics.[3,4,7,8] Future work will be directed at a more global refinement of the H^{eff} model for all observed $(n\nu_2, m\nu_4)$ progressions.

During the course of refining the H^{eff} with the pure bend progressions, several discrepancies were noticed between the eigenvalues and eigenvectors of the H^{eff} and the experimental spectra, see Figure 4.1.[8] Independent calculations by Sibert also displayed a discrepancy between the predicted and observed density of states for the pure bending

polyads.[10] They concluded that the discrepancy in the density of states could be resolved with the addition of the l=2 components. While this assumption may account for some of the difference in the density of states, the resolution of the dispersed fluorescence data used to extract the pure bending polyad energy positions was not sufficient to resolve **all** of the l=0,2 components. For the discrepancies noted by Sibert *et al.* and Herman *et al.*, it is probable that the additional features in the spectra assigned by eye belong to partially overlapped $N_s \neq 0$ polyad patterns that had been incorrectly identified as belonging to the pure bending N_s=0 polyads.

The polyad features are extracted and assigned by utilizing intra- and inter-polyad intensity differences which occur between several dispersed fluorescence (DF) spectra which originate from different $\tilde{A}$-state vibrational levels but which terminate on the same $\tilde{X}$-state levels. This assignment process is often complicated by overlap between adjacent polyad patterns and is limited by the quality of the recorded DF spectra. Initial pattern recognition techniques, which were performed manually by eye, were extremely valuable in providing initial insights into the qualitative molecular dynamics at $E_{Vib} < 10{,}000$ cm^{-1}.[3,4] However, most of the quantitative information, polyad intensities, line positions, and Franck-Condon factors, derived from previous pattern recognition was hampered by human error and lack of sufficiently high quality DF spectra.

Our research group has developed a statistical pattern recognition technique, based on the "extended cross correlation (XCC)".[11,12] Recent results have demonstrated that the technique is able to identify and separate complex patterns which occur in multiple molecular spectra

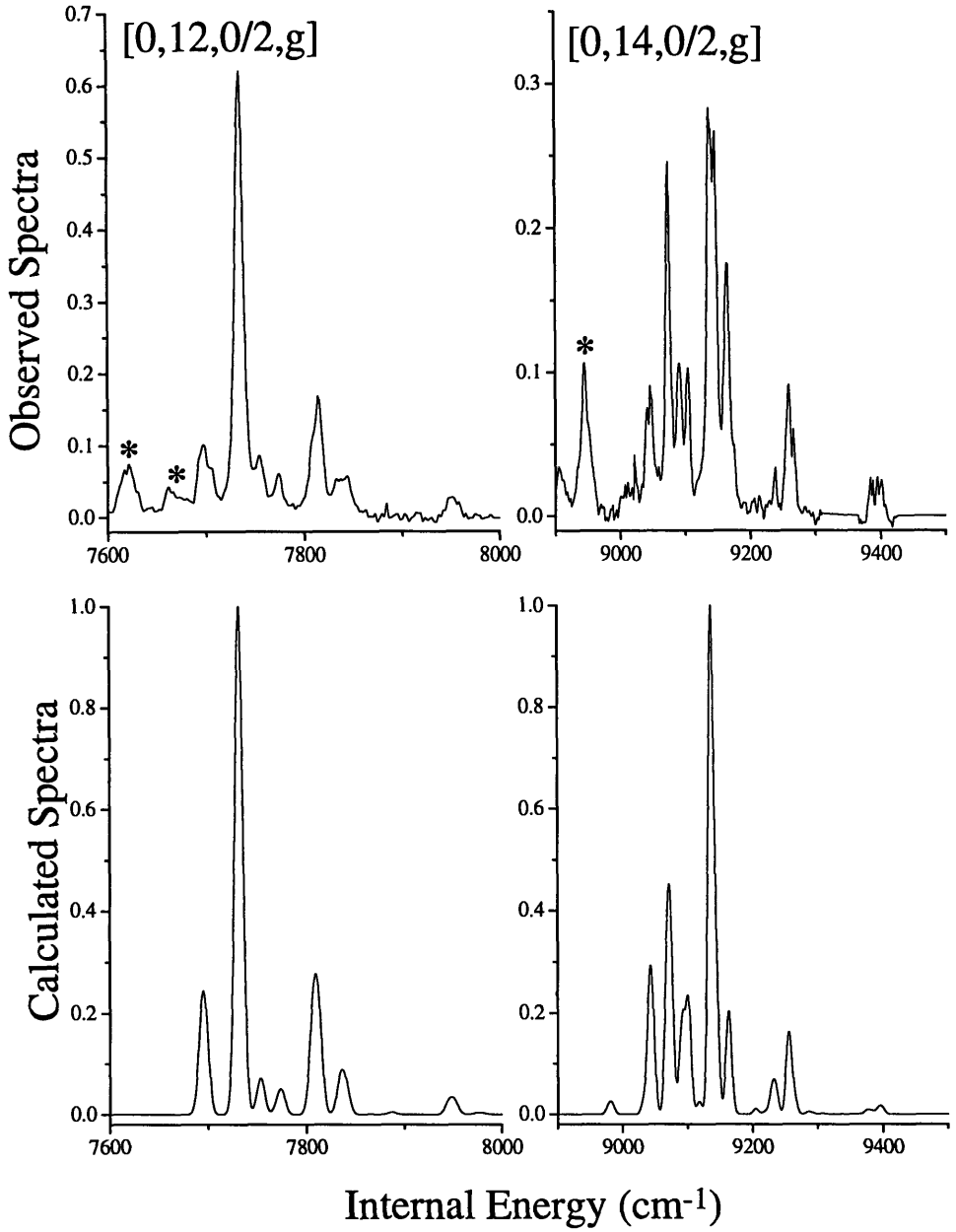

Figure 4.1: The top row displays observed polyad patterns extracted by eye from the $V_0^0K_0^1$ DF spectrum. The bottom row displays the calculated spectrum using the refined Hamiltonian from 8. The asterisks denote several features which were assigned to the observed polyads but are not present in the calculated polyads.

with no *a priori* knowledge about the nature or even existence of patterns, as encoded in the H^{eff}. This is the first in a series of chapters where I will demonstrate the usefulness of statistical pattern recognition for extracting the spectral energy and intensity information contained in the polyad patterns in acetylene.

This robust and unbiased XCC process reduces the ambiguity about previously assigned polyads and identifies several new spectral features. This is only feasible because we have been able to record and accurately calibrate, in terms of both frequencies (± 0.4 cm^{-1}) and relative intensities ($\pm 20\%$), a series of highly redundant data sets containing detailed information about the same $\tilde{X}$-state vibrational eigenstates. The application of the XCC to this data set enables *all* spectral patterns to be identified. Most of these patterns can be assigned a zero-order vibrational character based upon the H^{eff} model. Frequency and intensity information from the polyad patterns can be used to obtain deperturbed experimental Franck-Condon factors and deperturbed energy positions of the different zero-order bright states (ZOBS) of the acetylene $\tilde{A}\,^1A_u \rightarrow \tilde{X}\,^1\Sigma_g^+$ transition.

In this Chapter we will present the analysis of $\tilde{X}$-state polyads at $E_{vib} < 12{,}000$ cm^{-1}. The XCC numerical pattern recognition technique is used to extract polyad patterns from high (7-8 cm^{-1}) and low (15-18 cm^{-1}) resolution dispersed fluorescence spectra originating from five different $\tilde{A}$-state vibrational levels, see Figure 4.2. Once each polyad pattern is identified, empirical values of the Franck-Condon relative intensities and the energy positions for the zero-order bright states (ZOBS) (nv_2, mv_4) are derived. This information will be valuable in future refinements of the H^{eff} model for $N_s>0$ polyads and as a basis for direct comparison of experimental and *ab initio* Franck-Condon calculations for a linear $\leftrightarrow$ bent

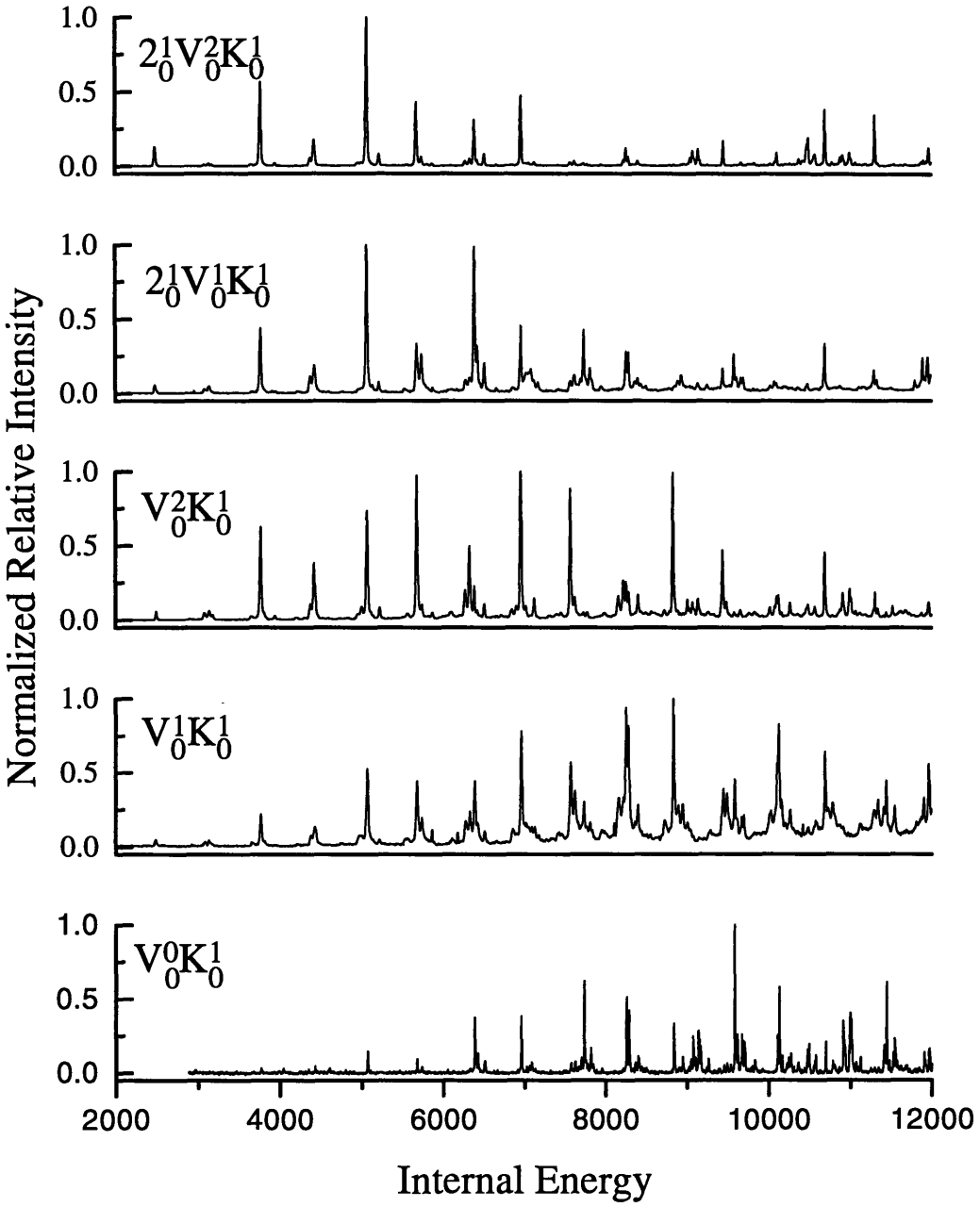

Figure 4.2: Five different DF spectra were excited via the ${}^rQ_0(1)$ transition. Each spectrum originates from a different $\tilde{A}^1A_u$ vibrational level but terminates on the same group of $\tilde{X}^1\Sigma_g^+$ rovibrational levels.

transition. The key obstacle for high E_{vib} Franck-Condon information from experiment is separation of Franck-Condon effects from IVR effects. Here, by working with the entire polyad as illuminated by a single ZOBS, rather than single eigenstate transition intensities, all of the IVR effects are suppressed. We eliminate the properties of the IVR effects by extracting one *deperturbed* ZOBS from each polyad.

4.2 Experimental

Chapter 3 contains a complete description of the dispersed fluorescence (DF) setup and data analysis. This section includes the additional details which pertain to the DF spectra recorded for numerical pattern recognition.

The high and low resolution DF spectra, which terminate on the $\tilde{X}\,^1\Sigma_g^+$ ground electronic state of acetylene-h_2 originate from five different vibrational levels of the $\tilde{A}\,^1A_u$ first excited singlet electronic state see Figure 4.2. Term values for the five intermediate levels are found in Table 4.1.

Table 4.1: $\tilde{A}\,^1A_u$ State Term Values[13]

$Q(1)\ V_0^0\ K_0^1$	$Q(1)\ V_0^1\ K_0^1$	$Q(1)\ V_0^2\ K_0^1$	$Q(1)2_0^1\ V_0^1\ K_0^1$	$Q(1)2_0^1\ V_0^2\ K_0^1$
42211.55 cm^{-1}	43260.15 cm^{-1}	44291.45 cm^{-1}	44646.54 cm^{-1}	45678.50 cm^{-1}

125 mJ of the 308 nm output of a XeCl excimer laser, run at 65 Hz, was used to pump a grating-tuned dye laser (Lambda-Physik FL2002) containing either coumarin 450 or 440 dye. The fundamental dye laser beam was frequency doubled in a β–BBO crystal to produce 1 mJ of tunable, 230-215 nm, radiation. The residual fundamental and doubled laser light were spatially separated by a series of 60° prisms. The residual fundamental laser beam is passed through a frequency calibration cell containing $^{130}Te_2$. To record the DF spectra, the dye laser

output was locked on the ${}^{r}Q_0(1)$, $J'_{Ka,Kc} = 1'_{1,0}$ line of the $V_0^1K_0^1$, $2_0^1V_0^1K_0^1$, $V_0^2K_0^1$, and $2_0^1V_0^2K_0^1$, vibrational bands of the $\tilde{A}\,{}^1A_u \leftarrow \tilde{X}\,{}^1\Sigma_g^+$ transition. (V represents the *trans*-bending mode, ν_3' in the $\tilde{A}$ state and ν_4'' in the $\tilde{X}$ state, and 2 represents transitions in the CC stretch.) Typically, a static gas cell is charged with 1 to 5 Torr of 99.8% pure acetylene-h_2 (Matheson), purified by several freeze (77K)-pump-thaw (300K) cycles.

For the low-resolution DF spectra, the total spontaneous emission is imaged by *f*/5.8 fused silica optics onto the entrance slit of a Jobin-Yvon HR 640mm monochromator equipped with a classical grating, 1200 gr/mm blazed at 500nm. The slit width of ~100 μm corresponds to ~18 cm^{-1} resolution in first order at 350 nm. For the high-resolution DF spectra, the total spontaneous emission is imaged by *f*/10.0 fused silica optics onto the entrance slit of a Spex 1802 1000mm monochromator equipped with a classical grating, 1200 gr/mm blazed at 500nm. A slit width of ~50 μm corresponds to ~7 cm^{-1} resolution in first order at 350 nm. The total spontaneous emission is also collected by *f*/1.7 fused silica optics and imaged through a Schott glass filter (UG11 or BG3) onto a solar blind photomultipler tube (PMT) (Hamamastu R166UH). The PMT signal is averaged on an oscilloscope (LeCroy 6903). This averaged signal is used to normalize the DF spectral intensities, see Chapter 3 for details of this procedure.

The protocol for recording and calibrating DF spectra has been modified slightly, see Chapter 3 and References 3 and 4. Briefly, the spontaneous emission is dispersed onto a Princeton Instruments Intensified charge coupled device (ICCD) Model1024-M059413. The array has 256 x 700 active pixels. Typically 97,500 laser shots are averaged on the array for each DF segment. The number of laser shots which are averaged on the array depends on the

laser repetition rate and ICCD exposure times. These are adjusted to increase the signal-to-noise of the more weakly emitting intermediate states. The DF spectra are recorded in overlapping segments. The segments for the low-resolution DF spectra are recorded in first order with 200 Å intervals from 2300-4900Å. The high-resolution DF spectra are recorded in second order with 100 Å intervals from monochromator setting of 4600-7200 Å (which corresponds to 2300-3600 Å). Each of the overlapping segments has at least 20 Å in common with both of the two adjacent segments. The exact amount of overlap depends on the grating position. For every monochromator position (each segment) two types of scans are recorded. First, the dispersed emission spectrum is recorded twice. By comparing multiple copies of the same segment, spurious noise spikes (e.g. cosmic rays) can be identified and removed. These scans are then averaged to give the final DF spectrum for that segment. Second, spectra of a series of wavelength calibration lamps, iron, neon, mercury, krypton, argon, and xenon, are recorded.

Calibration of the DF segments consists of six steps. First, a baseline function, indicative of the array DC offset, is subtracted from each segment. Second, the individual segments are calibrated using the spectra of the calibration lamps which were recorded for that segment. Third, all of the calibration segments are compared and refined to eliminate systematic errors. The refined calibration is applied to each DF segment. Fourth, the $\tilde{X}$ state energies are calculated by $T(\tilde{X})=T(\tilde{A})- 10^{-7}/\lambda_{Vac}$, where $T(\tilde{A})$ is the $\tilde{A}$-state term value and λ_{Vac} is the corrected wavelength (cm) in vacuum. Fifth, the intensity of each segment is normalized to the integrated undispersed spontaneous fluorescence intensity. Sixth, once calibrated, the individual segments are concatenated to produce a complete DF spectrum.

The relative intensities of the DF spectra can be normalized, corrected to account for wavelength dependence of the grating and ICCD response, by an absolute intensity responsivity function. The broad band emission from an Optronics Labotratories standard of spectral irradiance lamp (OL 220M, M877) is recorded and calibrated in the following manner. The intensity lamp is placed on the same optical axis as the collection optics/monochromator system used to record acetylene DF spectra. The broad band emission is imaged onto the entrance slits of the Jobin-Yvon monochromator and recorded on the ICCD in overlapping segments and frequency calibrated in the same manner as the acetylene DF spectra. The resulting absolute intensity response curve contains information about the true instrument response for each monochromator, see Chapter 3. Neglect of this intensity function will result in relative intensity errors in the DF spectra, which adversely affects the reported Franck-Condon Factors. For example, over the ~20,000 cm^{-1} E_{vib} span of a typical acetylene DF spectrum, neglect of this correction will result in relative intensity errors up to a factor of two. The maximum relative intensity error will occur in the two DF spectra which corresponds to the highest and lowest term values.

4.3 Pattern Recognition

4.3.1 Manual Pattern Recognition

The manual polyad identification process, used to extract peak positions and intensities from the experimental data, has been outlined in Chapter 2, or see Section 3.3 of Reference 3. Briefly, the ability to recognize polyad patterns in the acetylene DF spectrum relies on three important selection rules. First, the acetylene $\tilde{A} \rightarrow \tilde{X}$ emission can only access nonzero quanta only in the Franck-Condon active vibrational modes. These are primarily the CC stretch (V_2) and *trans*-bending vibrational modes (V_4). The zero-order

bright states are those with any number of quanta in the two Franck-Condon active modes in combination with zero quanta of all the other modes. For the $\tilde{A} \rightarrow \tilde{X}$ emission, Franck-Condon activity, in ν_1'', ν_3'', ν_5'' is approximately zero. Therefore, the ZOBS will have the following vibrational composition, $(0,nV_2,0,mV_4,0)$. Second, each zero-order bright state (ZOBS) couples to FC dark states through the set of anharmonic resonances, as defined in our H^{eff}.[3,4,7,8] The definition of the polyad quantum numbers combined with specific restrictions of the FC allowed transitions, leads to a single primary ZOBS in each polyad. The distribution of the intensity of this ZOBS throughout the polyad is independent of the initial $\tilde{A}$-state vibrational character but entirely determined by the $\tilde{X}$ state H^{eff}. Third, the absolute intensity of transitions into each ZOBS is derived from the $\tilde{A} \rightarrow \tilde{X}$ Franck-Condon factors. The DF spectra will contain similar ZOBS, $(0,nV_2,0,mV_4,0)$, with different relative intensities. Each DF spectrum will contain the same polyad patterns but with different relative intensity ratios. Polyad patterns can be extracted by recording several emission spectra which originate from different $\tilde{A}$-state vibrational levels, but terminate on the same $\tilde{X}$-state ZOBS. The work in References 3 and 4 provided conclusive proof that the H^{eff} could predict the **qualitative** molecular dynamics of acetylene at high vibrational excitation, E_{vib}<10,000 cm^{-1}. By combining the predictive power of the H^{eff} with the ability of the XCC to extract polyad patterns, we hope to extend our understanding of the early time molecular dynamics. This goal can only be attained after we have formed the strongest possible quantitative understanding of the molecular dynamics at low E_{vib}. Our goal is to develop a **quantitative** H^{eff} model at E_{vib}<10,000 cm^{-1}, which can be extrapolated to higher E_{vib} [and to different classes of ZOBS, e.g. those accessed via IR-UV-DR (infrared-ultraviolet double resonance)

or direct vibrational excitation] to describe the molecular dynamics near and above the barrier to acetylene↔vinylidene isomerization.

4.3.2 XCC Pattern Recognition

Space considerations limit our discussion of the XCC routines. These procedures are outlined in greater detail in references.[11,12] The power of this technique is that no *a priori* information about any spectral pattern is necessary! One spectrum is used to decode another. This technique is truly recognition-based, not model-based. In

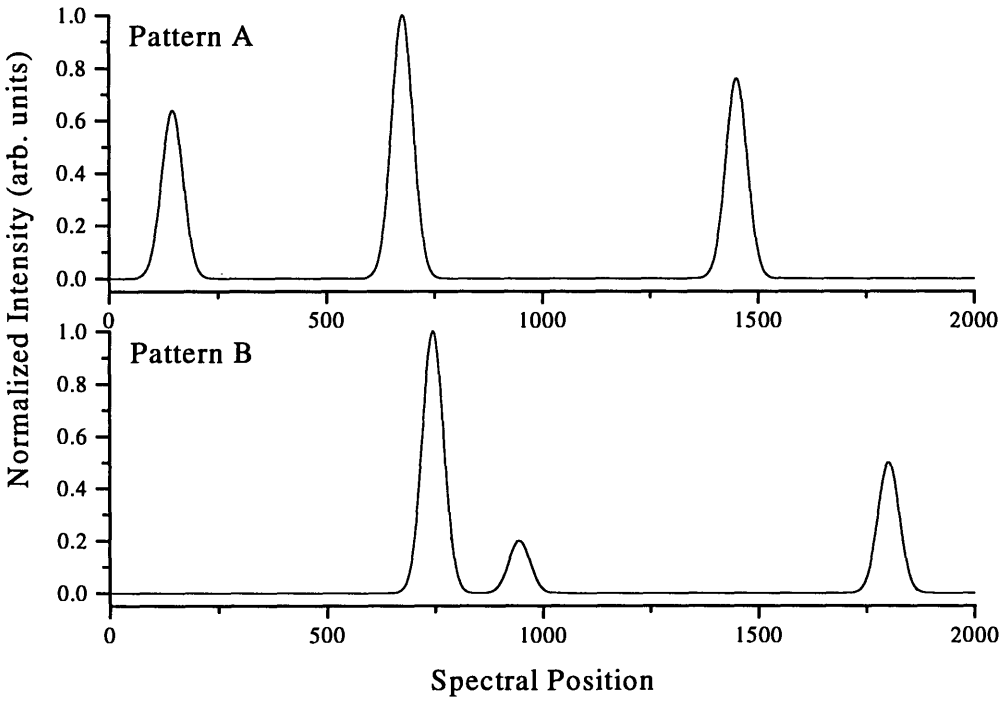

Figure 4.3: Two simulated spectral patterns, A and B, are used to create two spectra containing different amounts of each pattern, see Figure 4.4.

the context of identifying polyads in DF spectra, the XCC is capable of revealing numerically both how a given ZOBS fractionates and the values of the relative Franck-Condon factors for the transitions into all ZOBSs from each $\tilde{A}$-state vibrational intermediate. The XCC pattern

recognition routine utilizes the optimization of a multi-dimensional merit function , see equation (2), which is designed to locate an N-dimensional vector (N is the number of DF spectra used in the XCC routine) for each spectral intensity pattern. Each vector consists of the intensity ratios for one pattern contained in each of the N spectra. If there are three patterns in five spectra, there will be three distinct five dimensional vectors. Each spectrum will contain a percentage (weight) of the identified pattern. This weight is determined from the relative intensity vectors obtained from the XCC.

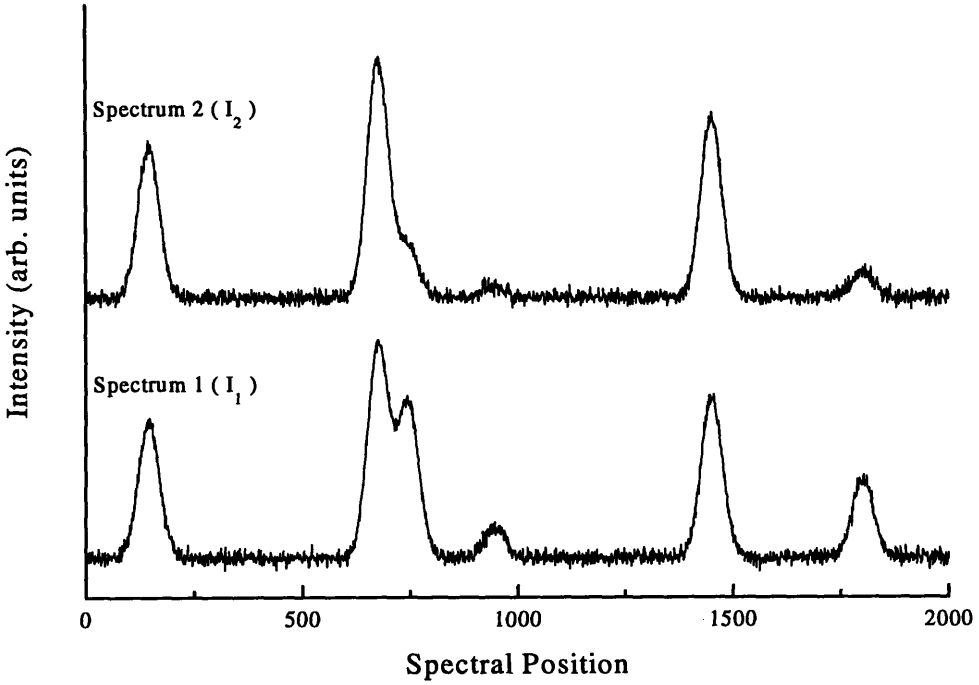

Figure 4.4: Two synthetic spectra produced by taking different linear combinations of patterns A and B. For Spectrum 1 the linear combination is $I_1=0.99I_a + 3.0I_b$. For Spectrum 2 the linear combination is $I_2=1.1I_a + 1.0I_b$.

The energy and intensity distribution of each identified pattern can be reproduced by either plotting (vs. E_{vib}) the weight of a given pattern for each spectrum or by using a linear

inversion method. In the case of overlapped lines, the inversion method has been shown to more accurately recover the lineshapes, line positions, and intensities of each pattern.[11,12] For this reason, the polyad patterns reported here were reproduced via the linear inversion method.

At first, it is much easier to think about how the XCC extracts spectral patterns in two dimensions. Therefore we will begin by creating two simple spectra which are composed of different amounts of two patterns. Figure 4.3 displays two patterns A and B (representative of

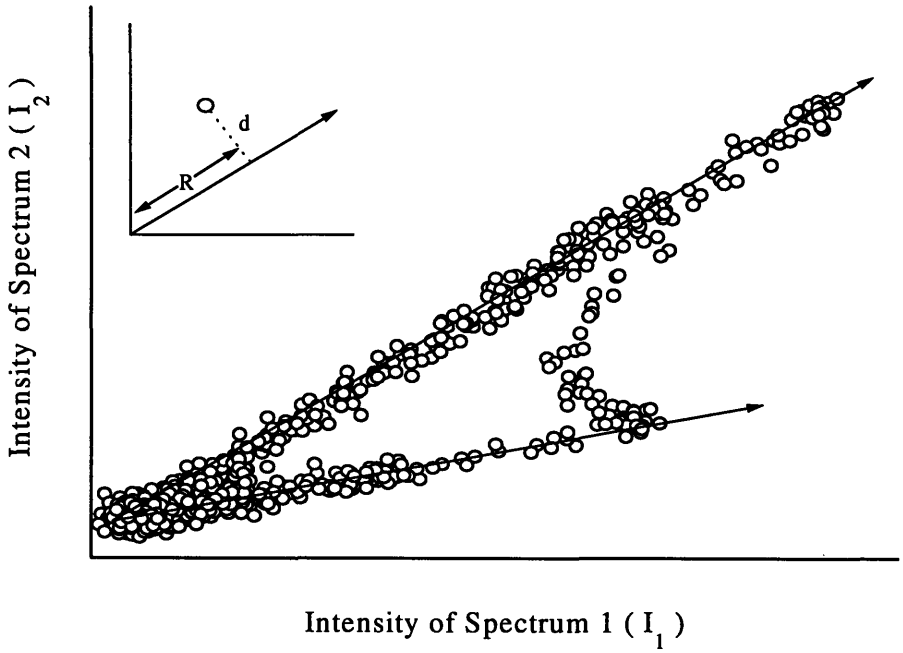

Figure 4.5: Scatter plot of the intensity of Spectrum 1 (I_1) versus the intensity of Spectrum 2 (I_2). This plot is called a recursion map in Ref. 11. The points which fall along the two lines with arrows represent intensity points due to either pattern A or B. The slope represents the ratio of the either pattern in both spectra. The slope is also called the ratio direction, see text. The inset graph displays the XCC weighting function, G(α), where the overall intensity, R, and distance from a slope line, d, is determined for each point.

two polyad patterns). By taking two different linear superpositions of patterns A and B, we create the spectra (representative of the DF spectra) displayed in Figure 4.4, such that the intensity of each spectrum is defined by

$$I_1=a_1I_A + b_1I_B \quad (4.1)$$

$$I_2=a_2I_A + b_2I_B, \quad (4.2)$$

where I_A and I_B represent the intensities of patterns A and B. The coefficients a_i (i=1,2) b_i (i=1,2) indicate the relative amounts of each pattern in the simulated spectra. The XCC routine is designed to compare the relative intensity patterns of the two spectra.

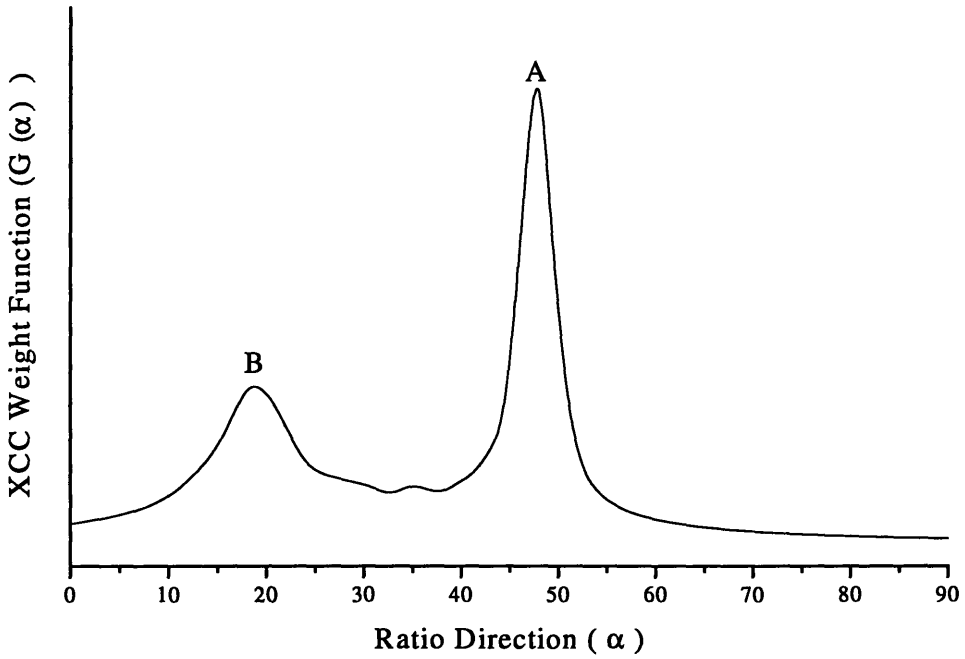

Figure 4.6: A plot of the weighting function, see Equation 2, versus the ratio direction, α. The two maxima correspond to the two patterns, A and B.

Figure 4.5 displays a scatter plot, called a recursion map in References 11 and 12, of I_2 versus I_1. Note, no information about spectral position is retained in this plot! The each point on the

recursion map represents one resolution element in each spectrum. Notice that Figure 4.5 contains two rays (emanating from the origin). Each of these rays defines a ratio of intensities for either pattern A or B. That is, the slope or ratio direction of each ray defines the intensity ratio for a particular pattern within the two spectra. In this example, we know *a priori* what the two ratio directions will be. (We set their values!) For pattern A they are 1.1:0.99 and for pattern B they are 1.0:3.0. Rather than use a least-squares technique to determine the ratio directions, we use a redescending weighting function, see ref. (Jacobson, Coy). Briefly, we define a weighting function as follows:

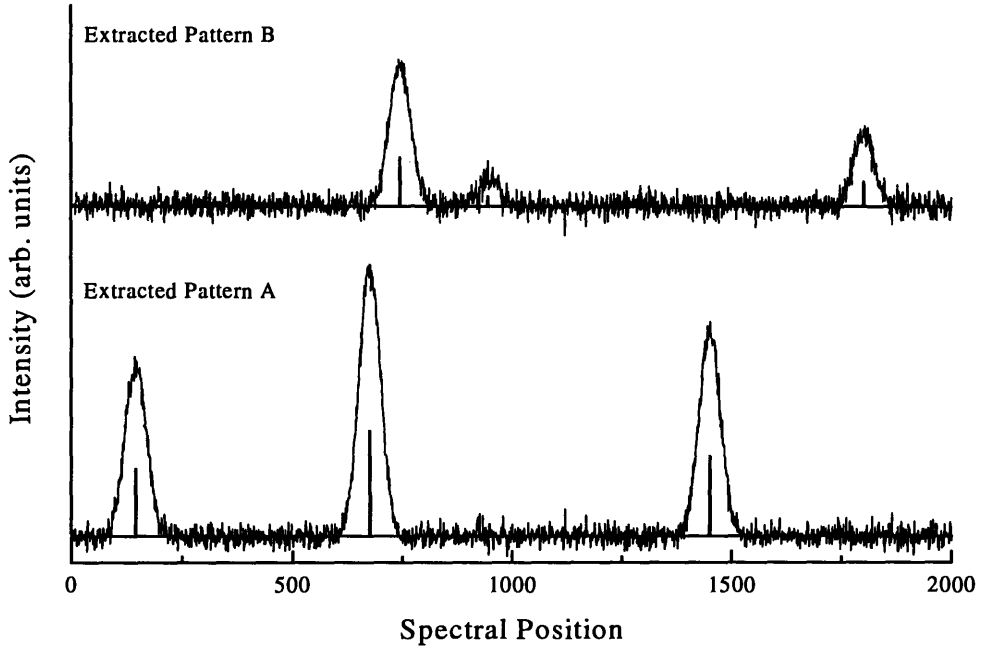

Figure 4.7: Extracted patterns A and B from the two synthetic spectra, see Figure 4.3 and 4.4.

$$G(\alpha) = \Sigma\, g_i(\alpha) = \sum_i R_i e^{\left(-di / 2V_d\right)} \qquad (4.3)$$

where α represents the ratio direction, i is the sum over all spectral elements, d is the distance of any point on the recursion map from the fit ratio direction (the points further away from the line are weighted less). R_i is the projection of the ith point onto the ratio direction, see the insert in Figure 4.5 (This R_i factor weights features with strong intensity). A plot of the XCC weight function versus ratio direction has two maxima, associated respectively, with the a_1:a_2 and b_1:b_2 ratios. Using the information from the ratio direction we can recover each pattern by inverting equation (1), see Figure 4.7.

At low energies, each of the acetylene DF spectra will be composed of several overlapping polyad patterns. The N_{res}= n and n ± 1 polyads will be separated by ≈650 cm^{-1}. Therefore, the XCC routine is performed over ≈800 cm^{-1} segments, centered on the N_{res}=n polyad. As mentioned earlier, in a given N_{res} region there may be two or three other polyads, with the same N_{res} but different values of N_s, which overlap in energy. For example, the [2,12,0/2,g] polyad overlaps the [0,12,0/2,g] polyad, see Figure 4.8. It is for this reason that we have recorded two complementary, high and low resolution, DF spectra. In severely

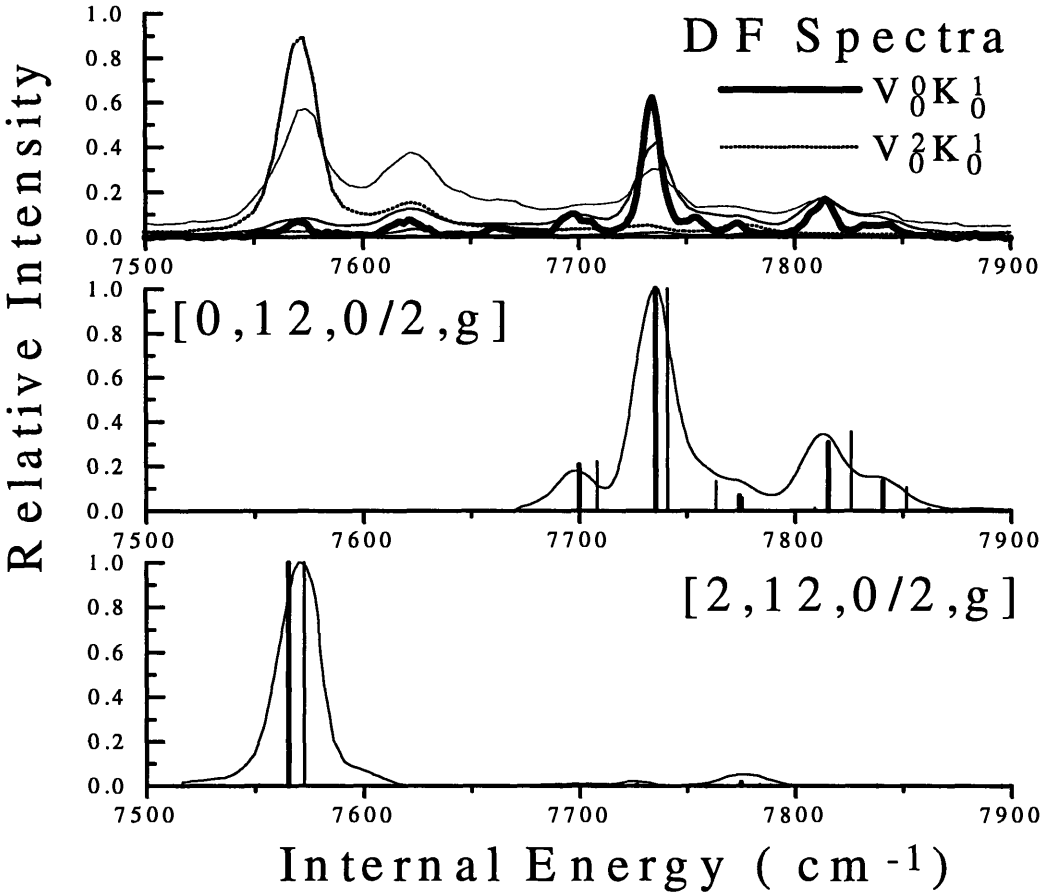

Figure 4.8: A detailed view of the N_{res}=12 polyad region. The top panel contains the five DF spectra used in this study. The middle panel contains the XCC results for the [0,12,0/2,g] polyad. The bottom panel contains the XCC results for the [2,12,0/2,g] polyad. Note that the [2,12,0/2,g] polyad overlaps the [0,12,0/2,g] polyad. The XCC routine is able to extract intensity features due to vibrational eigenstates with small relative intensities, 5%.

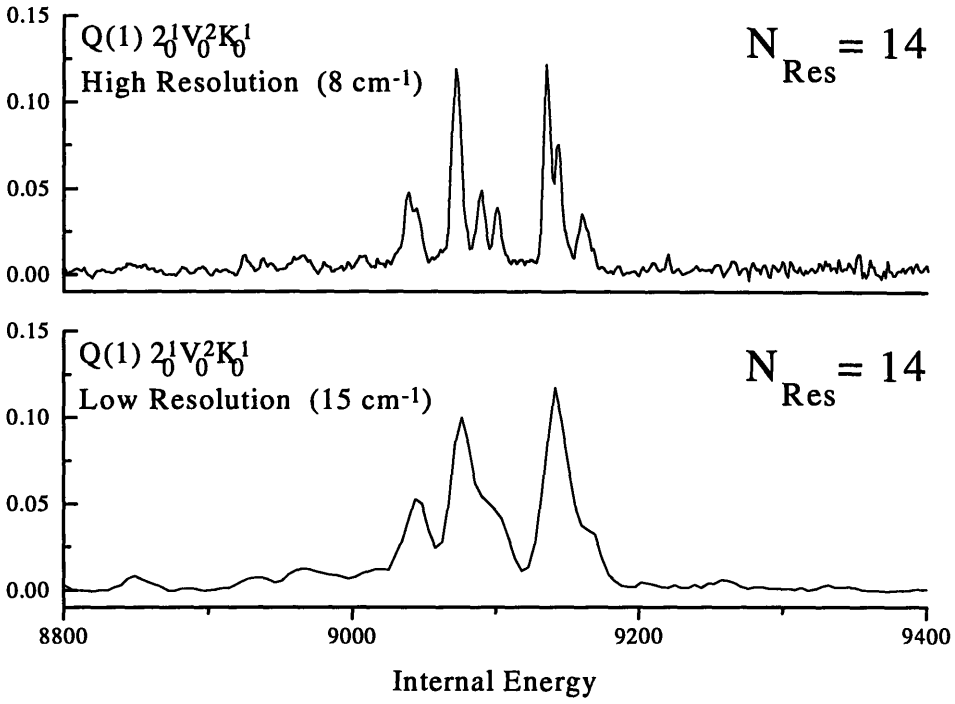

Figure 4.9: The high and low resolution V_0^2 K_0^1 DF spectra for the N_{res}=14 region.

congested regions, E_{vib}> 9,000 cm^{-1}, the high resolution spectra assist in the XCC identification of overlapped polyad patterns, see Figure 4.9. The lower panel of Figure 4.10 contains the XCC pattern representing the fractionation of the ZOBS as extracted from the low and high resolution spectra. The high resolution spectrum was convoluted with a Gaussian to reproduce the FWHM in the low resolution spectrum. The agreement of the two patterns, extracted from two different sets of spectra, indicates that the XCC routine has unbiased ability to disentangle severely overlapped spectral patterns. The upper panel in Figure 4.10 contains the XCC extracted pattern and the H^{eff} computed pattern for the [0,12,0/2,g] polyad. The qualitative nature, intensity, and energy distribution, of the predicted pattern is in good agreement with the observed XCC pattern. This type of agreement should not be surprising because the [0,12,0/2,g] levels were included

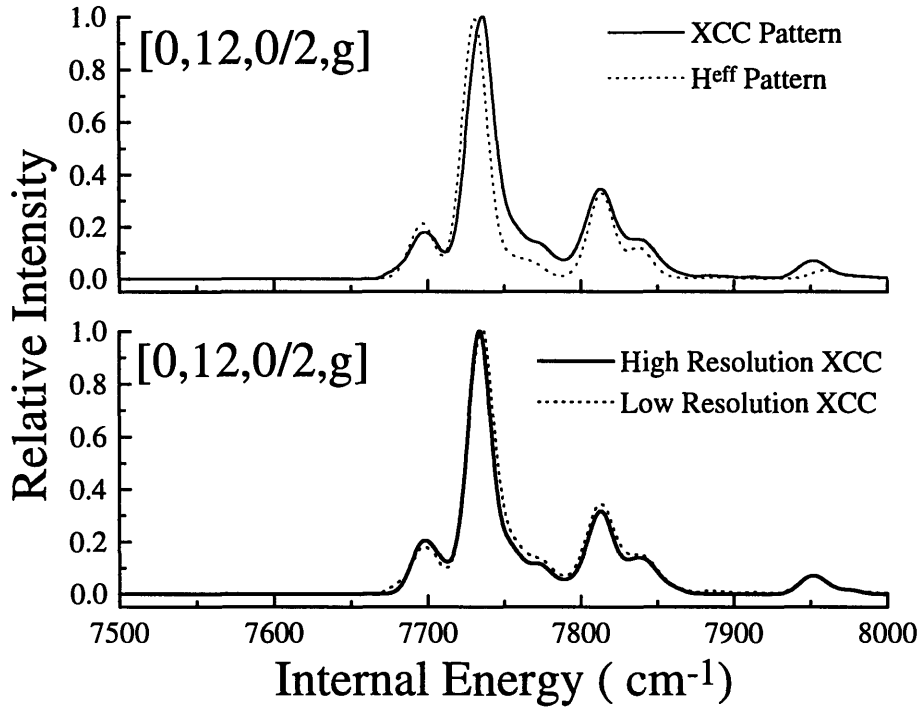

Figure 4.10: The top panel contains the XCC patter and the H^{eff} pattern for the [0,12,0/2,g] polyad. The XCC pattern was recovered from the low resolution DF spectra. The lower panel shows the XCC results from high and low resolution DF spectra for the [0,12,0/2,g] polyad. Not that the high resolution XCC pattern was convoluted with a Gaussian to reproduce the low resolution FWHM, 15 cm^{-1}.

in the preliminary H^{eff} fit. Significant deviations occur between the H^{eff} predictions and the observed patterns for *polyads which were not included in the original H^{eff} refinement*, see Figure 4.12. Identification of polyad patterns and the deperturbed ZOBSs at E_{vib}>10,000 cm^{-1} will become useful in future refinement of the H^{eff} model.

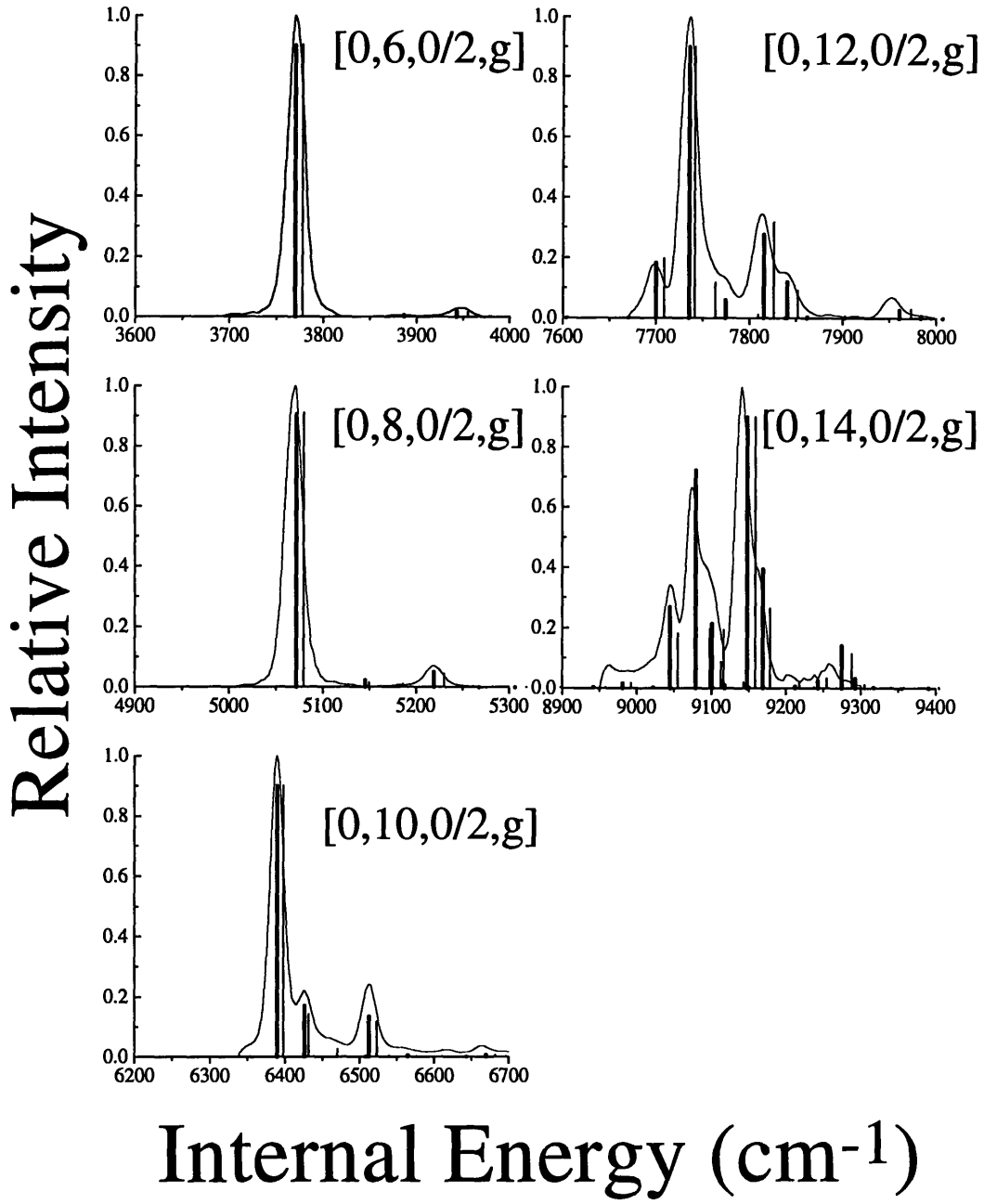

Figure 4.11: Results of the XCC routine for the N_s=0 polyads compared to the H^{eff} predictions. Notice the quantitative agreement of the observed and predicted polyad patterns.

4.4 Results

4.4.1 DF Features

We have identified *all* of the N_s= 0, N_{res}= 6-16 and N_s= 1, N_{res}= 5-17 polyads and several N_s>1 (N_s=2,3,4) polyads, see Figures 4.11, 4.12, 4.13, and 4.14. Several previously misassigned features have been reassigned. A complete line list of the intensities,

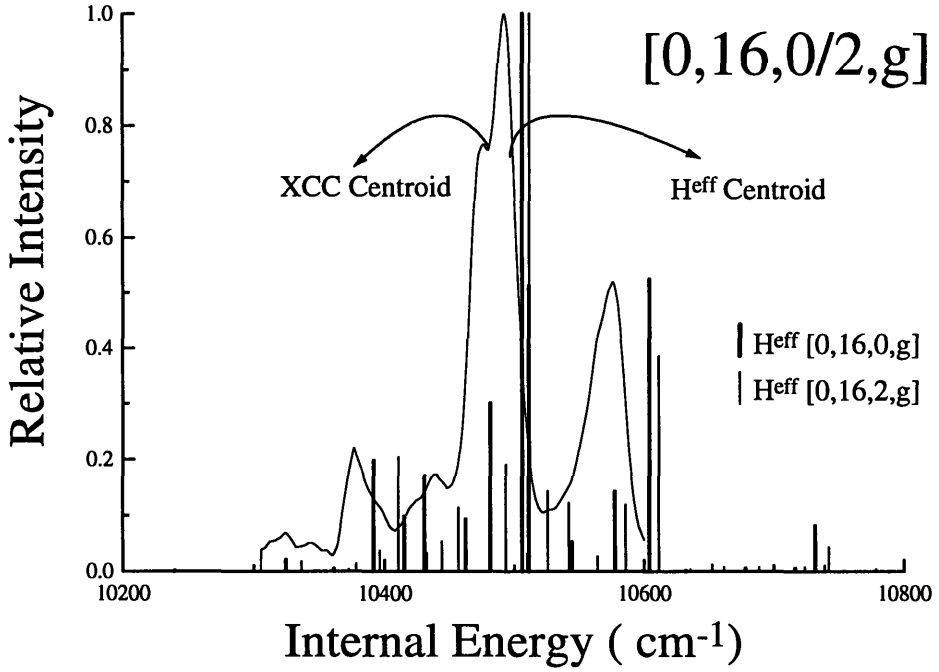

Figure 4.12: Results of the XCC routine, solid line, for the [0,16,0/2,g] polyad compared against the H^{eff} prediction, heavy and light sticks. Notice a quantitative agreement of the observed and calculated patterns no longer exists. The observed and predicted patterns appear to have intensity distributions whose centroids have been displaced. The heavy sticks represent the calculated [N_s, N_{res}, l=0,g] levels. The light sticks represent the calculated [N_s, N_{res}, l=2,g] levels.

energies, and eigenstate characters is found in Table 4.2. We have only included the DF features which were of moderate to strong relative intensity and were clearly due to one

Table 4.2: Line Positions and Relative Intensities

N_{res}	N_s	Energy (cm^{-1})	Rel. Int.	Description:
5	1	3182.3	1.0000	main peak
6	0	3770.3	0.7470	main peak
6	0	3942.5	0.0230	l=0
6	0	3949.5	0.0230	l=2
8	0	5068.8	0.9390	main peak
8	0	5216.0	0.0650	l=0
8	0	5221.0	0.0650	l=2
9	1	5676.3	0.7850	main peak
9	1	5872.0	0.0330	l=0
9	1	5875.5	0.0330	l=2
10	0	6386.1	0.8210	main peak
10	0	6423.0	0.1800	both
10	0	6507.0	0.1980	l=0
10	0	6511.0	0.1980	l=2
10	0	6658.5	0.1570	l=0
10	0	6664.5	0.1570	l=2
10	2	6329.4	1.0000	main peak
11	1	6960.0	0.9770	main peak
11	1	7120.0	0.0750	l=0
11	1	7127.0	0.0750	l=2
12	0	7733.6	1.1270	main peak
12	0	7753.9	0.1620	l=2
12	0	7696.5	0.1700	l=0
12	0	7704.5	0.1700	l=2
12	0	7808.5	0.2880	l=0
12	0	7814.0	0.2880	l=2
12	0	7773.3	0.1120	both
12	0	7836.0	0.1090	l=0
12	0	7843.0	0.1090	l=2
12	0	7950.0	0.0620	l=0
12	0	7958.0	0.0620	l=2
12	2	7570.5	0.7020	main peak
12	2	7773.0	0.0360	l=0
13	1	8255.2	0.7530	main peak
13	1	8284.4	0.5500	both

13	1	8395.5	0.1490	l=0
13	1	8400.0	0.1490	l=2
13	3	8225.5	1.0000	main peak
14	0	9073.4	0.5950	main peak
14	0	9090.3	0.2660	both
14	0	9102.6	0.2180	both
14	0	9041.0	0.2050	l=0
14	0	9046.0	0.2050	l=2
14	0	9136.2	0.5710	l=0
14	0	9143.5	0.5710	l=2
14	0	9259.0	0.1130	l=0
14	0	9266.0	0.1130	l=2
14	2	8836.3	0.7670	main peak
14	2	9009.0	0.0560	l=0
14	2	9017.0	0.0560	l=2
15	1	9586.2	0.3383	main peak
15	1	9619.3	0.1110	both
15	1	9527.5	0.0244	l=0
15	1	9532.5	0.0244	l=2
15	1	9700.0	0.1175	l=0
15	1	9710.0	0.1175	l=2
15	1	9673.8	0.0650	both
15	3	9449.4	0.2603	main peak
15	3	9662.0	0.0207	l=0
15	3	9670.0	0.0207	l=2
16	2	10132.7	0.2910	main peak
16	2	10111.5	0.1580	both
16	2	10167.4	0.0540	both
16	2	10271.6	0.0850	both
16	4	10107.5	1.0000	main peak
17	3	10698.1	0.2575	main peak
17	3	10886.4	0.0306	both

vibrational eigenstate. In some cases, for vibrational eigenstates which contain character having nearly equal quanta in ν_4 and ν_5, the splitting between the l=0 and l=2 levels was

visible. However, these lines are not fully resolved, so the reported values of the l=0 and l=2 levels are approximate.

4.4.2 N_s=0 Polyad Patterns

The results from the XCC pattern recognition on the N_s=0 polyads are presented in Figures 4.11 and 4.12. Comparison of the observed XCC patterns to the H^{eff} predictions exhibit remarkable agreement. At low $\tilde{X}$-state energies, the H^{eff} model constrains the $[0,N_{res},0]$ polyads such that they will contain a small number of eigenstates with observable intensities. One or two of these eigenstates will contain approximately 80% of the ZOBS character while most of the other eigenstates contain no more than 1-2%. Figure 4.8, is a detailed view of the N_{res}=12 region. Although the [2,12,0/2,g] polyad overlaps the [0,12,0/2,g] polyad, the [0,12,0/2] and the [2,12,0/2,g] polyad patterns identified here by the XCC routine exhibit uncanny agreement with the predicted polyads. Note that the XCC pattern captures intensity features that contain as little as 1% of the ZOBS character!

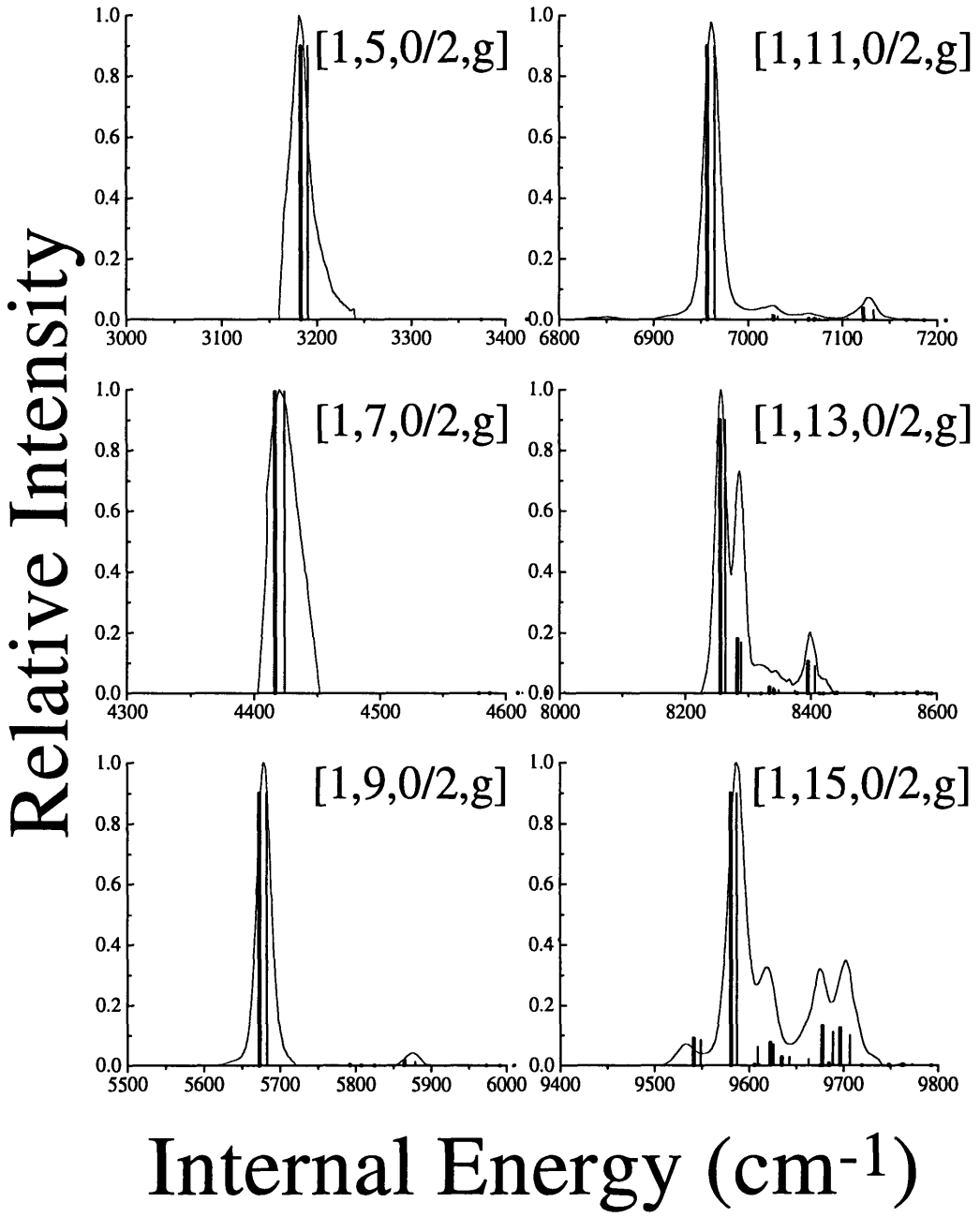

Figure 4.13: Results of the XCC routine for the N_s=1 polyads, solid lines, plotted against the H^{eff} predictions, heavy and light sticks. Notice that the predicted and observed polyad patterns no longer possess the quantitative agreement in terms of frequency *and* intensity distributions seen in Figure 4.11.

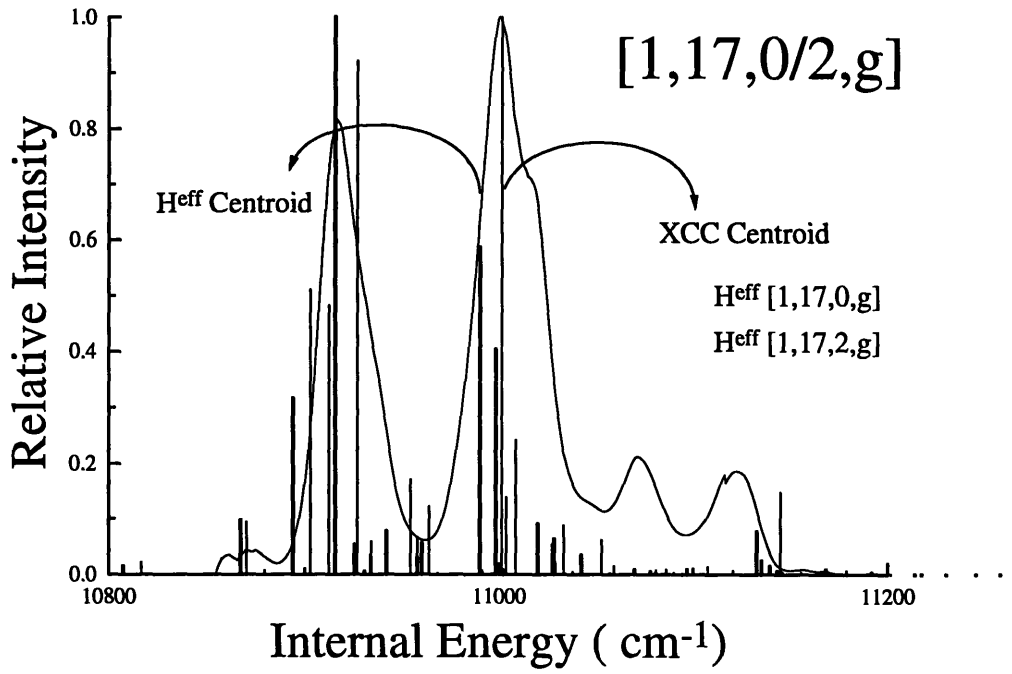

Figure 4.14: Results of the XCC routine for the [1,17,0/2,g] polyad, solid line, plotted against the H^{eff} predictions, heavy and light sticks. The discrepancies between the observed and predicted patterns are due to deviations in the intensity distributions. This results in a difference in the H^{eff} and XCC energy centroids.

As a measure of our ability to recognize N_s=0 polyad patterns, we have extrapolated the H^{eff} to predict polyad patterns at higher energies, E_{vib} >10,000 cm^{-1}. The N_{res}=16 energy region, at 10,500 cm^{-1}, has considerable dynamical importance, as it contains several bending levels which are all nearly degenerate. At N_{res}=16, due to the values of $(\omega_4^0, x_{44}^0), (\omega_5^0, x_{55}^0)$ and x_{45}^0, $E_{v_4, v_5}^0 = E_{16,0}^0 \approx E_{14,2}^0 \cdots \approx E_{0,16}^0$ occurs, leading to a "crash" in the bend-bend interaction scheme. A comparison of the H^{eff} model and experiment for the [0,16,0/2,g] polyad is shown in Figure 4.12. The predicted and observed polyad patterns no longer display the quantitative agreement evident at lower E_{vib}. The main discrepancy appears to be a slight shift between the centroids of the predicted and observed patterns. Since the [0,16,0/2,g]

polyad occurs right at the bend crash region, where $E^0_{v_4,\,v_5} = E^0_{16,\,0} \approx E^0_{14,\,2} \cdots \approx E^0_{0,\,16}$, the H^{eff} model will be very sensitive to the zero-order bend energies, diagonal and off diagonal bend-bend anharmonic coupling. The complete identification of the intensity and energy distribution for the [0,16,0/2,g] polyad as well as the assignments for the other [0,N_{res},0/2,g] polyads (where N_{res}=6,8,10,12,and 14) will permit a critical fine adjustment of the pure bending parameters. We have begun initial refinement procedures, and results are forthcoming.

4.4.3 N_s>0 Polyad Patterns

The low E_{vib}< 10,000 cm^{-1} predicted and observed N_s=1 polyads are compared in Figure 4.13. Note that the H^{eff} has not been refined for any N_s>0 polyads.[8] It is, therefore, *not* surprising that the N_s=1 observed and predicted polyads are not in quantitative agreement. However, it is encouraging that there is such remarkable qualitative agreement between the intensities and energy positions of the calculated and observed polyad patterns. The predictions were calculated with an H^{eff} model which was refined to bend-only ZOBSs!

We have terminated our low resolution polyad recognition at N_{res}=17, see Figure 4.14. This energy region, E_{vib}=12,000 cm^{-1}, is a logical stopping point. While the predicted and observed polyad patterns display semi-qualitative agreement at these energies, it make less sense for us to proceed to higher energies until we have refined the H^{eff}. A slight adjustment of the current stretch-bend parameters, based on the newly assigned N_s=1,2,3,4 polyads, should bring the predicted and observed polyad patterns into quantitative agreement at E_{vib}<12,000 cm^{-1}.

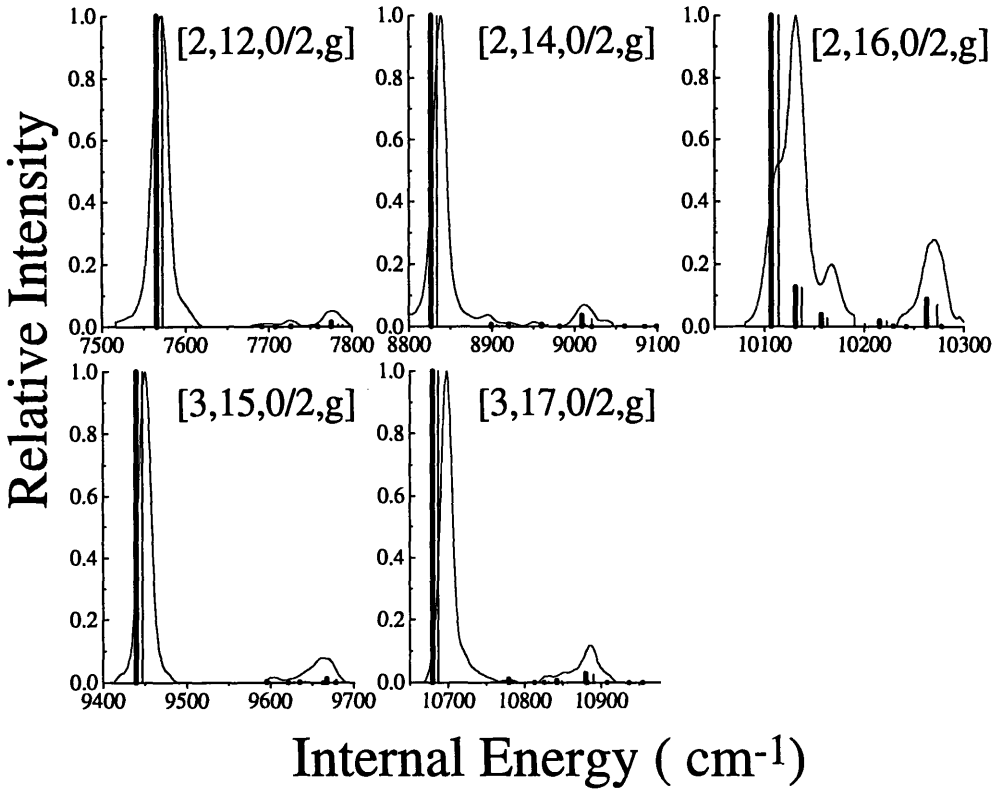

Figure 4.15: Results of the XCC routine for the N_s=2,3 polyads, solid line, plotted against the H^{eff} predictions, heavy and light sticks. These polyads display little fractionation even though they are located at high E_{vib}. See text for explanation. The energy centroids and Franck-Condon factors calculated from these XCC polyad patterns will be particularly helpful in refining the CC stretching parameters.

Several N_s=2 and 3 polyad patterns have been identified, see Figure 4.15. The N_s polyads (where N_s=n and n=2,3,4) will have polyad patterns very similar to the [0,N_{res}-3n,0/2,g] polyads. This trend can be understood from the nature of the ZOBS, (nV_2,2mV_4), and the polyad structure at low E_{vib}. For the N_s>1 polyads at low energy, the ZOBS have almost equal numbers of quanta in ν_2 and ν_4. The extent of IVR (fractionation) within the N_s >1 polyads is controlled by the amount of ν_4 excitation, see Chapter 2.[3,4] For example, the [1,15,0/2,g] polyad with a (1,12) ZOBS has an intensity pattern which is similar to the [0,12,0/2,g] polyad with a (0,12) ZOBS, see Figures 4.11 and 4.13. The zero-order

energy difference between (1,12) and (0,12) is ≈1,850 cm^{-1}. The [3,15,0/2,g] polyad with a (3,6) ZOBS has an intensity pattern similar to the [0,6,0/2,g] polyad with a (0,6) ZOBS, see Figures 4.15 and 4.11. The energy difference between these ZOBS is ≈5,250 cm^{-1}! This is consistent with a Darling-Dennison (DD) tier effect in the [*low* N_s, *high* N_{res}] polyads, see Chapter 2. At lower E_{vib} (small V_4), the polyads consist of one main feature which contains almost 90% of the ZOBS character. At higher E_{Vib} (larger V_4), the N_s=0 and 1 polyads start to display extensive fractionation (no eigenstate contains more than 50% of any basis state character). In contrast, the N_s >1 polyads have simple intensity patterns due to the DD tier effect, see Chapter 2. Accurate and precise identification of these special polyads will be extremely important in refining the effective Hamiltonian model in high E_{vib} regions in which the N_s= 0 and 1 polyads are hopelessly scrambled. These high-N_s polyads may be the last remnant of scaleable regularity in the DF or SEP spectra, and this could prove useful in characterizing the acetylene↔vinylidene isomerization.

4.4.4 ZOBS Zero-Order Energies

The complete polyad energy and intensity pattern is due to the distribution of the ZOBS character among the molecular eigenstates through the resonance structure of the H^{eff} model, see Chapter 1. Once the polyad patterns have been identified by the XCC routine, the zero-order energy positions of the ZOBS for each polyad can be obtained. These energy positions for progressions in (nV_2,$2mV_4$) can be used to refine the zero-order energies and diagonal anharmonicities in the H^{eff}. A stepwise refinement of the H^{eff} coupling parameters will strengthen the our predictive power and our ability to perform XCC pattern recognition at higher E_{vib}.

Table 4.3: Calculated Deperturbed ZOBS Energies and Franck-Condon Factors

Polyad $[N_s,N_{res}]$	ZOBS Energy (cm^{-1})	Origin FCF	$1\nu_3$ FCF	$2\nu_3$ FCF	$\nu_2+\nu_3$ FCF	$\nu_2+2\nu_3$ FCF
[0,6]	3776.03	N/A	0.0455	N/A	N/A	N/A
[1,7]	4424.38	N/A	0.0271	0.0819	N/A	N/A
[0,8]	5089.10	0.0580	0.1708	0.3038	0.2608	N/A
[1,9]	5689.94	0.0368	0.1426	0.4028	0.0970	N/A
[0,10]	6431.37	0.2795	0.2722	0.1659	0.5667	0.2683
[2,10]	6331.72	0.0253	0.1033	0.2942	0.0449	0.0321
[1,11]	6978.07	0.1496	0.3644	0.5385	0.1780	0.2665
[0,12]	7768.25	0.4688	0.2372	0.0391	0.3322	0.0249
[2,12]	7578.73	0.0404	0.2995	0.6974	0.0345	0.0204
[1,13]	8287.86	0.5007	1.0000	0.3909	0.3112	0.1427
[3,13]	8221.21	0.0161	N/A	0.0897	0.0117	0.0185
[0,14]	9116.50	0.4604	0.0266	0.2515	0.0837	0.3530
[2,14]	8855.81	0.1668	0.4811	0.7688	0.0107	0.0048
[1,15]	9625.33	0.7922	0.5320	0.0307	0.2834	0.0297
[3,15]	9473.62	0.0208	0.2059	0.2813	0.0807	0.1783
[0,16]	10495.15	0.3618	N/A	0.2682	0.0877	0.6346
[2,16]	10145.35	0.5004	N/A	0.2268	0.0267	0.0124
[4,16]	10109.75	N/A	N/A	N/A	0.0156	0.0546
[1,17]	10986.56	1.0000	N/A	0.6888	0.0540	0.2648
[3,17]	10726.68	0.1226	N/A	0.5117	0.2555	0.4536

The ZOBS energies are listed in Table 4.3. The ZOBS energies are obtained by calculating the intensity weighted average energy, or centroid, for each XCC polyad pattern as follows:

$$\text{Centroid} = \left(\sum_j (I_j * \bar{\nu}_j)\right) \Big/ \sum_j I_j \quad , \tag{4.4}$$

where the sum is over all j intensity elements of the XCC extracted polyad pattern and $\bar{\nu}_j$ represents the j-th energy position. The accuracy of the energy positions of features in the

low-resolution DF spectrum is 4 cm^{-1} (2σ) at 15 cm^{-1} resolution. This absolute accuracy was calculated by comparing the recorded DF spectra to known and fully resolved eigenstate transitions observed in stimulated emission spectra. The precision of each ZOBS centroid is 6-7 cm^{-1} (2σ). The precision is specified by comparing the ZOBS energy positions obtained by the XCC routine using high versus low resolution DF spectra.

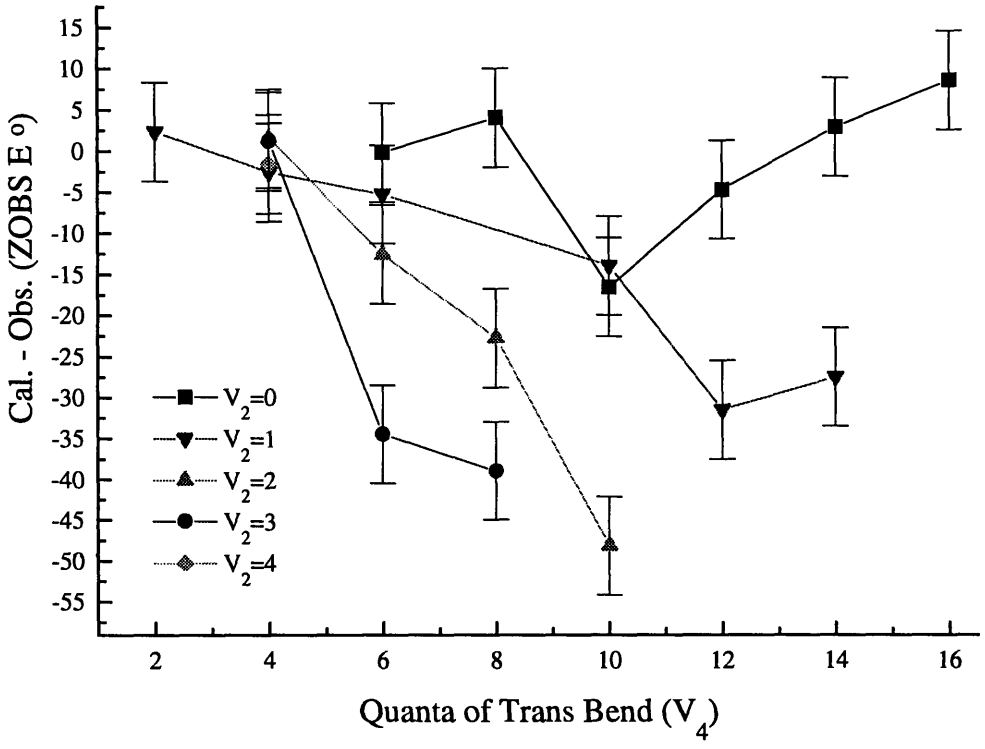

Figure 4.16: The difference of the calculated (from the H^{eff}) and observed (centroids from the XCC polyad patterns) ZOBS energy positions for N_s=n (nV_2) plotted versus $N_{res\text{-}3n}$= (mV_4). The systematic deviation of the differences for each nV_2 indicates that the CC stretching parameters require refinement.

Figure 4.16 contains a plot of the difference between the calculated ZOBS and observed ZOBS energies. The striking systematic deviation with increasing excitation in V_2 is

a clear indication that the current parameters for the CC stretching mode require refinement. Previous fits of experimental absorption data would not have contained many levels with more than one quantum of CC stretching. Therefore, our DF spectra and extracted polyad patterns provide an unique opportunity to refine the description of the CC stretching coordinate in the molecular Hamiltonian.

4.4.5 Franck-Condon Factors

The ZOBS intensity is due to the strength of the electronic transition, the vibrational overlap integral squared, and the population of the initial vibrational levels.[14]

$$I_{e'v'e''v''} \alpha |\int \psi_{e'}^{*} \mu_e \psi_{e''} d\tau_{el}|^2 \, |\int \psi_{v'}^{*} \psi_{v''} d\tau_{el}|^2 . \qquad (4.5)$$

The vibrational overlap integral squared, $|\langle v' | v'' \rangle|^2$, is called the Franck-Condon factor (FCF). In order to extract Franck-Condon factors (FCF) from experimental data, any systematic dependence of the electronic transition dipole on normal coordinate displacements must be removed. The ω^3 dependence of the Einstein A-coefficient[14] was removed by multiplying the DF intensities by a normalized (the largest value of ω^3 is normalized to unity) $1/\omega^3$ factor.

The experimental FCFs are obtained in the following manner. The XCC routine identifies and extracts the spectral energy and intensity distribution that belongs to one polyad. Recall that each spectral intensity pattern is derived from transitions terminating in a unique and perfectly known ZOBS. The integrated area of this pattern must be multiplied by a weight factor, as determined by the XCC routine, to yield a FCF. The weight factor describes how strongly a given pattern appears in one of the spectra. This number, pattern area times weight, serves as an estimate of the relative FCF for a specific ZOBS. Table 4.3 contains a list of the FCFs for the polyad patterns from the five low-resolution DF spectra used in this

study. The absolute uncertainty was calculated by observing the variations in the average intensities measured from identical DF spectra recorded on several different days and by comparing the intensities of spectral features located in the segment overlap regions. The average error per segment is estimated 5% (2σ). The FCFs reported in this chapter were recorded on four adjacent monochromator segments. The probable propagated error between FCFs in the region between 3,000 cm^{-1} and 12,000 cm^{-1} is 10% (2σ). The precision of the reported FCFs is 20% (2σ). This was determined by performing a least squares fit to a scatter plot of the high resolution versus the low resolution FCFs extracted from the $V_0^0\ K_0^1$ DF spectrum. For this study, the high resolution $V_0^0\ K_0^1$ DF spectrum is convoluted with a Gaussian to reproduce the low-resolution (15 cm^{-1}) linewidth. This convoluted copy of the high resolution $V_0^0\ K_0^1$ DF spectrum is used with the other 4 DF spectra in the low resolution XCC routines. If the XCC routine were perfect and each spectrum had identical signal to noise, the ratio of the low and high resolution $V_0^0\ K_0^1$ FCFs should be unity. However, the FCFs are determined by the integrated intensities of the polyad patterns obtained from the XCC routine containing five different DF spectra. The XCC precision will be affected by human error, the intrinsic signal to noise of each DF spectrum, and slight baseline deviations of the five different DF spectra.

Plots of the Franck-Condon Factors from the different DF spectra used in this study are presented in Chapter 5. These plots will contain both the FCF's determined, in this chapter, at $E_{vib}<12{,}000\ cm^{-1}$ and the FCFs determined at $E_{vib}>12{,}000\ cm^{-1}$ reported in the next chapter.

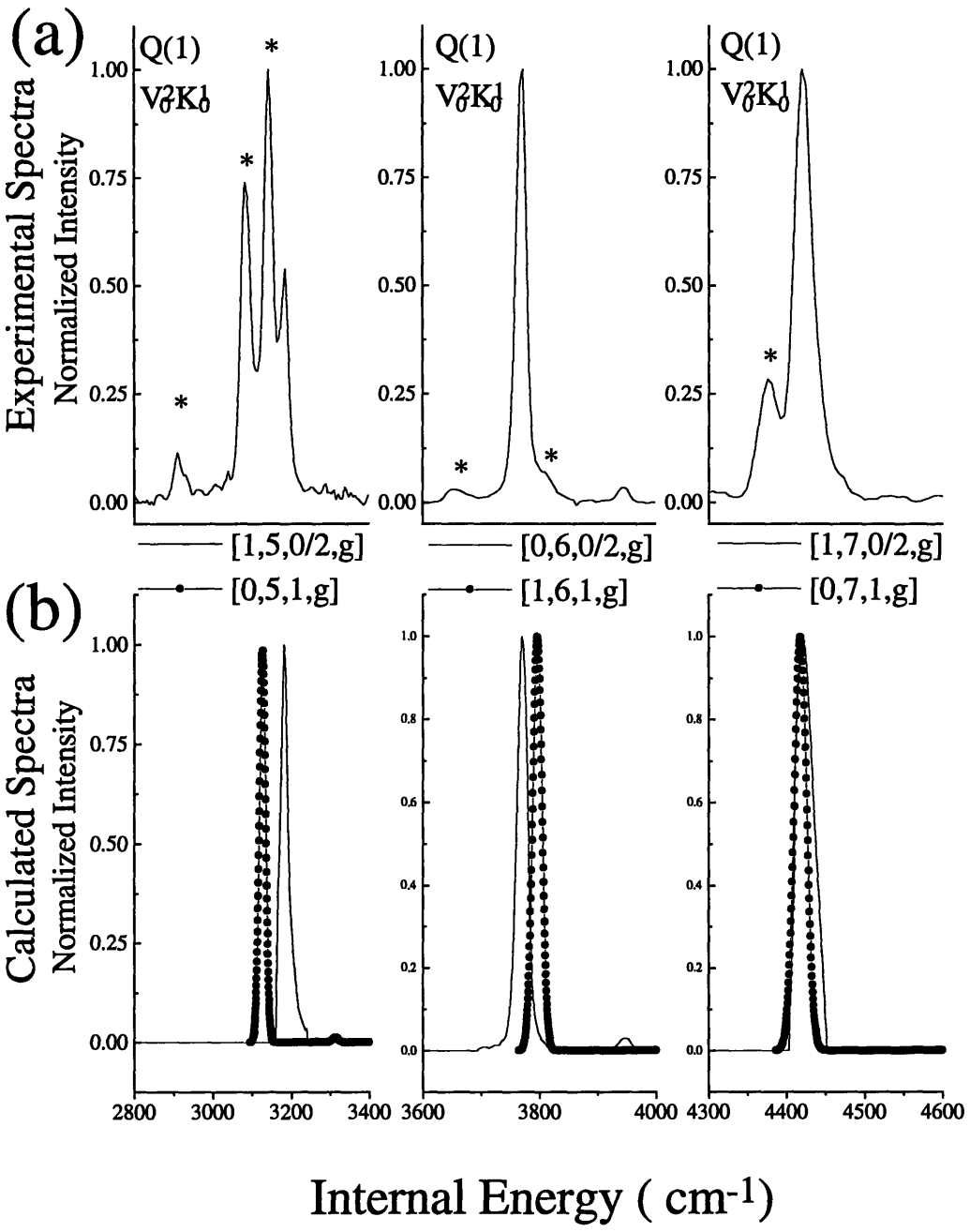

Figure 4.17: (a) DF spectra of the N_{res}=5-7 E_{vib} region excited via the $^rQ_0(1)$ transition of $V_0^2K_0^1$. The asterisks denote several extra DF features, see text. (b) Calculated polyad patterns in the N_{res}=5-7 E_{vib} region. The solid line represents the [1,5,0,g], [0,6,0,g], and [1,7,0,g] polyads. The solid line with circles represents the [0,5,1,g], [1,6,1g], and [0,7,1,g] polyads. See text for details.

4.5 Extra Emission Features

The original work on pattern recognition (Chapter 2) resulted in substantial interest by the theoretical community in modeling the pure bending dynamics at E_{vib}<16,000 cm^{-1}. Correction of discrepancies between the observed and calculated pure bending spectrum was a partial motivation for this work. The low-E_{vib} emission from the acetylene $\tilde{A}\,^1A_u \leftrightarrow \tilde{X}\,^1\Sigma_g^+$ transition is primarily composed of polyads due to a set of well defined ZOBS (nV_2,$2mV_4$). Careful examination of the new low resolution DF spectra reveals several small spectral features which cannot be attributed to the expected [N_s,N_{res},l,g] polyads. Of particular interest are the extra DF features which occur in the 3,000 to 4,400 cm^{-1} energy range. In this region, the polyads [1,5,0,g] and [1,7,0,g] will contain only three and six eigenstates. Note that the definition of N_{res} severely limits the allowed values of N_s in this region. The N_s=3 polyads are nonexistent below N_{res}=9. The [0,6,0,g] and [2,6,0,g] polyads will contain nine and two eigenstates, respectively. The [2,6,0/2,g] polyad is probably not detectable in our DF spectra due to a small FCF (we do not see the [2,8,0/2,g] polyad). The lowest [N_s=2, N_{res}] polyad is [2,10,0/2,g]. Figure 4.17a shows the $V_0^2\,K_0^1$ emission for the [1,5,0/2,g], [0,6,0/2,g], and [1,7,0/2,g] polyads. Each of the five intermediate levels used in this study had spectra that included similar extra DF features. Figure 4.17b contains the predicted [1,5,0/2,g], [0,6,0/2,g], and [1,7,0/2,g] polyads. The model predicts that most of the ZOBS intensity is localized in one or two eigenstates. This is consistent with the zero-order energy positions of the bright and dark states. The structure of the [*low* N_s, *high* N_{res}] polyads has been documented in Reference 3, see Chapter 2. The most significant feature of the low energy polyad structure is that the ZOBS always lies at the low energy extreme of a given [N_s,N_{res}] polyad. All of the fractionation of the bright state character will occur at energies greater than

the zero-order energy position of the bright state. Note that all of the extra features discussed here appear on the *low* energy side of the [1,5,0/2,g], [1,7,0/2,g], and [1,9,0/2,g] polyads, as indicated by asterisks in Figure 4.17a. The appearance of these extra DF features could be explained by any of the following seven hypotheses. We will systematically analyze each hypothesis below.

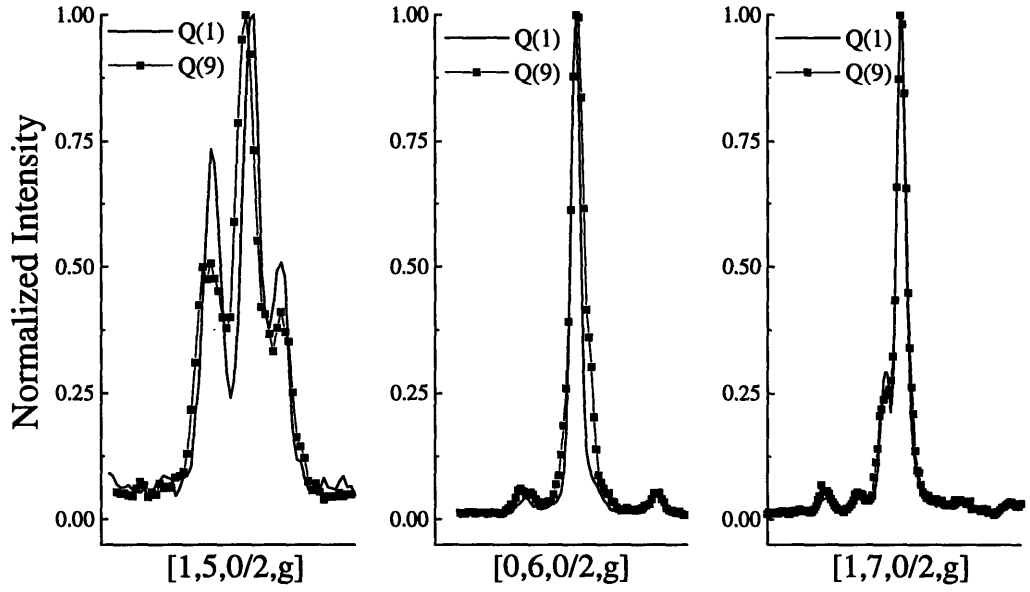

Figure 4.18: DF spectra excited via the ${}^{r}Q_0(1)$ and ${}^{r}Q_0(9)$ transitions of $V_0^2K_0^1$. The relative intensity differences in the N_{res}=5-7 energy region is approximately 20% (the lowest energy feature in [1,5,0/2,g] polyad displays the largest discrepancy, 50%, of the Q(1) and Q(9) intensities).

1. Asymmetry affects in the $\tilde{A}$-state rotational wavefunctions: The $\tilde{A}$-state is a near prolate top with A>B≈C (where A≅13, B≅1.12, C≅1.03). The true $\tilde{A}$-state rotational wavefunctions will be linear combinations of the prolate top wavefunctions. This effect

mixes K states that differ by $\Delta K=\pm 2$. For a nominal $^{r}Q_0(1)$ transition used to populate $J_{Ka,Kc}=1_{1,0}$ as an intermediate level in these experiments, the fractional mixing of $K_a>1$ values is zero. For J=1 there can be no $K_a>1$ levels!

2. $\tilde{A}$-state anharmonic perturbations: All of the vibrational intermediates used to record the DF spectra are totally symmetric (A_g). A anharmonic perturbation of the intermediate vibrational level can only occur by another totally symmetric vibrational level. While it is possible that some $\tilde{A}$-state vibrational levels have anharmonic interactions with nominally dark levels,[15] for the $V_0^0\ K_0^1$ intermediate the closest possible anharmonic interacting level is $V_0^1\ K_0^1$. The vibrational energy difference is 1,048 cm^{-1}. While the high-resolution studies of the $V_0^2\ K_0^1$ band reveal no strong perturbations,[16] a remote perturber will not cause a level shift or intensity anomaly. It is possible that a remote anharmonic interaction could exist between $V_0^0K_0^1$ and ν_3' or $\{2V_b\}$. Since $\omega_4^0 \approx \omega_6^0$, V_b refers to a combination of ν_4 and ν_6, either $2\nu_4$, $2\nu_6$ or $\nu_4+\nu_6$. A $\nu_3 \leftrightarrow \{2V_b\}$ anharmonic interaction will have the following scalable coupling matrix element:

$$\langle \nu_3, V_b | H | (\nu_3 \mp 1), (V_b \pm 2) \rangle \propto K_{3,2V_b} \left[\frac{(V_b \pm 2)(V_b \pm 1)(\nu_3)}{8} \right]^{\frac{1}{2}}. \qquad (4.6)$$

This interaction will scale as $V_b(\nu_3)^{1/2}$. Since we only use $\tilde{A}$-state levels with $\nu_3 \leq 2$ and at most $4V_b$, the $\nu_3 \leftrightarrow \{2V_b\}$ anharmonic matrix elements will not change from $\nu_3= 0$ to $\nu_3= 2$ by more than a factor of $2(2)^{1/2}$. The energy difference of the interacting states is smallest between $1\nu_3 \leftrightarrow 2V_b$ at $\approx$400 cm^{-1} and largest between $1\nu_2+2\nu_3 \leftrightarrow 1\nu_2+4V_b$ at $\approx$900 cm^{-1}. The only unknown parameter is $K_{3,2V_b}$.

3. $\tilde{A}$-state Coriolis Perturbations: The $1_{1,0}$ rotational level cannot be affected by B- or A-type Coriolis interactions.[17] However, all of the intermediate levels can be affected by C-type Coriolis interactions.[17] With a matrix element on the order of $C_\nu\sqrt{J(J+1)} \approx 1\text{cm}^{-1}$, the closest C-type Coriolis perturber to $V_0^0\ K_0^1$ would be $1\nu_3$. The energy difference between these levels is $\approx$1,048 cm^{-1}. An estimate of the amount of $K_a'=0$ character will be 0.0001%, which is far below the detection limit in these experiments. While it is possible that other intermediate levels will have greater fractional $K_a'=0$ character, the $V_0^0\ K_0^1$ DF spectrum contains extra features that are at least 1% as intense as the allowed features. The energy shift and intensity contributions due to C-type Coriolis interactions will scale roughly as J^2. Further evidence that the extra features are not due to C-type Coriolis interactions can seen from the DF spectra recorded via ${}^rQ_0(1)$ and ${}^rQ_0(9)$ $V_0^2\ K_0^1$ transitions, see Figure 4.18. The expected increase in Coriolis coupling by a factor of ~80 should result in easily detectable relative intensity changes of the extra and polyad DF features at low energy. The relative changes, seen in Figure 4.18, are only on the order of ±20%.

4. $\tilde{A} \leftarrow \tilde{X}$ Axis-Switching: Several Axis-Switching transitions, ΔK=0 and 2, have been identified in $\tilde{A} \leftarrow \tilde{X}$ absorption spectra.[13] The appearance of these transitions is *not* due to any perturbation. They derive their intensity from the slight difference, $\Theta_T=2.5^0$, in the Eckart *a*-axes of the $\tilde{A}$ and $\tilde{X}$ states.[18] For each intermediate state vibrational band, the observed T_0 values place the allowed K_0^1 subbands between the nominally forbidden K_0^0 and K_0^2 axis-switching subbands. High-J Q transitions of the K_0^2 subband will overlap low-J Q transitions in the K_0^1 subbands. For example ${}^sQ_0(20)$ of $V_0^2\ K_0^2$ and

$^{r}Q_0(1)$ V_0^2 K_0^1 are calculated to lie $\approx 1 cm^{-1}$ apart. Let us assume that these two transitions actually occur within our 0.06 cm^{-1} laser linewidth. If this were true, the emission from V_0^2 K_0^2 would access different $\tilde{X}$-state [N_s,N_{res},l,g] polyads which could coincide with the extra DF features. However, these types of transitions can be ruled out by further investigation of the DF spectra recorded via $^{r}Q_0(1)$ and $^{r}Q_0(9)$ transitions of the V_0^2 K_0^1 band. The $^{r}Q_0(9)$ transition of V_0^2 K_0^1 and the $^{s}Q_0(22)$ transition of V_0^2 K_0^2 are calculated to lie $\approx 1 cm^{-1}$ apart. The relative Boltzmann population differences between the ground state rotational levels, J"=1,9,20, and 22, used to access the $\tilde{A}$ state intermediates will cause relative intensity variations of the DF spectra recorded via $^{r}Q_0(1)$ V_0^2 K_0^1 : $^{s}Q_0(20)$ V_0^2 K_0^2 and $^{r}Q_0(9)$ V_0^2 K_0^1 : $^{s}Q_0(22)$ V_0^2 K_0^2. The calculated relative intensity differences between $N_{J"=1}/N_{J"=20}$ and $N_{J"=9}/N_{J"=22}$ is a factor of 40. Again, Figure 4.18 does not display relative intensity differences of this magnitude.

5. $\tilde{A} \rightarrow \tilde{X}$ Axis-switching: $\tilde{A} \rightarrow \tilde{X}$ axis-switching transitions have been observed in stimulated emission pumping experiments probing the E_{vib}= 7,000 cm^{-1} region of the $\tilde{X}$ state.[5,6,16,19] The calculated K_a'=0 character contribution to the nominal J'=1 K_a'=1 intermediate state is on the order of 0.0001%.[19] Furthermore, intensities for axis switching transitions have been shown to be proportional to ~J^2.[18] The relative intensities of the allowed and axis-switching transitions accessed via $^{r}Q_0(1)$ and $^{r}Q_0(9)$ intermediate states would differ by a factor of 80, see Figure 4.18.

6. $\tilde{X}$-State Rotational-l-Resonances: Rotational-l-resonance effects in the $\tilde{X}$ state have been observed by both high-resolution absorption and optical-optical double resonance experiments.[5,6,19,20] The rotational-l-resonance will couple states differing in l by $\Delta l = \pm 2$.

This effectively destroys the l polyad quantum number. For a level with predominantly ν_4 vibrational character, the separation between l=0 and 2 will be approximately 2 cm^{-1}. The actual splitting between the two l components depends upon the total amount of excitation in ν_4 and ν_5. At E_{vib}=10,000 cm^{-1}, the l splitting is resolvable in our low resolution DF spectra. Rotational-l coupling matrix elements will have a J^4 dependence.[19,20,21,22] DF spectra recorded via $^rQ_0(1)$ and $^rQ_0(9)$ transitions of V_0^2 K_0^1 would display an increase in the strength of the rotational-l-resonances by a factor of 9^4. This dependence is not evident in Figure 4.18.

7. $\tilde{X}$-state Coriolis Resonance: Both high-resolution absorption and optical-optical double resonance experiments have observed Coriolis effects in the $\tilde{X}$ state. A Coriolis interaction will couple $\Delta N_s=\pm1$, $\Delta l=\pm1$ polyads. For example, [1,5,0,g] will be coupled to [0,5,1,g] through a 2,444 third-order Coriolis interaction. Third-order Coriolis coupling matrix elements are on the order of 0.003 cm^{-1} and will scale as $(J(J+1))^{3/2}$.[19] Such a strongly J dependent trend is not visible in Figure 4.18.

Unfortunately, experimental evidence does not support any of the seven above hypotheses as being *solely* responsible for the observed extra $\tilde{A} \rightarrow \tilde{X}$ emission features. It is possible that the second, sixth, and seventh hypotheses can lend some insight into possible explanations. In order to define experiments to identify the extra features, all of the quantitative and qualitative information from the DF spectra must be examined.

There are five qualitative trends of the extra features. First, at low $\tilde{X}$-state energies, the extra features appear near each N_{res} energy region. Second, the extra features always appear at lower energies than the ZOBS. Some extra features also appear to the blue of the

ZOBS. Third, at higher $\tilde{X}$ -state energies, the gap between the extra features and the Franck-Condon bright ZOBS narrows. The two extra features cross, around N_{res}= 9. Fourth, at higher energies, extra features appear at both higher and lower energy than the ZOBS. Fifth, the intensities of the extra features are largest at low energies. It appears that the extra features almost disappear by 10,000 cm^{-1}.

The low energy region is the best place to identify quantitatively the extra features. The [1,5,0,g] polyad is located at 3,000 cm^{-1}. The acetylene density of vibrational states at this energy is very small, ρ_{vib}<0.1per cm^{-1}. Using the H^{eff} model we can specify *all* polyads that would exist in this energy region. This includes states which are not normally accessible in $\tilde{A} \rightarrow \tilde{X}$ transitions. Only one predicted polyad, [0,5,1,g], lies near the extra features, see Figure 4.17b. From hypothesis seven, this polyad could appear through a $\Delta N_s=\pm 1$, $\Delta l=\pm 1$ third-order Coriolis resonance, 2,444. This interaction was ruled out by the lack of strong J-dependence in the relative intensities of the extra features observed via DF spectra originating from ${}^{r}Q_0(1)$ and ${}^{r}Q_0(9)$ transitions of $V_0^2 K_0^1$ and the small, 0.003 cm^{-1}, coupling matrix elements. However, these polyads do follow the qualitative trends of *most* of the observed extra features. At E_{vib}= 3,000 cm^{-1}, the N_s=0, l=1 polyads *do* lie at lower energies than the N_s=1, l=0 polyads. Due to the difference in the x_{ij} anharmonicities for each ZOBS the N_s=0,l=1 polyads will tune, versus N_{res} through the N_s=1, l=0 polyads. The crossing occurs at N_{res}=9 for both the computed and experimental spectra for N_s=1. Similar arguments can be used to account for the extra features that occur near the [0,6,0,g], [0,8,0,g], and [0,10,0,g] polyads.

The 2,444 Coriolis coupling rules for [N_s,N_{res}, l] polyads suggest a plausible identification of the extra features based solely upon their energy positions. However, not all

of the extra features can be attributed to perturbations via the "2,444 resonance". The [1,5,0/2,g] polyad region contains three extra features. Only one of these extra features is accounted for by invoking a 2,444 coupling mechanism. In addition, the intensity trends for the extra features cannot be explained at present. In several cases, near the [1,5,0,g] and [1,7,0,g] polyads, the extra features are more intense than the allowed transitions! Moreover, the ratio of intensities between the extra and allowed DF features changes for each intermediate state used in these DF experiments! This may indicate that some interaction in the $\tilde{A}$ -state is responsible for the extra features. The possibility still exists that there are remote anharmonic interactions in the $\tilde{A}$ state, see Hypothesis 2. We are conducting a series of high-resolution DF and SEP experiments in the low energy region to determine conclusively the exact nature of the extra features.

It is important to note that the XCC pattern recognition technique did *not* have difficulty with the extra features. Since, all of the extra features were extracted as distinct spectral patterns, it is unlikely that the extra features represent a breakdown of the conserved polyad quantum numbers. If the extra features were attributed to $\tilde{X}$ -state resonances not currently considered in our H^{eff} model, the goodness of the $[N_s, N_{res}, l]$ polyad patterns would be destroyed! This would effectively scramble the polyad intensity patterns rendering them useless in any pattern recognition scheme. This is contrary to the fact that we can pull meaningful polyad patterns out of the DF spectra.

4.6 Discussion

We have implemented an XCC pattern recognition technique to extract information about the low E_{vib} acetylene $\tilde{X}$ -state polyad structure. The pattern recognition technique is complemented by our high quality DF spectra. The usefulness of a highly redundant data set

in extracting quantitative information about the vibrational excitation at chemically significant energies has been discussed. Our method has enabled us to extract unbiased information about the energy and intensity distributions for each acetylene polyad up to E_{Vib}=12,000 cm^{-1}. This information is useful to construct a series of zero-order energies and relative Franck-Condon factors for the (nV_2,mV_4) ZOBSs. Subsequent experiments and papers will utilize this information in a stepwise fashion to (1) refine our current H^{eff} with data from lower E_{vib} regions, (2) apply XCC to higher E_{vib} regions, (3) compare XCC patterns to H^{eff} , and (4) extract zero-order energies and FCF. This four step process is performed over sequential E_{vib} regions.

The DF spectra probe the molecular potential surface along specific directions, (Q_2, Q_4). Most of the optical experiments on acetylene have been restricted to lower E_{Vib} regions where the ZOBS does not contain high vibrational excitation in the CC stretch, *trans*- and *cis*-bending vibrations. The zero-order energies and FCFs of the ZOBSs observed in DF spectra complement the enormous amount of data available from a completely different set of ZOBSs observed in direct absorption spectra. From all of this work, we hope to extend our understanding of the molecular dynamics to the energy region of the acetylene $\leftrightarrow$ vinylidene isomerization at 16,000 cm^{-1} and beyond. Our goal is to identify these interactions by using DF spectra and our effective Hamiltonian.

4.7 References

1. F.F. Crim, *J. Phys. Chem.* **100**, 12725 (1996) *and references cited therein.*

2. D.J. Nesbitt, R.W. Field, *J. Phys. Chem.* **100**, 12735 (1996) *and references cited therein.*

3. S.A.B. Solina, J.P. O'Brien, R.W. Field, W.F. Polik, *J. Phys. Chem.* **100**, 7809 (1996).

4. S.A.B. Solina, J.P. O'Brien, R.W. Field, W.F. Polik, *Ber. Bunsen-Ges. Phys. Chem.* **99**, 555 (1995).

5. D.M. Jonas, S.A.B. Solina, B. Rajaram, R.J. Silbey, R.W. Field, K. Yamanouchi, S. Tsuchiya, *J. Chem. Phys.* **99**, 7350 (1993).

6. D.M. Jonas, S.A.B. Solina, B. Rajaram, R.J. Silbey, R.W. Field, K. Yamanouchi, S. Tsuchiya, *J. Chem. Phys.* **97**, 2813 (1992).

7. M.A. Abbouti-Temsamani and M. Herman, *J. Chem. Phys.* **102**, 6371 (1995).

8. M.A. Abbouti-Temsamani, M. Herman, S.A.B. Solina, J.P. O'Brien, R.W. Field, *J. Chem. Phys.* **105**, 11357 (1996).

9. P.R. Bunker, *Molecular Symmetry and Spectroscopy*, pp. 330-332, Academic Press, New York (1979).

10. A. McCoy, N.E. Sibert III, *J. Chem. Phys.* **00**, 0000 (1996).

11. M. Jacobson, S.L. Coy and R.W. Field, *J. Chem. Phys., accepted.*

12. S.L. Coy, M. Jacobson and R.W. Field, *J. Chem. Phys., submitted.*

13. J.K.G. Watson, M. Herman, J.C. van Craen, and R. Colin, *J. Mol. Spectrosc.* **95**, 101 (1982).

14. R.C. Hilborn, *Am. J. Phys.* **50**, 982 (1982).

15. G.J. Scherer, Y. Chen, R.L. Redington, J.L. Kinsey, and R.W. Field, *J. Chem. Phys.* **85**, 6315 (1986).

16. S.A.B. Solina, Ph.D. Thesis, Massachusetts Institute of Technology (1996).

17. H.L. Dai, R.W. Field, J.L. Kinsey, *J. Chem. Phys.* **82**, 2161 (1985).

18. J.T. Hougan, J.K.G. Watson. *Can. J. Phys.* **43**, 298 (February 1965).

19. D.M. Jonas, Ph.D. Thesis, Massachusetts Institute of Technology (1992).

20. M. Herman, *J.Chem. Phys.*, *accepted.*

21. G. Amat and H.H. Nielsen, *J. Mol. Spectrosc.* **23**, 359 (1967).

22. J. Pliva, *J. Mol. Spectrosc.* **44**, 165 (1972).

Chapter 5: Polyad patterns in the 12,000-16,000 cm^{-1} region of the $\tilde{X}^1\Sigma_g^+$ State of Acetylene

5.1 Introduction

In this chapter we will discuss the results of pattern recognition in the E_{vib} 12,000-16,000 cm^{-1} region of the $\tilde{X}^1\Sigma_g^+$ state of Acetylene. Chapters 1-3 contain detailed information about the $\tilde{A}^1A_u \leftrightarrow \tilde{X}^1\Sigma_g^+$ transition and the polyad structure on the ground electronic state, S_0. Briefly, we utilize a new statistical method, the extended cross correlation (XCC), for recovering the relative intensities and intensity weighted average energy positions of individual polyads.[1,2] The integrated intensity from each polyad pattern results in a zero-order bright state (ZOBS) Franck-Condon factor (FCF). The deperturbed energy positions of the ZOBS are extracted by calculating the mass weighted center, or energy centroid, of each polyad pattern. We can utilize the intensity and frequency information from the intrapolyad patterns to refine the molecular effective Hamiltonian, H^{eff}, model discussed in Chapters 1 through 4.[3] We are currently in the process of refining the H^{eff} model and only preliminary results will be presented in this thesis. The complete results of the H^{eff} model refinement and the XCC pattern recognition in the 12,000-16,000 cm^{-1} region of the $\tilde{X}^1\Sigma_g^+$ State of Acetylene will be described in a paper planned for publication in the *Journal of Chemical Physics.*

5.2 Experimental

The dispersed fluorescence (DF) experimental setup has been described in detail in Chapter 3. Briefly, we record a series of medium resolution, 8 cm^{-1} in the 350 nm region when recorded in second order, dispersed fluorescence spectra which originate from four different rovibrational levels of the $\tilde{A}^1A_u$ state but which terminate on the same rovibrational

eigenstates of the $\tilde{X}^1\Sigma_g^+$ state of Acetylene. The DF spectra were recorded by locking the dye laser output onto the ${}^rQ_0(1)$ transition which populates the , $J'_{K_a,K_c} = 1'_{1,0}$ level of the $V_0^1K_0^1$, $V_0^2K_0^1$, $2_0^1V_0^1K_0^1$, $2_0^1V_0^2K_0^1$ vibrational bands of the $\tilde{A}^1A_u \leftarrow \tilde{X}^1\Sigma_g^+$ transition. (V represents the *trans*-bending mode, ν_3' in the $\tilde{A}$ state and ν_4'' in the $\tilde{X}$ state, and 2 represents transitions in CC stretch. The subscript and superscript denote the lower and upper state quanta, respectively.) A static gas cell was charged with 5 Torr of acetylene, 99.6% pure (Matheson). The total spontaneous fluorescence from each rovibronic transition was imaged by a series of fused silica lens (described in detail in Chapter 3), *f*/10, onto the entrance slits of a Spex 1000mm monochromator. The fluorescence was dispersed and collected in second order from 5800 Å to 7000 Å in 100 Å segments. This corresponds to emission from 2900-3500 Å. A baseline function was removed from each DF segment prior to frequency calibration or segment concatenation. Multiple records of the same DF segment were useful in identifying and removing spurious peaks. The routines for frequency calibration and segment concatenation were used to produce the 4 DF spectra described above. An *additional* quasi-continuous baseline (Q-CB) function was removed from each concatenated DF spectrum prior to running the XCC pattern recognition routines. The form and probable physical source of the Q-CB will be discussed at length in Chapter 6.

We have not recorded an intensity response curve for the Spex 1000 mm monochromator in second order. Since the standard spectral intensity lamp has continuous emission from 2000 to 9000Å, the recorded intensity response in second order would include contributions from 1st and 2nd orders. Therefore, an appropriate cutoff filter must be used to block unwanted fluorescence. This should be done in the future and would allow meaningful

relative intensities to be extracted from DF spectra recorded in second order. For the work presented here, we have not applied any intensity calibration curve. The spectral intensity was normalized yielding *approximate* relative intensity information. The normalization procedure was conducted as follows. The intensity of the origin band spectra recorded in first order was divided by a grating response curve provided by Spex. The corrected intensity of each spectral feature recorded in first order was compared to the same feature recorded in second order. The relative intensities between first and second order were normalized such that the intensity response from each spectral feature recorded in first and second order were the same. The intensity normalization for the remaining four DF spectra was conducted as described in Chapter 3.

We have included the Origin band, $V_0^0K_0^1$, DF spectrum with the four DF spectra described above. The $V_0^0K_0^1$ DF spectrum was convoluted with a Gaussian to reduce its resolution to that of the FWHM of the other four DF spectra. Deperturbed ZOBS energies are given in Table 5.1. Table 5.1 also contains a list of the ZOBS FCF's. Detailed information about the procedure used to extract the zero-order energies and FCF's is given in Chapter 4.

Plots, see Figures 5.1-5.4, of the FCF agree with the Franck-Condon principle where the nodal properties of the $\tilde{A}$-state wavefunctions are projected onto the $\tilde{X}$-state FC ZOBS progressions. For example, the vibrationless level of the $\tilde{A}$ state will result in smooth FCF along both the V_2 and V_4 progressions. Similarly, the $V_0^2 K_0^1$ $\tilde{A}$-state intermediate will result in smooth FCF progressions along V_2, but the progression along the V_4 progression will have two nodes at 12 and 18, respectively. The $2^1 V_0^2 K_0^1$ DF spectrum displays nodes at V_2=2, V_4=12, and V_4=18 see Figure 5.4.

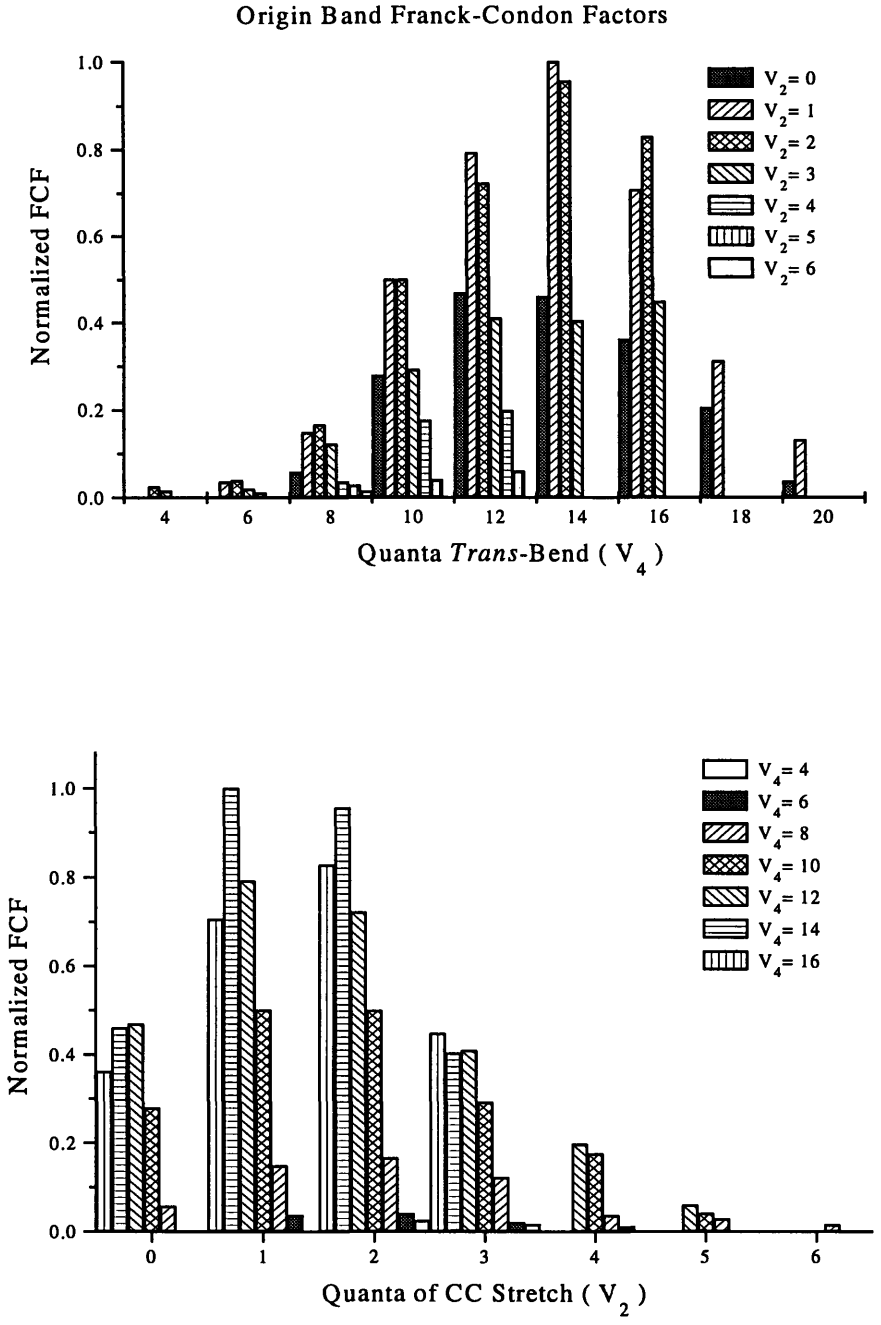

Figure 5.1: The upper plot displays the Franck-Condon Factors extracted from the DF spectrum recorded from $V_0^0K_0^1$ versus V_4. The lower plot displays the Franck-Condon Factors extracted from the DF spectrum recorded from $V_0^0K_0^1$ versus V_2. Note, the FCF's in both plots follow a smooth Gaussian-like function.

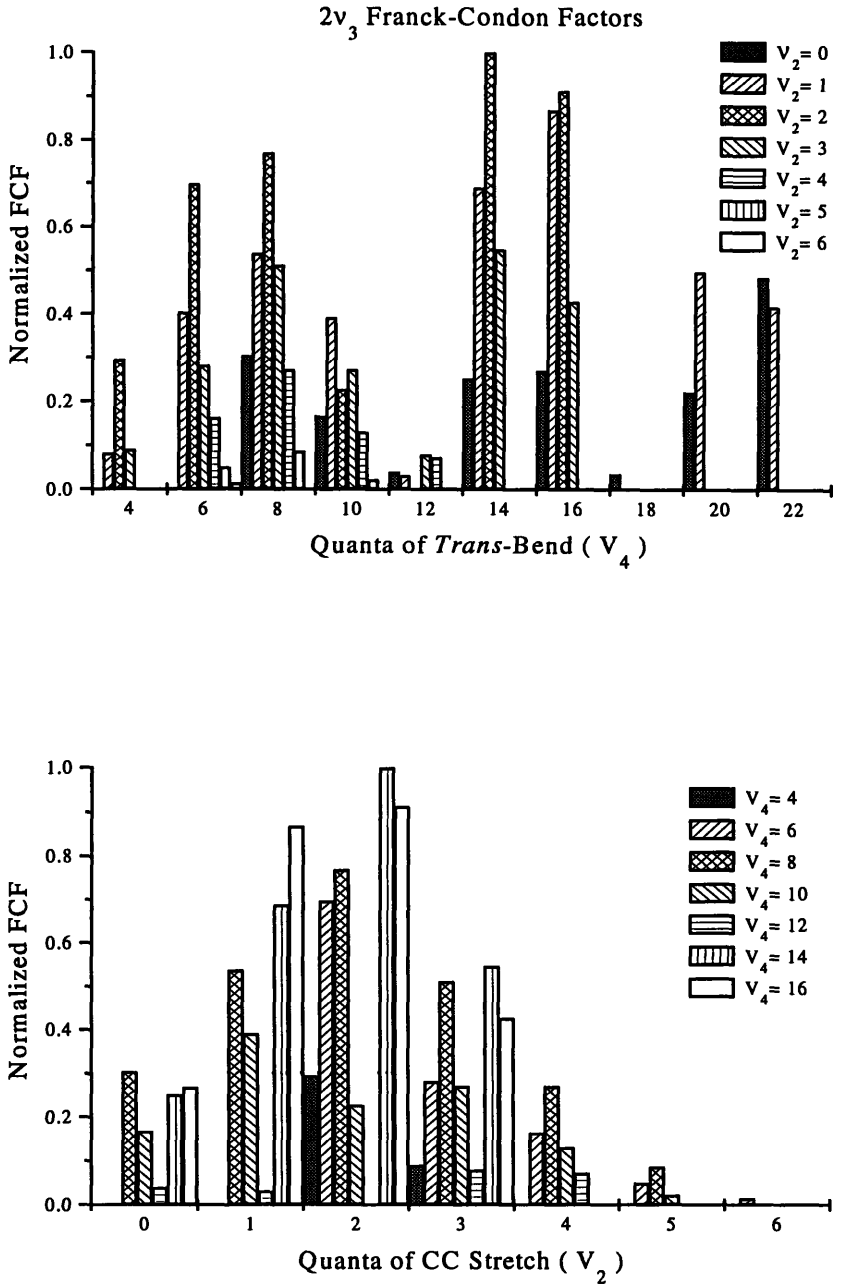

Figure 5.2: The upper plot displays the Franck-Condon Factors extracted from the DF spectrum recorded from the $V_0^2K_0^1$ level versus quanta of *Trans*-bend, (V_4). Note the two nodes at 12 and 18 quanta of V_4, respectively. The lower plot displays the Franck-Condon Factors extracted from the DF spectrum recorded from the $V_0^2K_0^1$ level versus quanta of CC stretch, (V_2). Note, the FCF envelope follows a smooth Gaussian-like function.

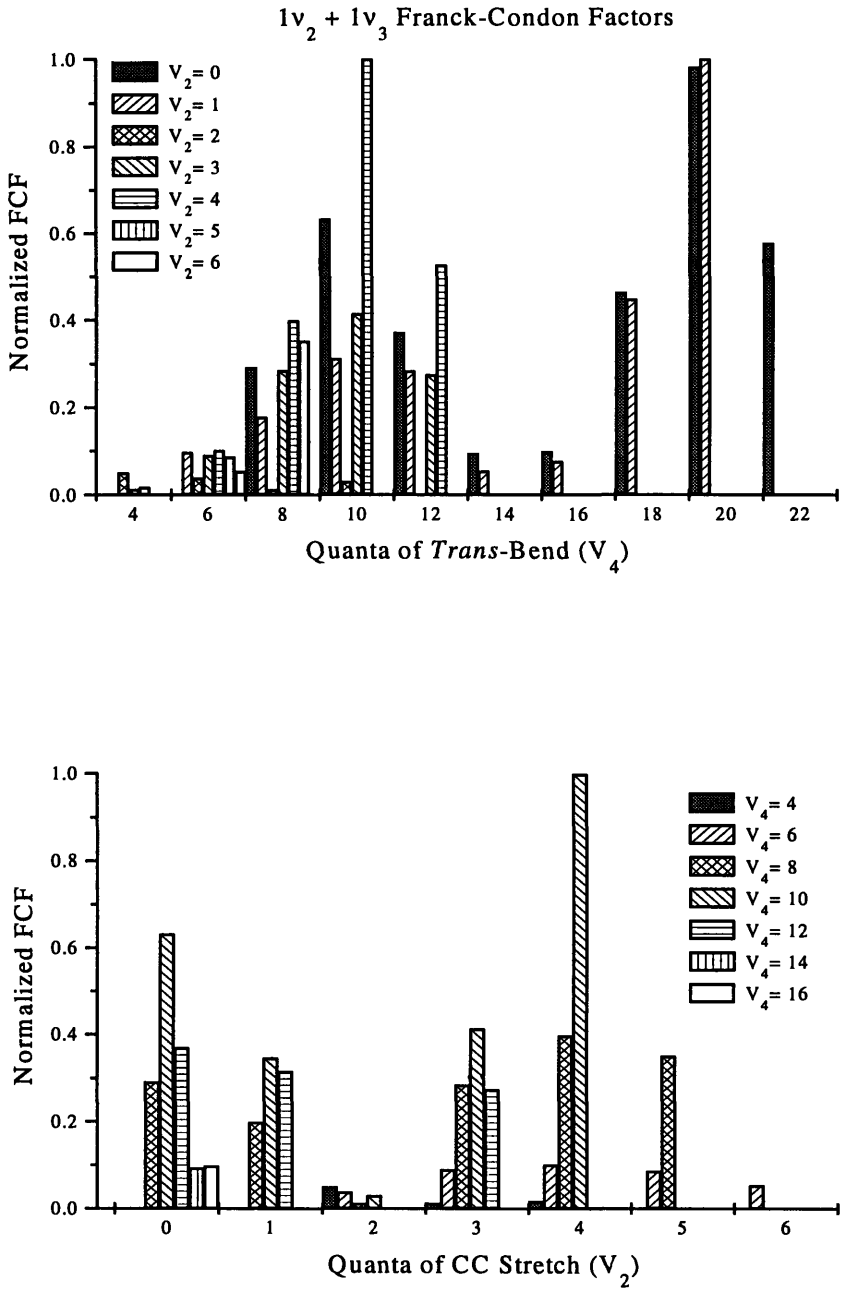

Figure 5.3: The upper plot displays the Franck-Condon Factors extracted from the DF spectrum recorded from the $2_0^1V_0^1K_0^1$ level versus quanta of *Trans*-bend, (V_4). Note the node at 14 quanta of V_4. The lower plot displays the Franck-Condon Factors extracted from the DF spectrum recorded from the $2_0^1V_0^1K_0^1$ level versus quanta of CC stretch, (V_2). Note the node at 2 quanta of V_2.

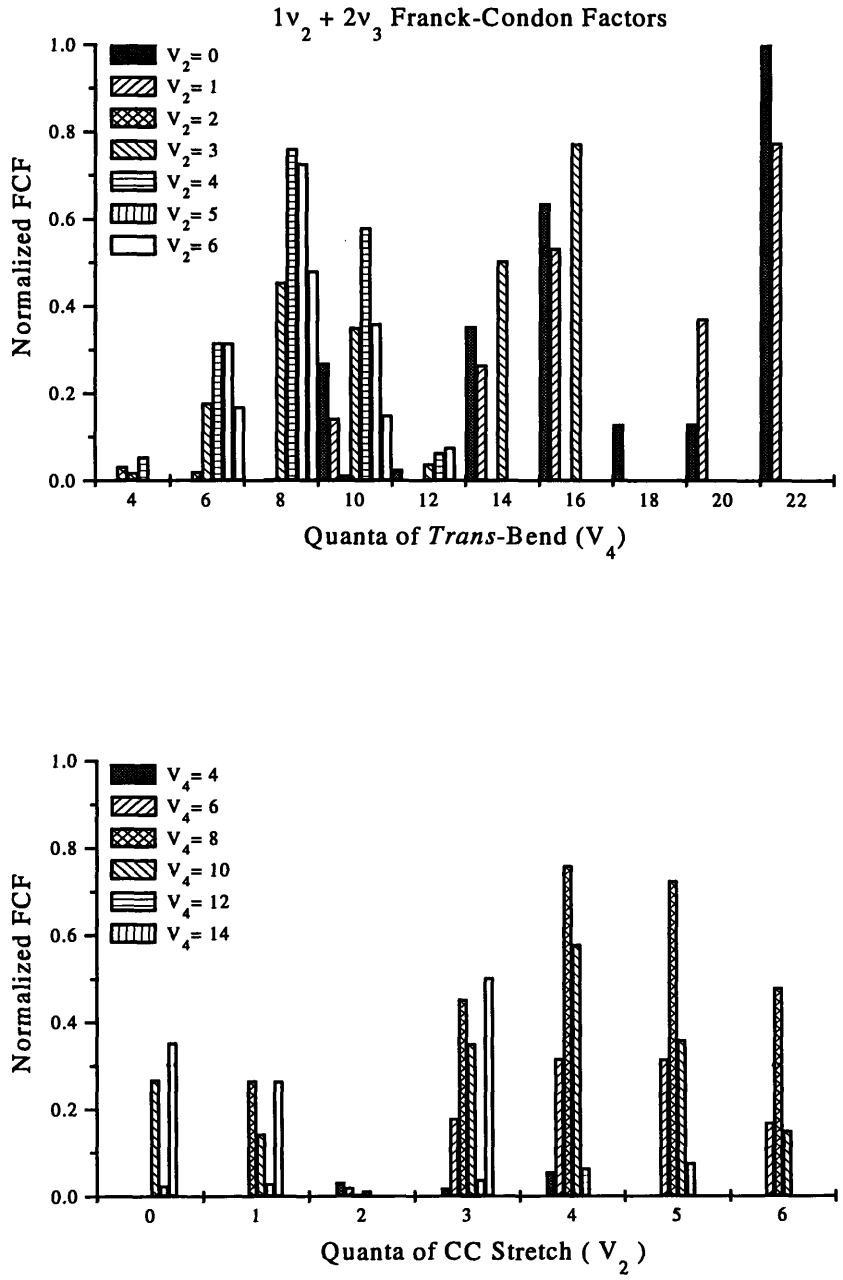

Figure 5.4: The upper plot displays the Franck-Condon Factors extracted from the DF spectrum recorded from the $2_0^1V_0^2K_0^1$ level versus quanta of *Trans*-bend, (V_4). Note the two nodes at 12 and 18 quanta of V_4, respectively. The lower plot displays the Franck-Condon Factors extracted from the DF spectrum recorded from the $2_0^1V_0^2K_0^1$ level versus quanta of CC stretch, (V_2). Note the node at 2 quanta of V_2.

Table 5.1: Deperturbed zero-order energy positions for the zero-order bright states (ZOBS) and the Franck-Condon Factors. Note that the [0,18,0/2,g], [3,19,0/2,g] and [5,19,0/2,g] polyads are not contained in this table. See text for details.

Polyad $[N_s,N_{res}]$	Deperturbed ZOBS Energies (cm^{-1})	FCF $V_0^0K_0^1$	FCF $V_0^2K_0^1$	FCF $2_0^1V_0^1K_0^1$	FCF $2_0^1V_0^2K_0^1$
[2,18]	11468.03	0.7228	0.0	0.0	0.0
[4,18]	11323.87	0.0114	0.1629	0.0904	0.3157
[1,19]	12342.83	0.7068	0.8685	0.0764	0.5319
[3,19]	12011.59	0.2926	0.2711	0.3712	0.3503
[0,20]	13336.61	0.0375	0.2212	0.8792	0.1299
[2,20]	12818.57	0.9562	1.0000	0.0	0.0
[4,20]	12561.39	0.0370	0.2711	0.3575	0.7597
[1,21]	13760.54	0.3124	0.0	0.4480	0.0
[3,21]	13304.30	0.4104	0.0792	0.2460	0.0381
[5,21]	13154.60	0.0	0.0498	0.0775	0.3151
[0,22]	14745.34	0.0	0.4835	0.5168	1.0000
[2,22]	14175.68	0.8286	0.9121	0.0	0.0
[4,22]	13839.86	0.1766	0.1299	0.8965	0.5797
[1,23]	15176.19	0.1313	0.4970	1.0000	0.3712
[3,23]	14651.51	0.4042	0.5470	0.0	0.5029
[5,23]	14400.68	0.0286	0.0863	0.3156	0.7254
[4,24]	15115.98	0.1985	0.0723	0.4716	0.0637
[6,24]	14985.31	0.0	0.0151	0.0480	0.1684
[1,25]	16621.39	0.0	0.4161	0.3948	0.7738
[3,25]	15986.52	0.4487	0.4272	0.1710	0.7717
[5,25]	15655.82	0.0409	0.0218	0.7512	0.3597
[6,26]	16179.97	0.0153	0.0	0.1734	0.4799
[5,27]	16926.88	0.0602	0.0	0.3999	0.0754
[6,28]	17464.19	0.0	0.0	0.2789	0.1499

5.3 Results

5.3.1 The N_s=0 Polyads

The XCC pattern recognition routine was used to extract several N_s=0 polyad patterns in the E_{vib}=12,000-16,000 cm^{-1} region. Figure 5.5 displays the observed and calculated N_s=0

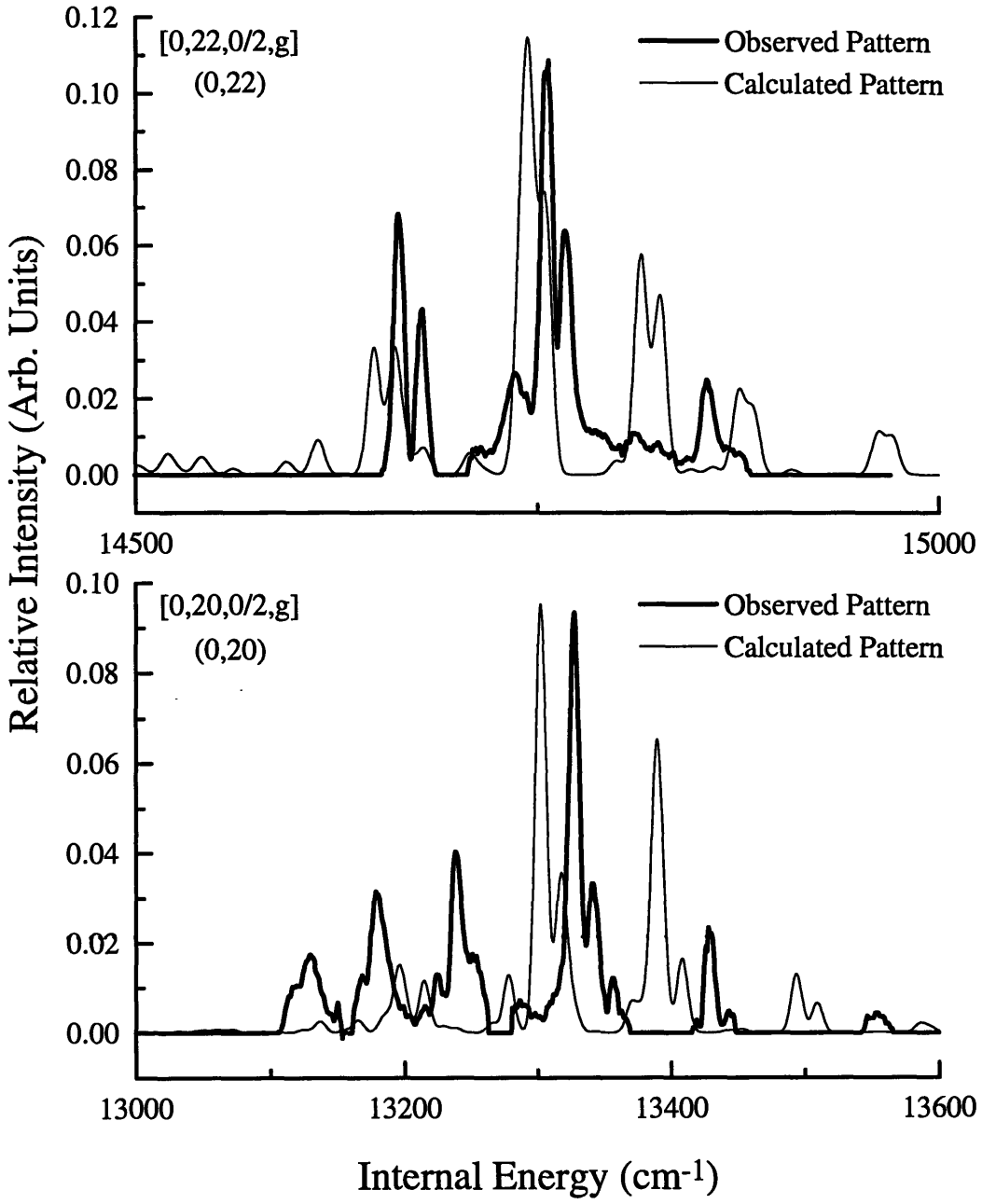

Figure 5.5: Observed (heavy line) and calculated (light line) polyad patterns, [0,20,0/2,g] (upper panel) and [0,22,0/2,g] (lower panel).

polyad patterns N_{res}=20 and 22. Notice that the qualitative agreement of the centroid and the intensity fractionation pattern between the observed and calculated spectra is observed to degrade at higher E_{vib}. This is not surprising because, in Chapter 4, we had discussed how the H^{eff} model which displayed quantitative agreement at E_{vib}<10,000 cm^{-1} began to degrade towards only qualitative agreement with the XCC polyad patterns by E_{vib}=12,000 cm^{-1}. At E_{vib}=16,000 cm^{-1}, the predicted and observed N_s=0 polyads exhibit the largest deviation.

The XCC pattern recognition routine failed to extract the intensity and energy information for the [0,18,0/2,g] polyad at E_{vib}≈11,950 cm^{-1}. Moreover, the [3,19,0/2,g] and [5,19,0/2,g] polyads also located in this energy region, at E_{vib}≈11,950 and 11,975 cm^{-1} respectively, could not be extracted by the XCC routine. Failure of the XCC routine to disentangle a polyad pattern could be due to a breakdown of the H^{eff} model caused either by a normally weak inter-polyad resonance, which becomes unusually important over a restricted E_{vib} region or through an acetylene interaction with a near degenerate vinylidene state. The zero-point level of the vinylidene minimum is computed to be located at ≈15,500 cm^{-1}. Therefore, it is unlikely that an acetylene ↔ vinylidene interaction could affect the [0,18,0/2,g] polyad at E_{vib}=12,000 cm^{-1}. It is possible that the change in the inter-polyad structure due to a weak inter-polyad resonance could cause a catastrophic breakdown of the H^{eff} model in this restricted energy range. However, the XCC routine is successful in extracting polyad patterns for a number of other nearby polyads, [4,18,0/2,g], [2,18,0/2,g], and [1,19,0/2,g], located at 11,340, 11474, and 12,329 cm^{-1}, as well as the [0,20,0/2,g] and [0,22,0/2,g] polyads located at 13,274 and 14,751 cm^{-1}, see Figures 5.5-5.7, and 5.9. In order for an inter-polyad resonance to result in such a localized effect, the resonance must be extremely selective to the specific E_{vib} region which contains the [0,18,0/2,g], [3,19,0/2,g] and

[5,19,0/2,g] polyads. Higher resolution DF studies should be performed over this region to determine whether the polyad structure is corrupted either by a breakdown of the H^{eff} model or by too severely overlapped polyad patterns.

5.3.2 N_s=1 Polyads

All of the predicted N_s=1 polyad patterns, from E_{vib}= 4,000 to 16,000 cm^{-1}, have been extracted by the XCC routine. The results from the XCC pattern recognition routine for the N_s=1 polyads in the E_{vib}=12,000-16,000 cm^{-1} region are displayed in Figure 5.6. It is encouraging that the [1,21,0/2,g] polyad was recovered. The ZOBS for this polyad, (1,18), is very similar to the (0,18) ZOBS for the non-extracted [0,18,0/2,g] polyad. The predicted amount of fractionation for the [1,21,0/2,g] polyad is greater than that for the [0,18,0/2,g] polyad. It may seem counter-intuitive that the polyad pattern with the greater fractionation could be extracted by the XCC routine while the pattern with less fractionation could not! However, this can be explained through detailed information about the location and the relative intensities of the neighboring polyads. The strong spectral features of the [3,19,0/2,g] and [5,19,0/2] polyads coincide with the strongest features of the [0,18,0/2,g] polyads. The observed relative intensities in the DF spectra between these polyads are almost equal, where as, the [4,22,0/2,g] and [6,22,0/2,g] polyads, located close to the maximum of the [1,21,0/2,g] polyad display very different relative intensities.

5.3.3 N_s>1 Polyads

Several N_s>1 polyads were extracted from the DF spectra in the E_{vib}=12,000-16,000 cm^{-1} region, see Figures 5.7-5.10. Notice that (1) for constant V_2 the extracted polyad patterns, with a ZOBS of (nV_2,mV_4), have increasing fractionation with increasing quanta of

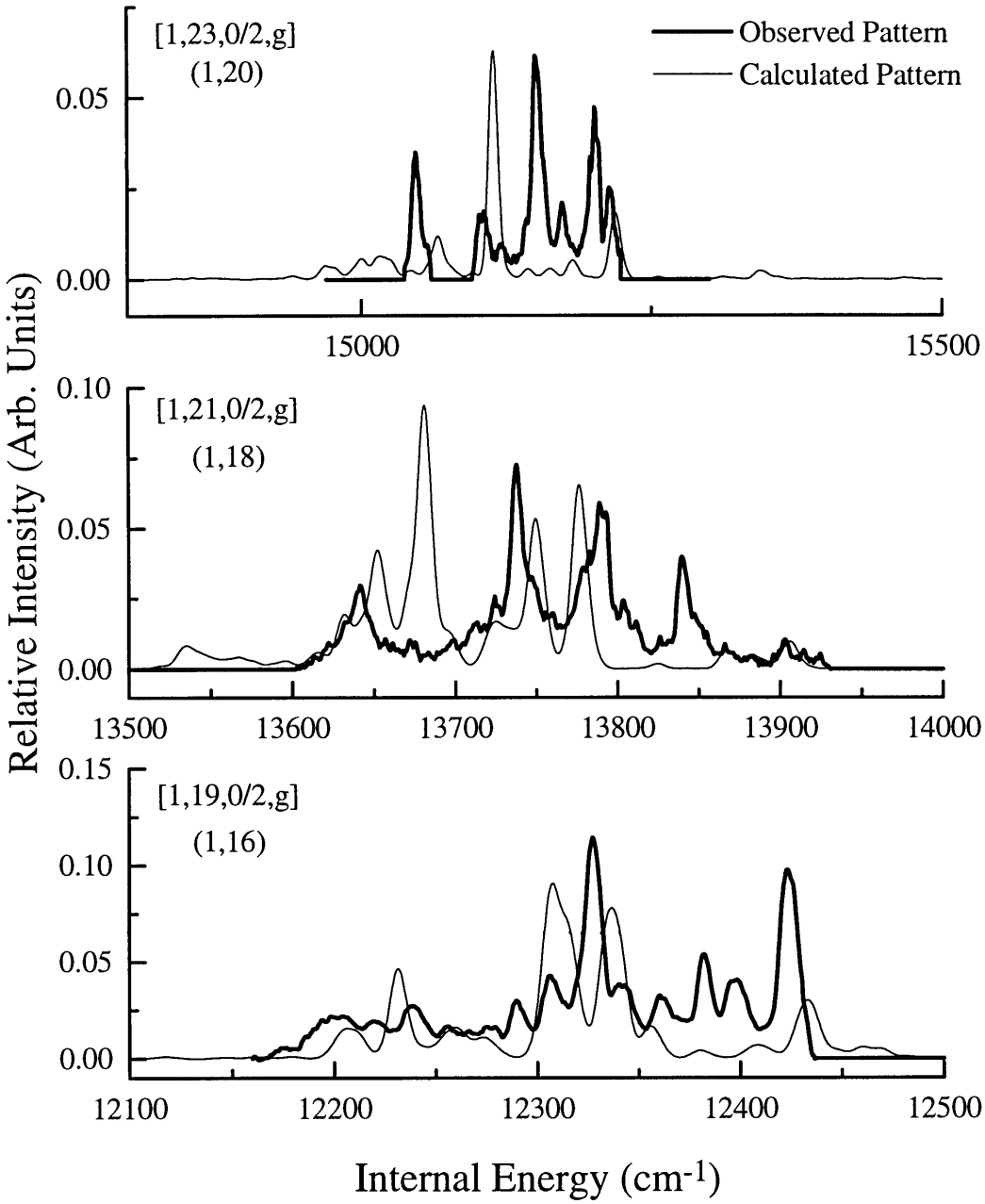

Figure 5.6: The observed (heavy lines) and calculated (light lines) N_s=1 polyad features.

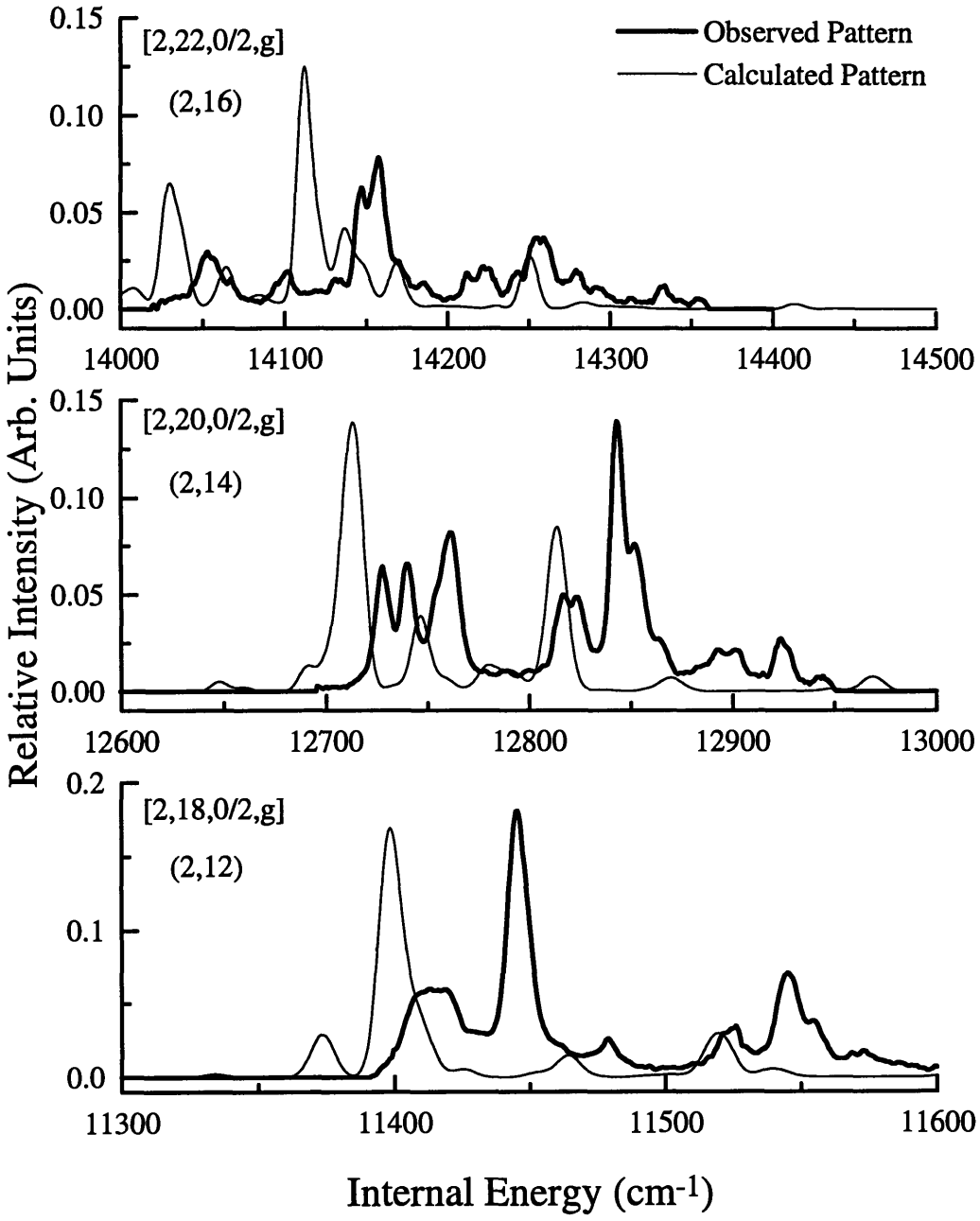

Figure 5.7: The observed (heavy lines) and calculated (light lines) N_s=2 polyad patterns.

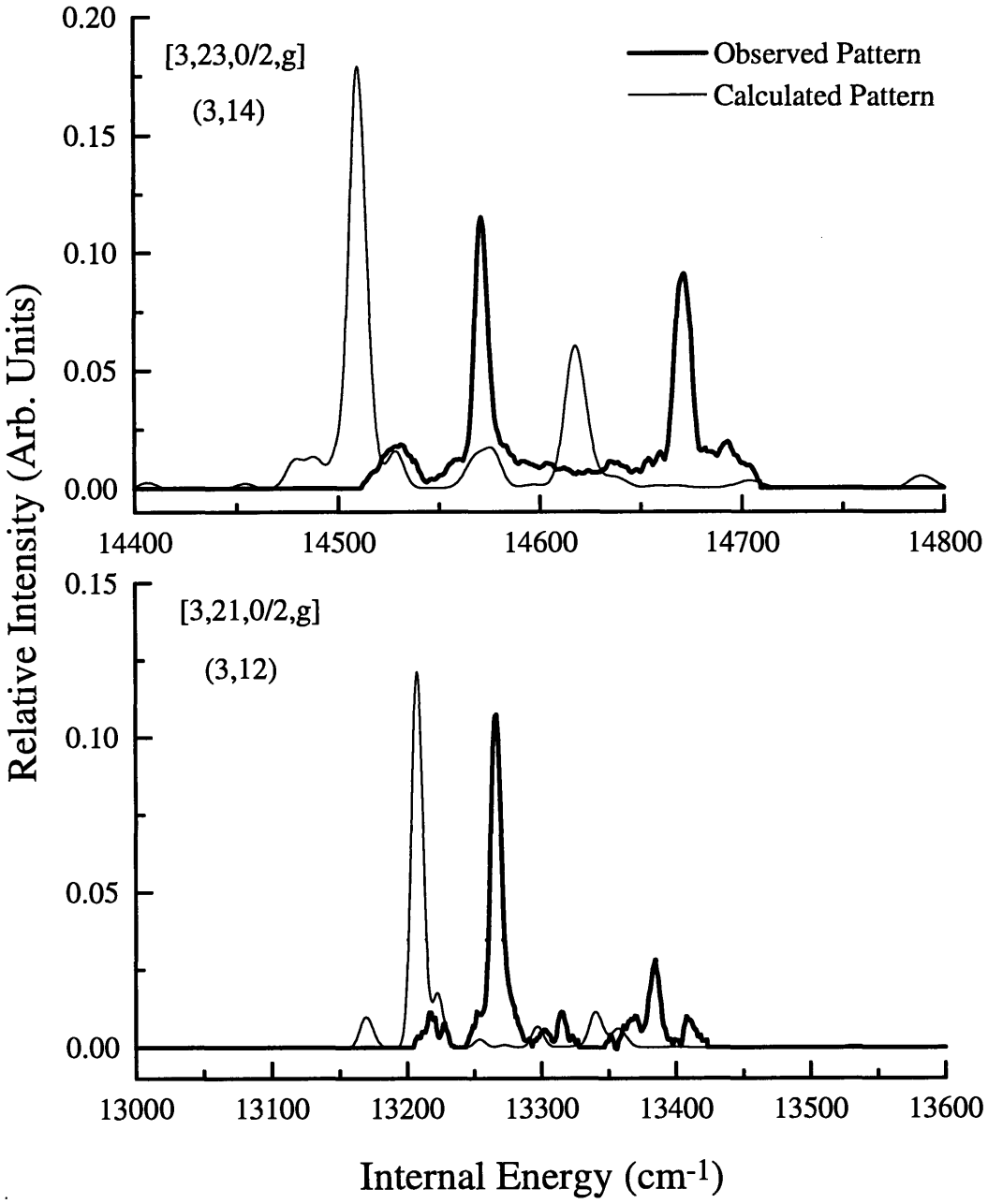

Figure 5.8: The observed (heavy lines) and calculated (light lines) N_s=3 polyad patterns.

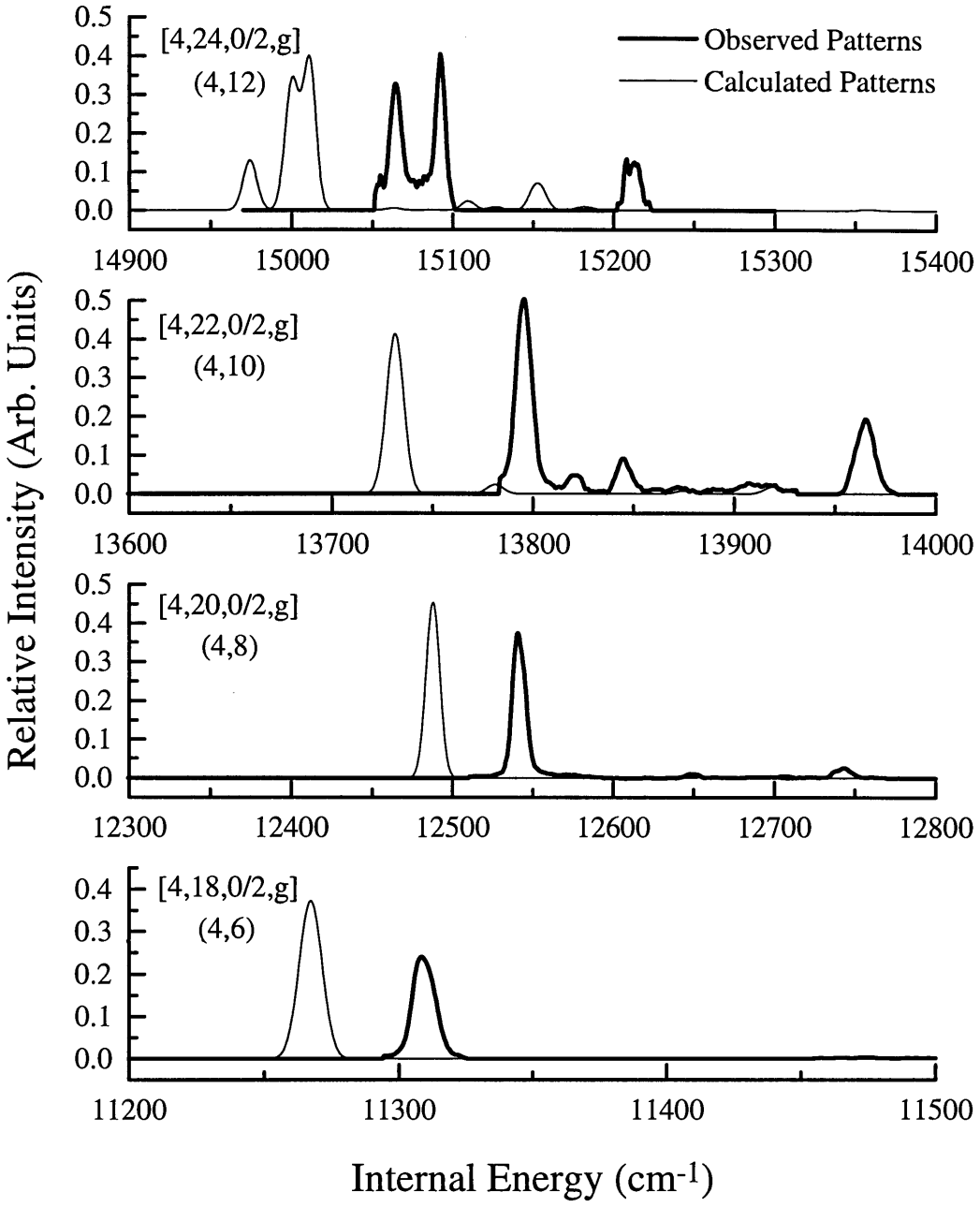

Figure 5.9: The observed (heavy lines) and calculated (light lines) N_s=4 polyad patterns.

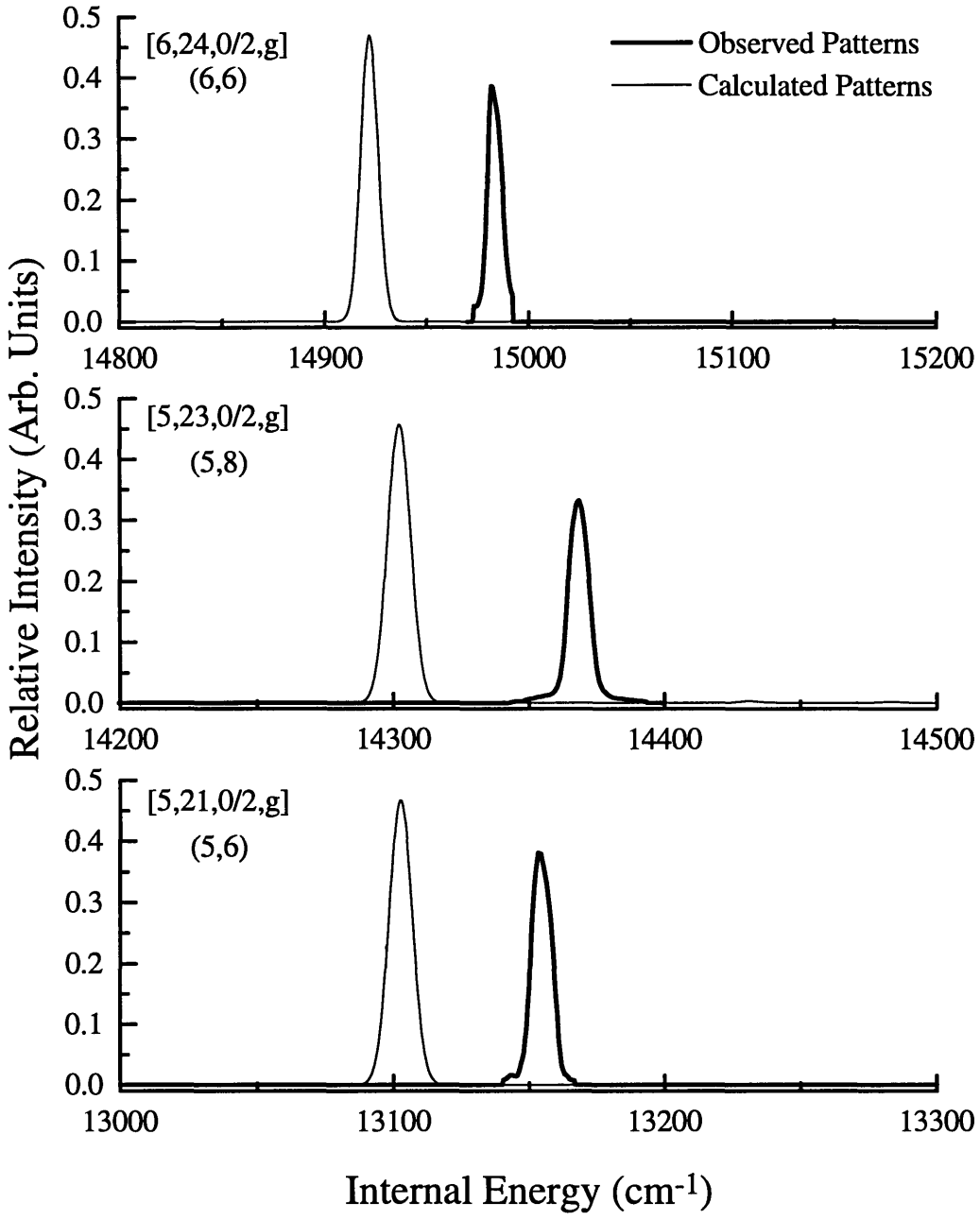

Figure 5.10: The observed (heavy lines) and calculated (light lines) N_s=5 and 6 polyad patterns.

V_4 and (2) the polyad fractionation patterns for a given ZOBS, (nV_2,mV_4) display qualitative agreement with the fractionation patterns of all polyads containing the same V_4, regardless of V_2. Chapter 2 contained a discussion of the IVR trends for polyads containing increasing V_2.[4,5] Briefly, we indicated that a decrease of fractionation with increasing quanta of V_2 was a consequence of a difference in the diagonal anharmonicities of the zero-order bright and dark states. Previous IVR trends were based upon patterns extracted by manual pattern recognition routine and upon an effective Hamiltonian model containing unrefined coupling parameters. It is clear from Figures 5.6-5.9 that the IVR trends, for constant V_4 with increasing V_2, display very *similar* not *simpler* fractionation patterns relative to each other. For example the relative intensity patterns of the [2,18,0/2,g] polyad (with a ZOBS=(2,12)) and the [3,21,0/2,g] polyad (with a ZOBS=(3,12)) are similar. This is a direct result of a resonance tier effect. The Darling Dennison bend-bend interactions are considerably stronger than the stretch-bend interactions, so the fractionation patterns are primarily the result of strong bend-bend interactions and are only secondarily the result of stretch-bend interactions. Figures 5.9 and 5.10 display polyads containing N_s>3 with ZOBS containing $V_2 \approx V_4$ character. Although these polyads contain moderate amounts of stretching, there is no appreciable polyad fractionation. We know that the fractionation due to bend-bend interactions is very small in these polyads due to the widely spaced zero-order energy positions of the bright and dark states, see Chapter 2.[4,5] Briefly, all of the stretch-bend interactions require quanta in the CC stretching *and* in either the *trans*- or *cis*-bending modes. Fractionation due to stretch-stretch interactions can only occur after several stretch-bend resonances have transferred some vibrational energy to the CH stretches. The [5,21,0/2,g] polyad with a (5,6) ZOBS *could* transfer vibrational energy to the CH stretches via several

successive 1,244 resonances. However, these resonances are weak with a typical mixing ratio of $H_{ij}/\Delta E \approx 0.15$ cm^{-1}.[4,5] These resonances are seen in some highly fractionated N_s=1,2 polyads. In general the polyads with high N_s=5,6,7 will not contain visible fractionation due to 1,244.

5.4 Effective Hamiltonian

Presented here is a preliminary refinement of the effective Hamiltonian model. We have embarked on a strategy designed to *sequentially* refine sections of the H^{eff} model. First, as indicated in the previous Chapter, the x_{22}, x_{44}, and x_{24} anharmonicities needed slight adjustments and this was accomplished by correcting them relative to the observed deperturbed energies of the ZOBS, (V_2,V_4), reported in the previous chapter and those listed in Table 5.1. Second, we combine 32 N_s=0 levels from absorption and Raman data with 40 N_s=0 levels extracted from the DF spectra. We weight 5:1 the absorption and Raman:DF N_s=0 levels relative to the DF N_s=0 levels.[6] We perform a least-squares refinement of the N_s=0 pure bending coupling parameters. Figure 5.11 shows the success of the N_s=0 refinement in reproducing the relative intensities and energy positions. Note that the H^{eff} model adequately reproduces the [0,16,0/2,g] polyad (where $E^0_{V_4,V_5} \approx E^0_{16,0} \approx E^0_{14,2} \cdots \approx E^0_{0,16}$)! It is remarkable that the H^{eff} model reproduces all of the N_s=0 polyads in the 4,000-16,000 cm^{-1} region. Third, we combine 40 additional levels from N_s>0 polyads with the levels used in the N_s=0 refinement and perform a global refinement of all parameters in the H^{eff} model. The fitting results from this stage are not complete at this time. The final refinement results will be included in a paper being prepared for publication in the *Journal of Chemical Physics* and in Matthew Jacobson's dissertation.

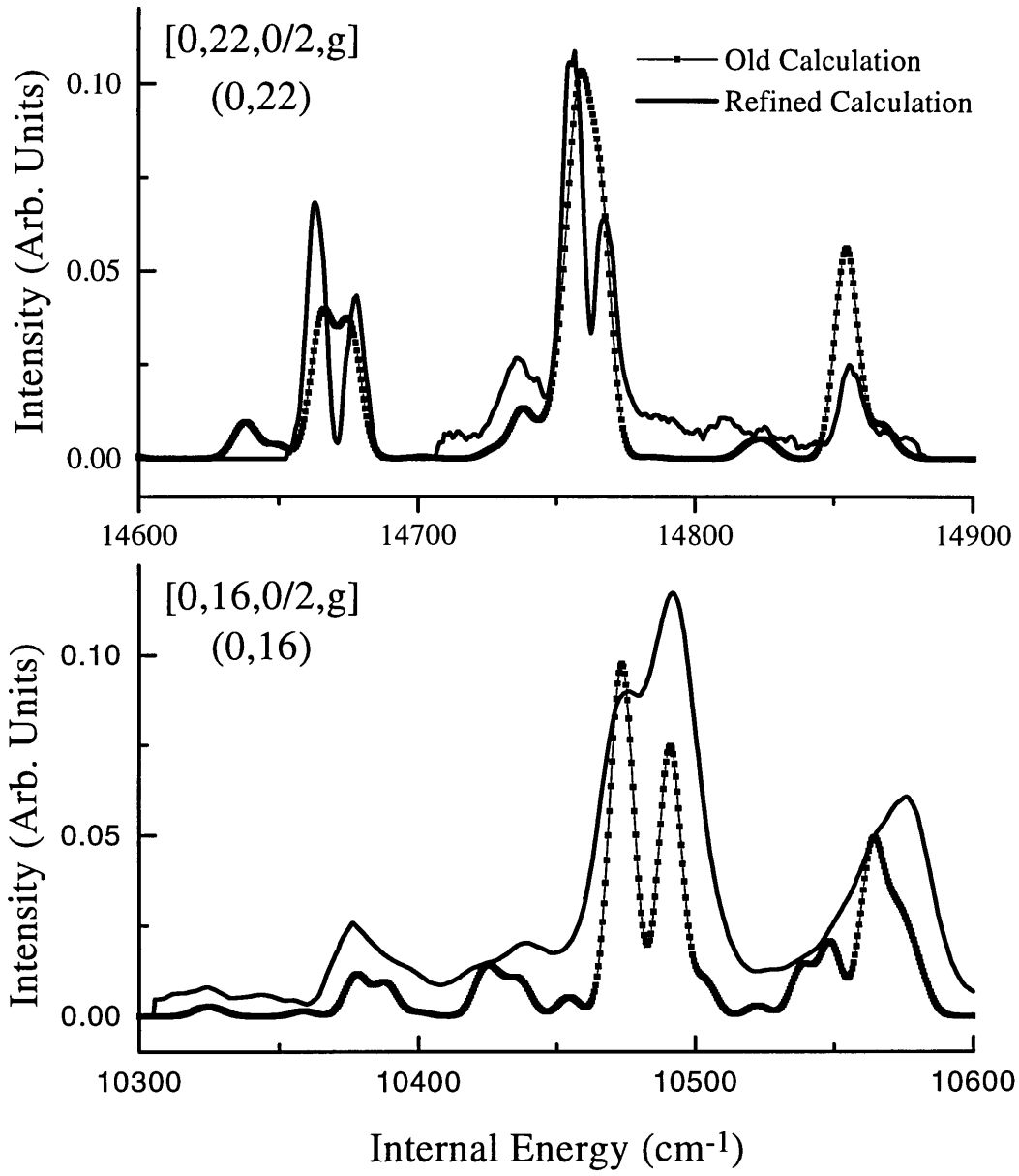

Figure 5.11: The top panel displays the observed (heavy line) and the refined H^{eff} model calculation (light line with squares) for the [0,22,0/2,g] polyad. The lower panel displays the observed (heavy line) and the refined H^{eff} model calculation (light line with squares) for the [0,16,0/2,g] polyad.

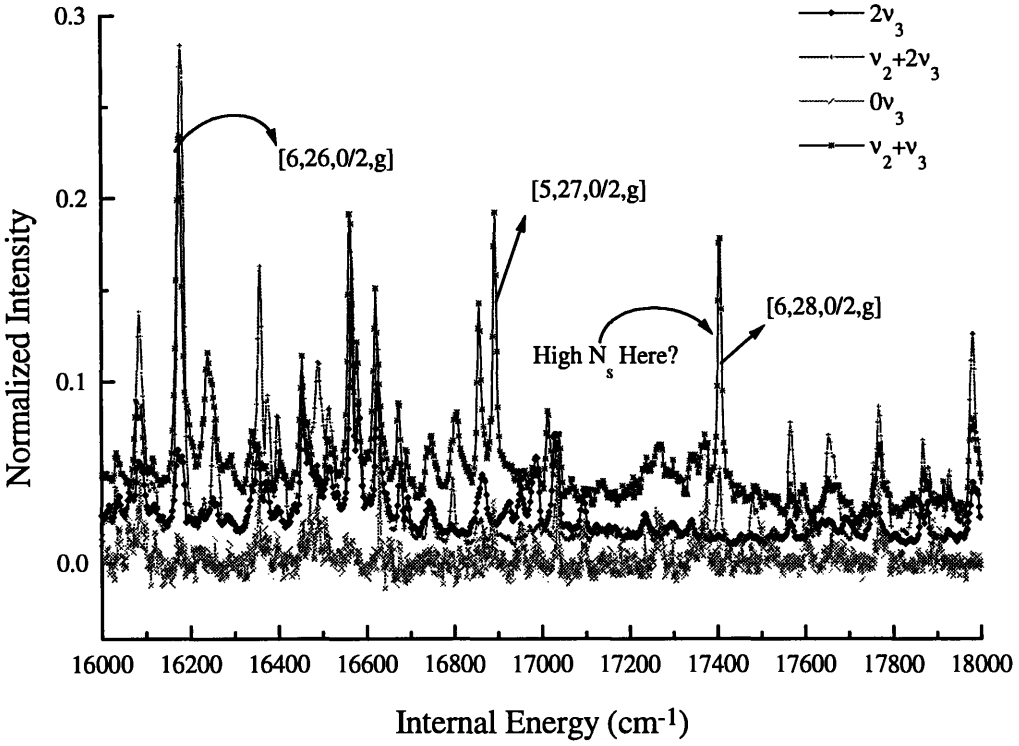

Figure 5.12: DF spectra recorded from the $V_0^0K_0^1$, $V_0^2K_0^1$, $2_0^1V_0^1K_0^1$, $2_0^1V_0^2K_0^1$ $\tilde{A}^1A_u$ state levels. Note several high N_s polyads are clearly visible in this region.

5.5 16,000-18,000 cm^{-1} and $V_2 \approx V_4$ ZOBS

We are confident that the use of our statistical pattern recognition technique and the effective Hamiltonian model will allow us to develop a stronger understanding of the acetylene dynamics at $E_{vib} \geq 15{,}500$ cm^{-1}. Figure 5.12 displays the 16,000-18,000 cm^{-1} region of the $\tilde{A}^1A_u \rightarrow \tilde{X}^1\Sigma_g^+$ DF spectra recorded via $V_0^0K_0^1$, $V_0^2K_0^1$, $2^1V_0^1K_0^1$, and $2^1V_0^2K_0^1$ excited transitions. Notice that each of these spectra contains several sharp and strong features. If the polyad quantum numbers are not destroyed by acetylene $\leftrightarrow$ vinylidene interactions, there is hope that the XCC technique could extract relative intensities and energy positions for several

additional polyads at E_{vib} higher than the predicted vinylidene zero-point level. It is likely that some of these strong features will be due to polyads which have ZOBS containing $V_2 \approx V_4$ character. These will be the best candidates for pattern recognition in this E_{vib} region, because these polyads have a unique fractionation pattern which consists of only one main feature.

It would be highly beneficial to record an additional DF spectrum from the $2_0^1 K_0^1$ vibrational level. Figure 5.14 displays a DF spectrum recorded via the ${}^rQ_0(3)$ excitation transition of the $2_0^1 K_0^1$ vibrational level. The fluorescence intensity of this band is very weak.[7] Because the DF spectrum originates from one quantum of CC stretch in the $\tilde{A}^1A_u$ state, the transitions which terminate on the CC stretching levels in the $\tilde{X}^1\Sigma_g^+$ state will be visible at higher quanta in ν_2 due to an increase in the high ν_2 Franck-Condon factors for progressions in the CC stretch. Therefore, the $2_0^1 K_0^1$, $2^1 V_0^1 K_0^1$, and $2^1 V_0^2 K_0^1$ DF spectra will contain the strongest progressions in V_2. We recommend that the $2_0^1 K_0^1$, $2_0^1 V_0^1 K_0^1$, and $2_0^1 V_0^2 K_0^1$ DF spectra be recorded with the highest possible resolution. This should minimize pattern recognition problems which arise from severely overlapping polyad patterns.

5.6 Acetylene ↔ Vinylidene Interactions

We begin this section by referring the reader to many references whose sole purpose has been to discuss the acetylene ↔ vinylidene interaction.[8,9,10] The original motivation for studying the highly excited vibrational levels of acetylene was to gain insight into the isomerization between acetylene, with $D_{\infty h}$ symmetry, and vinylidene, with C_{2v} symmetry.

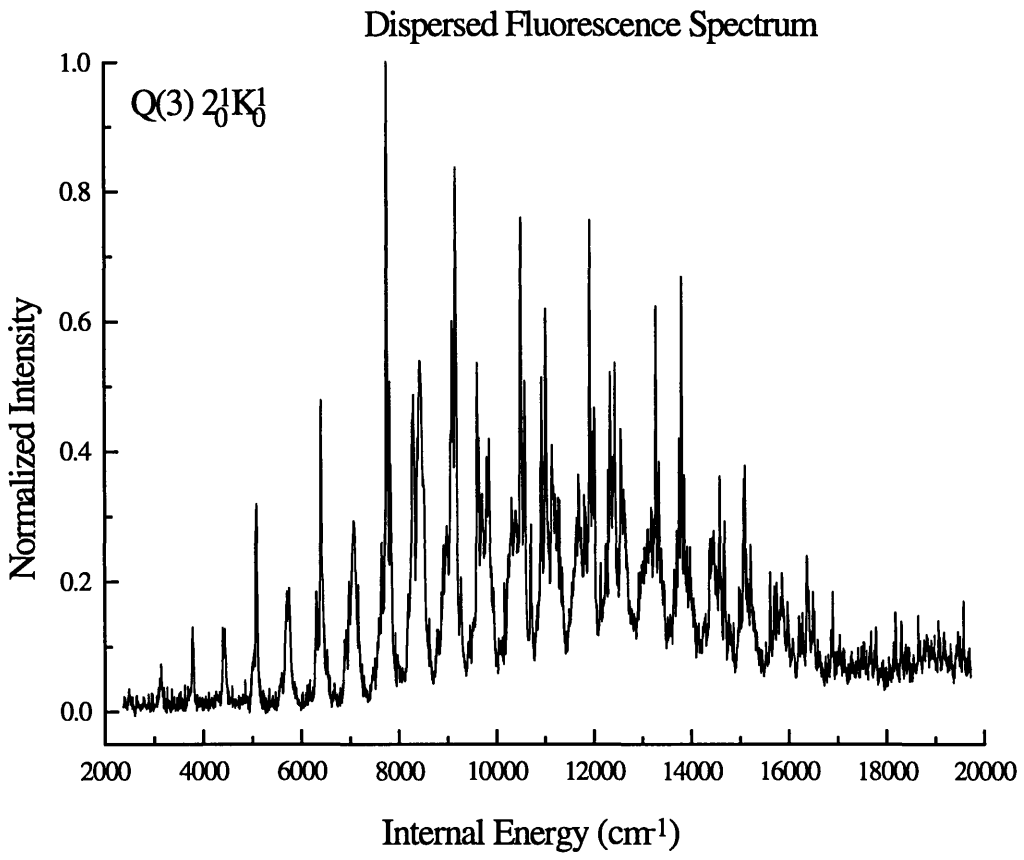

Figure 5.14: The DF spectrum excited via the ${}^rQ_0(3)$ excitation transition of the $2_0^1 K_0^1$ vibrational level. This spectrum was recorded on the Jobin-Yvon 640mm monochromator with a 200 μm slit width. The resolution for a 250 nm photon, recorded in first order, is approximately 110 cm^{-1}. Note the broad quasi-continuum baseline (Q-CB) visible from E_{vib}=6,000-20,000 cm^{-1}. The Q-CB will be addressed in Chapter 6.

The vinylidene zero point level has been calculated to be located at 15,500 cm^{-1} (relative to the acetylene zero-point level).[11] The barrier to isomerization is calculated to lie ≈1,200 cm^{-1} (3-4 kcals) above the vinylidene minimum. Without going into great detail, certain vinylidene rovibrational levels are of the right symmetry to interact with the dense manifold of acetylene levels observable in our DF spectra.[10,12] These interactions could effectively create interpolyad interactions resulting in the degradation or breakdown of the

polyad quantum numbers and the XCC pattern recognition. The fact that we have been able to extract polyad patterns in the 15,000-16,000 cm^{-1} energy region indicates that the polyad structure of the H^{eff} model is conserved at least on the short time scale of our DF experiments for certain ZOBS.

Jacobson has addressed questions regarding the coupling strength and the selectivity of the acetylene $\leftrightarrow$ vinylidene interactions.[13] He has shown that interpretations of the results from previous experiments were incorrect. Briefly, Y.Chen and co-workers employed a cross-correlation technique (not to be confused with the XCC technique) to detect a vinylidene resonance by cross-correlating two stimulated emission pumping spectra.[8,9] They assumed that their SEP spectra, which originated from different $\tilde{A}^1A_u$ state vibrational levels terminated in two distinct sets of $\tilde{X}^1\Sigma_g^+$ state vibrational levels. The presence of a vinylidene interaction at a given E_{vib} would effectively couple all nearby acetylene levels, thereby destroying the assumed distinction between the two sets of levels. Thus, for two SEP spectra, the vinylidene interaction mixes all acetylene levels over a localized E_{vib}, causing the two SEP spectra to sample the same molecular eigenstates. Unfortunately, the global nature of anharmonic couplings between the ZOBS and the dark states was not fully appreciated at that time. We now know that the polyad structure of the $\tilde{X}^1\Sigma_g^+$ state couples many of the dark states in a given energy region.[4,5,13] Therefore SEP spectra originating from the two different $\tilde{A}^1A_u$ state vibrational levels selected by Y.Chen and co-workers will terminate on many of the *same* $\tilde{X}^1\Sigma_g^+$ state polyads and the *same* members of each polyad. Thus, a cross-correlation technique would *fail* to locate any acetylene $\leftrightarrow$ vinylidene interactions.

For a given E_{vib}, we do not have direct knowledge about which acetylene levels will couple most strongly to a vinylidene level. From a naïve point a view, favorable overlap of the transition state with acetylene vibrational levels must contain large amplitude *local*-bending motions. The [*low* N_s, *high* N_{res}] polyads contain many states which would have favorable overlap with both the transition state and the ZOBS. However, the [*high* N_s, *high* N_{res}] polyads contain few states which would have favorable overlap. In fact, the [*high* N_s, *high* N_{res}] polyads are only composed of one main DF eigenstate which usually contains 99% of the ZOBS character. For example the [5,21,0/2,g] polyad pattern consists of one peak which corresponds to the (5,6) ZOBS. The (0,5,0,6,0) vibrational state will certainly not have as favorable overlap with the transition state as eigenstates containing e.g. (0,0,1,7,9) zer-order vibrational character.[14] In the 15,000-16,000 cm^{-1} energy region, it may be plausible that the [*high* N_s, *high* N_{res}] polyads will not interact with vinylidene whereas, the [*low* N_s, *high* N_{res}] polyads will! Breakdown of the polyad quantum numbers *may depend* upon the N_s quantum number.[15]

5.7 Discussion

We have implemented a statistical pattern recognition technique, XCC, to extract spectral polyad patterns in several $\tilde{A}^1A_u \rightarrow \tilde{X}^1\Sigma_g^+$ DF spectra. It should be reiterated that the XCC procedure does not rely on *a priori* knowledge of the H^{eff} model. Polyad information, peak positions and relative intensities, are useful in refining the H^{eff} model. The complementarity of the XCC technique, the effective Hamiltonian model, and our high quality DF spectra has been instrumental in developing deeper insights into the acetylene molecular dynamics at high vibrational energies, $E_{vib} \leq 16{,}000\ cm^{-1}$. In addition, we can use the

predictive power of our H^{eff} model to extrapolate our understanding of the spectrum and the molecular dynamics to higher vibrational energies, E_{vib}>16,000 cm^{-1} where systemactic deviations from the predictions will have diagnostic significance.

Several polyad patterns have been extracted in the $\tilde{X}^1\Sigma_g^+$ state 15,000-16,000 cm^{-1} energy region. The H^{eff} polyad quantum numbers are conserved on the timescale (0.25 ps) of our DF experiments. Future work should focus on recording higher resolution DF spectra of the 16,000-18,000 cm^{-1} energy region where acetylene $\leftrightarrow$ vinylidene interactions may become visible. We have begun a refinement of the effective Hamiltonian model starting with the N_s=0 polyads. The refined bend-only constants are listed in Table 5.2.

Table 5.2: Refined Bend parameters for $^{12}C_2H_2$

Parameters	Fit Values (cm^{-1})[b]
ω_4^0	608.657(34)
ω_5^0	729.137(38)
x_{44}^0	3.483(13)
x_{55}^0	–2.389(14)
x_{45}^0	–2.256(28)
g_{44}^0	0.677(22)
g_{45}^0	6.670(30)
g_{55}^0	3.535(20)
y_{444}	–0.03060(72)
y_{445}	0.0242(48)
y_{455}	0.0072(52)
y_{555}	0.00955(84)
S_{45}^0	–8.574(52)
r_{45}^0	–6.193(32)
r_{445}	0.0304(70)
r_{545}	–0.0110(64)

b The number in parentheses correscponds to the 1σ uncertainty in the last quoted digit.

5.8 References

1. 1. M. Jacobson, S.L. Coy and R.W. Field, *J. Chem. Phys., accepted.*

2. S.L. Coy, M. Jacobson and R.W. Field, *J. Chem. Phys., submitted.*

3. M.A. Abbouti-Temsamani, M. Herman, S.A.B. Solina, J.P. O'Brien, R.W. Field, *J. Chem. Phys.* **105**, 11357 (1996) and *references cited therein.*

4. Solina, S.A.B.; O'Brien, J.P.; Field, R.W. *J. Phys. Chem.* **100**, 7797 (1996) and *references cited therein.*

5. Solina, S.A.B.; O'Brien, J.P.; Field, R.W. *Ber. Bunsen-Ges. Phys. Chem.* **99**, 555 (1995).

6. The weighting of the absorption, infrared, and Raman levels was implemented because the linepositions are typically known to 0.05 cm^{-1}. Where as, the linepositions of the DF levels are known to only 4.0 cm^{-1}.

7. J.K.G. Watson, M. Herman, J.C. van Craen, and R. Colin, *J. Mol. Spectrosc.* **95**, 101 (1982).

8. Y. Chen, Ph.D. Thesis, Massachusetts Institute of Technology, (1988).

9. Y.Chen

10. J.K. Lundberg, *The SEP Spectrum of Acetylene: Symmetry Properties and Isomerization*, Molecular Dynamics and Spectroscopy by Stimulated Emission Pumping, World Scientific, New Jersey (1995) and *references cited therein.*

11. M.M. Gallo, T.P. Hamilton, H.F. Schaefer III., *J. Am. Chem. Soc.* **112**, 3714 (1990) *and references cited therein.*

12. P.R. Bunker, *Molecular Symmetry and Spectroscopy*, pp. 330-332, Academic Press, New York (1979).

13. M.P. Jacobson, Private Communication, (1995).

14. The $(0,0,1,7,9)^0$ basis state is found in the [1,21,0] polyad. The initially excited state, $(0,1,0,20,0)^0$, is coupled to the dark $(0,0,1,7,9)^0$ state by several Bend-Bend resonances and one stretch-bend resonance. At least one Bend-Bend resonance must occur prior to the Stretch-Bend resonance.

15. The most favorable acetylene$\leftrightarrow$vinylidene interactions may also have a slight dependence upon the value of V_4. This would lead to a dependence upon N_{res}.

Briefly, the transition state of the acetylene ↔vinylidene isomerization is composed of a pure local bending motion with a very slight increase in the CC bond length.[11] Favorable overlap of the acetylene vibrational wavefunctions with the transition state will produce vinylidene. The local bending motion of the transition state may be replicated in terms of the acetylene normal mode picture by having equal amounts of *trans*- and *cis*-bending motions. Besides the N_s=0 polyads which always contain basis states with (0,0,0, nV_4, nV_5) only specific polyads with N_s>0 will contain basis states, (0,(m-1)V_2, mV_3, nV_4, nV_5), that are coupled to the ZOBS by strong resonances. The strength of the anharmonic resonances are dependent upon both the zero-order energy positions and the scalable coupling matrix elements.

Chapter 6 : Unexpected Emission Features from the $\tilde{A}^1A_u \rightarrow \tilde{X}^1\Sigma_g^+$ Dispersed Fluorescence Spectra

6.1 Introduction

The high quality of the new DF spectra has enabled us to extract spectral information, energies and intensities, that was difficult to obtain from previous spectral data. The possibility of recording reliable relative intensities over a 20,000 cm^{-1} region of E_{vib} is probably the greatest advance. While optical double resonance spectra would have far superior resolution and absolute frequency calibration, typically 0.03 cm^{-1}, than the DF spectra, the relative intensities are not reliable, especially over energy separations larger than one ~20 cm^{-1} continuous scan region. During the course of extracting polyad energy and intensity patterns from the DF spectra, we have been able to recover and compare polyad spectral intensities that are accurate to better than 20% (on a normalized scale). This is truly remarkable! The high quality DF spectra have also led to some other interesting and unexpected observations (for example the extra DF features discussed at the end of Chapter 4). Experimental and theoretical investigations into these observations is forthcoming but will be unavailable for this thesis. A description of the initial observations and a series of preliminary experiments are included in this chapter to assist with future experiments and/or theoretical work.

All of the dispersed fluorescence spectra which were recorded for the work presented in the earlier chapters contained a quasi-continuous background signal. That is, all of the allowed transitions terminating on the $\tilde{X}$ -state vibrational levels appeared to be 'riding' atop a broad baseline function, see Figure 6.1. A systematic study of the baseline feature was undertaken to prove (1) that the baseline was a molecular feature, not merely

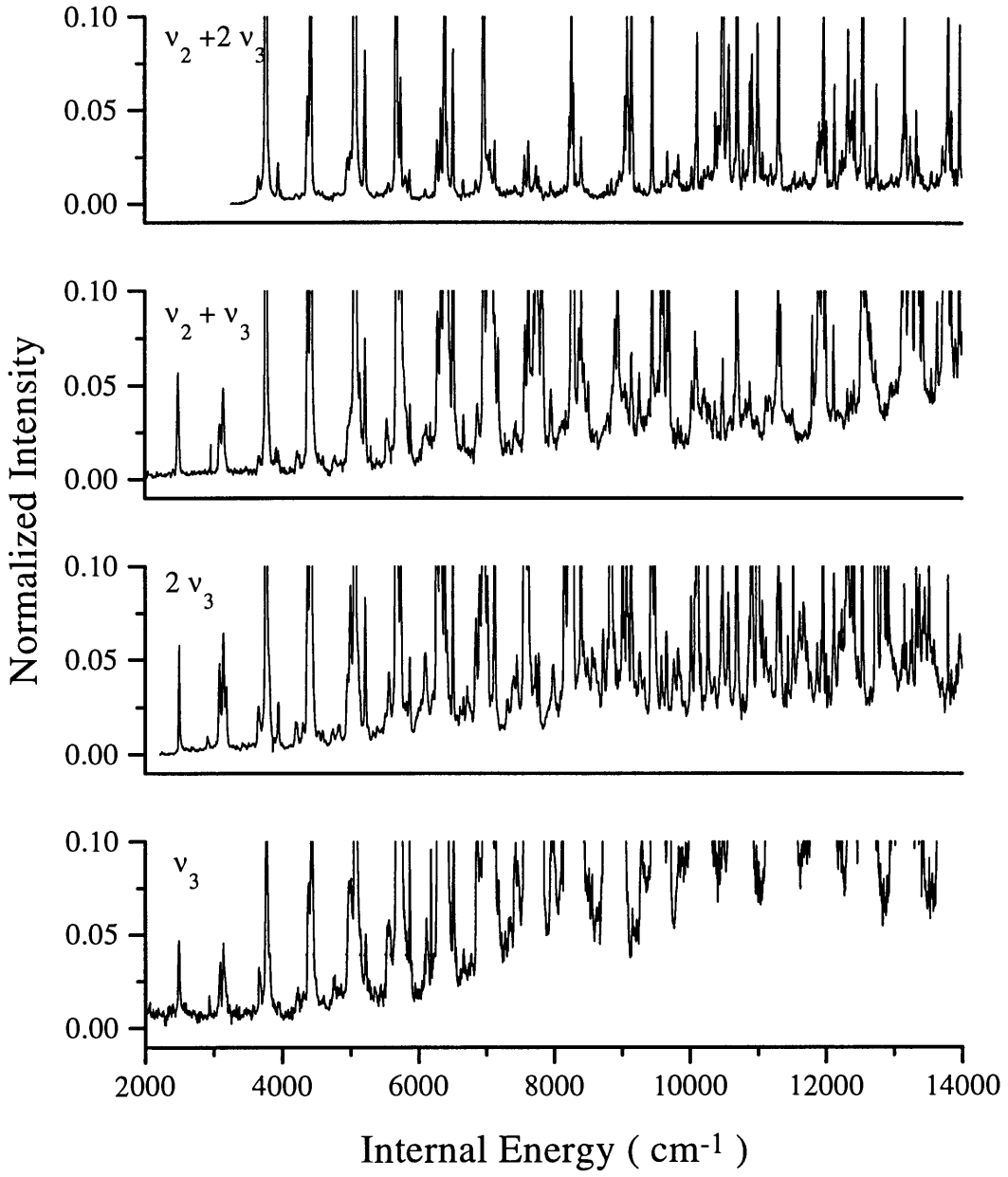

Figure 6.1: DF spectra excited via the ${}^{r}Q_0(1)$ transition of $V_0^1K_0^1$, $V_0^2K_0^1$, $2_0^1V_0^1K_0^1$, and $2_0^1V_0^2K_0^1$. Each spectrum has the tallest feature in the [0,8,0/2,g] normalized to one. The quasi-continuum baseline (Q-CB) function is visible in each spectrum. Note, however, that the amount and gross structure of the Q-CB changes for each DF spectrum.

an experimental artifact, and (2) that the baseline feature is not relevant to the acetylene short time dynamics controlled by our H^{eff}.

6.2 Molecular Emission or Experimental Artifact

As is evident in Figure 6.1, each of the 4 DF spectra contain different relative contributions of a quasi-continuous baseline (Q-CB). The Q-CB has gross structure from 4,000 to 14,000 cm^{-1}. At low internal energy, the Q-CB appears to resemble a Gaussian function. At higher internal energy, the shape of the Q-CB function appears to vary in each DF spectrum. For example, the DF spectrum recorded from the V_0^2 K_0^1 intermediate state contains a Q-CB that is remains constant at higher E_{vib}, where as, the Q-CB in the V_0^1 K_0^1 DF spectrum increases. Originally, the Q-CB feature was treated as an instrument function and was removed from the first DF spectra, excited via V_0^0 K_0^1, recorded at Hope College, see Figure 6.2. There was no intended deception. After all, the $\tilde{A} \leftrightarrow \tilde{X}$ band of acetylene has been studied for almost half a century and no one else had observed or **reported** a quasi-continuous baseline. In addition, the quasi-continuum from the V_0^0 K_0^1 band is a smooth structure with a very small contribution to the overall intensity of the DF spectrum. We will distinguish between the relative intensity of the regular DF features, sharp peaks, and the quasi-continuous baseline in latter sections of this chapter.

Since the DF spectra were recorded on an intensified charge coupled device (ICCD), we investigated the possible mechanism by which the detector could artificially create a quasi-continuum. Older linear arrays, diode arrays, have been known to be prone to exposure and read/write artifacts which lead to anomalies in the intensity readings.

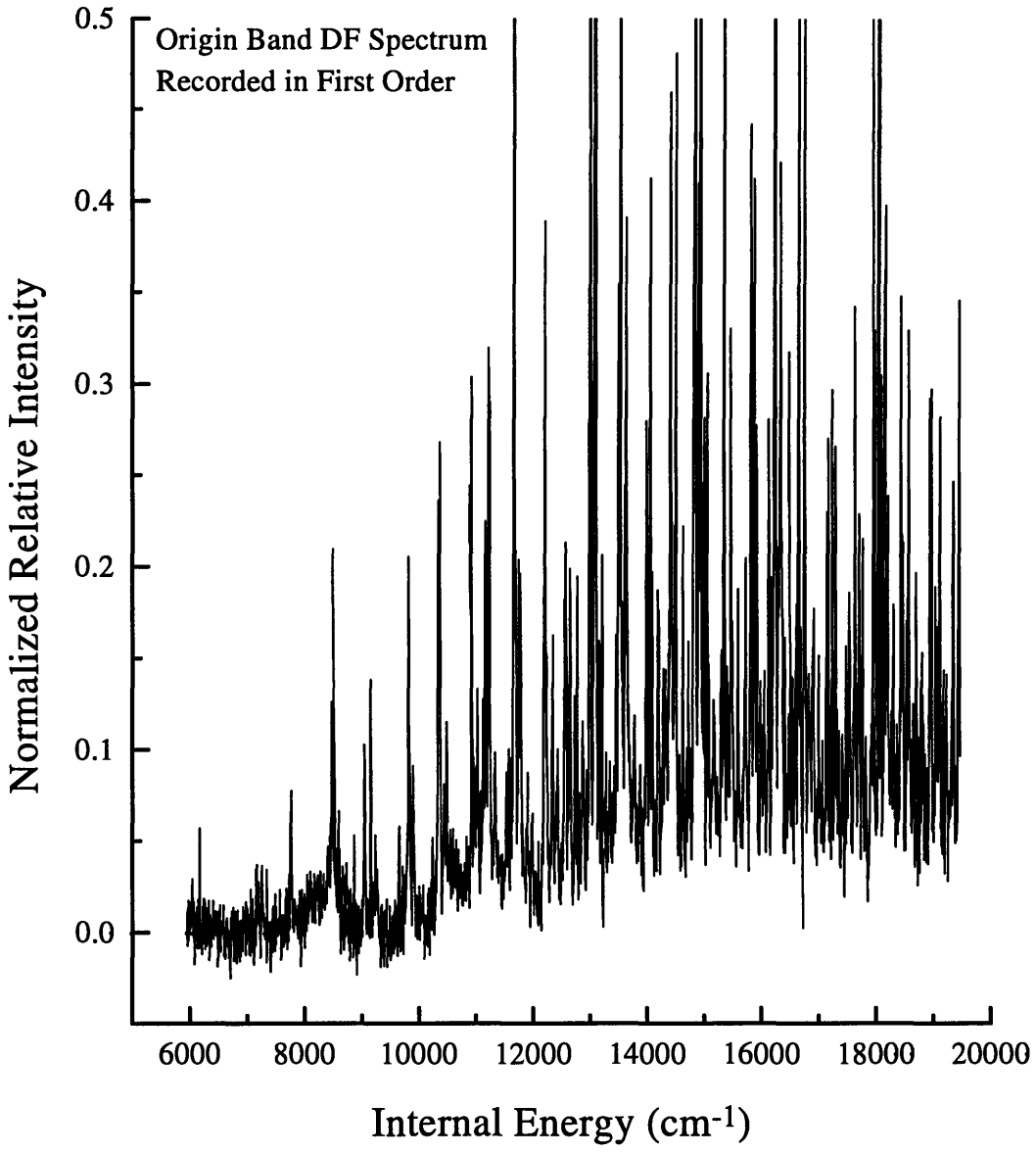

Figure 6.2: DF spectrum recorded in first order from $V_0^0K_0^1$. The spectrum was normalized to the tallest feature in the [1,15,0/2,g] polyad. Notice that a quasi-continuum baseline feature is visible.

Extremely intense emission recorded on a diode array would be degraded by leakage or cross-talk of signal between adjacent diodes. This effect is often visible in a

spectrum, where strong sharp features have a distorted pedestal at the base of each peak.[1] These effects have been diminished by improvements in the array technology. However, if these effects were present on our ICCD, they still could not account for the observed baseline function. The baseline function has its global maximum near the wavelength of the minimum of the acetylene fluorescence. If there were cross-talk between the diodes, one would expect the baseline contribution to be larger near the maximum of the acetylene fluorescence. Of course, one could argue that the integrated area of emission features and the baseline should be correlated, i.e. a few sharp peaks will result in a smaller baseline effect than a dense spectral region where there is a much larger integrated signal. Figure 6.3, contains a plot of the integrated area of the sharp and baseline features for the $V_0^2K_0^1$ DF spectrum versus monochromator position. The integrated area of the sharp and baseline features do not follow the Q-CB function. In several instances, segments with a large integrated contribution from sharp features have a smaller integrated baseline contribution than other segments which contain a smaller contribution from the sharp features.

Older arrays also exhibited read/write errors. As the signal is read from the array, the intensity recorded on one diode from a single exposure gets smeared or distributed across the entire array. Successive exposure/read/write/erase cycles will cause a DC baseline signal to increase slowly. This artifact can be minimized by 'cleaning' the array with multiple erase cycles between successive exposures.[1] Beyond experimenting with multiple erasures of the array after each exposure, we have purposely recorded successive segments on separate days. For example, we have recorded a series of segments where the first recorded segment of the day coincides with the last recorded segment from the previous day. A comparison of the two segments shows no difference in the baseline function. These observations rule out the

possibility that the baseline contains a contribution due to an accumulation of DC signal over the course of a day.

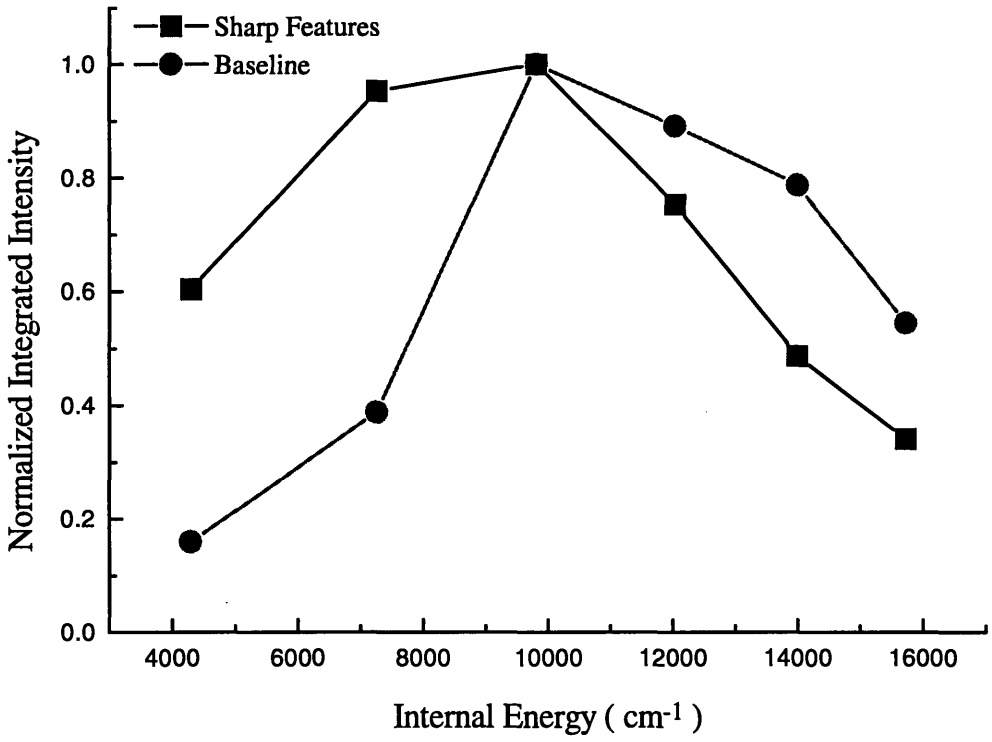

Figure 6.3: The integrated areas of the sharp and baseline features from the $V_0^2K_0^1$ DF spectrum. At higher E_{vib} the sharp and baseline integrated areas cross. Notice that at 4,000 cm^{-1} the ratio of the sharp and baseline features is approximately 0.3, but at 14,000 cm^{-1} the ratio is approximately 0.05.

We must also determine the intensity response function for the DF experimental setup. The intensity response function is usually recorded versus wavelength or frequency. Every optical element will have a characteristic spectral response curve. The entire monochromator intensity response is dominated by that of the dispersive element, the grating. Our system uses a classically ruled grating blazed at 500 nm. A typical spectral response curve for these gratings is shown in Figure 6.4. Note that there is significant enhancement of the grating

efficiency at 450nm and to the red. However, the Q-CB maximum occurs at 350 nm. If the instrument response was in some way

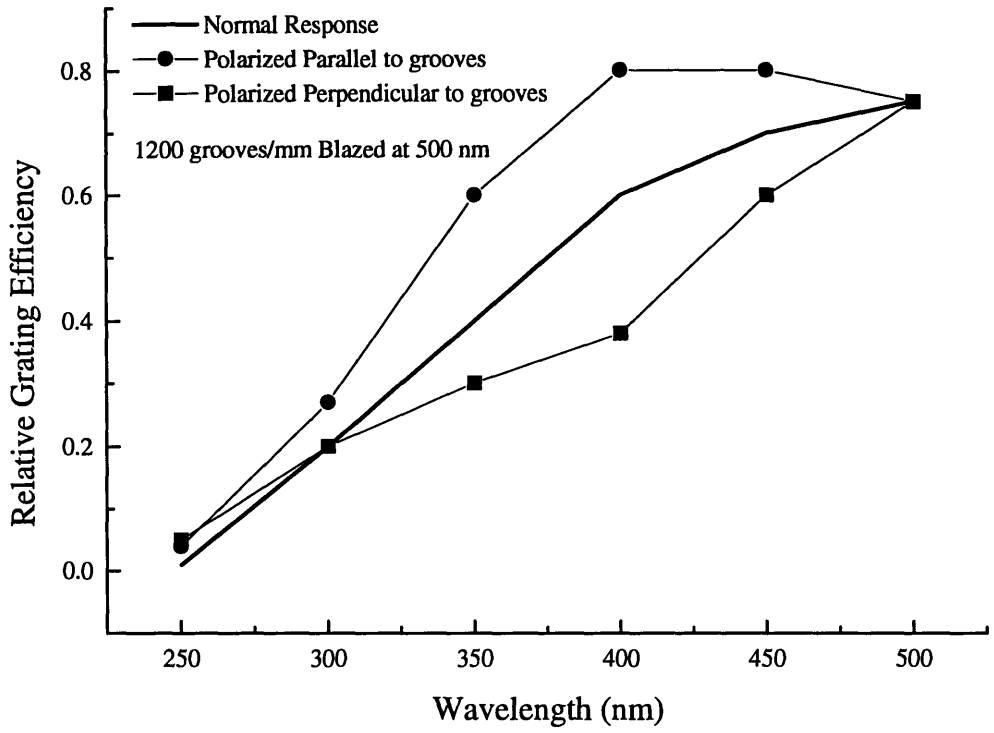

Figure 6.4: Characteristic response of a classically ruled grating with 1200 grooves per mm blazed at 500nm. The plot contains three traces. They are the characteristic responses for polarized light orientated perpendicular and parallel to the grooves as well as the response for unpolarized light.

responsible for the baseline, the baseline should follow the spectral response curve of the instrument. Therefore, the grating cannot be solely responsible for the baseline function. In reality, the instrument response is actually a combination of the spectral response from the imaging optics, monochromator, and detector. The efficiency response of the ICCD array (Princeton Instruments 1024M-059413) is displayed in Figure 6.5. Notice that these curves do not display appreciable spectral enhancement in the 350nm region. We can quantitate the

spectral response of the entire DF system by comparing the recorded spectrum of the intensity calibration lamp, which was described in Chapter 3, with the calculated lamp intensity spectral emission. See Figure 6.6b, where each of the intensity spectra, calculated and observed, have been normalized so that the strongest emission feature has unity intensity. Figure 6.6a displays ratio of the observed and calculated emission spectrum, the total instrument function.

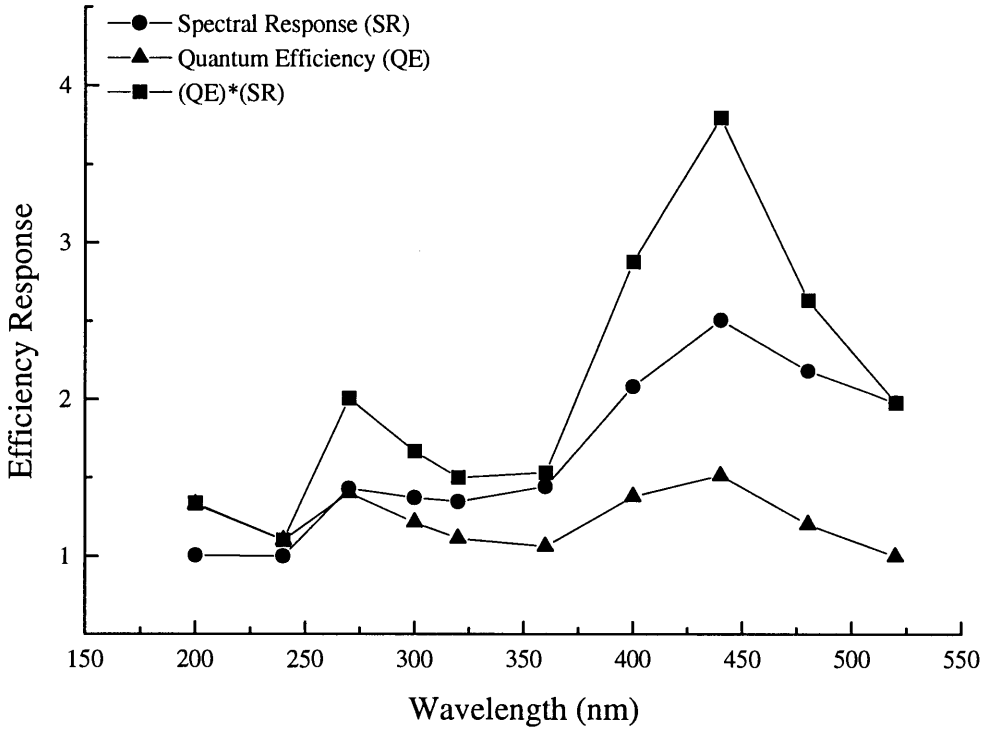

Figure 6.5: Efficiency response of the ICCD array (Princeton Instruments 1024M-059413). The efficiency response of the ICCD array is due to both the spectral response and quantum response efficiency. Note that there is a slight enhancement in the efficiency at 275nm. At the maximum of the Q-CB, 350nm, the ICCD response not significantly enhanced.

The calculated emission spectrum is derived from the intensity function supplied by Optronics Laboratories (OL 220M-M877) with each spectral irradiance calibration lamp. There is not an

appreciable difference between the observed and calculated intensity curves at 350nm. This implies that the relative intensity response of the entire optical train for emission in the 270 to 350 nm region is flat, ±1%. Therefore, the optical response of the DF system is not responsible for the Q-CB.

We have ruled out an enhancement or distortion of the intensity spectral response as being responsible for the observed quasi-continuum baseline. We have also searched for independent measurements, not conducted on this particular DF experimental setup, that would confirm our findings. Several experiments, some conducted by other research groups, have recorded low resolution DF spectra with a scanning monochromator and photomultiplier tube. Those spectra also exhibit a broad baseline function! The first reported DF spectra of acetylene, by Stephenson et. al., resulted in the assignment of progressions of vibrational eigenstates (nV_2,mV_4). No quasi-continuous baseline function could be discerned from their low resolution (200 cm^{-1}) DF spectrum.[2] However, other DF spectra were recorded, by Scherer and co-workers, to observe the effect of an $\tilde{A}$ -state perturbation. This perturbation and DF spectra from these levels will be discussed in the Chapter 7. Figure 6.4 from Scherer and co-workers, Reference 4, clearly displays a broad quasi-continuum baseline function.[3] Modest resolution (50-80 cm^{-1}) DF spectra, see Figure 6.1 of Reference 4, recorded by Yamanouchi and co-workers, also contained a baseline feature similar to the ones observed in the DF spectra presented here.[4] Note, that the work by Scherer *et. al.* and Yanamouchi *et. al.* recorded DF spectra with a monochromator and photomultiplier tube.

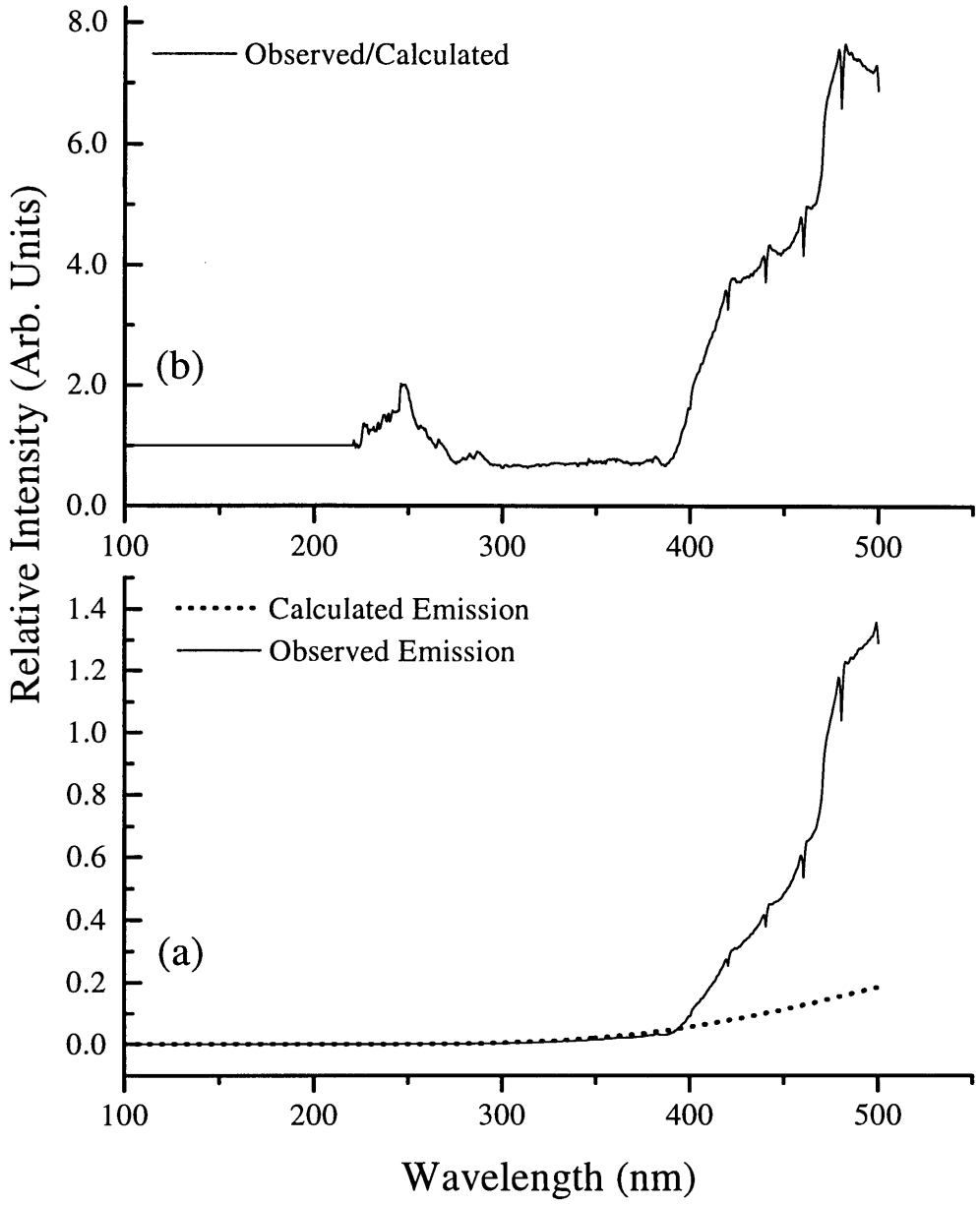

Figure 6.6: Plot (a) contains the recorded spectral emission from the Optronics standard of Irradiance (OL 220M M877). The calculated emission was derived from the intensity standard information supplied by Optronics Labaroatories. Plot (b) displays the true instrument function for the Jobin-Yvon HR640 monochromator. This was generated by plotting the ratio of the observed and calculated spectral emission. Note that the response curve is flat in the 300-400 nm region.

Recently, DF spectra, with 25 cm^{-1} resolution, recorded by Tsuchiya and co-workers in Japan using a monochromator and MCP detector also revealed a quasi-continuous baseline.[5]

We have shown that the possible instrumental contributions to a quasi-continuum emission are incapable of producing the baseline function observed in the present acetylene DF spectra. If the baseline is not an instrumental artifact, it must be molecular. Independent observations of the baseline feature in the acetylene DF spectra also confirm that the quasi-continuum is molecular in nature. The remaining possibility of artifact is centered on what species is responsible for this quasi-continuum. Is the baseline due to acetylene emission? Is the emission due to a species produced by a multi-photon absorption?

Several of the excited states accessible from the acetylene $\tilde{A}^1A_u$ state are represented in Figure 6.7.[6] A two-photon process, resonant through the $\tilde{A}^1A_u$ state of C_2H_2, could populate the $\tilde{A}^2\Pi$ state of C_2H. The second photon of this two photon process accesses predissociated Rydberg level of C_2H_2 which dissociates to highly excited vibrational levels of the $\tilde{A}^2\Pi$ state of C_2H. Recently, Wittig and co-workers showed that photodissociation of acetylene at 121.6 nm yields highly excited vibrational levels of the $\tilde{A}^2\Pi$ state at ≈36,000 cm^{-1} above the $\tilde{X}^2\Sigma^+$ state of C_2H (ΔT_0 for $\tilde{A}^2\Pi \leftrightarrow \tilde{X}^2\Sigma^+$ is approximately 5,000 cm^{-1}).[7] From a 225nm 1+1 photodissociation of acetylene, the C_2H $\tilde{A}^2\Pi \rightarrow \tilde{X}^2\Sigma^+$ emission could in principle approximately cover the 230 to 2,500 nm region. The radiative lifetime of the C_2H $\tilde{A}^2\Pi$ state has been estimated to be ~5μs.[6] Hsu and co-workers have also investigated the production of several

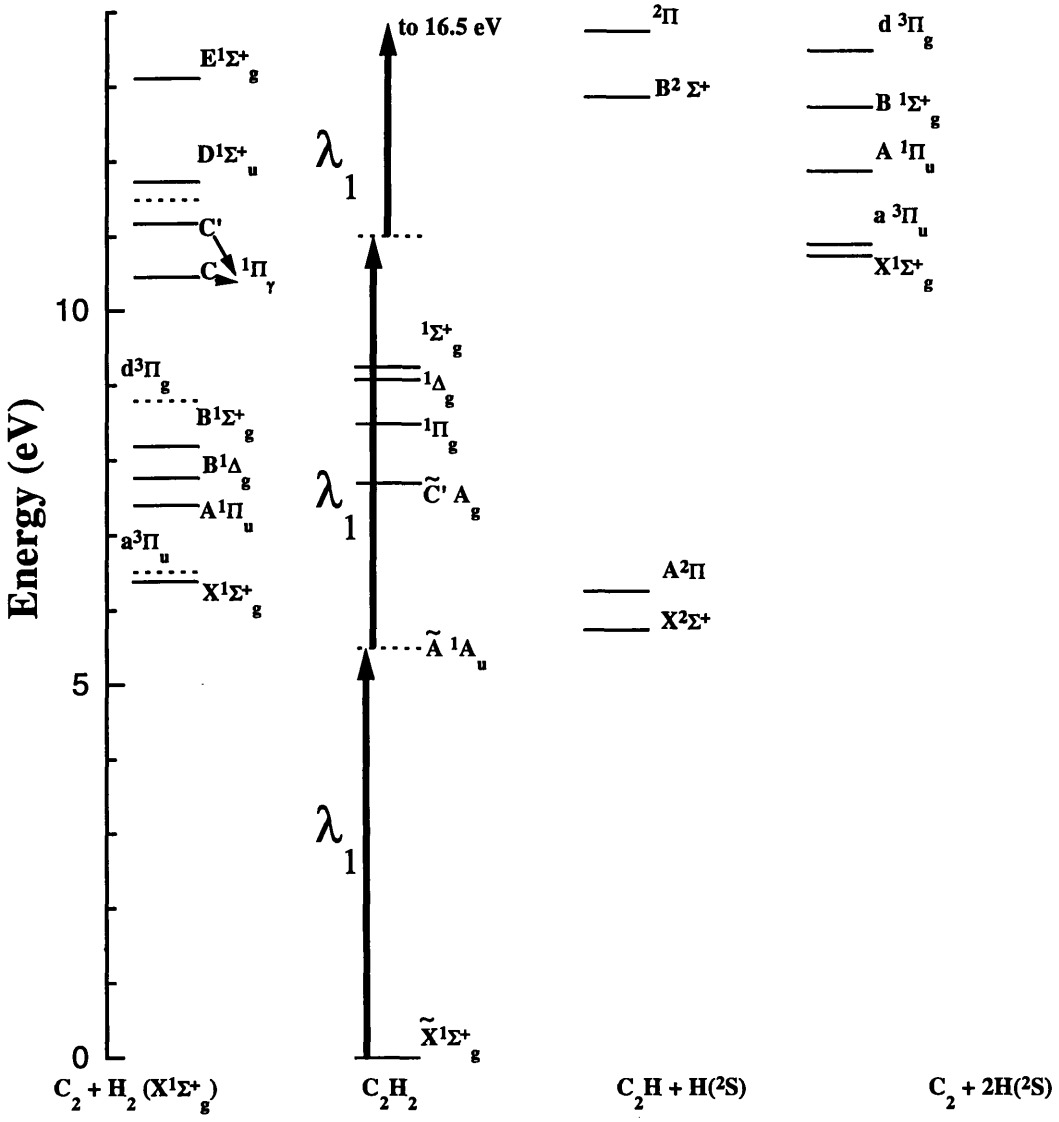

Figure 6.7: Energy diagram of the photodissociation states of acetylene. A 1+1 process can produce high vibrational levels of the $A^2\Pi$ state of C_2H and many C_2 states. A 2+1 process could produce C_2H in the $B^2\Sigma^+$. See text for details.

states of C_2 produced by, 1+1 and 2+1, multiphoton excitation of C_2H_2 at λ=269.17 nm.[8] They observed emission from 200-600nm due to the C_2 $d^3\Pi_g \rightarrow a^3\Pi_u$ (Swan Band), $C^1\Pi_g \rightarrow A^1\Pi_u$ (Deslandres-d'Azambuja band), $e^3\Pi_g \rightarrow a^3\Pi_u$ (Fox-Herzberg band), and $D^1\Sigma_u^+ \rightarrow X^1\Sigma_g^+$ (Mulliken band) transitions. They also determined that the vibrational population of the C_2 states is primarily in $v \leq 2$ levels.[8] A three photon process might be able to populate all of the following states: high lying states of C_2, the $B^2\Sigma^+$ and/or $C^2\Pi$ state of C_2H. Nevertheless, the emission properties of a diatomic molecule such as C_2 could not generate the broad baseline feature seen in the acetylene $\tilde{A}^1A_u \rightarrow \tilde{X}^1\Sigma_g^+$ DF spectra. C_2 is a diatomic molecule whose emission will consists of vibrational progressions of sharp C-C vibrational eigenstates, spaced at approximately 1,200 cm^{-1}. Furthermore, the spectral characteristics of the baseline feature: large energy range, 10,000 cm^{-1} (between 270-370nm), and overall integrated intensity, 30% the observable emission, limit the type of molecular species which could be the source of such emission. It seems very unlikely that a three photon process with an unfocused laser beam could produce such a large quasi-continuum baseline. One could perform a series of DF power studies to determine the nonlinear dependence of the emission intensity due to a multiphoton process.

The $\tilde{A}$ state of acetylene supports at least three minima corresponding to different isomeric species of C_2H_2: *trans*-bent, *cis*-bent, and vinylidene.[9] The $\tilde{A}^1A_u \leftarrow \tilde{X}^1\Sigma_g^+$ tranition has been well documented and is known to terminate in the *trans*-bent isomer on the S_1 surface.[10] For the different isomers, well depth and minima are presented in Figure 6.8. The S_1 vibrational levels used in this DF study are also indicated in Figure 6.8. One

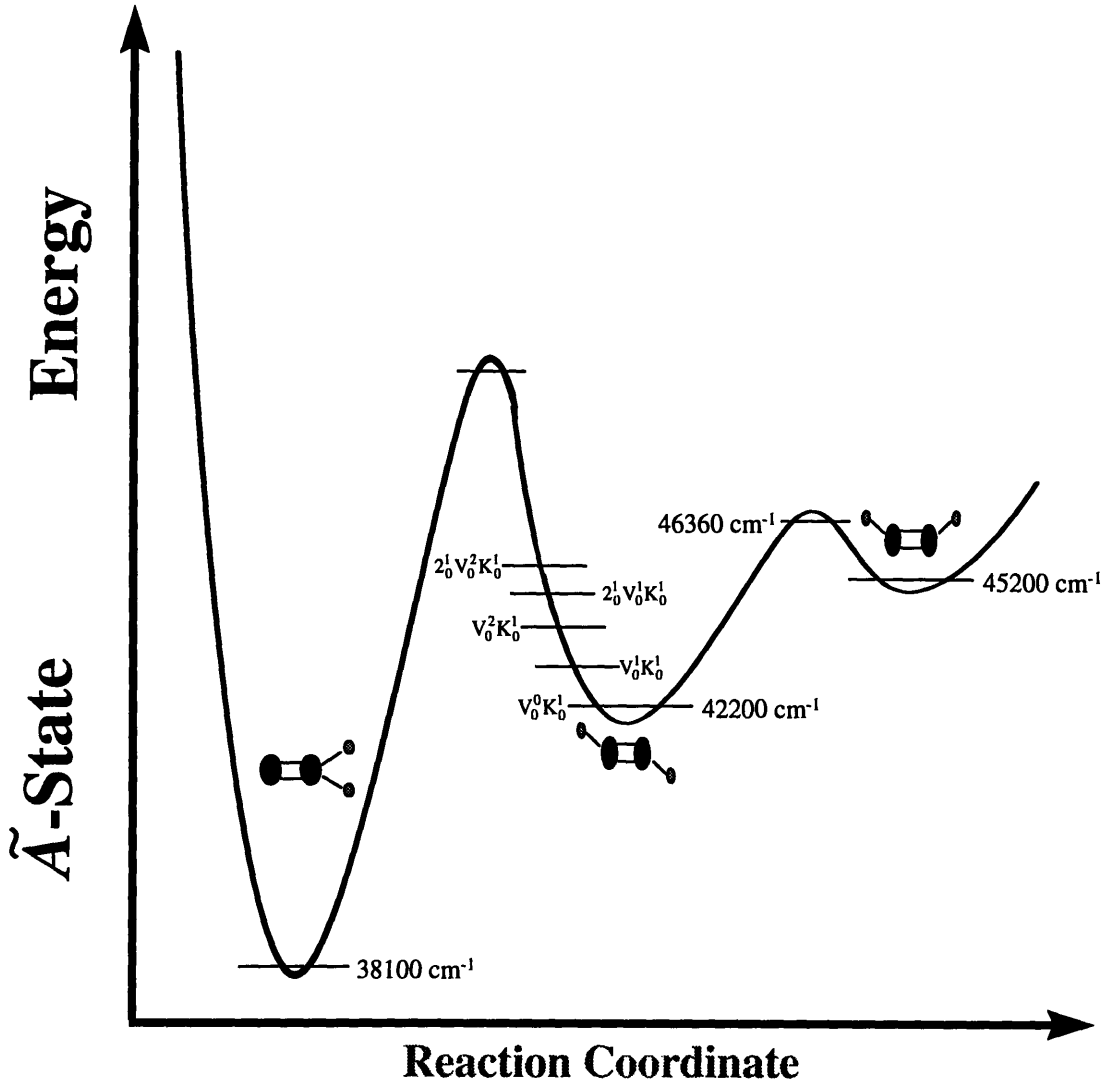

Figure 6.8: The first excited singlet state of acetylene contains at least three different isomeric species, vinylidene (C_{2v}), *trans*-(C_{2h}) , and *cis*-bent (C_{2v}). All of the vibrational levels in the trans-bending $\tilde{A}^1A_u$ state are also displayed. Note that all but one of the vibrational levels lies below the predicted minima of the *cis*-bending well.

hypothesis is that the quasi-continuum is due to a *trans*↔*cis* interaction in the $\tilde{A}$ state. However, the *cis*-bent minimum is calculated to lie 1,700 cm^{-1} above the vibrationless level of the *trans*-bent minimum.[9] All of the intermediate levels used in these experiments lie at energies below the *cis*-bent minimum. This rules out the possiblity of interaction with the *cis* isomer as being responsible for the quasi-continuum baseline. What about interactions with

the vinylidene isomer? The $\tilde{A}\ ^1A_u\ J'_{1,1}$ rotational intermediate will have a symmetry allowed interaction with a rotational level of vinylidene. If this interaction were strong, the emission from the vinylidene levels in the S_1 state will terminate at or above the $\tilde{X}$-state (S_0) zero-point level of vinylidene. The vinylidene zero-point level is calculated to lie at E_{vib}= 15,500 cm^{-1} above the zero-point level of the acetylene S_0 state.[11] The baseline feature starts at E_{vib}= 8,000 cm^{-1} and continues to E_{vib}= 20,000 cm^{-1}. Thus, the Q-CB can not be attributed to emission from vinylidene levels in the S_1 state.

6.3 Interpolyad Interactions

Recent work by Herman and co-workers has shown, at J >>1, that there are several additional weak $\tilde{X}$-state resonances which couple levels belonging to different l and N_s quantum numbers.[12] These resonances have the effect of destroying these l, N_{res} polyad quantum numbers. The only conserved quantity remaining will be the N_{res} quantum number. The weak resonances observed by Herman are primarily due to rotational-l resonances and Coriolis interactions. The rotational-l resonance matrix elements have the following form:[12,13]

$$\langle V_b^{\ell_b}, l, \mathrm{J} \mid V_b^{\ell_b \pm 2}, l \pm 2, \mathrm{J} \rangle = \tag{6.1}$$

$$\frac{q_b}{4}\sqrt{(V_b \mp \ell_b)(V_b \pm \ell_b + 2)[\mathrm{J}(\mathrm{J}+1) - l(l \pm 1)][\mathrm{J}(\mathrm{J}+1) - (l \pm 1)(l \pm 2)]}$$

where

$$q_b = q_b^0 + q_{bb}V_b + q_{bb'}V_{b'} + q_b^l \mathrm{J}(\mathrm{J}+1)$$

These interactions have an approximate J^2 dependence. The average off diagonal matrix element for levels in the N_{res}=15 polyad region will be 0.005 cm^{-1} for J=15. The Coriolis matrix elements have the following form:[12,13]

$$\left\langle V_s, V_b^{l_b} \left| (V_s + 1)(V_b - 1)^{l_b \mp 1} \right\rangle = \right. \tag{6.2}$$

$$\pm\left(B/4\right)\zeta^x_{s,b}\Omega_{b,s}\sqrt{(V_s + 1)(V_b \pm l_b)}\sqrt{(J \pm l)(J \mp l + 1)}$$

where $$\Omega_{b,s}=\left[\left(\omega_b/\omega_s\right)^{(1/2)} + \left(\omega_s/\omega_b\right)^{(1/2)}\right],$$

B is the rotational constant, and $\zeta^x_{b,s}$ is called the Coriolis zeta constant which couples normal vibrations V_s and V_b about the molecule fixed x-axis. The main point is that the Coriolis matrix elements will also have an approximate J dependence. The average matrix elements, determined by Herman, in the N_{res}=15 energy region are on the order of 0.003 cm^{-1} for J=15.[12] The Coriolis interaction is called a 2,444 resonance, where $\Delta N_s=\pm1$ and $\Delta l=\pm1$. For example, the [0,12,0/2,g] and [2,12,0/2,g] polyads will be connected to the [1,12,1,g] polyad. If these interactions were strong, the XCC routine would have been unable to separate overlapping polyad patterns belonging to different [N_s,N_{res},l,g] values. This interaction would destroy the N_s and l polyad quantum numbers. The fact that polyad patterns, with the three polyad quantum numbers, were extracted from the DF spectra suggests that the rotational-l and 2,444 Coriolis resonances are not strong enough to be detected at our resolution. For the N_{res}=15 energy region, the interaction matrix elements will be 0.003 cm^{-1} (J=15) between states that are separated by ≈20 cm^{-1}.[12] The vibrational dependence of the separation of the interacting states will be controlled by the diagonal x_{ij} anharmonicities. The anharmonicity of the different ZOBSs causes the 2,444 resonance to have only localized (as opposed to global resonance which is visible over a large E_{vib} region) effects at low energies. At low energies, the interaction effect will be greatest when the ZOBS of the main polyad, [N_s=0, N_{res}=m, l=0,2, g], is nearest to the $(0,+1,0,m\text{-}3^{+1},0)^1$ state of the [N_s=+1, N_{res}=m-3, l=+1,g] polyad.

These zero-order levels lie closest at low N_{res}. At higher N_{res} these levels tune away from each other due to the specific values of the x_{22}, x_{24} and x_{44} anharmonicities. Of course, this is a simplified picture. At higher energies, the vibrational eigenstate chararacters are composed of small and state-specific amounts of many basis states. These polyads are said to be highly fractionated. The fractionation of the polyad may allow for some 2,444 interactions between outlying component of two polyads. Specificically, the states located at the high energy end of the [N_s=0, N_{res}=m, l=0,2, g] polyad may interact with the states located at the low energy region of the [N_s=+1, N_{res}=m-3, l=+1,g] polyad. This interaction will probably not distort the overall polyad structure, because the highly fractionated states on the interacting edges of the polyads will not contain appreciable intensity. It is possible that there are additional weak resonances which are activated at higher E_{vib}. The effects of these additional unknown interactions may become especially large as different zero-order levels tune through ΔE^0=0 resonances.

A series of experiments was conducted to understand the dependences of the baseline quasi-continuum on rotational quantum number and pressure. Several DF spectra were recorded from the V_0^2 K_0^1 intermediate state. The DF spectra were recorded from either J_{K_a,K_c} = $1_{1,1}$, $3_{1,3}$,or $9_{1,9}$ rotational intermediates. For each rotational intermediate three DF spectra were recorded at 1,3, and 9 Torr of acetylene. (The entire study is composed of 9 DF spectra.) The spectra are shown in Figures 6.9 and 6.10.

The Coriolis rotational dependence, $|H_{ij}|^2 \propto J^2$, should increase by a factor of at least 80 for J=9 versus J=1. If the quasi-continuum has any direct relationship to Coriolis interactions, the baseline function should change as a function of J. The change in acetylene pressure over

a factor of 9 will cause additional collisions, randomizing the rotational population in the $\tilde{A}$ state. In particular, low-J, low K_a levels of the $\tilde{A}$ state will be converted into higher-J,K_a levels, thereby resulting in DF spectra with the greater complexity postulated for intermediates states originiating from higher- J and K_a levels in S_1. The pressure will also cause collisional quenching of any long lived species (e.g. the $\tilde{A}^2\Pi$ state of C_2H) that could be responsible for the quasi-continuum baseline. In order to determine the rotational and pressure dependent effects on the quasi-continuum, the ratio of the integrated intensities of the sharp features and quasi-continuum is plotted for each DF spectrum, see Figure 6.11. The smooth baseline function is created using a fourth order polynomial fitting routine. This function is fit to the enitre DF spectrum by a series of 20 points located at the base of the sharp features, see Figure 6.12. The area of the sharp features is determined by first subtracting the baseline function from a DF spectrum, followed by integration of the remaining DF features. The baseline area is simply the integrated area of the baseline function. Note that this baseline function is not independent of the $\tilde{A}$ state vibrational level from which each DF spectrum is recorded. While the qualitative nature and general shape of each

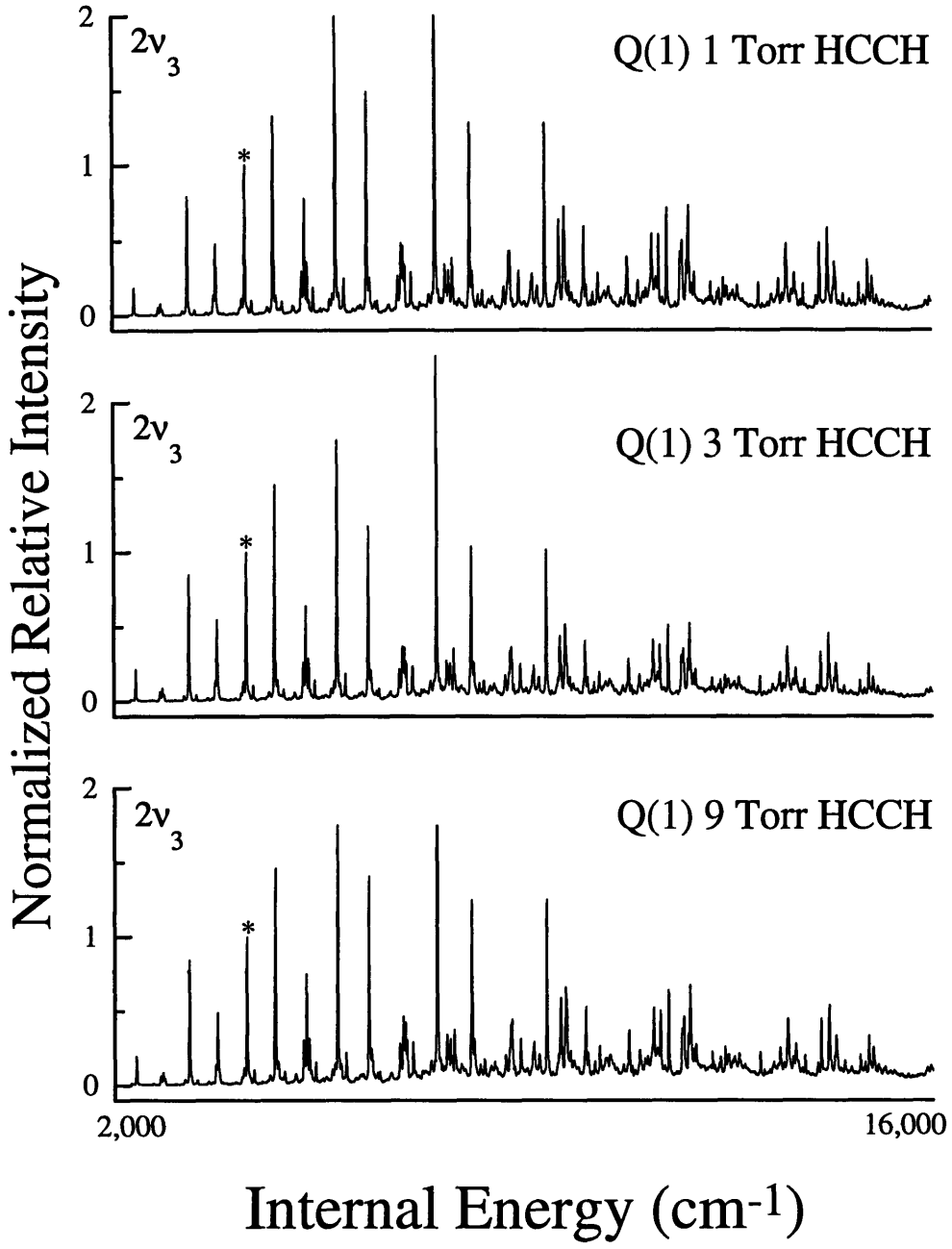

Figure 6.9: DF spectra excited via the ${}^{r}Q_0(1)$ transition of $V_0^2K_0^1$. The spectra are recorded with 1,3, and 9 Torr of Acetylene, respectively. The tallest feature, denoted by an asterisk, in the [0,8,0/2,g] polyad in each spectrum is normalized to unity.

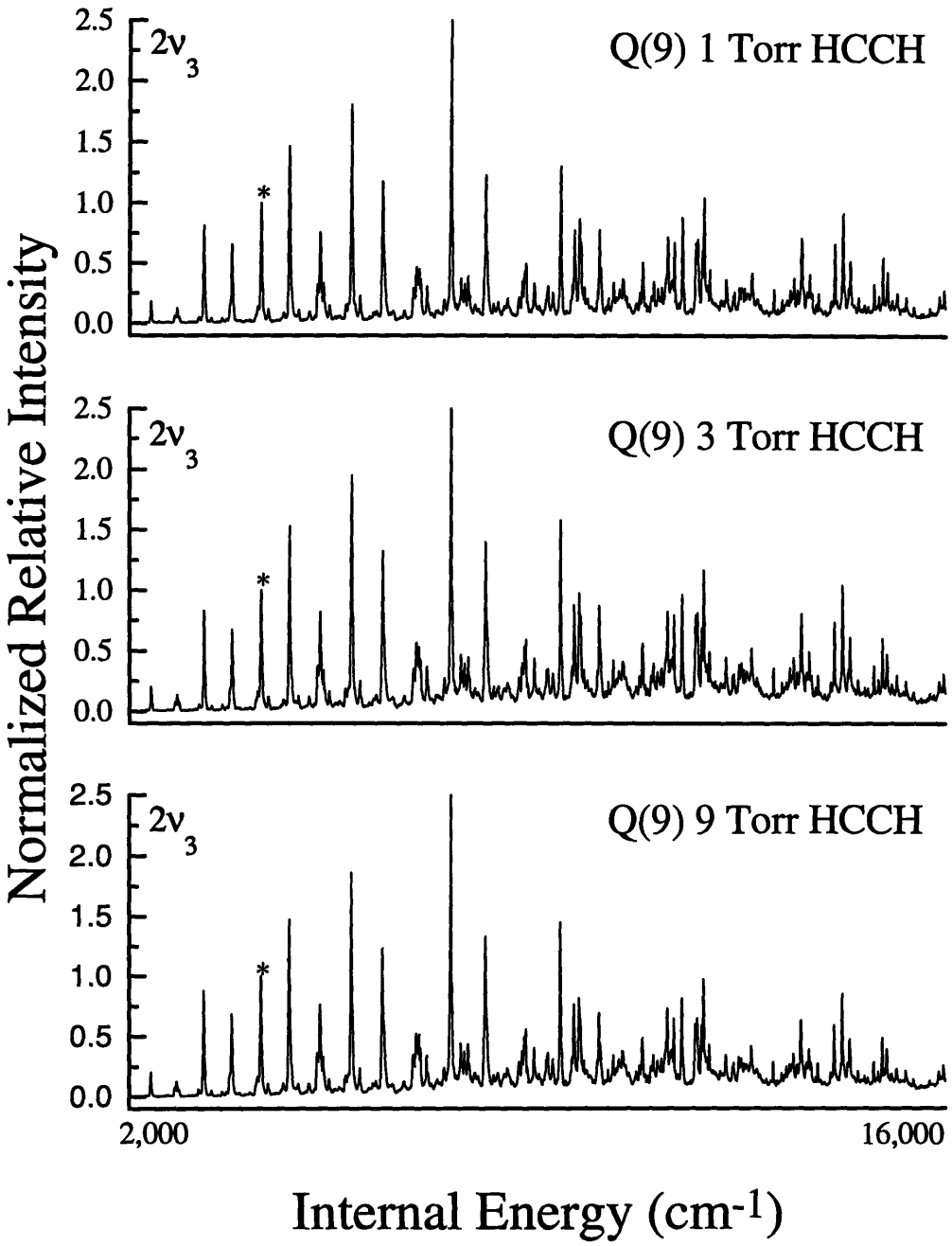

Figure 6.10: DF spectra excited via the ${}^{r}Q_0(9)$ transition of $V_0^2K_0^1$. The spectra are recorded with 1,3, and 9 Torr of Acetylene, respectively. The tallest feature, denoted by an asterisk, in the [0,8,0/2,g] polyad in each spectrum is normalized to unity.

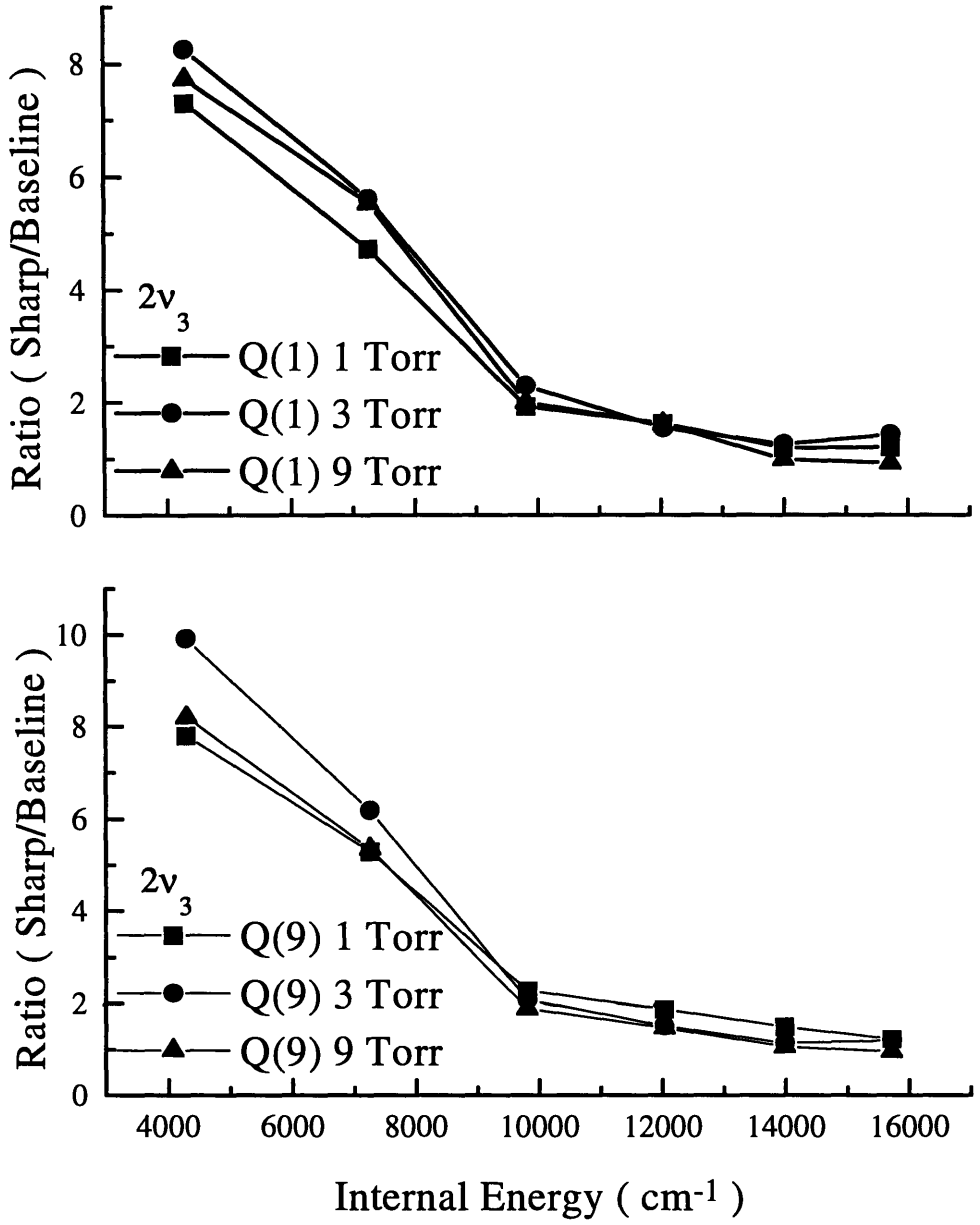

Figure 6.11: The upper plot contains the ratio of the sharp to baseline integrated area for each DF spectrum excited via the ${}^{r}Q_0(1)$ transition of $V_0^2K_0^1$ but recorded at 1,3,and 9 Torr of acetylene. The lower plot contains the ratio of the sharp and baseline integrated area for each DF spectrum excited via the the ${}^{r}Q_0(9)$ transition of $V_0^2K_0^1$ but recorded at 1,3, and 9 Torr.

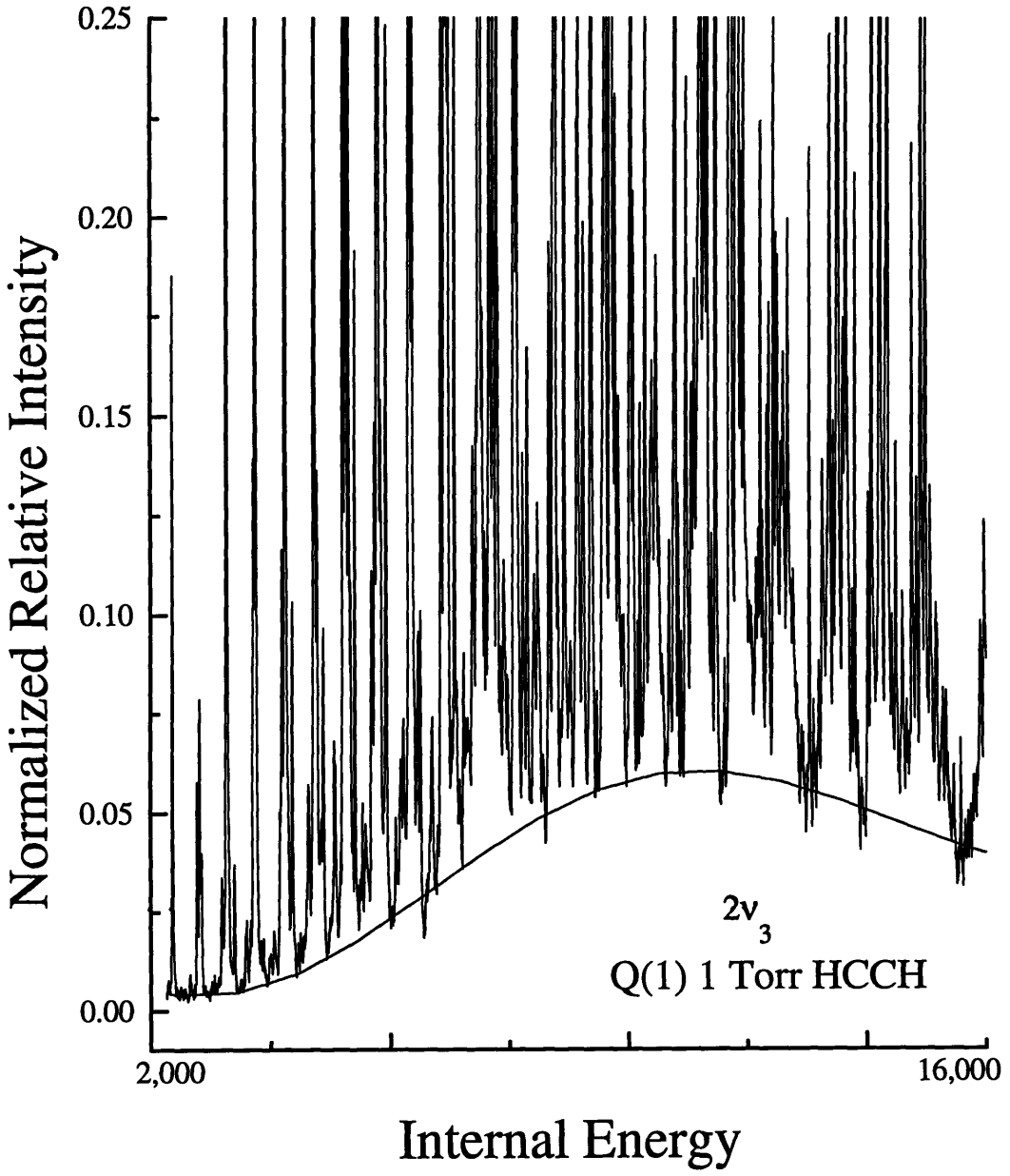

Figure 6.12: The baseline function for the Q(1) $V_0^2K_0^1$ DF spectrum. The function is fit to a series of 20 points located at the minima of the sharp features.

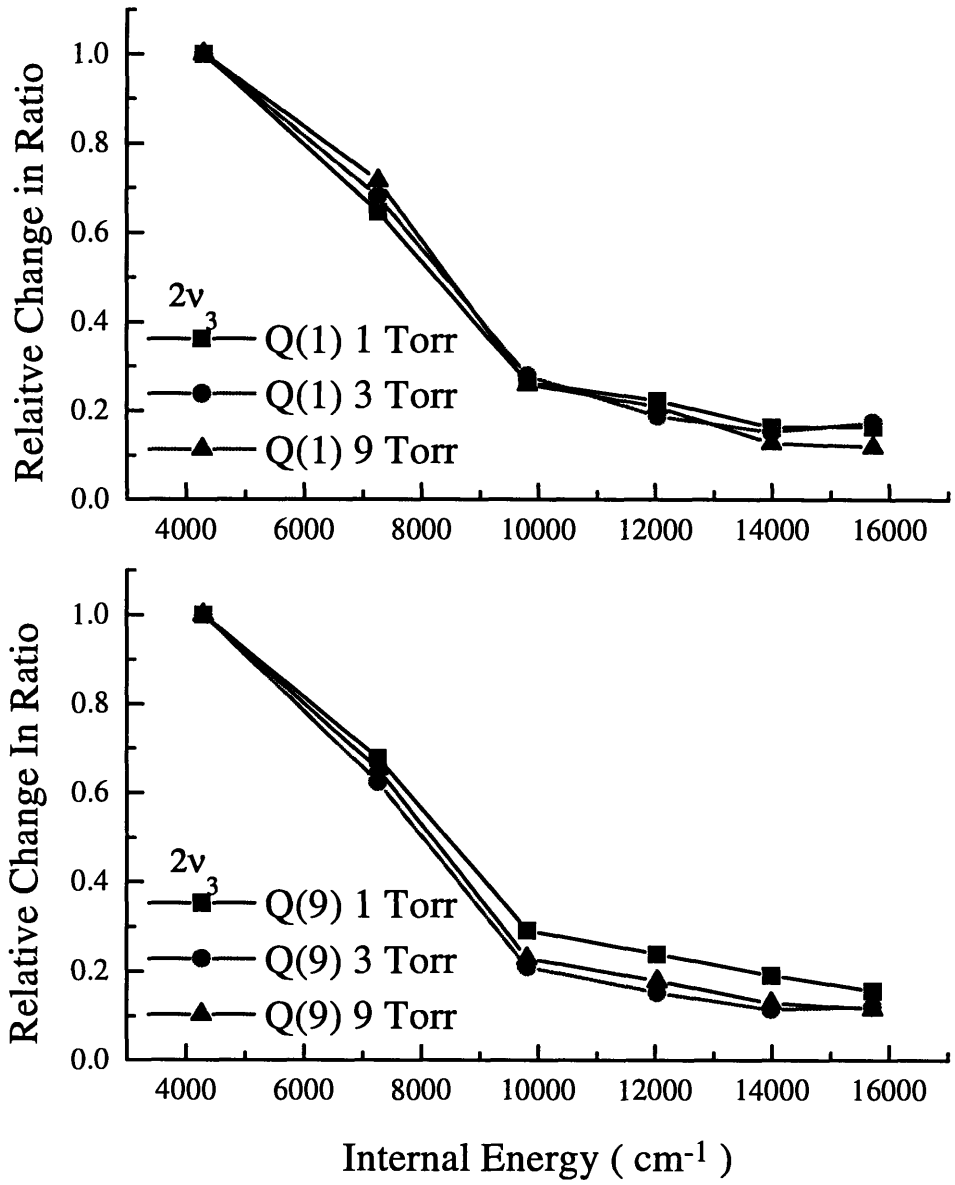

Figure 6.13: The upper plot contains the relative ratio of the sharp to baseline integrated area for each DF spectrum excited via the ${}^{r}Q_0(1)$ transition of $V_0^2K_0^1$ but recorded at 1,3,and 9 Torr of acetylene. The lower plot contains the relative ratio of the sharp and baseline integrated area for each DF spectrum excited via the the ${}^{r}Q_0(9)$ transition of $V_0^2K_0^1$ but recorded at 1,3, and 9 Torr. Each spectrum from Figure 6.11 has had the largest ratio normalized to unity.

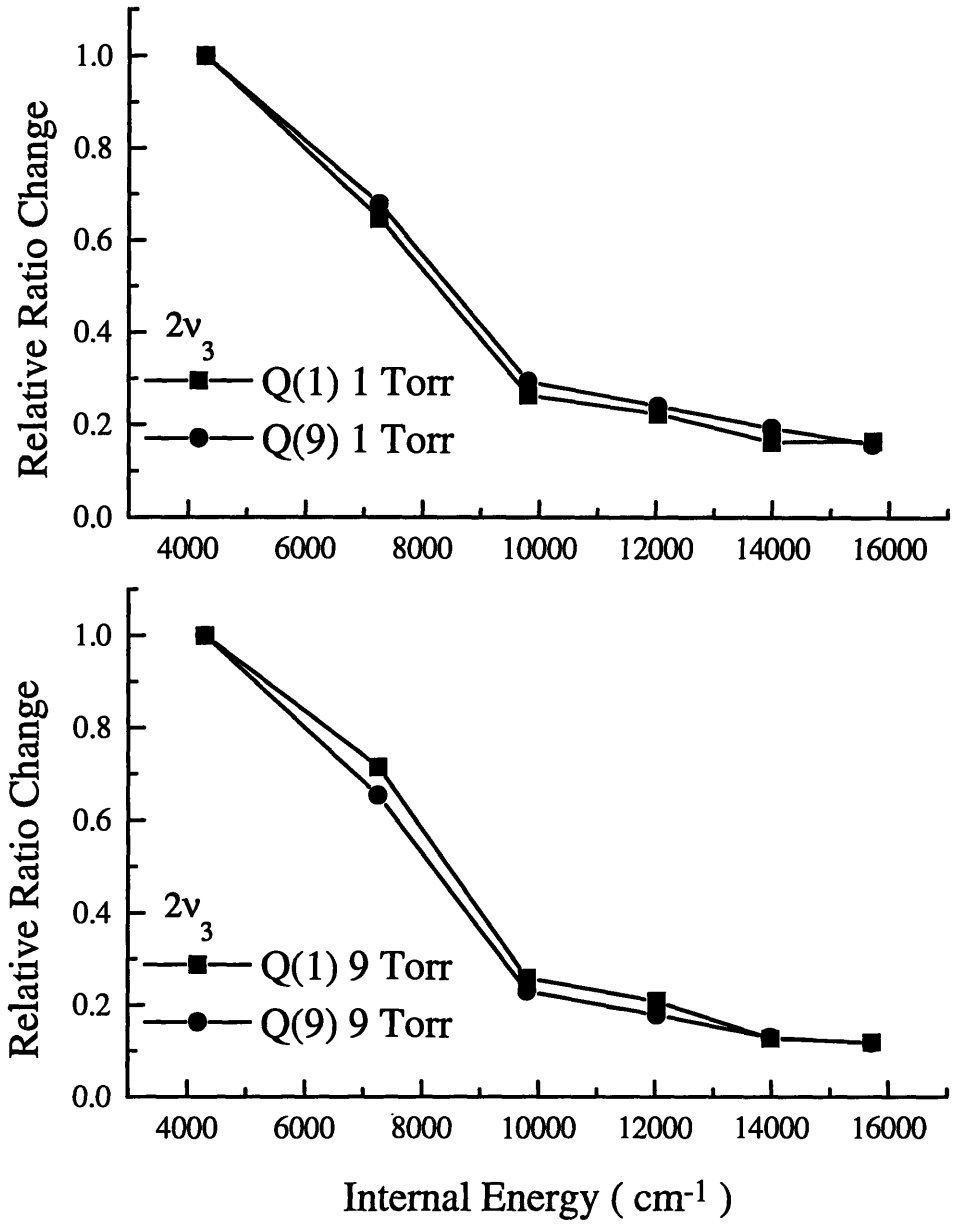

Figure 6.14: The upper plot contains the relative ratio change of the sharp and baseline features for different rotational intermediates, Q(1) and Q(9), recorded at 1 Torr of acetylene. The lower plot contains the relative ratio change of the sharp and baseline features for different rotational intermediates, Q(1) and Q(9), recorded at 9 Torr of acetylene. Note that the relative change in the ratio is the same for different rotational intermediates.

baseline is similar, the absolute integrated area is not constant. That is, the amount of Q-CB cannot be scaled from one DF spectrum to the next. The functional form changes slightly for each upper state vibrational level. It is plausible that the baseline area should increase at high J or at high pressure because of the stronger average Coriolis coupling, but one would also expect that the baseline functional form should also change. In particular, as J is increased, due to the J^2 dependence of the squared Coriolis matrix elements, one would expect that the effects of Coriolis interactions should start to be detectable (at our resolution) at lower E_{vib}.

We are interested in the *relative* strength of the baseline as a function of pressure and rotational quantum number. The results of the DF study are presented in Figures 6.13 and 6.14. Figure 6.13 displays the relative strength of the baseline as a function of pressure. The baseline is almost neglebible at 5%. Figure 6.14 displays the relative strength of the baseline as a function of rotational quantum number. It is at most 10% in the E_{vib}=14,000 cm^{-1} region. These findings indicate that the baseline function is not due to extensive Coriolis mixing or emission from a long lived species, such as C_2H.

The amount of Coriolis mixing can be **semi-quantified** by the following method. The normal DF spectrum from $1_{1,1}$ rotational level of V_0^2 K_0^1 will terminate on the $|J, l, {}^{e}/_{f}\rangle = |$ 1,0,e⟩ and | 2,2,f⟩ rotational levels for each vibrational band in the $\tilde{X}$-state. From a Dunham expansion we can calculate the energy difference between the | 1,0,e⟩ and | 2,2,f⟩ rotational levels:

$$T_{vr}=G_v + F_r \qquad (6.3)$$

where

$$G_v = G_v(v_1, v_2, v_3, v_4^{l_4}, v_5^{l_5}; J_l) =$$

$$\sum_{i=1}^{5} \omega_i^0 v_i + \sum_{i=1}^{5}\sum_{j=i}^{5} x_{i,j}^0 v_i v_j + \sum_{t=4t'=t}^{5}\sum^{5} g_{tt'}^0 l_t l_{t'} + \sum_{t=4t'=tt''=t'}^{5}\sum^{5}\sum^{5} y_{tt't''} v_t v_{t'} v_{t''} + \sum_{i=1}^{5}\sum_{t=4t'=t}^{5}\sum^{5} y_i^{tt'} v_i l_t l_{t'} + \ldots - B_v l^2$$

$$F_r = F_r(v_1, v_2, v_3, v_4^{\ell_4}, v_5^{\ell_5}; J_\ell) = B_v J(J+1) + \ldots$$

and

$$\mathbf{B}_v = \mathbf{B_0} - \sum_{i=1}^{5} \alpha_t^0 v_t + \sum_{t=4t'=t}^{5}\sum^{5} (\gamma_{tt'} v_t v_{t'} + \gamma_\ell^{tt'} \ell_t \ell_{t'}) + \ldots$$

For the $1_{0,e}$ and $2_{2,f}$ pairs of rotational levels with the same $\mathbf{V} = (v_1, v_2, v_3, v_4, v_5)$ and l_4=0 or l_5=0, $T_{vr}(V;1_{0,e}) \cong T_{vr}(V;2_{2,f})$ since

$$F_r(V;1_{0,e}) - F_r(V;2_{2,f}) = B_v(1)(2) - B_v(2)(3) + \ldots \approx -4B_v$$

and

$$G_v(V;1_{0,e}) - G_v(V;2_{2,f}) = \ldots -B_v(0)^2 + B_v(2)^2 \approx 4B_v$$

These $1_{0,e}$ and $2_{2,f}$ levels will be approximately degenerate. The resolution of the DF spectra, 15 cm^{-1}, is not sufficient to resolve the two rotational transitions at low E_{vib}. The $9_{1,9}$ V_0^2 K_0^1 DF spectrum will terminate on |9,0,e⟩, |9,2,e⟩, |8,2,f⟩ and |10,2,f⟩ rotational levels. The overall rotational spacing between the |8,2,f⟩ and |10,2,f⟩ rotational transitions is ≈30 cm^{-1}. This spread in rotational transitions at J=9 is seen in each DF spectrum as a broadening of the normal FWHM, 15 cm^{-1}, DF features. A difference spectrum is constructed to assess how much of the broadening is due to Coriolis interactions. First, four copies of the Q(1) V_0^2 K_0^1 DF spectrum are made. Second, these spectra are shifted to match the energy positions of the rotational transitions which terminate on the |9,0,e⟩, |9,2,e⟩, |8,2,f⟩ and |10,2,f⟩ levels. For example one copy of the Q(1) V_0^2 K_0^1 DF spectrum is shifted to the blue to coincide with the

$|9,0,e\rangle$ rotational level of the Q(9) $V_0^2\ K_0^1$ DF spectrum. Third, once the four copies are shifted by the appropriate energy, the relative intensities of the different rotational transitions must be adjusted. For a given vibrational transition, the four copies of the Q(1) $V_0^2\ K_0^1$ DF spectrum are all normalized to one. Then each of the rotational transitions is scaled by their appropriate Hönl-London factors in the following manner. The DF intensity for the transition:

$$\left|\tilde{X}^1\Sigma_g^+, v_0, l_0\right\rangle \rightarrow \left|\tilde{A}^1A_u, v_i, K_i\right\rangle \rightarrow \left|\tilde{X}^1\Sigma_g^+, v_f, l_f\right\rangle$$

is proportional to

$$I = \left|\left\langle \tilde{X}^1\Sigma_g^+ \left|\mu(\alpha)_{0,i}\right| \tilde{A}^1A_u\right\rangle\right|^4 \times \left|\left\langle v_0 \mid v_i\right\rangle\right|^2 \left|\left\langle v_i \mid v_f\right\rangle\right|^2 \times$$

$$\sum_{m,m_f} \left|\left\langle J_0, l_0, m \left|\phi_\alpha\right| J_i, K_i, m\right\rangle\right|^2 \left|\left\langle J_i, K_i, m \left|\phi_\alpha\right| J_f, l_f, m\right\rangle\right|^2 \qquad (6.4)$$

The first term represents the electronic transition moment. The second term is the Franck-Condon factor. The last term determines the relative rotational intensities. ϕ_α is the direction cosine operator. These can be found in Table 4.4 of Townes and Schawlow. Changing the relative polarizations of the PUMP and DUMP lasers in an SEP experiment causes the relative intensities of the rotational transitions to change. This has been well documented in References 13, 15, and 16. Our DF experiment *does not* utilize two polarized laser beams. However, our pump laser *is* horizontally polarized perpendicular to the propagation direction along which the acetylene spontaneous fluorescence is collected, the z-direction. The polarization is also perpendicular to the grooves on the grating. The grating has a different efficiency for light which is polarized perpendicular or parallel to the grating grooves, see Figure 6.4. In our case, the grating will disperse, unequally, the perpendicular and parallel components of the acetylene fluorescence. (Each component contains different relative

intensities due to the differences in the Hönl-London factors). This is due to the orientation of the linear polarization of the pump laser, along the z-axis, and the polarization components of fluorescence collected along the z-axis, which lie along the x and y axes (perpendicular and parallel to the grating grooves). The relative rotational intensities are given in Table 1. The exact efficiency for the different polarizations is not explicitly known for our grating. We have obtained a efficiency response for a grating with similar characteristics (grooves per mm and blaze angle). From Figure 6.4, the efficiencies are almost equal at blue wavelengths, 250 nm, and the parallel component is almost twice the perpendicular component at redder wavelengths, 350 nm.

Table1: Calculated rotational relative intensities from the $9_{1,9}$ V_0^2 K_0^1 DF spectrum.

J_0	K_0	J_i	K_i	J_f	K_f	Intensity//	Intensity $\perp$
9	0	9	1	8	2	0.1844	0.2132
9	0	9	1	9	0	3.7860	0.6369
9	0	9	1	9	2	1.8509	0.3113
9	0	9	1	10	2	0.4840	0.4290

A comparison of the Q(9) DF spectrum to the translated and scaled (pseudo Q(9)) DF spectrum is presented in Figure 6.15. When scaling the relative rotational intensities, we have assumed that the parallel and perpendicular components have equal efficiencies, see Figure 6.16. Figure 6.17 contains a comparison of the Q(9) DF spectrum to the translated and scaled (pseudo Q(9)) DF spectrum, where we have assumed that the parallel components are twice as efficient as the perpendicular components, see Figure 6.18. Notice that Figure 6.16 and 6.17 are very similar. Therefore, the polarization effects of the grating are very small. In several wavelength regions, the genuine Q(9) spectrum contains DF features which do not occur in

the pseudo spectrum. These anomalies are highlighted in the difference spectrum, Q(9) minus the pseudo-Q(9), and most likely arise either from Coriolis mixing or from differences in the energy positions (due to the diagonal anharmonicity constants) of the l=0 and 2 components which occur at higher E_{vib} or from the assumptions about the polarization efficiencies. Note that the quasi-continuum as a whole is slightly more (2%) intense in the Q(9) DF spectrum than the in Q(3) or

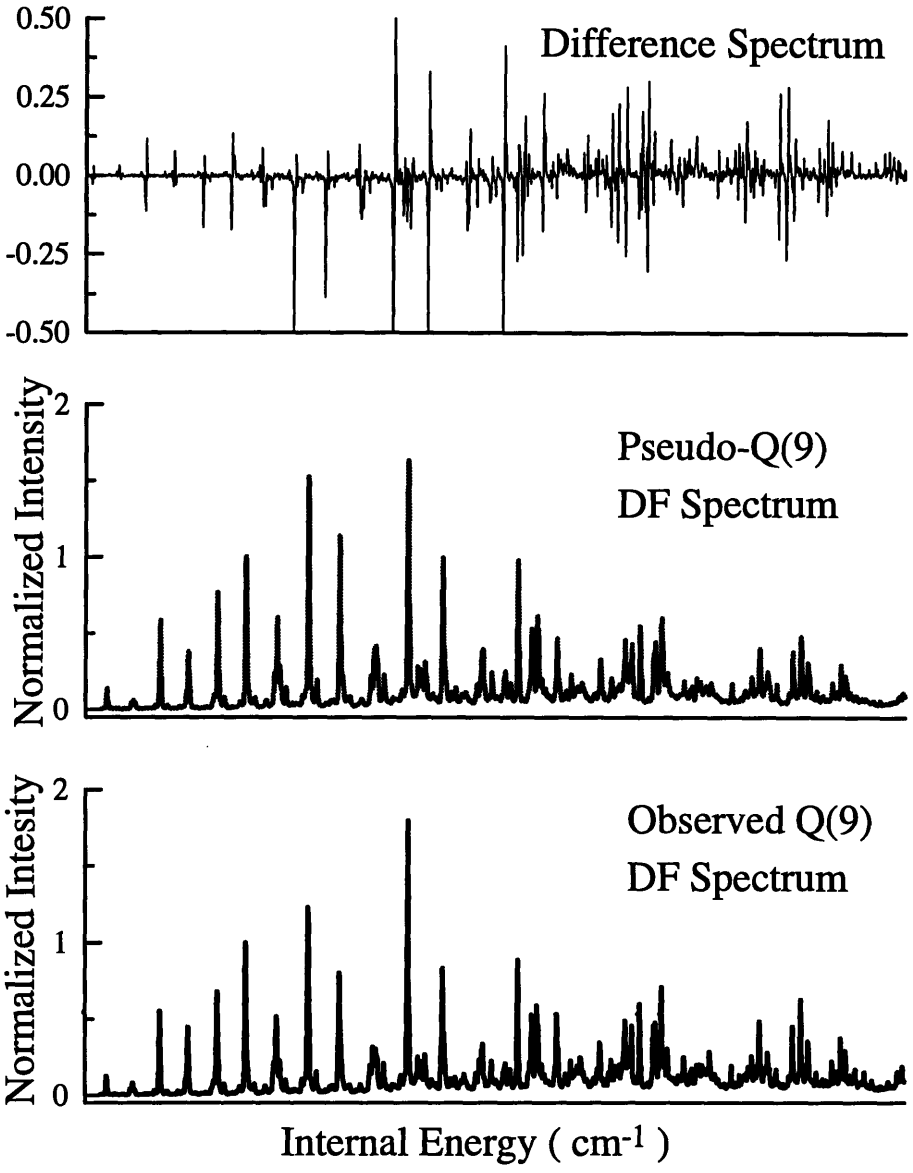

Figure 6.15: The top panel contains a difference spectrum of the observed Q(9) DF spectrum, lower panel, minus the pseudo-Q(9), middle panel spectrum. Note that the pseudo-Q(9) spectrum was generated per the instructions in the text and the relative polarization components were assumed to be equal in intensity, see Figure 6.16. Most of the sharp peaks in the top panel are due to errors in frequency calibration.

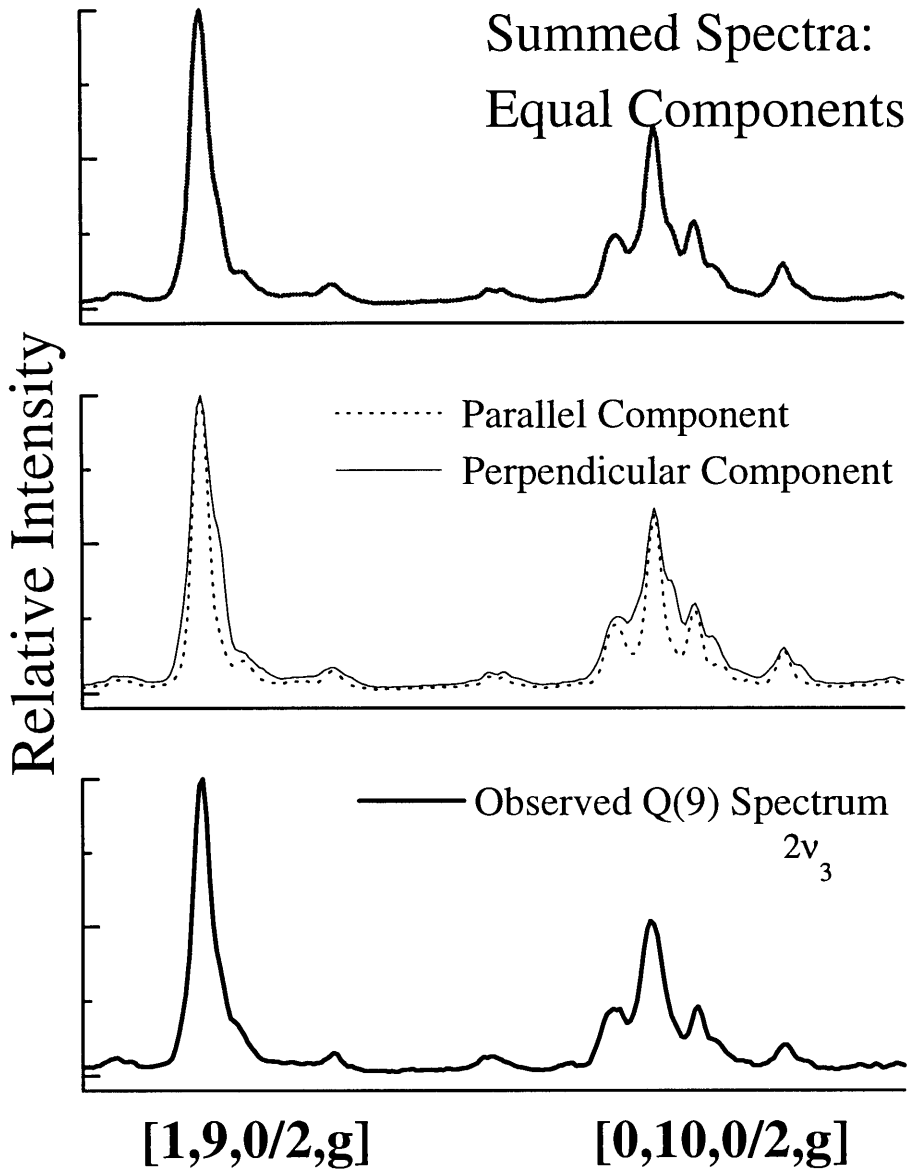

Figure 6.16: The top panel contains the summed spectra of equally weighted parallel and perpendicular polarization components, middle panel. The lower panel displays the observed [1,9,0/2,g] and [0,10,0/2,g] polyad energy regions. Note that the summed spectra closely resemble the observed spectra, see Figure 6.15.

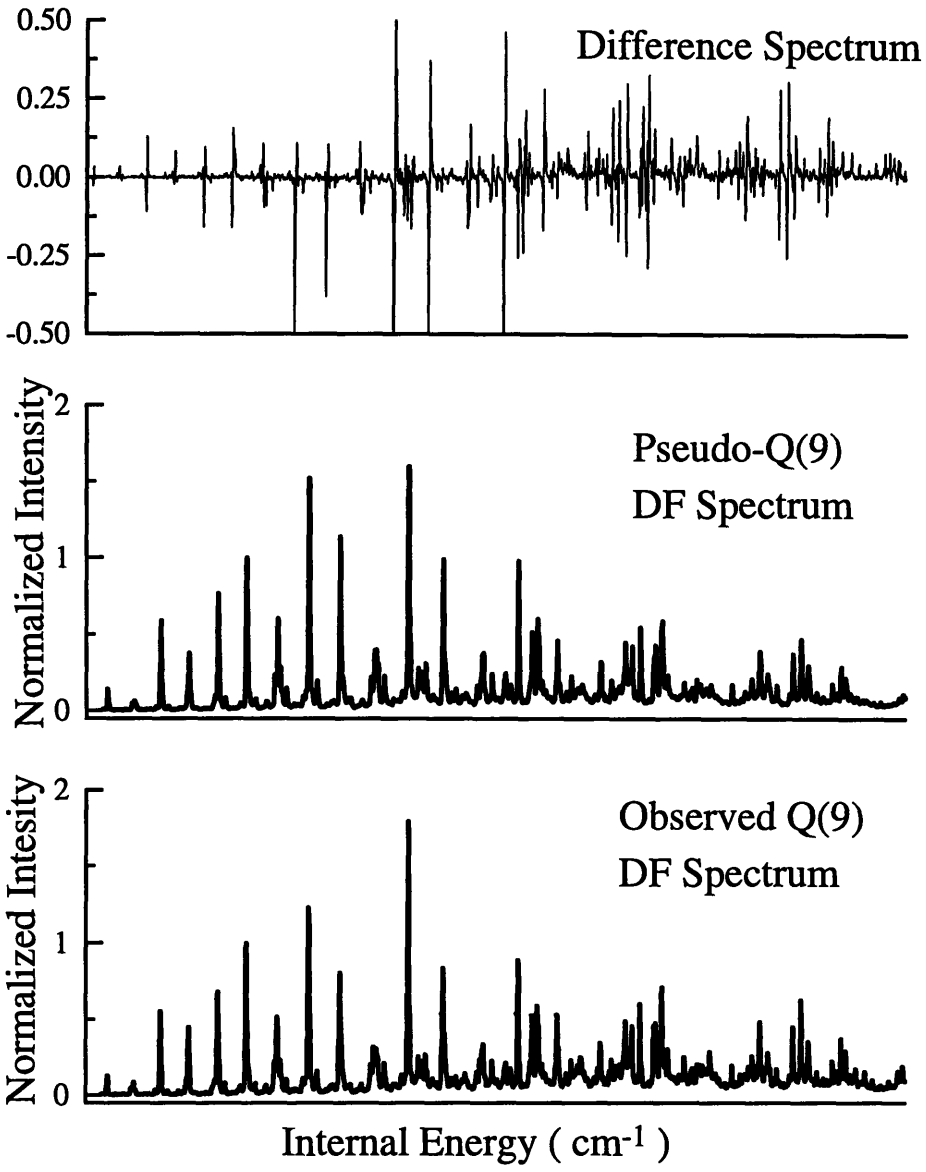

Figure 6.17: The top panel contains a difference spectrum of the observed Q(9) DF spectrum, lower panel, minus the pseudo-Q(9), middle panel spectrum. Note that the pseudo-Q(9) spectrum was generated per the instructions in the text and the relative polarization components were assumed to be in a 2:1 ratio of parallel:perpendicular compenents, see Figure 6.18. Most of the sharp peaks in the top panel are due to frequency calibration errors.

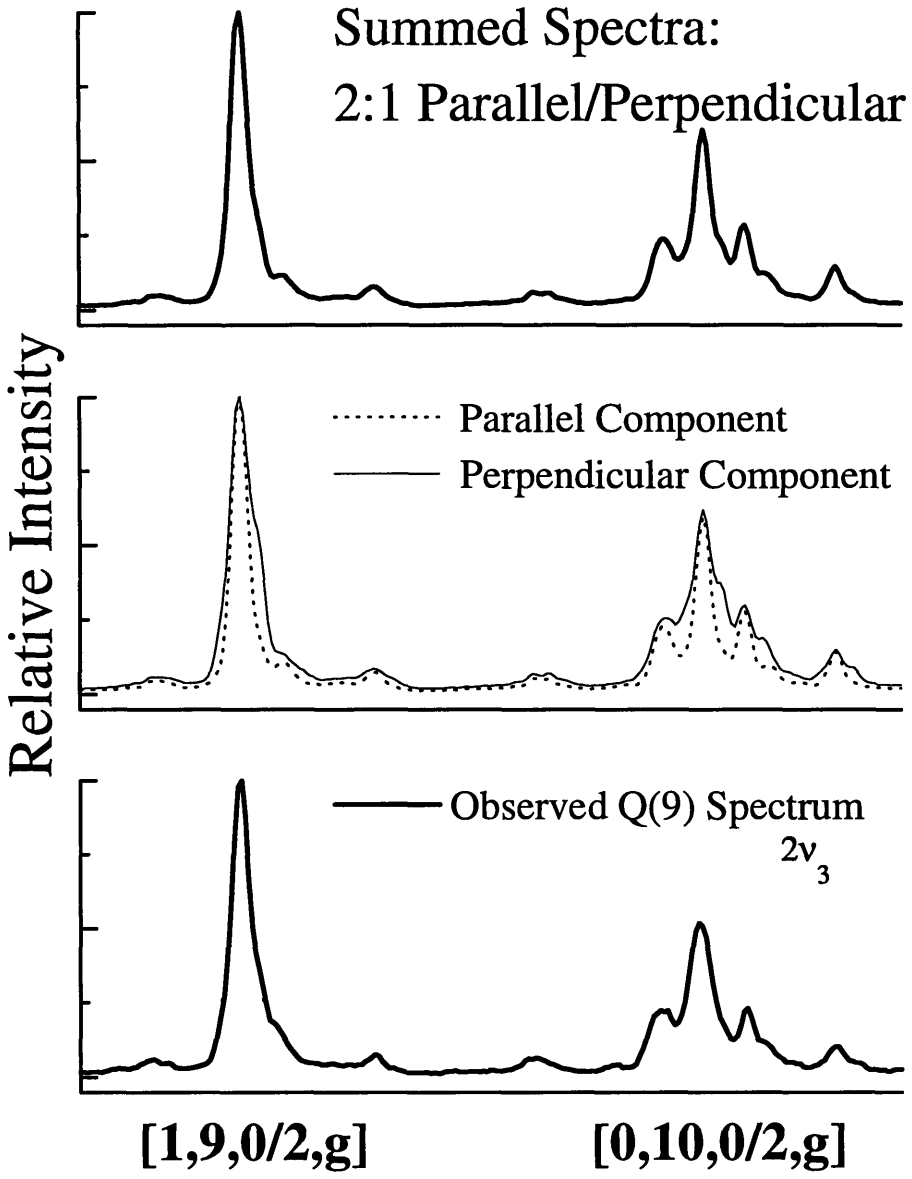

Figure 6.18: The top panel contains the summed spectra of 2:1weighted parallel and perpendicular polarization components, middle panel. The lower panel displays the observed [1,9,0/2,g] and [0,10,0/2,g] polyad energy regions. Note that the summed spectra closely resemble the observed spectra, see Figure 6.17. Also note that the upper panel of Figure 6.15 is very similar to the upper panel of the 2:1 weighted sum.

Q(1) spectra. However, the J-dependent change in the intensity of the quasi-continuum is only on the order of 2%, see Figures 6.9 and 6.10.

6.4 Discussion

The DF study conducted with different pressures and rotational quantum numbers clearly indicates that any attempt to describe all of the quasi-continuum baseline in terms of Coriolis interactions will fail. It is possible, based on the observed J-dependence of the overall Q-CB intensity, that the Coriolis interactions account for approximately 1-2% of the baseline feature of the Q(9) DF spectrum. If this were true, then the Coriolis contribution to the baseline feature in the Q(1) DF spectrum should have been a factor of 80 weaker than the Q(9) DF spectrum, due to the Coriolis matrix element scaling. Currently, our DF experiments can only measure relative intensities with an accuracy of ±20%. Therefore, we cannot detect the relative intensity change described above, because we cannot record DF spectra which would be sensitive to ≈0.01% intensity changes!

The attempt to use a weak interaction, such as Coriolis mixing, to describe the quasi-continuum baseline suggests an alternative hypothesis. Perhaps there is a higher order coupling which does couple the different polyads, intrapolyad coupling, without having any rotational quantum number dependence. Since our basis set is composed of harmonic oscillators whose energies and anharmonicities are included as diagonal elements in our H^{eff}, it is possible that there are higher order couplings, cubic and quartic, in the potential which mix the harmonic oscillator basis states. In effect, the H^{eff} model will no longer be block diagonal. From an extremely simplified picture, when there is a random distribution of matrix elements, H_{ij}, which inter-connect a variety symmetry allowed states, the observed spectrum

will be dependent upon three variables. First, which zero-order states have the optical intensity. Second, what is the average spacing of the levels. Third, the average coupling matrix element between the levels. It would be possible to run simulations where the energy positions and ZOBS characters are well known. A simplified distribution of matrix elements could be used initially. Such extensive coupling will at least partially destroy the polyad structure in our H^{eff}. It is plausible that our DF spectra and polyad recognition routine are insensitive to these extremely weak but dense couplings.

Recently, it has been proposed that the quasi-continuum baseline could be the result of many weak overlapping features. For example, there are approximately 105 eigenstates in the [2,22,0/2,g] polyad block at $E_{vib} \approx 15{,}000$ cm^{-1}. Only a small subset, 10-15%, of these eigenstates contains appreciable, >5.0%, of the ZOBS character. These states contain 70% of the ZOBS character. These states are visible in the DF spectrum as the sharp features. The rest of the eigenstates in the polyad contain insufficient ZOBS character to be visible in the DF spectrum by themselves. However, the density of weak transitions into these nominally dark eigenstates might be sufficient to produce a quasi-continuum baseline out of many overlapping weak features in the DF spectrum. We are conducting a series of DF spectral simulations to test this hypothesis. The results from this study will not be completed prior to the submittal of this thesis. Briefly, we are using a least squares adjusted effective Hamiltonian, see Chapter 5, to calculate all of the eigenstates, probed by our DF spectra, up to 16,000 cm^{-1}. (We are calculating the eigenstates and relative transition intensities for each polyad.) We scale the eigenstates for each polyad by a relative intensity factor based upon the Franck-Condon factors obtained from the DF spectra. Finally, we convolute the eigenstate spectrum with a Gaussian to reproduce the DF linewidth of $\approx$18 cm^{-1}.

We can estimate the upper limit contribution of this effect to the baseline. The calculated density of states at 15,000 cm^{-1} is approximately 0.5 states per cm^{-1}. Within one 18 cm^{-1} resolution element there will be approximately 9 states. On average, only 10% of the eigenstates contain >5.0% ZOBS character, with a relative intensity of 70%. This leaves 30% of the total intensity to be distributed among approximately 90% of the eigenstates. Therefore, the overlap of 8 adjacent weak lines could account for a quasi-continuum baseline with a relative intensity of 30% at E_{vib}=15,000 cm^{-1}. In fact, the observed relative intensity of the Q-CB is approximately 30% with respect to the sharp features at E_{vib}=15,000 cm^{-1}. At $E_{vib}\approx$11,000 cm^{-1} the density of states is approximately 0.09 states per cm^{-1}. There will be 1.6 states in a 18 cm^{-1} resolution element. The [0,16,0/2,g] polyad, at $E_{vib}\approx$11,000 cm^{-1} contains 25 eigenstates, 7 of which contain >5% ZOBS character (30% of the eigenstates contain 92% of the ZOBS character.) Therefore, 70% of the 1.6 states (1.12) could contain as much as 8% of the ZOBS character. The observed relative intensity of the Q-CB is approximately 2% with respect to the sharp features at E_{vib}=11,000 cm^{-1}. The reader should be approach these results cautiously. They represent an upper bound. The actual contributions from weak eigenstates should be less than this! This arises from the density of states and ZOBS character which is *not* evenly distributed throughout each polyad!

6.5 References

1. See for example Princeton Instruments Inc. Manuals for proper use of Intensified Charge Coupled Devices (ICCD).

2. The first low resolution DF spectrum of Acetylene was reported by L.E. Brus, *J. Mol. Spectrosc.* **75**, 245 (1979). J.C. Stephenson, J.A. Blazy, D.S. King, *Chem. Phys.* **85**, 31 (1984) reported a DF spectrum of acetylene at slightly higher resolution.

3. G.J. Scherer, Y. Chen, R.L. Redington, J.L. Kinsey, and R.W. Field, *J. Chem.Phys.* **85**, 6315 (1986).

4. K. Yamanouchi, N. Ikeda, S. Tsuchiya, D.M. Jonas, J.K. Lundberg, G.W. Adamson, R.W. Field, *J. Chem. Phys.* **95**, 6330 (1991).

5. S. Tsuchiya, *Private Communication* (Summer 1996).

6. Y-C. Hsu, M-S. Lin. and C-P. Hsu. *J. Chem. Phys.* **94**(12), 7832 (1991). Y-C. Hsu, P-R. Wang, M-C. Yang, D. Papousek, Y-T Chen, W-Y Chaing. *Chem. Phys. Let.* **190**, 507 (1992). M. Suto, L.C. Lee. *J. Chem. Phys.* **80**, 4825 (1984).

7. F. Shokoohi, T.A. Watson, H. Reisler, F. Kong, A.M. Renlund, and C. Wittig, *J. Phys. Chem.* **90**, 5695 (1986). J.Zhang, C.W. Riehn, M. Dulligan, C. Wittig, *Private Communication* (1996).

8. Y-C. Hsu, J.J-M. Lin, D. Papousek, J-J. Tsai. *J. Chem. Phys.* **98**, 6690 (1993).

9. J.F. Statnton, C-M Huang, P.G. Szalay. *J. Chem. Phys.* **101**, 356 (1994). J.F. Stanton, J. Gauss. *J. Chem. Phys.* **101**, 3001 (1994).

10. C.K. Ingold, and G.W. King, J. Chem. Soc. **00**, 2702 (1953).

11. M.M. Gallo, T.P. Hamilton, H.F. Schaefer III., *J. Am. Chem. Soc.* **112**, 3714 (1990).

12. M. Abbouti Temsamani, M. Herman, Private Communication (1996).

13. D.M. Jonas, Ph.D. Thesis, Massachusetts Institute of Technology (1992) *and references cited therein.*

14. C.H. Townes, A.L. Schawlow. *Microwave Spectroscopy.* Dover Publications, Inc. New York, NY (1975).

15. Y. Chen, Ph.D. Thesis, Massachusetts Institute of Technology, (1988).

16. C. Kittrel, "*Stimulated Emission Pumping by Fluorescence Dip: Experimental Methods*," Molecular Dynamics and Spectroscopy by Stimulated Emission Pumping, World Scientific, New Jersey, (1995).

Chapter 7: $\tilde{A}^1A_u \rightarrow \tilde{X}^1\Sigma_g^+$ Dispersed Fluorescence Spectra from $V_0^3K_0^1$ and $[4V_b]$

7.1 Introduction

The $V_0^3K_0^1$ vibrational band of the $\tilde{A}^1A_u$ state has been studied extensively and has been implicated in the $S_1 \sim T_n$ (n=1,2,3) intersystem crossing.[1-3] Experiments to probe the activity of the $V_0^3K_0^1$ level in intersystem crossing are discussed in the following Chapter. Scherer and co-workers assigned a previously undetected anharmonic perturbation in the $V_0^3K_0^1$ vibrational band to the $\nu_2+2\nu_4$ combination band.[4] Recently, Crim and co-workers conducted a series of infrared-ultraviolet double resonance experiments where they reassigned the anharmonic perturbation to the $[4V_b]$ level.[5] Since $\omega_4^0 \approx \omega_6^0 \approx 765$ cm^{-1}, the $[4V_b]$ level corresponds to either $4\nu_4$ or $4\nu_6$ or $2\nu_4+2\nu_6$. In this chapter, we report initial observations based upon a pair of dispersed fluorescence spectra recorded from the $V_0^3K_0^1$ and the $[4V_b]$ levels. We must stress that this chapter does not contain *any* complete analysis. We are including these DF spectra for completeness and as a future guide to anyone who might wish to explore these levels.

7.2 Experimental

The dispersed fluorescence (DF) experimental setup has been described in detail in Chapter 3. Briefly, we record a series of low resolution, 18 cm^{-1} for the 350 nm photon recorded in first order, dispersed fluorescence spectra which originate from two different rovibrational levels of the $\tilde{A}^1A_u$ state of Acetylene. The DF spectra were recorded by

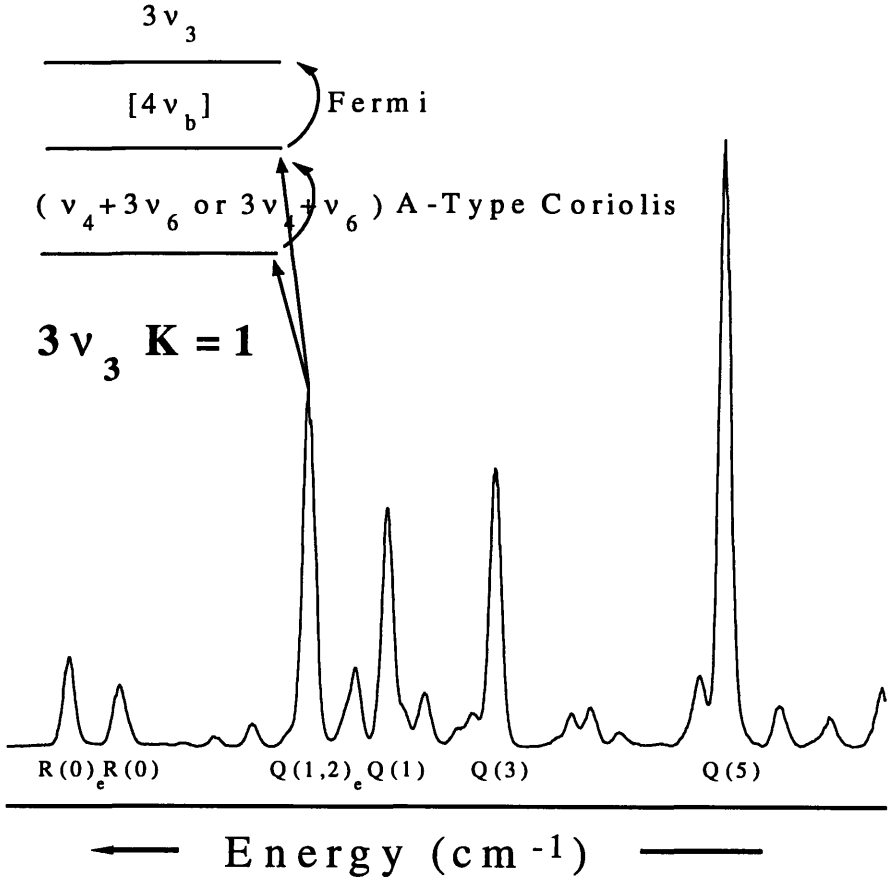

Figure 7.1: Fluorescence excitation spectrum of the $\tilde{A}^1A_u$ $V_0^3K_0^1$ vibrational band. The plot contains low J transitions for the R and Q Branches. The transitions denoted by a subscript 'e' label the [$4V_b$] levels.

locking the dye laser output onto either ${}^rQ_0(1)$, $J'_{K_a,K_c} = 1'_{1,1}$, or ${}^rQ_0^e(n)$, $J'^e_{K_a,K_c} = n'^e_{1,1}$ of the $V_0^3K_0^1$ vibrational band of the $\tilde{A}^1A_u \leftarrow\tilde{X}^1\Sigma_g^+$ transition, see Figure 7.1. (V represents the *trans*-bending mode, ν_3' in the $\tilde{A}$ state and ν_4'' in the $\tilde{X}$ state. The subscript and superscript denote the lower and upper state quanta, respectively) and where ${}^rQ_0(1)$ refers to rotational transitions in the optically allowed $V_0^3K_0^1$ vibrational band. ${}^rQ_0^e(n)$

represents transitions into the [$4V_b$] anharmonic perturber of the $3\nu_3$ level. These transitions are nominally Franck-Condon forbidden but gain oscillator strength from the $V_0^3K_0^1$ vibrational band through the anharmonic interaction. The *n* refers to three rotational levels, $J'_{K_a,K_c} = 1'^e_{1,1}, 2'^e_{1,2}, 3'^e_{1,3}$, transitions which all occur within an 0.08 cm^{-1} region of the $V_0^3K_0^1$ band. Our laser linewidth (FWHM) is approximately 0.03 cm^{-1}. These perturbed levels have been examined and assigned by the high resolution spectroscopy of Drabbels.[6,7] A static gas cell was charged with 5 Torr of acetylene, 99.6% pure (Matheson). The total spontaneous fluorescence from each rovibronic transition was imaged by a series of fused silica lenses, *f*/5.8, onto the entrance slits of a Jobin-Yvon 640mm monochromator. The fluorescence was dispersed and collected in 20nm spectral segments from 230 to 370 nm.

7.3 Discussion

We were originally drawn to the $V_0^3K_0^1$ vibrational level because the $\tilde{A}^1A_u$ -state anharmonic perturber, [$4V_b$], corresponds to the *cis*-bending vibrational levels in the $\tilde{X}^1\Sigma_g^+$ state, $(\nu'_4(a_u) \,\&\, \nu'_6(b_u) \cup \nu''_5(\pi_u))$. As discussed in previous Chapters, the nominal $\tilde{A}^1A_u \rightarrow \tilde{X}^1\Sigma_g^+$ transitions only access CC stretch and *trans*-bending ZOBS character. However, use of the [$4V_b$] levels as an $\tilde{A}^1A_u \rightarrow \tilde{X}^1\Sigma_g^+$ dispersed fluorescence intermediate state would create Franck-Condon intensity in the *cis*-bending levels (primarily $\nu''_5 = 4$). Therefore, our DF spectra could exploit a different ZOBS that would sample moderate quanta of V_5 as well as V_2 and V_4! A major drawback to the analysis of DF spectra recorded with a ($0,V_2,0,V_4,V_5$) ZOBSs is that each polyad will no

longer contain a single zero-order bright state. However, we believe that it will be possible to separate the relative contributions from two ZOBSs at low E_{vib}.

Only one or two polyads belonging to different values of N_s will exist in a given N_{res} energy region at low E_{vib}. The dark levels which contain large amounts of *cis*-bending character will lie above the $(0,V_2,0,V_4,0)$ ZOBS. Therefore, effects of a $(0,V_2,0,V_4,V_5\neq0)$ ZOBS may be visible at the high E_{vib} end of a $[N_s,N_{res},0/2,g]$ polyad. A deperturbation analysis by Scherer and co-workers indicated that the Q(1) and $Q(1)^e$ levels were approximately a 50:50 mixture of each other. (The Q(2):$Q(2)^e$ and Q(3):$Q(3)^e$ are approximately 60:40 and 80:20 admixtures of each other, respectively.)[4] Figure 7.2 displays the DF spectra recorded from the Q(1) and $Q(n)^e$ excitation transitions. Notice that the two DF spectra hardly resemble each other. However, at low E_{vib}, the Q(1) and $Q(n)^e$ DF spectra show qualitative agreement, see Figure 7.3. The two spectra contain approximately 80% of the same DF features. Furthermore, there are several instances at low E_{vib} where the Q(1) and $Q(n)^e$ DF spectra are qualitatively (90%) similar but upon closer examination have significant quantitative differences. For example, Figure 7.4 displays the N_{res}= 8-10 polyad energy region. Arrows indicate areas where either extra features appear in the $Q(n)^e$ DF spectrum or where there is a clear discrepancy between the Q(1) and $Q(n)^e$ spectra in the relative intensities. The latter observation may prove to be useful in extracting information about the relative contributions of the different ZOBSs. The discrepancies denoted by arrows in Figure 7.4 are located on eigenstates that are normally composed of basis states that are primarily composed of *trans*- and *cis*-bent vibrations. The $(0,V_2,0,V_4,0)$ and $(0,V_2,0,V_4,V_5\neq0)$ ZOBSs may have the largest visible intensity interference with these eigenstates.

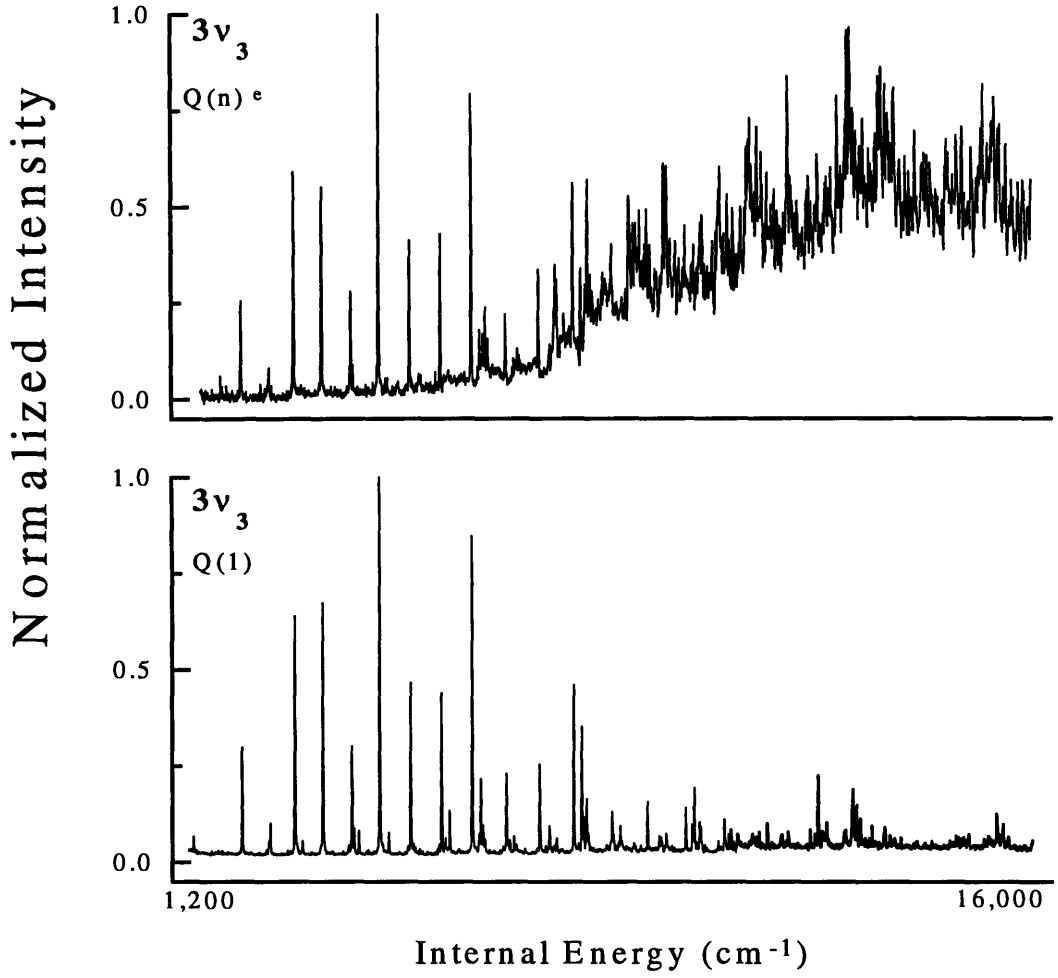

Figure 7.2: DF spectra excited via the ${}^{r}Q_0(n)^{e}$ transition, upper panel, and the ${}^{r}Q_0(1)$ transition, lower panel, of the $V_0^3K_0^1$ vibrational band in the $\tilde{A}^1A_u$ state. Note the extreme deviation at high $E_{vib.}$

Since the Q(1) and Q(1)^e transitions populate levels in $V_0^3K_0^1$ that are 50:50 mixtures of the same zero-order basis states,

$$\Psi_{\pm} = 0.5\Phi_{4\nu_b} \pm 0.5\Phi_{V_0^3K_0^1},$$

one should expect the DF spectra recorded from both intermediate states to resemble each other. It is puzzling why there is such a profound difference. Even though we are

exciting $Q(n)^e$ and not a single $Q(1)^e$ level, Drabbel's work indicated that the $Q(1)^e$ transition populates levels that are *at least* 5 times bigger than the $Q(2)^e$ and $Q(3)^e$ levels ($Q(2)^e$ and $Q(3)^e$ contain equal intensity).[6,7] Therefore, the DF spectra recorded from the $Q(n)^e$ transition will be due mostly to $Q(1)^e$. It seems unlikely that these differences in mixing fraction would significantly affect the *global* (over 15,000 cm^{-1}) structure of the DF spectra. There will be some local constructive and destructive interference in each polyad.

At low rotational quantum numbers in the $V_0^3K_0^1$ vibrational band, Scherer and co-workers also indicated that there was an additional perturbation, that primarily affected the extra levels, which was due to a Coriolis interaction.[4] For the purposes of their deperturbation, they ignored this interaction. In fact, there is an extensive network of levels in the $V_0^3K_0^1$ energy region all of which can be coupled by anharmonic and Coriolis inteteractions, see Figure 7.5. Briefly, the $J'_{K_a,K_c} = 1'_{1,1}$ $V_0^3K_0^1$ rovibrational level has a anharmonic interaction with the $J'_{K_a,K_c} = 1'_{1,1}$ [$4V_b$] levels. All of the $J'_{K_a,K_c} = 1'_{1,1}$ [$4V_b$] levels, $4\nu_4$ or $4\nu_6$ or $2\nu_4+2\nu_6$, are coupled to the $J'_{K_a,K_c} = 1'_{0,1}$ [$4V_b$] levels by a C-type Coriolis ($\Delta K_a=\pm1,\Delta K_c=$ even). The $J'_{K_a,K_c} = 1'_{1,0}$ $\nu_4+3\nu_6$ and $3\nu_4+1\nu_6$ levels can also be coupled to the $J'_{K_a,K_c} = 1'_{1,1}$ [$4V_b$] levels by A-type Coriolis ($\Delta K_a=0,\Delta K_c=$ odd) interactions.

It may be possible to understand the Q(1) and $Q(n)^e$ DF spectra by carefully mapping out all of the $\tilde{A}^1A_u$ state perturbations which occur in the $V_0^3K_0^1$ energy region.

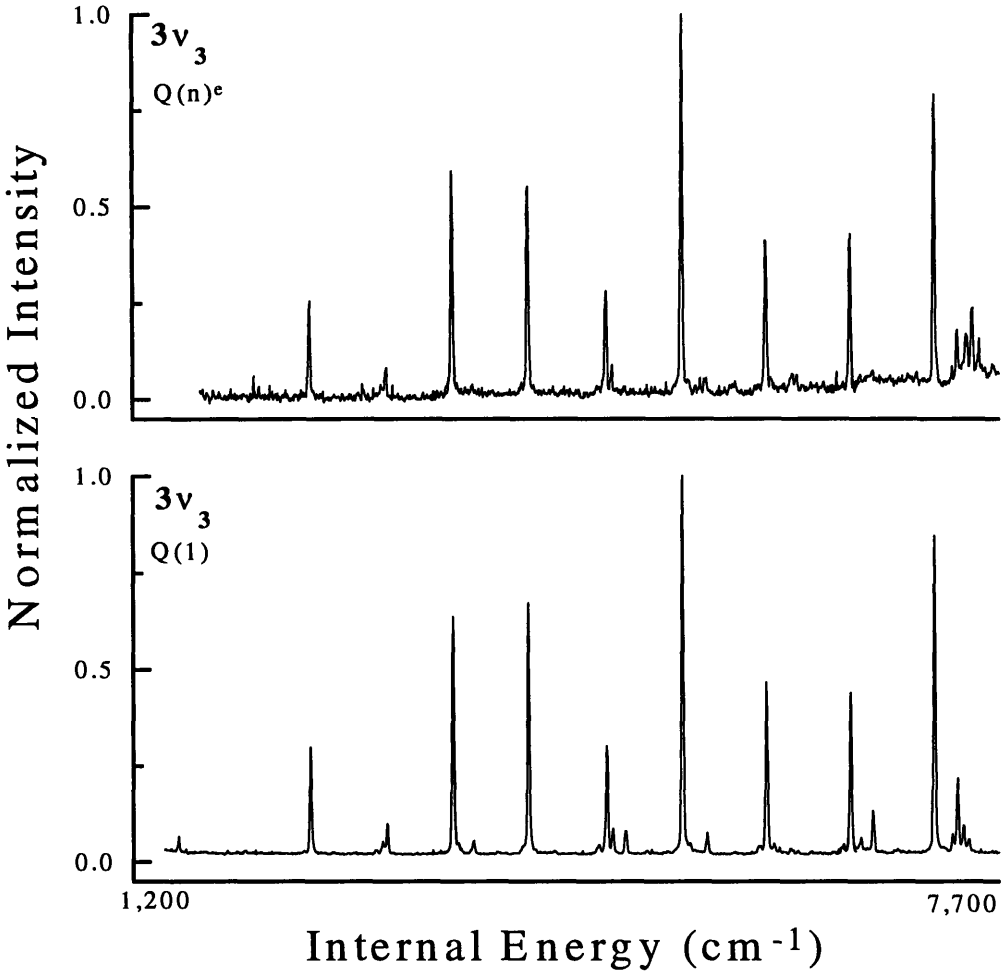

Figure 7.3: Low internal energy region of the DF spectra recorded from Q(n)^e, upper panel, and Q(1), lower panel. In general, the low energy region of the two DF spectra appear very similar. A closer view of the N_{res}=8-10 polyad region reveals several discrepancies, see Figure 7.4.

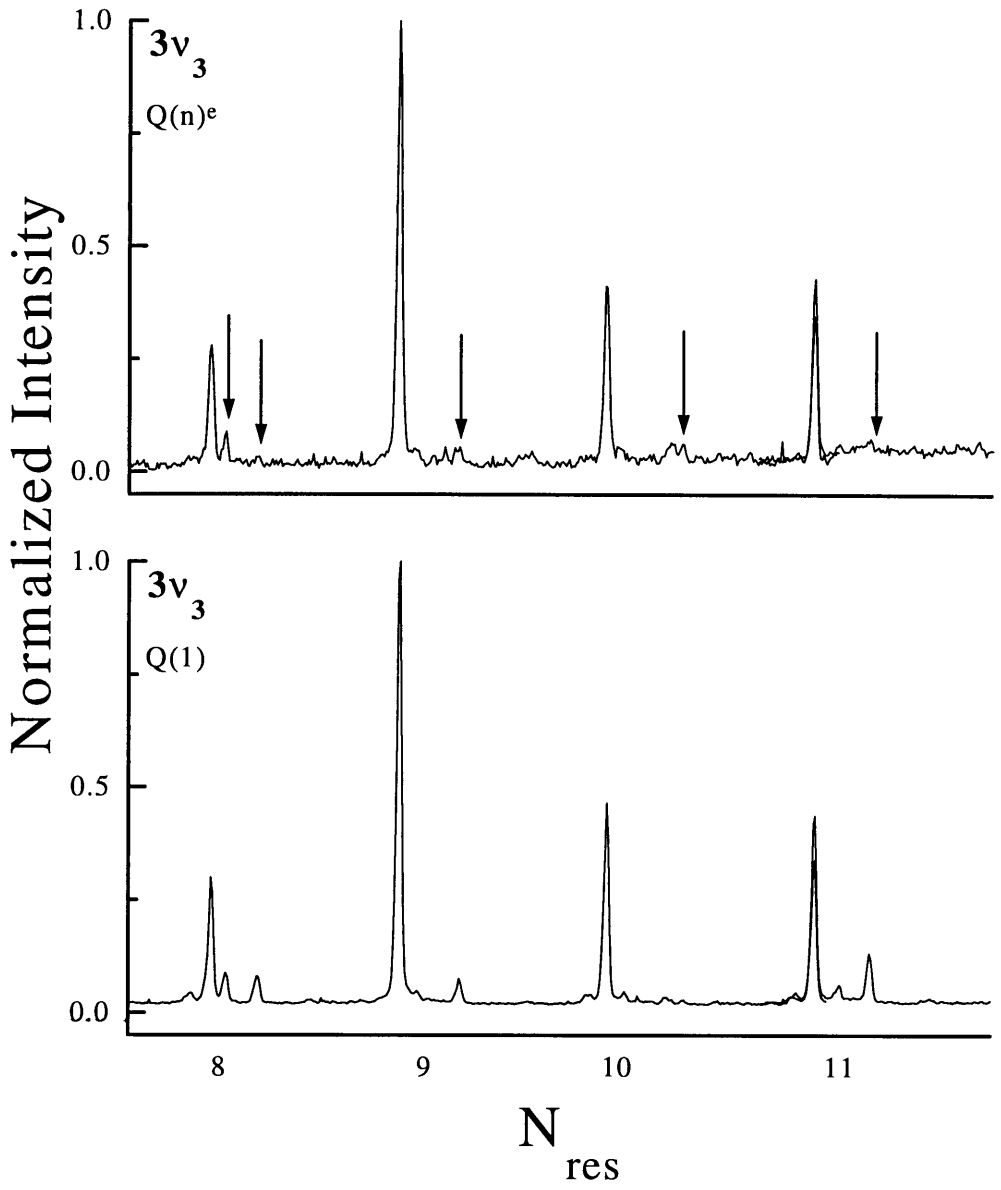

Figure 7.4: DF spectra from Q(n)^e, upper panel, and Q(1), lower panel, in the N_{res}=8-11 polyad energy region. The arrows indicate several places where the Q(n)^e and Q(1) spectra do not agree. Note that all of the discrepancies occur to the high energy side of the polyad, see text for details.

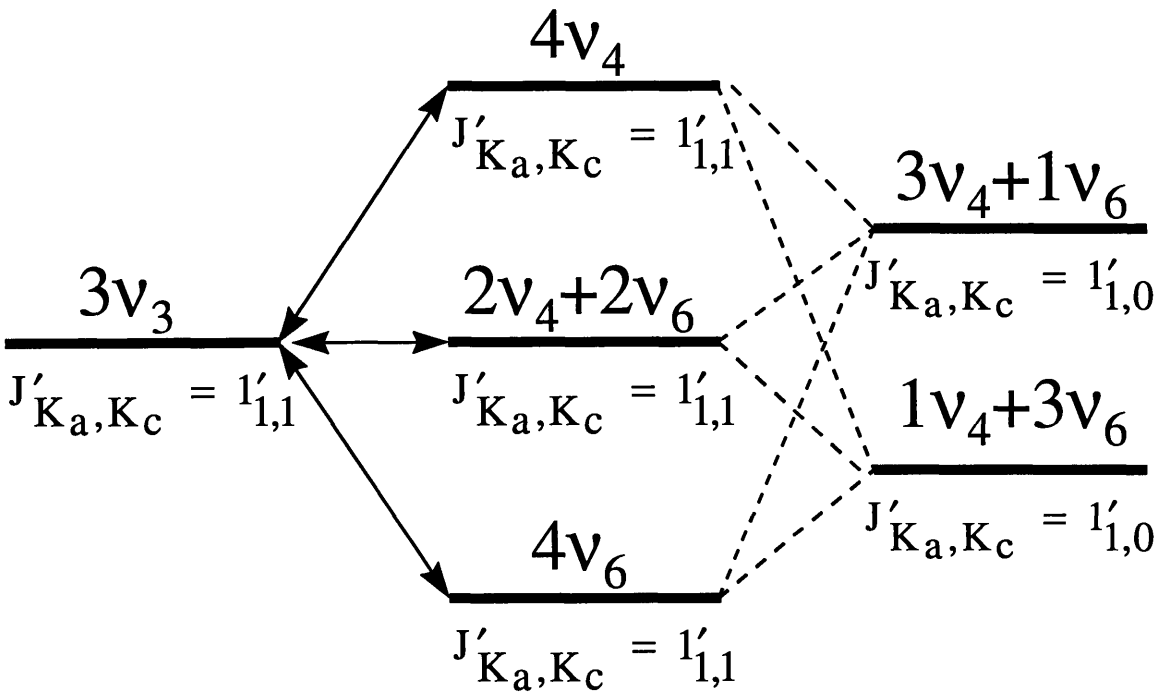

Figure 7.5: The optically allowed transition to the $1'_{1,1}$ $V_0^3K_0^1$ rovibrational level in the $\tilde{A}^1A_u$ state is coupled by a Fermi resonance, solid lines with double sided arrows, to the $1'_{1,1}$ [$4V_b$] levels. The $1'_{1,1}$ [$4V_b$] levels are connected to the $1'_{0,1}$ rotational levels of ($3\nu_4+1\nu_6$) and ($1\nu_4+3\nu_6$) by A-type Coriolis, dashed lines. All of the $1'_{1,1}$ rotational levels within totally symmetric vibrations will have a C-type Coriolis interaction with the $1'_{0,1}$ rotational levels of totally symmetric vibrations, not shown.

7.4 References

1. J.K. Lundberg, R.W. Field, C.D. Sherrill, E.T. Seidl, Y.Xie, and H.F. Schaefer, *J. Chem. Phys.* **98,** 8384 (1993).

2. P. Dupré, R. Jost, M. Lombardi, P.G. Green, E. Abramson, and R.W.Field, *Chem. Phys.* **152,** 293 (1991).

3. S. Drucker, J.P. O'Brien, P.Patel, R.W. Field, *J. Chem. Phys.* **00**, 0000 (1996) *and references cited therein.*

4. G.J. Scherer, Y. Chen, R.L. Redington, J.L. Kinsey, and R.W. Field, *J. Chem. Phys.* **85**, 6315 (1986).

5. A.L. Utz, J.D. Tobiason, M.E. Carrasquillo, L.J. Sanders, and F.F. Crim, *J. Chem. Phys.* **98**, 2742 (1993).

6. M. Drabbels, J. Heinze, and W.L. Meerts, *J. Chem. Phys.* **100**, 165 (1994).

7. M. Drabbels, Ph.D. thesis, University of Nijmegen, (1995).

Chapter 8 The Effects of Triplet Perturbers on Photophysical Processes in the $\tilde{A}\ ^1A_u$ State of Acetylene

This chapter has been published in the *Journal of Chemical Physics*. This work represents the initial attempt of our research group to probe the triplet states of acetylene. While the triplet states of larger molecules have been the focus of general spectroscopic studies, very little is known about the triplet states of small molecules, especially hydrocarbons.

8.1 Introduction

The lowest energy triplet states of acetylene have been comprehensively characterized by *ab initio* calculations[1-4], yet very few direct experimental observations[5,6] of acetylene triplet states have been reported. One series of experimental studies has focused on the triplet perturbations evident in the *trans*-bending (ν_3) levels of the $\tilde{A}^1A_u$ (S_1) state[7-10]. Zeeman anticrossing spectra of $\nu_3 = 0$-3 levels indicate that the strength of $S_1 \sim T$ interactions increases monotonically with ν_3[7]. In this chapter, we report several unexpected photophysical consequences of this increased coupling strength, as revealed in fluorescence excitation spectra of the $\tilde{A} \leftarrow \tilde{X}$ transition.

Fluorescence excitation (LIF) spectra are recorded by simultaneously monitoring ultraviolet (UV, 250-400 nm) and near infrared (NIR, 0.9-1.5 μm) emission. The rotationally-resolved patterns in the UV- and NIR-detected LIF spectra are nearly identical, for excitation in the 225 nm ($2\nu'_3$) region. Changing the excitation region to 220 nm ($3\nu'_3$) significantly decreases the correlation between the UV and NIR responses. We will explain how the anomalous behavior in the $3\nu'_3$ band signals an expansion in the photophysical repertoire of the excited species. We conclude that the numerous zero-field $S_1 \sim T$ perturbations in this band give rise to mixed eigenstates that can provide access to widely separated regions of the triplet manifold.[11]

8.2 Experiment

We recorded simultaneously UV- and NIR-detected fluorescence excitation spectra of the $V_0^2K_0^1$ and $V_0^3K_0^1$ subbands of the C_2H_2 $\tilde{A}\ ^1A_u \leftarrow \tilde{X}^1\Sigma_g^+$ transition. (V represents the *trans*-bending mode, ν_4" in the $\tilde{X}$ state and ν_3' in the $\tilde{A}$ state.) The third harmonic of a Continuum NY-61 Nd:YAG laser pumped a Lambda Physik 3002 dye laser equipped with an intracavity etalon. The Coumarin 440 or 450 output of the dye laser was doubled in a β-BBO crystal to produce 300 μJ of 220 nm or 225 nm radiation. The doubler output was focused by a 40 cm focal length lens and passed through a 2 mm hole in an off-axis parabolic mirror (see below) placed at the lens focus. The laser beam entered a static gas cell (36 cm long × 5 cm diam) containing 150 mT acetylene (Matheson, 99.6 % minimum) which had been subjected to several freeze--pump--thaw purification cycles. At the end of every half hour of data collection, the cell was evacuated and refilled to 150 mT, in order to minimize cell contamination caused by radical reactions secondary to acetylene photodissociation.

For UV detection, the fluorescence was collected perpendicularly to the laser beam and focused onto an RCA 4501 V1 photomultiplier tube through a UG-11 bandpass filter (Schott). For NIR detection, a 10 cm focal length off-axis parabolic mirror was used to focus the end-on fluorescence onto an ultra-pure germanium detector (North Coast, model EO817) equipped with a long pass (1.0 μm cutoff) filter (Oriel) and cold mirror (Oriel). The amplified outputs of the photomultipier tube and germanium detector were sent to a gated integrator (SRS, model SR250), digitized, and stored.

8.3 Results

For each observed subband, transitions Q(1)-Q(9) and R(0)-R(7) were recorded. The scatterplots in Figure 8.1 indicate the extent of correlation between the UV- and NIR-detected emission signals in the Q branch of each subband. Each point on the scatterplot represents one bin of recorded data, corresponding to a single A/D conversion. About 80 bins of spectral data are encompassed by one resolution element, about 0.1 cm^{-1} wide. (This is the observed rotational line FWHM resulting from the convolution of the Doppler lineshape with the spectral output of our dye laser.) In constructing the scatterplots, the UV and NIR spectra were separately normalized by setting to unity the highest-valued data point within each branch recorded. Least-squares fits to a straight line were performed on the Q-branch scatterplots shown in Figure 8.1, yielding correlation coefficients of 0.97 for $2\nu_3$ and 0.79 for $3\nu_3$. (A correlation coefficient of 1.0 signifies a perfect straight-line fit.) The same procedure applied to the R-branch data yielded correlation coefficients of 0.98 for $2\nu_3$ and 0.77 for $3\nu_3$. These correlation coefficients suggest that the two excitation bands are affected by quite different photophysical processes. The fitted slope from the scatterplot for each data set was used to rescale the NIR spectrum, thereby minimizing the systematic differences between the UV- and NIR-detected spectra. Figure 8.2 shows representative UV, rescaled NIR, and difference spectra. The difference spectra confirm the impression from Figure 8.1 that the agreement between UV- and NIR-detected signals is considerably better in the $2\nu_3$ than in the $3\nu_3$ band. However, this comparison cannot be statistically meaningful, since the amplitudes in a difference spectrum depend slightly on the originally chosen normalization procedure.

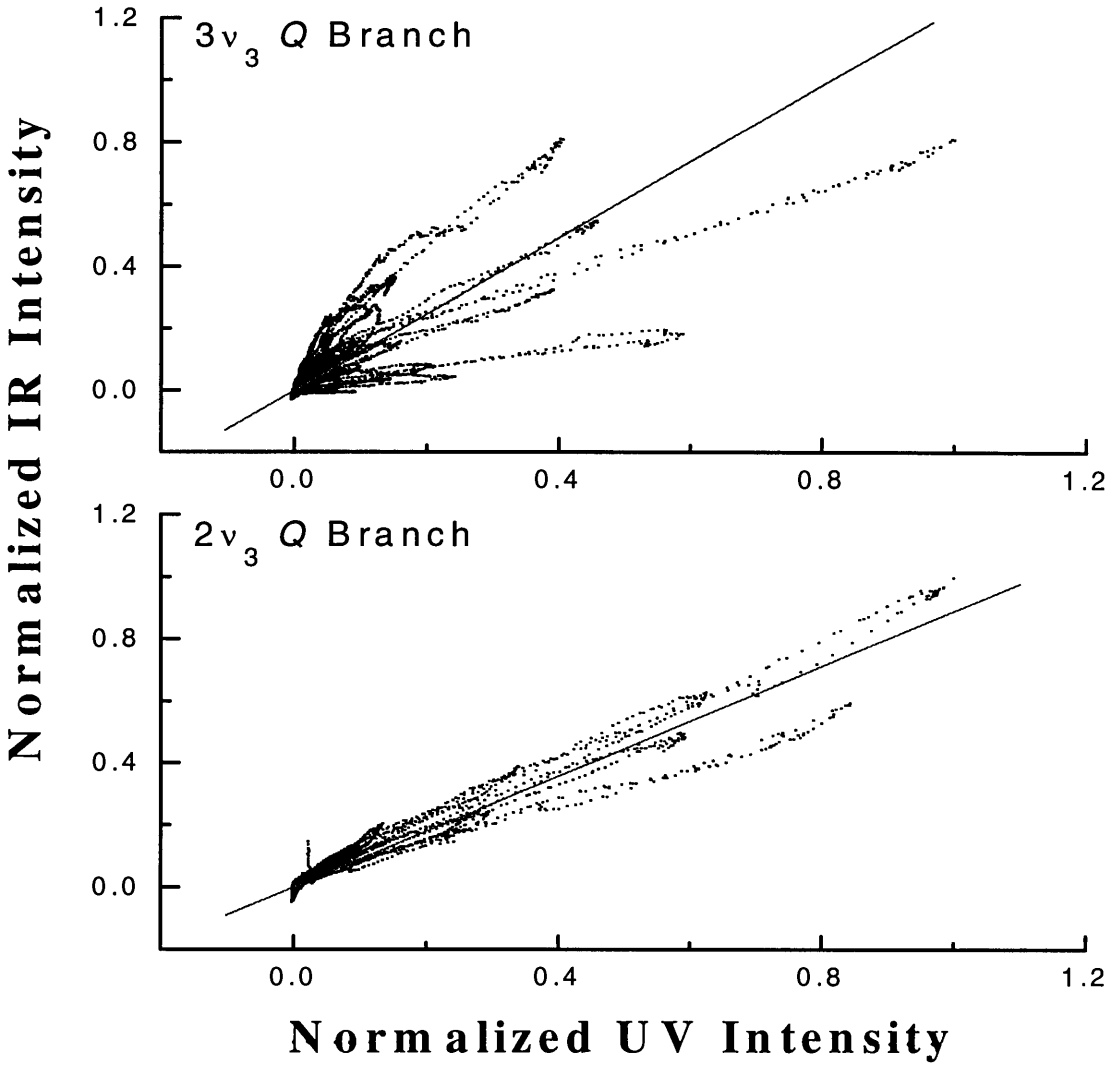

Figure 8.14: Scatterplots indicating the correlation between corresponding data points in the UV- and NIR-detected spectra. The solid line is the result of a least-squares fit through the origin.

To measure the absolute agreement between the intensities in the UV- and NIR-detected spectra for a given subband, we used the Kolmogorov--Smirnov (K-S) test[12], which assesses the probability (between 0 and 1) that two samples of data are drawn from the same underlying distribution function. Individual spectral features were compared by performing the Kolmogorov--Smirnov test on samples of 80 data bins (constituting the width of one rotational

line) from each spectrum. Probability maps, shown in Figure 8.3, were created by stepping the sample's center bin through the spectrum. These maps indicate significant agreement between the

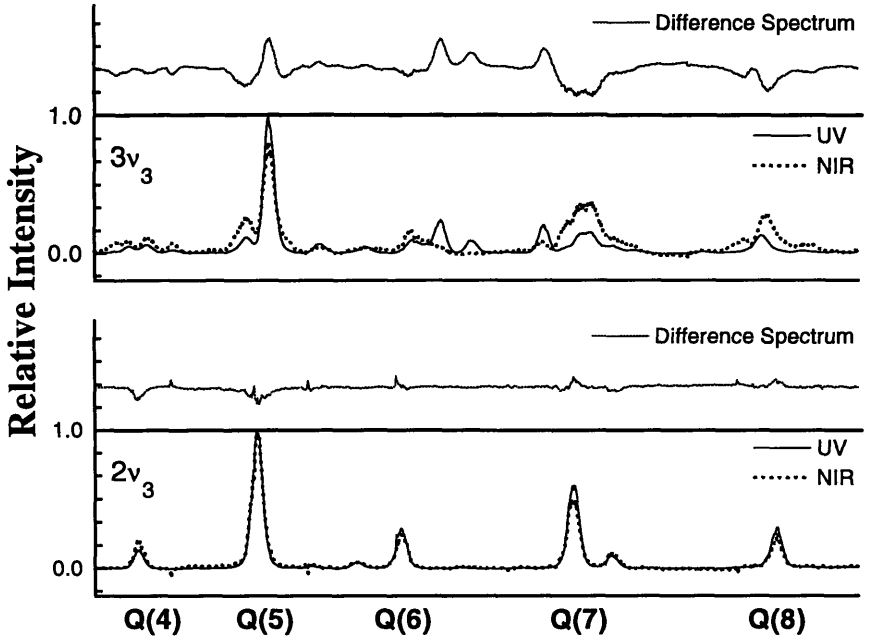

Figure 8.15: UV- and NIR-detected fluorescence excitation spectra. For a given subband, the UV-detected spectrum was normalized by setting the highest valued data point to unity. The NIR-detected spectrum was then scaled (using the slope information from the corresponding scatterplot in Fig. 1) to minimize the differences between the UV- and NIR-detected spectra.

UV and NIR intensities on nearly every peak in $2\nu_3$, but virtually no agreement in $3\nu_3$. For 17 observed transitions in each band, the average K-S value was 0.50 in $2\nu_3$ and 0.03 in $3\nu_3$.

8.4 Discussion

To interpret these observations, we first identify the carriers of the UV and NIR emission signals. UV emission is due to well-characterized $\tilde{A} \rightarrow \tilde{X}$ transitions.[13] The NIR signal, however, *cannot* contain an appreciable contribution from $\tilde{A} \rightarrow \tilde{X}$ fluorescence, due to exceedingly poor Franck-Condon (FC) factors.[1] But triplet (T_n, n= 2 or 3) admixture in the laser-prepared, nominally S_1 state, could mediate NIR emission *via* $T_n \rightarrow T_1$ transitions, which are

expected to occur in this region on the basis of *ab initio* calculations.[1,3,4] These NIR transitions could originate in either the initially prepared eigenstate or in a pure T_n state populated by rotational (collision-induced) relaxation of the S_1~T_n mixed state.[14]

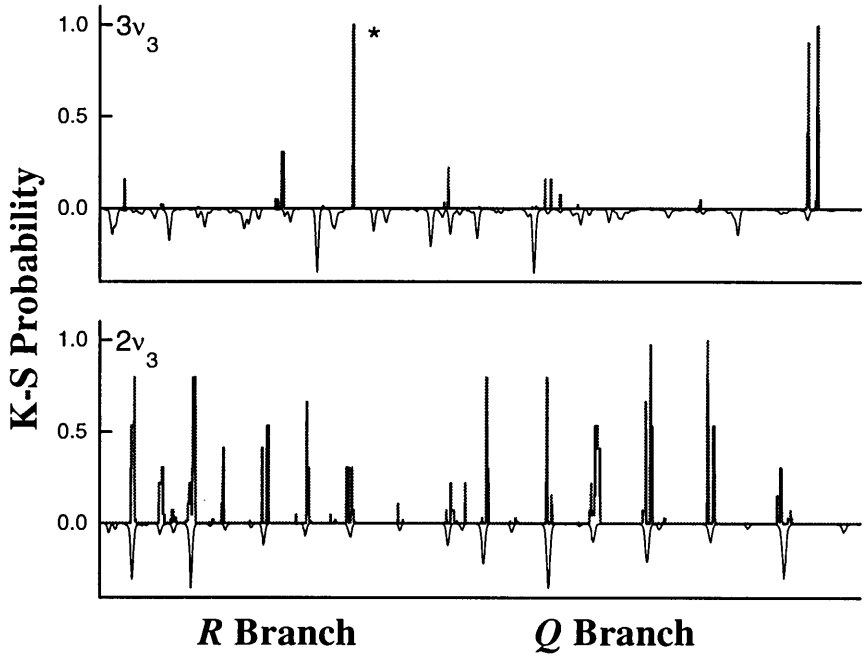

Figure 8.16: Results of the Kolmogorov-Smirnov (K-S) test (heavy lines), measuring the probability that the UV and scaled NIR-detected spectra for a given subband are derived from same intensity distribution; see text for details of the sampling procedure. The UV-detected spectra (inverted for clarity) are also plotted (light lines). Note that the K-S probability is zero off-resonance, due to baseline noise. The asterisk denotes an incidence of large K-S outcome due to an accidentally exact coincidence of the baselines of the UV- and NIR-detected spectra.

A second likely carrier of the NIR signal is C_2H $\tilde{A}^2\Pi \rightarrow \tilde{X}^2\Sigma^+$ emission, where the C_2H $\tilde{A}$ state is formed by photodissociation of the initially prepared C_2H_2 species. The dissociation mechanism is suggested by the work of Ito *et al.*[15], in which two-photon, two-color excitation is used to prepare 3p Rydberg states of C_2H_2 *via* an $\tilde{A}$-state $\nu_3 = 3$ resonant intermediate. If the two-photon energy is increased by ~15,000 cm^{-1}, as in the present one-color experiment, then *n*p

(n=6-9) *gerade* Rydberg states ($^{1,3}R_g$) are expected.[16,17] These higher Rydberg states are known to have predissociation lifetimes of less than 1 ps, decaying to long-lived (~5 μs) C_2H + H species.[17] Emission from photolytically generated C_2H has been detected in the 1-2 μm region and assigned to the $\tilde{A} \rightarrow \tilde{X}$ transition.[18]

We studied the dependence of NIR emission intensity on laser fluence for several rotational transitions in the $2\nu_3$ and $3\nu_3$ bands. The intensity of NIR emission originating from C_2H fragments should depend quadratically on laser fluence, while the NIR emission signal due to $T_n \rightarrow T_1$ C_2H_2 transitions should show a linear depependence. For each rotational transition studied, the NIR intensity *vs.* laser fluence curve could be fit to a polynomial with both linear and quadratic terms. However, because the resulting fit parameters were highly correlated in each case, it is not possible to state with certainty the relative contributions to the NIR signal made by intact *vs.* photofragmented acetylene.

As we discuss below, both of these sources of IR fluorescence are affected by the triplet content of the initially excited C_2H_2 species. We contend that triplet perturbations influence the extent of correlation between NIR and UV emission intensities in a particular subband. To show how this could occur in the observed spectra, we first examine the mechanisms by which triplets could contribute to NIR emission intensities.

The excitation laser in this experiment prepares incoherently a collection of eigenstates that are created from S_1 ($\tilde{A}$ ^1A_u) and T_n (n=1-3) states. The oscillator strength for the excitation is provided by the S_1 ν_3 overtone (FC-active [19]) component of the eigenstate. As noted above, $\tilde{A}$ -state fluorescence in the NIR is FC-forbidden, so significant triplet content (T_n, n > 1) is *required* in order to observe NIR emission directly from the prepared eigenstates. The other

source of NIR signal, C_2H $\tilde{A}^2\Pi \rightarrow \tilde{X}^2\Sigma^+$ fluorescence, is also influenced by the admixture of triplets, but in a more complicated way. The $S_1 \sim T_n$ mixed eigenstates resonantly enhance the two-photon production of high-lying triplet gerade Rydberg states (^3R_g). The Rydberg states exist in singlet--triplet pairs (the triplet predicted to lie ~ $22{,}000 \times (n^*)^{-3}$ cm^{-1} below the singlet[20]). Triplet components of the intermediate state can either accelerate or retard the overall production of $\tilde{A}$-state C_2H, depending upon the oscillator strength and homogeneous linewidth of the $^3R_g \leftarrow T_n$ transition, and the extent to which the frequency used to pump this transition (fixed by the constraint of one color double resonance) is detuned from the center of the line.[21] Participation by the ^3R_g state further influences NIR emission intensity by possibly affecting the branching ratio for predissociation to C_2H $\tilde{A}$ - *vs.* $\tilde{X}$ - state products.

We see that the NIR intensity could be influenced both by the amount of triplet admixture in an eigenstate and by the identity of the triplet perturber(s). Moreover, each J'-level represented in the $\tilde{A}\ ^1A_u \leftarrow \tilde{X}^1\Sigma_g^+$ spectrum is subject to perturbation by a *distinct* group of accidentally isoenergetic triplet states.[10] Consequently, triplet contributions to the NIR signal will vary *completely unsystematically* with J'. On the other hand, the singlet-mediated component of the NIR signal depends on J' in a *completely predictable* way: only the $\tilde{A}$-state portion of the initially excited eigenstate contributes to this NIR component, through resonant enhancement of C_2H $\tilde{A}$-state production. Therefore, the singlet-mediated NIR signal is expected (and observed) to follow the UV (C_2H_2 $\tilde{A} \rightarrow \tilde{X}$) signal, to within a constant proportionality factor (provided that anharmonic perturbations within the S_1 state are insignificant [22]). This is the key to interpreting the $3\nu_3$ fluorescence excitation spectrum; because

the NIR:UV intensity ratio is uniform throughout the observed subband, the NIR emission is free of contributions attributable to perturbing states.

By contrast, extensive triplet perturbations in the observed $3\nu_3$ ($V_0^3K_0^1$) subband are indicated by the large variations of the NIR:UV intensity ratio throughout regions of the spectrum known to be free of S_1 anharmonic perturbations. We conclude that the ν_3= 3, but not the ν_3 =2 state, interacts strongly with a special class of background triplet states that can either relax (*via* fluorescence to T_1) or be further excited (to a predissociated ^3R_g state), where the efficiency of the latter process differs from that of the corresponding singlet-mediated photodissociation.

One possible group of interacting triplet states consists of those in a region of energy and configuration space near the top of a linear or half--linear barrier to *cis*-trans isomerization.[4] Such triplet states have favorable FC overlap with the near-linear turning point of $\tilde{A}$-state vibrational levels that undergo large-amplitude motion in the *trans*-bending (ν_3) coordinate. This is the rationale given by Dupré *et al.* [7] for the monotonic increase of $S_1 \sim T$ coupling strength with ν_3 that was observed in Zeeman anticrossing experiments. Some of the $3\nu_3$ perturbations we invoke here could be due to triplet states trapped near a linear or half--linear configuration. Recent *ab initio* calculations[4] (which include zero-point energy) have located a linear ($^3\Delta_u$) stationary point on the $T_{2/3}$ surface about 300 cm^{-1} below the S_1 $3\nu_3$ level.[23] (Also predicted in this energy region on the T_3 surface is a half—linear stationary point associated with a C_s-symmetry *cis*-trans isomerization barrier.[4]) These triplet perturbers could thus facilitate $T_{2/3}$ (or T_3) $\rightarrow$ T_1 transitions occurring in the NIR. The $T_{2/3}$ ($^3\Delta_u$) state would also have enhanced FC overlap with the linear[24] ^3R_g states, causing the $^3R_g \leftarrow T_{2/3}$ oscillator strength to exceed

greatly that of the ^1R_g (linear[15]) ← S_1 (*trans*-bent) transition. Thus, mixed $S_1 \sim T_n$ eigenstates with significant $T_{2/3}$ ($^3\Delta_u$) character would be exceptionally effective in promoting NIR emission by accelerating the production of C_2H $\tilde{A}$-state. As outlined above, this type of anomaly could occur in the $3\nu_3$ band whenever a $T_{2/3}$ perturber is accidentally degenerate with a particular S_1 J'-state.

We also observe anomalies in the $3\nu_3$ fluorescence excitation spectrum that are attributable to a *nonlinear* perturber. Several intense rotational lines in the UV-detected spectrum show a *dramatically diminished* NIR response. These lines, labeled in Fig. 4 with $_e$ for "extra", are due to an S_1 anharmonic perturber of S_1 $3\nu_3$.[26,10]

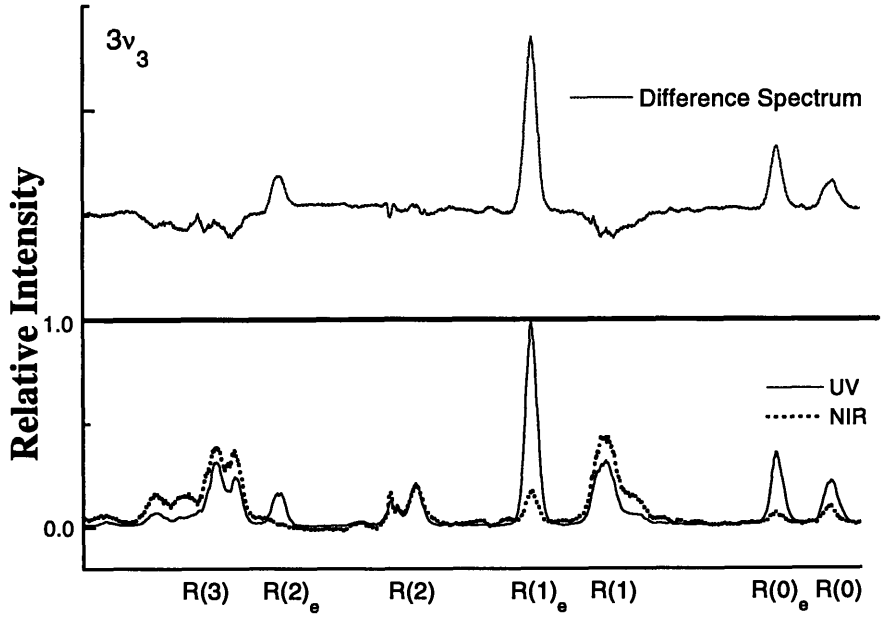

Figure 8.17: UV- and NIR-detected fluorescence excitation spectra, plotted as in Fig. 2, showing a region of the of the $V_0^3K_0^1$ subband that contains extra lines due to a previously characterized (Refs. 10,24,25) anharmonic perturber.

The perturbing state has recently been identified as $4\nu_b$, where ν_b represents either ν_4' (torsion) or ν_6' (antisymmetric in-plane bend), and $4\nu_b$ has A_g vibrational symmetry.[25] The large-amplitude angular excursions (without a near-linear turning point) occurring in this state lead to smaller FC factors, for both the $S_1 \leftarrow S_0$ and $^1R_g \leftarrow S_1$ transitions, than those involving the $3\nu_3$ level. Consequently, the C_2H production and resulting NIR emission are suppressed for the extra lines which have predominant $4\nu_b$ character. Moreover, triplet-mediated NIR contributions are expected and observed to be absent for these extra lines, which have been observed by very high resolution fluorescence excitation to be free of triplet perturbations.[10]

The $3\nu_3$ and $4\nu_b$ states are closest in energy for J'=1 and tune out of resonance with increasing J', due to the difference in the B-rotational constants.[26,10] This leads to an undetectably small NIR signal for the J' > 2 extra lines, which have greater than 90% $4\nu_b$ character.[26] In contrast, the UV emission is detectable up to $R(4)_e$; in fact, the most intense R-branch feature in the UV detected spectrum is the $R(1)_e$ line, whose terminal state has about 75% $4\nu_b$ character. This reflects the considerably enhanced UV fluorescence quantum yield for mixed states, owing to their resistance to further excitation to a predissociated linear Rydberg state, combined with their undiminished capability for UV emission *via* fully FC-allowed $\tilde{A} \rightarrow \tilde{X}$ transitions.[26]

8.5 Preliminary Conclusions

In summary, the *trans*-bent acetylene $\tilde{A}^1A_u$ state participates in a variety of radiative and nonradiative processes, by virtue of favorable FC overlap with linear states. Simultaneous NIR/UV fluorescence detection of $\tilde{A} \rightarrow \tilde{X}$ transitions has shown that excitation of ν_3' overtone

levels, in addition to producing $\tilde{A} \rightarrow \tilde{X}$ emission, can lead to further excitation to linear and predissociated Rydberg states.

The $\tilde{A}$-state ν_3=3 level, as a consequence of its large-amplitude bending motion, indeed serves as the centerpiece for this remarkable array of photophysical processes. As originally hypothesized by Dupré *et al.*[7], the photophysics extends to the triplet manifold because significant *trans*-bending excitation in $3\nu_3$ affords enhanced vibrational overlap with triplet levels trapped near the top of a linear (or half--linear) isomerization barrier. Such triplet levels are predicted by recent *ab initio* calculations[4] to be nearly coincident with the $\tilde{A}$-state $3\nu_3$ level. Our detection of perturbation-facilitated inter-triplet ($T_n \rightarrow T_1$ or $^3R_g \leftarrow T$) transitions, upon excitation of $3\nu_3$, is fully consistent with the *ab initio* calculations[4] and predicted FC propensities.

8.6 Recent Work

Further studies[28] on the proposed $S_1 \sim T$ interactions in the $\tilde{A}^1A_u$ state have been conducted using laser excited metastable (LEM) and fluorescence excitation (FE) spectroscopies. In these experiments, Humphrey *et al.* simultaneously recorded the LEM and FE spectra for several vibronic subbands of the C_2H_2 $\tilde{A}\ ^1A_u \leftarrow \tilde{X}^1\Sigma_g^+$ transition. The LEM signal is produced by the Auger effect, in which an excited molecular species has electronic excitation, T_0, that is greater than the workfunction, ϕ, of a metal surface. Furthermore, this LEM signal is particularly sensitive to metastable species due to a molecular beam flight time, τ, which is greater than the S_1 radiative lifetime, 250 ns.

Humphrey *et al.* discovered that the $S_1 \sim T$ interactions were due to a "gateway mediated intersystem crossing", where the S_1 state interacts strongly with the T_3 state. The T_3 state is

coupled a to dense manifold of T_2, T_1, and possibly S_0 states. The $S_1 \sim T_3$ interactions are observed for each vibronic subband. The $V_0^3K_0^1$ subband shows a much more extensive $S_1 \sim T_3$ interaction relative to the other subbands.[28] The experiments presented in the main part of this chapter *also* point to the special nature of the $V_0^3K_0^1$ subband in promoting strong $S_1 \sim T$ interactions. Quantitative characterization of the $S_1 \sim T$ interactions by the UV:NIR fluorescence studies were hampered by the presence of NIR fluorescence from the C_2H $\tilde{A}^2\Pi \rightarrow \tilde{X}^2\Sigma^+$ transition. Using time of flight properties, the LEM and FE experiments were able to exclude any effects of metastable photodissociation fragments.

Perturbation facilitated stimulated emission pumping (PF-SEP) experiments were proposed, prior to the LEM and FE experiments, to probe $S_1 \sim T_3 \rightarrow T_1$ transitions. The results of the LEM and FE experiments suggest why PF-SEP is, in fact, infeasible using traditional fluorescence dip detected SEP. Prior to the LEM results, we thought that the observable signal for the$T_3 \rightarrow T_1$ PF-SEP would have been limited by the amount of S_1 character in the T_3 basis state.

$$\Psi = a_{S_1}\varphi_{S_1} + b_{T_3}\varphi_{T_3} \quad .$$

Since, the S_1 character contains the allowed optical oscillator strength of the pump transition, a successful experiment would have to optimize the amount of S_1 and T_3 character in any given eigenstate to maximize the amount of triplet character and minimize the amount of singlet character. However, if we were to have chosen an intermediate state that had 1% S_1 character, there would be 99% triplet character. The number density of T_3 molecules populate by the pump laser is limited by the S_1 character. Therefore we tried to locate S_1 transitions that would be close to 50% of both singlet and triplet character. We believed that this would be the best intermediate

state for PF-SEP. However, the results of the LEM experiment show that this picture is somewhat simplified! In fact, the T_3 character, which acts as a chromostate or ZOBS, is coupled to a dense manifold of $T_3 \sim T_{1,2}$ interactions diluting the amount of T_3 character!

$$\Psi = \phi_{T_3} + \sum_{i=1}^{N} c_i \phi_{T_{1,2}} .$$

The dilution of the T_3 character effectively decreases the allowed oscillator strength in the $T_3 \rightarrow T_1$ transitions observable in a fluorescence dip experiment. Traditional SEP is only able to detect features which provide at least 0.1% fluorescence depletion. Because of the dilution effect, the $T_3 \rightarrow T_1$ transitions were most likely below this detectable limit. A variant of SEP, frequency modulated stimulated emission puming (FM-SEP) which has a significantly higher sensitivity range could be useful in probing these weak transitions. Our group has proposed many additional experiments to probe the low lying triplet states in acetylene.

8.7 References:

1. J.K. Lundberg, R.W. Field, C.D. Sherrill, E.T. Seidl, Y.Xie, and H.F. Schaefer, *J. Chem. Phys.* **98,** 8384 (1993).

2. Y. Yamaguchi, G. Vacek, J.R. Thomas, B.J. Deleeuw, and H.F. Schaefer III, *J. Chem. Phys.* **100**, 4969 (1994).

3. C.D. Sherrill, G. Vacek, Y. Yamaguchi, and H.F. Schaefer III, „*J. Chem. Phys.*, in press.

4. G. Vacek, C.D. Sherrill, Y. Yamaguchi, and H.F. Schaefer III, „*J. Chem. Phys.*, in press.

5. H.R. Wendt, H. Hippler, and H.E. Hunziker, *J. Chem. Phys.* **70,** 4044 (1979).

6. K. Tanigawa and H. Kanamori, 50th International Symposium on Molecular Spectroscopy, Talk FD03, Columbus, Ohio, 1995.

7. P. Dupré, R. Jost, M. Lombardi, P.G. Green, E. Abramson, and R.W.Field, *Chem. Phys.* **152,** 293 (1991).

8. P. Dupré and P.G. Green, *J. Chem. Phys.* **212**, 555 (1993).

9. N. Ochi and S. Tsuchiya, *Chem. Phys.* **152**, 319 (1991).

10. M. Drabbels, J. Heinze, and W.L. Meerts, *J. Chem. Phys.* **100**, 165 (1994).

11. Li Li and R.W. Field, *J. Phys. Chem.* **87**, 3020 (1983).

12. W.H. Press, S.A. Teukolsky, W.T. Vetterling, and B.P. Flannery, , em Numerical Recipes in FORTRAN, 2nd ed. (Cambridge University Press, New York, 1992).

13. D.M. Jonas, S.A.B. Solina, B. Rajaram, R.J. Silbey, R.W. Field, K. Yamanouchi, and S. Tsuchiya, *J. Chem. Phys.* **99**, 7350 (1993).

14. At the acetylene pressure of 150 mT used in this experiment, several collisions could occur during the fluorescence lifetime of ^1A_u $3\nu_3$ levels; see E. Abramson, C. Kittrell, J.L. Kinsey, and R. W. Field, *J. Chem. Phys.* **76,** 2293 (1982).

15. M. Takahashi, M. Fujii, and M. Ito, *J. Chem. Phys.* **96**, 6486 (1992).

16. M.N.R. Ashfold, B. Tutcher, B. Yang, Z.K. Jin, and S. L. Anderson, *J. Chem. Phys.* **87**, 5105 (1987).

17. Y.-C. Hsu, M.-S. Lin, and C.-P. Hsu, *J. Chem. Phys.* **94**, 7832 (1991).

18. F. Shokoohi, T.A. Watson, H. Reisler, F. Kong, A.M. Renlund, and C. Wittig, *J. Phys. Chem.* **90**, 5695 (1986).

19. E. Abramson, C. Kittrell, J.L. Kinsey, and R.W. Field, *J. Chem. Phys.***76**, 2293 (1982).

20. This estimate was based on singlet-triplet splitting parameters for isoconfigurational N_2 given in R.W. Field, A. Lagerqvist, and I. Renhorn *Physica Scripta* **14**, 298 (1976), and references therein.

21. The oscillator strength for the $^3R_g \leftarrow T_n$ transition is diluted among the states in the predissociation continuum comprising the homogeneous linewidth. Hence the effective oscillator strength is greatly diminished if our narrow-band laser excites far into the wings of the predissociation-broadened line.

22. $\tilde{A}$-state anharmonic perturbers of the ν_3 overtone state would affect the $^1R_g \leftarrow S_1$ oscillator strength and would thereby alter the NIR intensity.

23. This notation signifies that the T_2 and T_3 surfaces share the orbitally degenerate $^3\Delta_u$ stationary point.

24. Linear geometries have been established experimentally for both the $C_2H_2^+$ $\tilde{X}$ state and C_2H_2 ^1R_g states.[15] Hence the Rydberg orbital interacts so weakly with the ion core that it provides negligible stabilization *via* bending. Accordingly, the C_2H_2 ^3R_g states are expected to be linear.

25. A.L. Utz, J.D. Tobiason, M.E. Carrasquillo, L.J. Sanders, and F.F. Crim, *J. Chem. Phys.* **98**, 2742 (1993).

26. G.J. Scherer, Y. Chen, R.L. Redington, J.L. Kinsey, and R.W. Field, *J. Chem.Phys.* **85**, 6315 (1986).

27. C.K. Ingold and G.W. King, J. Chem. Soc., 2725 (1953).

28. S.J. Humphrey, C.G. Morgan, A.M. Wodtke, K.L. Cunningham, S. Drucker, R.W. Field, J. Chem. Phys. **00,** 0000 (1997).

6293-15